Design van stents met eindige elementen

Finite Element Stent Design

Matthieu De Beule

UNIVERSITEIT
GENT

Supervisors:

Prof. Dr. ir. Rudy Van Impe (promotor)
Prof. Dr. ir. Pascal Verdonck (promotor)
Prof. Dr. ir. Benedict Verhegghe

Examination Committee:

Prof. Dr. ir. L. Taerwe (chairman)	Ghent University
Prof. Dr. ir. B. Verhegghe (secretary)	Ghent University
Prof. Dr. Eng. F. Auricchio	Università di Pavia (I)
Prof. Dr. ir. J. Degrieck	Ghent University
Dr. ir. F. Gijsen	Erasmus MC Rotterdam (NL)
Prof. Dr. ir. P. Segers	Ghent University
Prof. Dr. Y. Taeymans	Ghent University Hospital
Prof. Dr. ir. R. Van Impe	Ghent University
Prof. Dr. ir. P. Verdonck	Ghent University
Prof. Dr. F. Vermassen	Ghent University Hospital

Research Units:

LMO	IBiTech
Faculty of Engineering	Faculty of Engineering
Ghent Universtity	Ghent University
Technologiepark-Zwijnaarde 904	De Pintelaan 185 - Blok B5
B-9052 Zwijnaarde	B-9000 Gent
Belgium	Belgium
	Tel: +32 (0)9 332 43 20
	Matthieu.DeBeule@UGent.be
	www.stent-IBiTech.UGent.be

To my beautiful wife, Mu,
and to Milla and Noa,
(really) the loveliest kids in the world
who have disrupted and enriched my life
more than I ever could have imagined.

Acknowledgements

Finally I would like to express my gratitude to my family and parents for the constant support and to all of my (soccer and other) friends for being curious to know how this thesis advanced, for the fun we had and for looking after the kids while I was abroad, working on 'my book' or spending some well deserved quality time with my wife, Mu. Which brings me to my last (but most important) thank you note! Mu, you intimately know both the joys and sacrifices that have accompanied this path. Really thank you for your continuous support and encouragement and for your unfailing patience and unconditional love. THANK YOU for bringing Milla and Noa (early) into our lives. Their smiles and enthusiasm are the best possible relaxation you can imagine. Milla and Noa, dad's book is finally finished. I am sorry that I was not able to put one of your beautiful drawings in it, but I'll try to make it up to both of you.

Gent, Februari 2008

Matthieu

Contents

Samenvatting

Dé trend in de hedendaagse chirurgie is de evolutie naar minimaal invasieve technieken (Eng. Minimally Invasive Surgery (MIS)) waarbij slechts één of een paar zeer kleine insnijdingen nodig zijn in plaats van één grote zoals bij conventionele chirurgie. Via deze incisies kan de chirurg zeer kleine instrumenten en/of implantaten in het operatiegebied brengen. MIS heeft een heleboel voordelen voor bepaalde patiënten, zoals een kleiner litteken, een laag risico op infecties, een korter verblijf in het ziekenhuis en een snellere revalidatie. Belangrijke nadelen op dit moment zijn de grootte en manoeuvreerbaarheid van de instrumenten, de beperkte nauwkeurigheid bij het positioneren, de duur van de training van de chirurg en eventuele complicaties. Een hechte samenwerking tussen artsen en ingenieurs maakt het mogelijk om MIS ingrepen, implantaten en instrumenten nog verder te verbeteren via innovatieve computersimulaties.

Een mooi voorbeeld van MIS is het gebruik van stents voor het openen van slagadervernauwingen via een sneetje in de lies of de arm, heden een dagdagelijkse praktijk in de kliniek. Deze ingreep is voor de patiënten minder belastend in vergelijking met het plaatsen van een overbrugging. Op jaarbasis implanteren artsen wereldwijd dan ook meer dan één miljoen van deze 'hartveertjes'. Het gebruik van stents is vooral bekend voor, maar is niet beperkt tot het heropenen van slagadervernauwingen. Stents kunnen omhuld worden met een membraan om de beschadigde en uitgezette vaatwand van aneurysmas te beschermen tegen verdere uitzetting ten gevolge van de bloeddruk. Verder kunnen vernauwingen in de slokdarm en het spijsverteringsstelsel via stents minimaal invasief verholpen worden. Ook vernauwingen van de lucht- en urinewegen zijn behandelbaar met stents. Gezien het zeer ruime toepassingsgebied is het niet verwonderlijk dat er momenteel een enorm aanbod van stents bestaat in een grote verscheidenheid aan materialen, concepten en expansiemechanismen. Ondanks dit (over)aanbod blijven belangrijke tekortkomingen van deze techniek bestaan: (i) het na verloop van tijd terugkeren van de vernauwing, (ii) migratie van de stent, (iii) beperkte nauwkeurigheid bij het positioneren, enz. Bijgevolg is verder onderzoek naar deze levensreddende implantaten noodzakelijk om op termijn de huidige tekortkomingen te overwinnen.

Een veelbelovende ontwerptechniek in de zoektocht naar de 'ideale' stent is computergesteund ontwerpen (Eng. Computer Aided Design (CAD)). Computersimulaties maken het mogelijk om zeer snel van idee tot product over te gaan zonder tijdrovende 'trial and error' experimenten, zeker wanneer deze experimenten heel moeilijk of nagenoeg onmogelijk zijn (bv. door de kleine afmetingen, de kostprijs). Op die manier kan de ontwerper vlug verschillende designs met elkaar vergelijken en zo de impact van de vorm en het materiaal van de stent nagaan, zonder telkens deze voorlopige ontwerpen te moeten fabriceren. Concreet betekent dit dat a priori kan gekeken worden of het nieuwe concept voldoet aan de vooropgestelde vereisten (bv. is de stent sterk genoeg, flexibel genoeg, etc.). Daardoor verkort het ontwerpproces van de stents en wordt de kostprijs ongetwijfeld gereduceerd. Naast de belangrijke informatie die dit computermodel levert bij het ontwerp van nieuwe stents, kan het ook gebruikt worden om verschillende stents (bv. van verschillende fabrikanten) objectief met elkaar te vergelijken. Door de verschillende stents virtueel aan exact dezelfde testen te onderwerpen, krijgen ingenieurs en artsen een objectief beeld van hoe de ene stent zich gedraagt ten opzichte van een andere waardoor ze extra informatie krijgen om de juiste stent voor de juiste patiënt te kiezen.

In dit doctoraatsonderzoek werd een virtuele ontwerpomgeving gecreëerd om via de eindige elementenmethode de mechanische eigenschappen van stents te onderzoeken en te optimaliseren. Deze generieke ontwerpomgeving is toepasbaar voor zowel ballon- als zelfexpandeerbare stents in een grote verscheidenheid aan materialen (bv. roestvast staal, kobalt-chroom, nitinol, enz.) en fabricatietechnieken (uit buis snijden, vlechten). In het inleidende **Hoofdstuk 1** worden een aantal basisbegrippen van de vaatziekte atherosclerosis verduidelijkt en een aantal mogelijke behandelingen voor uitgesproken vaatvernauwingen (als gevolg van deze vaatziekte) besproken. De nadruk wordt gelegd op de minimaal invasieve aanpak waarbij het bloedvat wordt heropend met een stent en een aantal (huidige) tekortkomingen van deze techniek worden toegelicht. Het creëren van een virtuele omgeving om via computersimulaties deze tekortkomingen aan te pakken wordt vervolgens gedefinieerd als het doel van dit onderzoek.

Aangezien het goed begrijpen en gebruik maken van de bestaande kennis een essentieel startpunt is bij onderzoek, wordt een globaal beeld geschetst van de state-of-the-art wat betreft eindige elementenmodellering van stents in **Hoofdstuk 2**. In eerste instantie worden de basisprincipes voor het modelleren van stents bondig beschreven, gevolgd door een literatuurstudie (1997 - 2007) betreffende computationele studies over het mechanisch gedrag van ballon opblaasbare stents. Vervolgens wordt een aantal alternatieve methodes besproken om eigenschappen van stents te bestuderen (bv. zelf expandeerbare stents, numerieke stromingstechnieken, enz.). Finaal wordt een aantal toekomstperspectieven wat betreft stentmodellering geschetst. Uit deze literatuurstudie blijkt duidelijk dat de eindige elementen meth-

ode een enorm potentieel heeft voor het verbeteren van de huidige mini-maal invasieve technieken om (bloed)vaten te heropenen. Het toepassen van dergelijke numerieke technieken in dit onderzoeksdomein is zeer recent (1997) en heeft de laatste jaren een enorme evolutie gekend. Zonder enige twijfel hebben alle besproken artikels bijgedragen tot de huidige kennis over het ontwerp en gebruik van stents en moeten deze studies vanzelfsprekend gekaderd worden binnen de beschikbare voorkennis en computerkracht (van het moment van publicatie). In de beginjaren werden de studies vooral uitgevoerd met de *Palmaz-Schatz* stent (Johnson & Johnson) en vereenvoudigde (symmetrische) modellen van vernauwingen, vermoedelijk gedreven door de eenvoud van de geometrie (bv. het pionierswerk van Auricchio et al. [1]). Tevens was de *Palmaz-Schatz* stent de enige stent die gebruikt werd in grote klinische studies in de beginjaren. Sindsdien is deze numerieke (r)evolutie gekenmerkt door een aantal belangrijke mijlpalen, zoals (i) de introductie van patiëntspecifieke modellen van vaatvernauwingen door Holzapfel en zijn medewerkers in 2000 [2], (ii) het bestuderen van nieuwe stentdesigns door Migliavacca et al. in 2002 [3] en het introduceren van optimalisatietechnieken door Timmins en zijn collega's in 2007 [4]. Een vaak terugkerend fenomeen in talrijke studies is echter het ontbreken van experimenteel bewijs voor de numerieke resultaten, wat een (begrijpelijke) sceptische reactie uitlokt ten opzichte van numerieke modellen en de daaruit voortvloeiende conclusies. De weinige validatie die wordt beschreven is voornamelijk kwalitatief en dus niet altijd geschikt voor het volledig interpreteren en verifiëren van de numerieke resultaten. De enige consistente kwantitatieve validatie met betrekking tot de vrije expansie van ballon opblaasbare stents is beschreven door Migliavacca et al. [5] en toont duidelijk aan dat er een wezenlijk verschil is tussen de numerieke resultaten en de realiteit wanneer de ballon uit het model wordt weggelaten.

In **Hoofdstuk 3** worden verschillende numerieke testen beschreven om het mechanische gedrag van ballon opblaasbare stents te bestuderen. In eerste instantie werd een realistisch en gevalideerd model opgesteld om de expansie van angioplastie ballonnen te onderzoeken. De voorgestelde techniek laat toe om benaderende materiaaleigenschappen en randvoorwaarden (die de tapse uiteinden van de ballon simuleren) op te stellen voor de ballon enkel en alleen op basis van de druk-diameter gegevens van de fabrikant. De numerieke resultaten sluiten zeer mooi aan bij experimentele gegevens van de fabrikant en bijgevolg is het voorgestelde ballon model een waardevolle component voor het opstellen van realistische modellen van ballon opblaasbare stents. Vervolgens worden verschillende expansie strategieën vergeleken voor een in de huidige kliniek gebruikte coronaire stent. In de beginfase van het stentontwerp kan een expansie gedreven door een verplaatsingsgestuurde cilindrische ballon zeer nuttige en relatief nauwkeurige informatie leveren omtrent de vorm van de stent in de geëxpandeerde toestand. Wanneer men echter het stent ontwerp wil verbeteren qua expan-

sie eigenschappen lijkt de voorgestelde strategie waarbij rekening gehouden wordt met de opplooivorm van de ballon vele voordelen te hebben aangezien deze expansie gekarakteriseerd wordt door het ontplooien en expanderen van de ballon. Bovendien vertoont deze strategie zeer goede overeenkomsten met data van de fabrikant en uitgevoerde experimenten. Daarnaast is de impact van de lengte van de ballon, de opplooivorm en de positie van de stent op de ballon op de expansie van de stent onderzocht. Daaruit blijkt dat zowel de ballonlengte als de opplooivorm het transiënte expansie gedrag van de stent enorm kunnen beïnvloeden. Bijgevolg kan via de voorgestelde technieken de optimale ballonlengte en opplooivorm gekozen worden voor een bepaald stent ontwerp. Voorts kunnen kleine onnauwkeurigheden bij het positioneren van de stent op de ballon het expansiegedrag aanzienlijk wijzigen. Bijgevolg moet dit positioneren gebeuren met grote nauwkeurigheid. Ten slotte wordt een nieuwe virtuele ontwerpomgeving voorgesteld waarbij parametrisch modelleren (met pyFormex) gecombineerd wordt met eindige elementensimulaties om flexibiliteit, expansie en radiale sterkte van stents te onderzoeken. Deze ontwerpomgeving kan het design proces aanzienlijk verkorten en laat toe om zeer snel variaties van het originele prototype te evalueren. Het toepassen van deze techieken op de commercieel beschikbare *Cypher* stent onthult dat zowel de flexibiliteit als de radiale sterkte verbeterd kan worden door het design aan te passen (reduceren van het aantal bochten van zes naar vijf). Deze geometrische wijziging verhoogt echter de verkorting van de stent en kan vermoedelijk ook het gebruik van dezelfde stent met andere (grotere) ballonnen limiteren.

Zowel een analytisch als een numeriek kader om het mechanische gedrag van zelf expandeerbare gevlochten draadstents onder complexe (maar realistische) belastingsconditie te onderzoeken is beschreven in **Hoofdstuk 4**. Eerst worden de fundamentele mechanische concepten van draadstents toegelicht en wordt het analytische model voorgesteld. De (gecorrigeerde) analytische formules verschaffen bruikbare informatie voor metallische (elastische) materialen, eenvoudige vlechtpatronen en ongecompliceerde belastingsgevallen. De theoretische voorspellingen van het mechanische gedrag zijn experimenteel bevestigd en laten toe om de stijfheid, de verkorting, het contactoppervlak van de stent en de mechanische spanningen in de draden te begroten. Vervolgens wordt uitgeweid over een innovatieve script gebaseerde aanpak voor het bestuderen van draadstents aan de hand van parametrisch aanpasbare geometrische en eindige elementen modellen met pyFormex. Deze aanpak laat toe om gevlochten draadstents met arbitraire geometrie en materiaal en onder complexe belastingsconditie te bestuderen. Op een zeer efficiënte manier kunnen immers vele varianten van de originele geometrie gegenereerd worden wat een essentiële vereiste is voor doeltreffend stent design. Deze methodiek wordt toegepast op de *Urolume (Wall)stent* en parametrisch aanpassen van de originele geometrie leidt tot de volgende ontwerp aanbevelingen: (i) zowel het verhogen

van de draaddiameter als het aantal draden verhoogt de stijfheid van de stent (axiaal en radiaal), (ii) het verhogen van de hoek tussen de gevlochten draden doet de axiale stijfheid toenemen en de radiale stijfheid dalen, (iii) de draaddiameter is de belangrijkste parameter voor het (af)regelen van de stijfheid van de stent en (iv) de verkorting van de stent daalt bij toenemende vlechthoek, maar is onafhankelijk van de draaddiameter en het aantal draden. Vervolgens wordt de interactie van de stent met de positioneringscatheter van naderbij bekeken en deze studie toont aan dat plastische vervorming van de stent te allen tijde vermeden moet worden, aangezien deze het mechanische gedrag en de performantie van de stent serieus beinvloedt. Het (experimenteel gevalideerde) numerieke model is in staat om deze ongewenste plastische vervormingen te voorspellen en dus kunnen zowel catheter afmetingen als stent materiaal geëvalueerd worden. Elastische materiaaleigenschappen hebben een beperkte impact op de vorm van de stent wanneer die uit de catheter geschoven wordt. Naast parametrisch modelleren biedt de virtuele ontwerpomgeving voor draadstents ook de mogelijkheid om efficiënte optimalisatiealgoritmes uit te voeren. Bijgevolg is het mogelijk om belangrijke stent eigenschappen doelgericht te verbeteren door te variëren in relevante geometrische ontwerpparameters (draaddiameter, aantal draden en vlechthoek). Om de precieze positionering van de *Urolume* endoprothese te verbeteren door de verkorting van de stent met 20 % te verminderen terwijl radiale stijfheid en draadoppervlak behouden blijven, stelt het algoritme automatisch voor om de originele draaddiameter te vermeerderen van 0.22 mm tot 0.27 mm en de hoek van 30.85 ° tot 37.4 °. Ten slotte wordt de ontwikkelingsomgeving aangewend om het mechanische gedrag van een nieuwe generatie meerlagige 3D structuur stents te bestuderen aan de hand van reverse engineering. pyFormex heeft hierbij duidelijk bewezen geschikt te zijn voor het bestuderen van bestaande complexe stentontwerpen aangezien het de mogelijkheid biedt om nauwkeurige virtuele parametrisch aanpasbare modellen op te stellen (rechtstreeks op basis van de fabricagesoftware). Het mechanische gedrag van de meerlagige 3D structuur is onderzocht naar centrale radiale stijfheid. Over heel de lijn kwamen de numerieke en experimentele resultaten zeer sterk overeen waarbij een exponentiële toename in radiale stijfheid geobserveerd werd bij afnemende stent diameter.

Summary

The trend in contemporary surgery is the evolution toward minimally invasive techniques where smaller, more minute incisions are made, as opposed to traditional 'open' surgery. Through these small incisions (or keyholes) the surgeon is able to manoeuvre minuscule surgical instruments and/or implants to the target site. The advantages of Minimally Invasive Surgery (MIS) include: smaller cicatrice (or scars), less chance for infection and shortened hospitalization and rehabilitation time. However, the concept of MIS still has several disadvantages: the limiting size and manoeuvrability of the instruments, the limited positioning accuracy, the required training and experimentation and possible complications. A close collaboration between surgeons and engineers has the potential of improving MIS, implants and instruments by advanced computational models.

A good example of MIS is the use of stents to reopen arterial stenoses during a percutaneous (i.e. via needle-puncture of the skin) intervention, nowadays routine in clinical practice. This minimally invasive intervention has less impact on the patient's quality of life as compared to bypass surgery. Annually, over one million of stents are implanted world-wide. The use of stents is most known for, but certainly not limited to unblocking coronary arteries. Stents can be covered with a membrane and used to protect the injured and dilated regions of aneurysms from further expansion under the influence of the blood pressure. Furthermore, the majority of strictures in the esophagus and gastrointestinal tract can be treated with the use of minimally invasive alternatives to classic surgery such as balloon dilation or metallic stent deployment. In addition, the symptoms of tracheobronchial obstructions and urethral strictures can rapidly be alleviated by the use of stents. Given this wide range of applications, an enormous number of stents is available in current clinical practice in a variety of materials, concepts and expansion mechanisms. Despite this immense supply of stent designs, important limitations are still present: (i) reoccurrence of the stenosis, (ii) stent migration, (iii) limited positioning accuracy, etc. Consequently, further refinements of these life-saving devices are required to overcome these shortcomings.

A promising design strategy in the quest for the 'ideal' stent is Computer

Aided Engineering and Design (CAE and CAD). Complementary to experimental studies, computational models provide an excellent research tool to optimize the mechanical properties of a stent, especially when physical test methods are difficult or even impossible to implement (e.g. due to implant size, cost). Numerical simulations may sometimes be the only alternative. The main advantage of numerical modeling is that numerous 'What if?' scenarios addressing different materials and designs can easily be tested and evaluated before devices are actually manufactured. Consequently, the design can be evaluated a priori in terms of strength, flexibility, etc. which shortens the design process and undoubtedly influences the cost in a favourable way. In addition to the important information revealed by the computer model in the stent design phase, these computational models are also useful to compare different existing designs (e.g. from different manufacturers). Subjecting stents to exactly the same virtual tests offers engineers and physicians an objective comparison of the performance of the investigated designs, providing them with extra information to decide which stent to use for which patient.

In this thesis, a validated virtual design space is created to investigate and optimize the mechanics of stents with the finite element method. This general design tool is applicable to both balloon and self expandable stents in a variety of materials (stainless steel, cobalt-chromium, nitinol, etc.) and configurations (laser-cut, braided). In the introductory **Chapter 1** some basic knowledge of atherosclerosis and possible treatments for severe stenoses (resulting from this disease) are briefly discussed. The main focus is put on the minimally invasive option, restoring the vessel lumen with a stent, and some drawbacks of this procedure are given. Developing a virtual environment to overcome the current shortcomings is subsequently defined as the aim of this work.

As understanding of and taking advantage of the existing knowledge is essential, the progress that has already been made by other scientists regarding (finite element) modeling of stents is reviewed to provide an overall picture in **Chapter 2**. First, the basics of stent modeling are briefly described, followed by a survey (1997 - 2007) regarding solid mechanical computational models of balloon expandable stents. Subsequently, alternative approaches to study the (bio)mechanical behavior of stents are described (e.g. self expandable stents, computational fluid dynamics, etc.). To conclude, future prospects for stent modeling are briefly addressed. From this review, it is obvious that the finite element method offers numerous possibilities in the optimization of (coronary) revascularization procedures. The application of such a numerical approach in this specific biomechanical research domain is quite recent (1997) and has known an enormous evolution during the last couple of years. Undoubtedly, all reviewed papers have contributed to the current level of understanding of the mechanics of both stent designs and angioplasty procedures and the quality of these studies should be evaluated

taking the available prescience and computational facilities (at the moment of publication) into account. In the early years, numerical simulations were based on the *Palmaz-Schatz* (Johnson&Johnson) like stent and simplified symmetrical stenosed arteries, mainly due to their straightforward geometry (e.g. the pioneering study published by Auricchio et al. [1]). Furthermore, the *Palmaz-Schatz* stent was the only stent used in a multitude of large clinical studies at that time. Since then this numerical (r)evolution is characterized by some important milestones, such as (i) the introduction of patient-specific stenosis models by Holzapfel and co-workers in 2000 [2], (ii) the introduction of next generation stent geometries by Migliavacca et al. in 2002 [3] and the introduction of stent design optimization techniques by Timmins and his colleagues in 2007 [4]. However, an observed fact in numerous studies is the lack of experimental evidence for the obtained numerical results, creating a missing-link with reality and provoking an (understandable) skepticism with respect to numerical models and to the conclusions drawn from them. The little validation that is performed is often merely qualitatively, and thus not always applicable to interpret and verify the numerical results. The only consistent quantitative validation regarding the free expansion of stents is from Migliavacca et al. [5], showing the considerable discrepancy between numerical results and reality when discarding the presence of the balloon.

In **Chapter 3**, several computational bench-mark tests are described to study the mechanical behavior of balloon expandable stents. First, a realistic and validated model is developed to study the expansion of folded angioplasty balloons. The proposed methodology allows to determine approximate balloon material properties and appropriate boundary conditions (which mimic the balloon tapering) based solely on the manufacturer's compliance chart. The numerical results show very good agreement with data provided by the manufacturer and consequently the proposed balloon model seems a valuable tool to study realistic balloon/stent interactions. Subsequently, different expansion modeling strategies are studied and compared for a new generation balloon expandable coronary stent. In the early stent-design phase, a radial displacement driven cylindrical balloon expansion can provide useful and (relatively) accurate information regarding the stent shape when reaching its nominal diameter. However, to further optimize the stent design in terms of its expansion, using the proposed trifolded balloon methodology seems to great advantage, since the free expansion of a stent is governed by the unfolding and expansion of the balloon. Moreover, the trifolded balloon expansion methodology shows very good quantitative and qualitative agreement with both manufacturer data and in-house experiments. In addition, the impact of balloon length, folding pattern and stent positioning on the stent expansion is examined in the proposed virtual design space. Changing the balloon length and/or folding pattern can have a significant influence on the transient stent expansion behaviour. Therefore,

the proposed methodology has the potential to select the most appropriate balloon length and folding pattern for a particular stent design. Furthermore, small positioning inaccuracies of the stent with respect to the balloon catheter can considerably modify the stent deployment. Consequently, the positioning of the stent on the balloon catheter should be done with the greatest care and accuracy. Finally, a computational stent design platform, combining parametric geometrical modeling (with pyFormex) with different finite element bench-mark tests to study stent flexibility, expansion and radial strength is presented. The developed design platform can shorten the design process significantly and allows easy evaluation of the original design and its variations. Applying the proposed virtual design tool to the *Cypher* stent reveals that both the flexibility and the radial strength can be increased by reducing the number of bends from six to five. However, this geometrical change increases the stent foreshortening and probably limits the use of the same stent geometry with larger balloon diameters.

Both a theoretical and numerical framework to investigate the mechanical behavior of braided wire stents under complex (though realistic) loading conditions is described in **Chapter 4**. First, the fundamental concepts regarding the mechanics of wire stents are enlightened and a dedicated analytical model to describe their mechanical response is proposed. The (revised) analytical model provides useful information regarding wire stent mechanics for metallic (elastic) materials, simple braiding patterns and straightforward load cases. The theoretical predictions of the stent mechanical behavior are experimentally confirmed and allow quantification of the stent stiffness, foreshortening, wire surface ratio and the (von Mises) stresses in the stent wires. Subsequently, an innovative pyFormex script-based approach for geometrical and finite element (parametric) modeling of wire stents is enlarged upon. This approach allows to study braided stents with arbitrary geometry and arbitrary material under complex loading conditions. The proposed modeling strategy easily generates lots of variations of the original geometry, an essential prerequisite for efficient stent design. In addition, the mechanical behavior of the *Urolume (Wall)stent* is studied in the developed framework, serving as a reference bench-mark to analyze geometrical variants. Parametrically adapting the original (bench-mark) geometry leads to the following design guidelines: (i) increasing the wire diameter and the number of wires increases the stent stiffness (axial and radial), (ii) increasing the pitch angle increases the axial, though decreases the radial stiffness, (iii) the wire diameter is the most important impact factor for stent stiffness regulation and (iv) the stent foreshortening, independent of the wire diameter and the number of wires, decreases with increasing pitch angle. Next, the interaction of the wire stent with its constraining catheter is investigated virtually and shows that plastic deformation during stent insertion in the catheter should be avoided as it compromises the stent delivery and (mechanical) performance. The (experimentally validated) numerical modeling tool is

able to predict these undesirable plastic deformations and, thus, allows for both material and catheter size evaluation. The elastic material properties do not significantly influence the stent shape exiting the catheter. In addition to parametric modeling, the developed virtual wire stent design tool is subsequently extended with an efficient design optimization algorithm. Consequently, it is feasible to reconcile competing stent characteristics in the quest for the 'perfect' stent by altering the relevant geometrical design variables (wire diameter, wire number and pitch angle). To facilitate precise positioning of the *Urolume endoprosthesis* by reducing the foreshortening with 20 %, while maintaining both the radial stiffness and the wire surface ratio, the algorithm automatically proposes to increase the original wire diameter from 0.22 to 0.27 mm and the pitch angle from 30.85 to 37.4 °. Finally, the virtual design tool is applied to study the mechanical behavior of a new generation multilayer *3D structure stent* by reverse engineering. pyFormex has proven to be a suitable tool for reverse engineering of complex existing stent designs as it allows to create parametrically adaptable accurate virtual models (directly from the manufacturing software). The mechanical behavior of the multilayer *3D structure stent* is examined in terms of central radial stiffness. Overall a close correlation between numerical and experimental results is obtained and an exponential increase in radial stiffness is observed with decreasing stent diameter.

Chapter 1

Introduction

NO body is perfect! Despite the evolution of the human body over millions of years, nature's 'trial and error' experiment has not yet resulted in perfection, leading in some cases to serious problems limiting normal life, or in the worst cases, leading to death. One of the main causes of death in the western world is atherosclerosis, a pathology disrupting the normal (healthy) arterial wall architecture.

1.1   Atherosclerosis

With exception of the wall of the small blood vessels (arterioles, capillaries and venules), the vessel wall consists of three distinct layers, the tunica intima, the tunica media and the tunica adventitia, as shown in Figure 1.1. The tunica intima is the thin layer closest to the lumen in healthy vessels, built up of a single layer of endothelial cells on a layer of connective tissue. The tunica media consists of smooth muscle cells surrounded by a matrix of elastin and collagen fibers, supplying mechanical strength to the intimal layer. The outermost layer, the tunica adventitia, forms a protective layer around the vessel. It consists of connective tissue with elastin and collagen fibers.

Atherosclerosis is an inflammatory vascular pathology and central in its developmental process (i.e. atherogenesis) stands the development of an atheromatous plaque, a fatty fibrotic sedimentation potentially with calcified parts, found between the tunica intima and media [7]. The (molecular) mechanism leading to atherosclerosis is not yet fully understood. However,
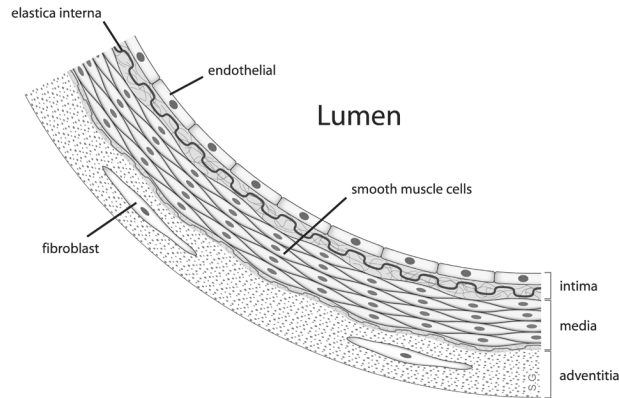
Figure 1.1: Structure and composition of the arterial wall [6].

it is known that injury of the endothelial layer and inflammatory processes play a central role in each phase of the atherogenesis [8]. The development of a plaque starts with a dysfunction of the endothelial wall [9]. More exactly, the permeability to the endothelial layer for active proteins, such as low density lipoprotein (LDL), changes. LDL is the transport medium of cholesterol and it is necessary for the metabolism of the muscle cells in the tunica media. However, this increase in permeability of LDL causes an accumulation of LDL between the tunica intima and media. Things start to go (really) wrong when part of this LDL oxidizes. The presence of oxidized LDL is directly correlated with the presence of plaques [10] and also triggers the release of phospholipids, which further activates the endothelial cells. In a complex process (details can be found in the work of Tedgui and Mallat [11]) monocytes migrate through the endothelial layer to the tunica media and differentiate into macrophage cells. The presence of the macrophages initiates a cascade process resulting in the migration of smooth muscle cells and the development of a fibrotic collagen cap around the plaque. The vessel wall tries to compensate for the presence of the plaque by vascular remodeling. Initially the exterior of the vessel grows, without narrowing of the lumen. However, in an advanced stage a considerable reduction of the lumen is seen. Such a narrowing of the lumen is called a stenosis [12] and the pathological evolution is depicted in Figure 1.2.

Atherosclerosis is one of the main causes of death in the western world. Indeed, a significant narrowing of the lumen of a stenosed vessel may induce oxygen deficiency in downstream organs and tissues, especially in the heart or in the brain. Another serious complication occurs when a part of the plaque breaks loose and blocks a downstream vessel (through thrombus
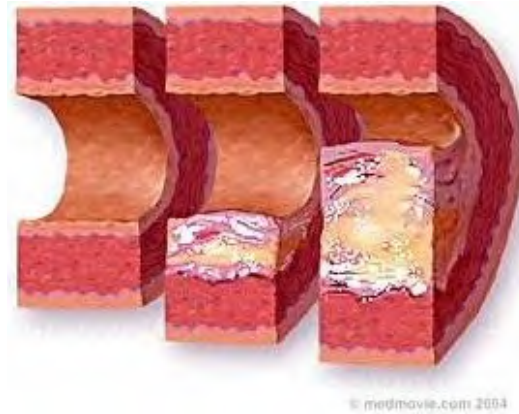
Figure 1.2: Progression of atherosclerosis: normal artery (left panel), mild atherosclerosis (middle panel) and severe atherosclerosis (right panel) [13].

and/or embolus formation). When the blood flow to (parts of) the heart is severely restricted, the portion of the heart muscle supplied by that artery becomes necrotic (this is known as a myocardial infarction or a heart attack). A severe obstruction of a cerebral artery can lead to a stroke, due to the death of brain tissue supplied by that artery. Risk factors of atherosclerosis include smoking, high blood pressure and diabetes [14, 15]. Both plaque content and development stage are important factors to determine the risk of plaque rupture, and thus morbidity and mortality. The American Heart Association (AHA) has set up criteria by which plaques are classified according to their content and structure [16]. It is important to differentiate young stable plaques with a low extracellular lipid content (that are not dangerous) from unstable more dangerous types prone to rupture. Besides prevention, identification of vulnerable plaques is therefore essential to enable the development of treatment modalities to stabilize such plaques. Current diagnostic modalities for vulnerable plaque detection and treatment are described by Schaar et al. [17] and Waxman and colleagues [18].

1.2   To stent or not to stent

Severe stenoses can be treated with bypass surgery, angioplasty and stent placement. With a bypass surgery the flow through the narrowed vessel is given a new pathway through a relocated blood vessel (e.g. Internal Mammary Artery) of the patient which is placed across the stenosis (see Figure 1.3). In case of a coronary stenosis this procedure requires a ster-

notomy[1] and the patient's heart is connected to a heart-lung machine which is used to provide circulation and oxygenate the blood while the heart is stopped by the surgeons to work on it. In some cases the operation can be done without the heart-lung machine, performing the surgery while the heart continues to beat (off-pump bypass surgery). Being an invasive surgical procedure, patients are usually admitted to an intensive care unit for one or two days and usually regain sufficient strength so that they can be discharged within 5 to 7 days after surgery [19].
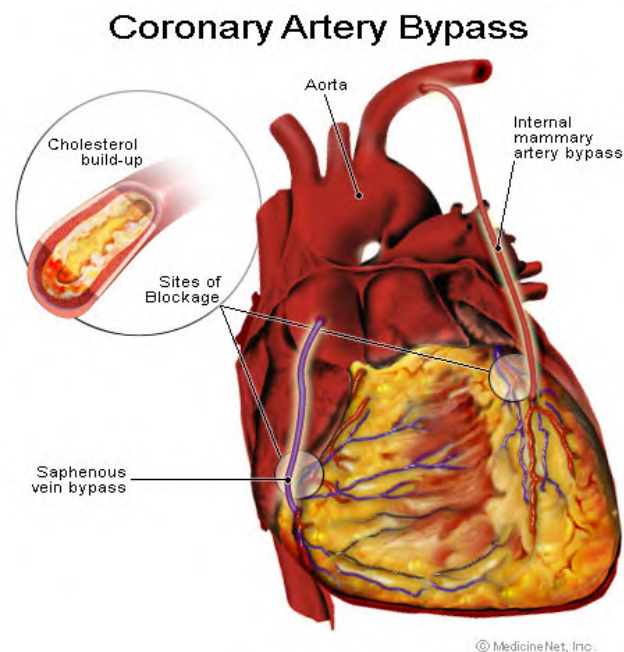
Figure 1.3: Bypass surgery: a section of a blood vessel is grafted from the aorta to the coronary artery to bypass the blocked section of the coronary artery and improve the blood supply to the heart [20].

In order to reduce the hospital stay, the risks and costs associated with (major) invasive surgery, stenoses can (depending on the clinical state of the patient) be treated with less (or minimal) invasive techniques such as angioplasty procedures (with or without stent). Angioplasty is a much less invasive technique first performed on September 16, 1977 by Andreas Gruentzig, dilating the stenosed coronary artery by balloon inflation (see Figure 1.4). This minimally invasive procedure consists of a balloon catheter insertion into the diseased vessel from a small incision in the femoral, radial

---

[1]A type of incision in the center of the chest that separates the sternum (chestbone) to allow access to the heart.

or brachial artery. The collapsed balloon catheter is positioned in the narrowed segment of the target vessel. Subsequently, the balloon is inflated and when the physician is satisfied with the achieved luminal gain, the balloon is deflated and the catheter removed (see Figure 1.5). Due to the limited invasive nature, the patient recovers faster compared to bypass surgery. However, two mechanisms limit the advantage of angioplasty over bypass surgery. On the short term elastic recoil from the vessel is seen as soon as the balloon is removed due to the energy released by the elastic fibers in the vessel wall after balloon deflation. On the long term restenosis (literally the reoccurrence of stenosis) of the vessel wall is responsible for renarrowing of the lumen. The major complications of balloon angioplasty relate in large part to arterial dissection and acute (abrupt) closure, which is most often due to arterial dissection. Some dissections result from overly vigorous attempts at guidewire passage, however most are due to the controlled injury induced by inflation of the dilation catheter. Dissections are found in 50 % of patients immediately after balloon angioplasty[21]. To overcome these complications, stent placement is performed in most percutaneous coronary procedures.
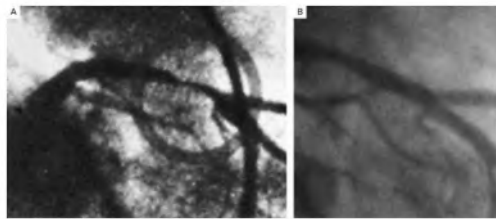
Figure 1.4: Coronary angiograms in a patient before the first human coronary angioplasty in 1977 (left panel) and normal patency at 23-year follow-up (right panel) [22].

An estimated 664000 percutaneous (i.e. via needle-puncture of the skin) coronary interventions were performed on 658000 patients in 2004 in the United States[2] to overcome the deficiency of oxygen-rich blood due to an obstruction of the coronary arteries (i.e. stenosis) [24]. Most of them involve the implantation of a stent (i.e. a mechanical supporting framework) to restore the perfusion of downstream heart tissue. This mechanical scaffolding device minimizes the possible luminal loss due to elastic recoil and possible dissections after balloon angioplasty. The majority of stents are balloon expandable and crimped on a folded (angioplasty) balloon to obtain a low crossing profile, which allows good deliverability and access through the coronary stenosis. After minimally invasive insertion into the stenosed artery, the stent is deployed by gradual inflation of the balloon. Upon

---

[2]From 1987 to 2004, the number of procedures increased by 326 %.
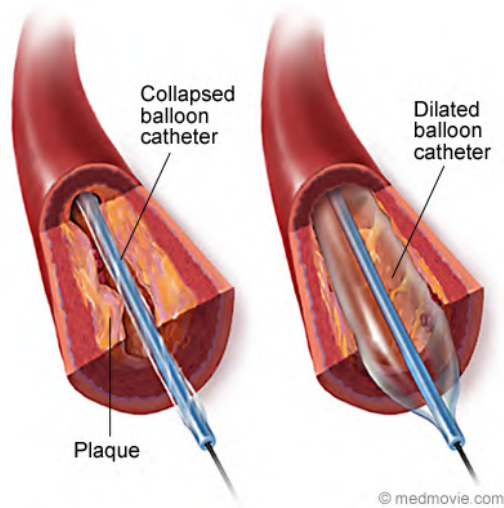
Figure 1.5: Angioplasty procedure: after minimally invasive positioning of the balloon catheter, the lumen is restored by balloon inflation compressing the plaque and/or stretching the disease free vessel side [23].

reaching the targeted deployment diameter, the stent delivery procedure is completed by deflating and extracting the balloon catheter. The plastically deformed stent is left in situ to keep the artery open and to restore (normal) blood flow (see Figure 1.6).

In recent years, advances in stent technology, in particular improving deliverability and flexibility, have expanded the clinical application of stenting to complex coronary lesions [25]. However, in 20 to 50 % of stenoses treated with Bare-Metal Stents (BMS), in-stent restenosis occurs and this phenomenon is partially linked to the stent design [26, 27] and balloon-artery interaction [28], partly to an inflammatory response of the vessel wall against the stent struts and in part to local hemodynamic factors such as wall shear stress [29]. In order to reduce in-stent restenosis rates, Drug-Eluting Stents (DES) - coated with specific anti- inflammatory and anti-proliferative agents - have emerged as a clinically better alternative for BMS. Despite the early promising results, reducing the restenosis rates to less than 10 % [30, 31, 32], it is important to highlight that the mechanical vascular injury by stent insertion is not eliminated with these recently developed pharmacological coatings. Basically, vascular injury is due to a combination of stent-artery and balloon-artery interactions, both of which depend among other things on the stent design [33, 28]. Examination of the patterns of endothelial damage shows a higher incidence of injured regions at the stent ends [34, 35]. This observation has been explained by Squire [35] as the re-
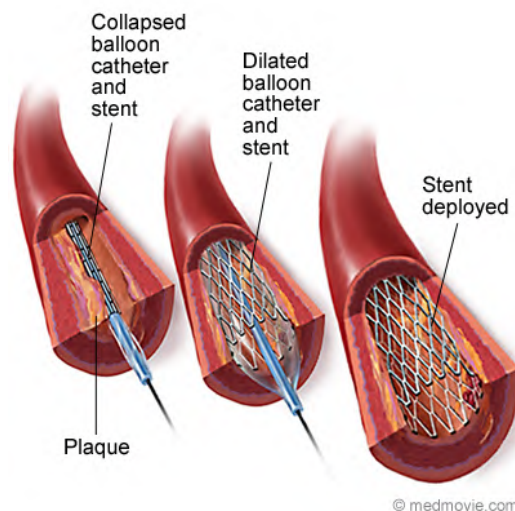
Figure 1.6: Balloon expandable stenting procedure: after minimally invasive positioning of the balloon catheter, the lumen is restored by balloon inflation deploying the (laser cut) stent in the stenosis. In general, the stent acts subsequently as a permanent scaffold maintaining the restored lumen. [23].

sult of three facts: (i) the stent expands in an non-uniform ends-first manner (dogboning), causing high local contact stresses, (ii) an axial contraction of the geometry during the stent expansion (foreshortening) and (iii) contact between the balloon, which is longer than the stent, and the artery. Furthermore, it was suggested in literature that restenosis after DES implantation may be partially related to non-uniform stent strut distribution [36]. This observation can be explained by the local drug concentrations and gradients, resulting from inhomogeneous strut placement [37]. In addition, both the cost-effectiveness of DES compared with new-generation BMS [38] and one year and beyond in-stent thrombosis (i.e. blood clot formation) risks after DES implantations [39] are nowadays important concerns. Finally, as the healing process of the vessel is considered to be temporary, the permanent metallic stents might rather be replaced by biodegradable stents. Therefore, further optimization of stent design, material and (drug) coatings is warranted to improve coronary revascularization procedures.

As stated by Balossino [40], surgeons have to provide the best possible operation in terms of safety, outcome and cost-effectiveness depending on the situation and the clinical state of the patient. Despite the succesfull evolution of percutaneous coronary interventions from balloon angioplasty, to bare-metal stents and the new drug-eluting stents in terms of reducing restenosis rates and the need for reintervention, the relief of the patient's symptoms has not still equalled that obtained with bypass grafting [41]. Nonetheless, a

randomized comparison between off-pump bypass surgery and (bare-metal) stenting revealed at 1 year that stenting was more cost-effective (26.2 % reduction of total cost per patient)[3] than off-pump surgery while maintaining comparable cardiac outcome and quality of life. Therefore, stenting can be recommended as a first-choice revascularization strategy in selected patients [42].

A rather complete survey regarding stent delivery, design requirements, classification and stent delivered therapies has recently been published by Lally and colleagues [43]. In general, stent designs can be categorized according to their expansion mechanism, geometrical shape and manufacturing process. Stents can be either balloon expandable (see Figure 1.6) or self expandable. Self expandable stents are retracted inside a delivery catheter and subsequently deployed by the gradual removal of this restraining catheter sheath. This elastic stent behavior can be explained by the stent material (a shape memory alloy [44]) and/or the geometrical design (e.g. a braided stent, see Figure 1.7).
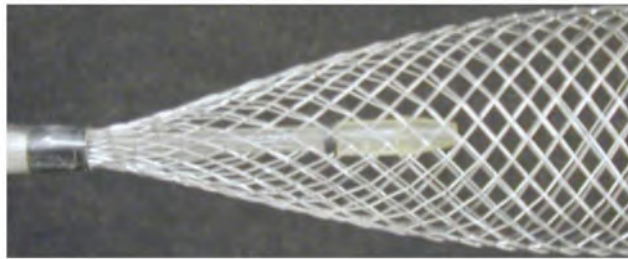
Figure 1.7: Self expandable (braided) stent deployment by the gradual removal of the catheter sheat [45].

From the introduction of this survey it is clear that the use of stents is certainly not limited to unblocking coronary arteries. Stents are nowadays also a minimally invasive treatment for stenosed peripheral arteries, including the carotid, cerebral and femoral arteries and to prevent rupture of aneurysms[4]. Furthermore, the majority of (benign and malignant) strictures in the esophagus and gastrointestinal tract can be treated with the use of minimally invasive alternatives to classic surgery such as balloon dilation or metallic stent deployment. Virtually any obstructing lesion in the esophagus, stomach, duodenum, colon and rectum can be treated with these

---

[3]Hospital stay after initial hospitalization was 1.43 days in the stent group and 5.77 days in the surgery group.

[4]Stents can be covered with PTFE (polytetrafluoroethylene) or polyester and used to protect the injured and dilated regions of aneurysms from further expansion under the influence of the blood pressure.

methods [46]. In addition, the symptoms of tracheobronchial obstructions (e.g. patients presenting with severe dyspnea, often to the verge of suffocation) can rapidly be alleviated by the use of airway stents [47]. Also urethral strictures and prostatic obstructions can currently be treated with stents [48]. However, some drawbacks of these minimally invasive procedures still need further attention (e.g. restenosis, stent migration, artery straightening, side branch covering, etc.) [32, 49, 50]. Therefore, further refinements of the current generation stents and dedicated stents designed to meet the specific behavior and geometry of the target lesion are required to overcome these shortcomings.

Complementary to experimental studies [51, 52, 53, 54], computational models provide an excellent research tool to optimize the mechanical properties of a stent, especially when physical test methods are difficult (or even impossible) to implement. Numerical simulations may sometimes be the only alternative. The main advantage of numerical modeling is that numerous 'What if?' scenarios addressing different materials, geometries and loading conditions can easily be tested and evaluated before devices are actually manufactured [55]. Therefore, computational models are a valuable part of the stent design and development process. As numerical models are always approximations of the physical reality, it is of utmost importance to validate the numerical results by (targeted) experiments.

1.3   Aim of the doctoral research

The main aim of this research is to create a validated virtual design space to investigate the mechanics and optimize the performance of stents using the finite element method. This design tool should be applicable to both balloon and self expandable stents in a variety of materials (stainless steel, cobalt-chromium, nitinol, etc.) and configurations (laser-cut, braided).

1.4   Organisation of the dissertation

Given the aim, the dissertation is organized as follows:

- Chapter 2: Literature review

  As understanding of the existing knowledge is essential, the research work that has already been done by others regarding (finite element) modeling of stents is reviewed to provide an overall picture. First, the basic principles of stent modeling are briefly described, followed by a survey (1997 - 2007) regarding state of the art solid mechanical computational models of balloon expandable stents. Subsequently,

alternative methodologies to study the (bio)mechanical behavior of stents are described and to conclude, future prospects for stent modeling are briefly addressed.

- Chapter 3: Balloon expandable stent design

  In this chapter, several numerical bench-mark tests are described to study the mechanical behavior of balloon expandable stents. First, a realistic and validated model is developed to study the expansion of folded angioplasty balloons based on the manufacturer's compliance chart. Subsequently, different expansion modeling strategies are studied and compared for a new generation balloon expandable coronary stent. In addition, the impact of balloon length, folding pattern and stent positioning on the stent expansion is examined in the proposed virtual design space. Finally, a computational stent design platform, combining parametric geometrical modeling with different finite element bench-mark tests to study stent flexibility, expansion and radial strength is presented. To allow parametric variation, the three-dimensional stent (geometrical) models are built with an in-house script-based geometrical and finite element preprocessor, called pyFormex[5] A brief description of pyFormex and its modus operandi can be found in Section 4.2.

- Chapter 4: Self expandable wire stent design

  Here, a theoretical and numerical framework is described to study the mechanical behavior of braided wire stents under complex (though realistic) loading conditions. First, the fundamental concepts regarding the mechanics of wire stents are enlightened and a dedicated analytical model to describe their mechanical response is proposed. Subsequently, an innovative pyFormex script-based approach for geometrical and finite element (parametric) modeling of wire stents is elaborated upon. This approach allows to study braided stents with arbitrary geometry and arbitrary material under complex loading conditions. In addition, the mechanical behavior of the *Urolume (Wall)stent* is studied in the developed framework, serving as a reference bench-mark, followed by analyzing geometrical variants. Next, the interaction of the wire stent with its constraining catheter is examined virtually and subsequently an optimization procedure is developed in the quest for a less shortening stent. Finally, the virtual design tool is applied to study the mechanical behavior of a promising new generation multilayer *3D structure stent* by reverse engineering.

---

[5]pyFormex, currently under development at Ghent University, is a tool for generating, manipulating and operating on large geometrical models of 3D structures by sequences of mathematical transformations [56].

- Chapter 5: Final remarks

  The original contributions of the doctoral study are outlined. Possible extensions to the presented design framework are discussed.

Chapter 2

Modeling of stents

We didn't start the fire.
—B. Joel

THE aim of this chapter is to provide an (educational) review on finite element modeling of stents. First, the basic principles of stent modeling are briefly described, followed by a survey (1997 - 2007) regarding state of the art solid mechanical computational models of balloon expandable stents. This review is organized chronologically according to the applied stent expansion methodology: (i) neglecting the presence of the balloon and (ii) assuming the balloon to have a cylindrical shape. Subsequently, alternative methodologies to study the (bio)mechanical behavior of stents are described and to conclude, future prospects for stent modeling are briefly addressed.

2.1   Introduction

In essence, (bio)mechanical modeling of stents can be categorized in three distinct domains. A first domain consists of numerical studies regarding the solid mechanical aspects of stenting (e.g. evaluation of the stresses in the vascular wall caused by stent deployment) based on the Finite Element Method (FEM). A second field studies the impact of the stent design (e.g. strut shape, interstrut distance, ...) on the blood flow patterns using Computational Fluid Dynamics (CFD). Finally, the kinetics of the drug release - in the case of DES - can also be examined numerically. Furthermore, the above described techniques can also be coupled (e.g. Fluid-Structure Interaction (FSI)), where the interaction between the fluid flow (CFD) and the structural response to this flow (FEM) is investigated[1]. This review focuses

---

[1]An interesting overview of existing fluid-structure interaction methods is given by Lanoye [57]

on FEM based studies dealing with the mechanical behavior of stents. In particular, the possible methods to simulate the stent expansion process and the validation of the numerical results are discussed in this work. For a more general bibliographical review of the finite element modeling and simulations in cardiovascular mechanics and cardiology, the paper of Mackerle [58] is recommended. The chapter organization is as follows: in paragraph 2.2, the basics of finite element stent modeling are briefly described. Next, paragraph 2.3 offers an overview of the state of the art regarding solid mechanical computational models of balloon expandable stents presented in literature to date (i.e. summer 2007). Subsequently, alternative methodologies for biomechanical modeling of stents are described in paragraph 2.4 and to conclude, future prospects for stent modeling are briefly discussed in paragraph 2.5.

2.2   Finite element modeling of stents

The basics of finite element stent analysis are well described by Perry et al. [55] and partly summarized hereafter. In general, a finite element model is defined by its geometry, material properties, and some appropriate loading and boundary conditions. To simulate the (free) expansion of balloon expandable stents, these prerequisites are described below. The accuracy of these prerequisites can, in many aspects, ensure the success of a simulation, or explain its failure. Finite element stent models are presently an important component of the design process. The actual practice has even evolved to the point that a detailed stress analysis is required by the regulatory agencies - such as the U.S. Food and Drug Administration (FDA) - prior to approval of a new stent design [59].

2.2.1   Finite element basics

Briefly stated, a Finite Element Analysis (FEA) is the investigation, by numerical means, of the mechanics of physical systems. The continuum (e.g. a stent) is divided into a finite number of discrete regions, named elements (Figure 2.1), whose behavior can be described mathematically. Partitioning the continuum into elements is generally automated through a special-purpose Graphical User Interface (GUI). An approximate solution of the entire continuum is solved from the assembly of the individual elements. The mechanical behavior (displacement, strain, stress, ...) in any point of an element is described in function of the behavior at a small number of control points (nodes) in the element. Usually, the displacements of the nodes are taken as the fundamental unknown quantities. At any other point in the element, the displacements are obtained by interpolating from the nodal displacements. The interpolation order is dependent upon the number of

nodes in the element. From the displacements, the strains are evaluated by taking the appropriate derivatives. The material constitutive behavior provides the necessary basis for computing stress levels from these strains. Application of the principle of virtual work to an element yields the forces exerted by the nodes on the element, which are statically equivalent with the built-up stresses, and by Newton's third law the actions of the element on a particular node are easily found. Force contributions from all elements connected to a particular node are summed up, and must be in equilibrium with any externally applied loading or force applied to the continuum.

Thus, the Finite Element Method essentially transforms the unknowns from the various continuous fields into equations of discrete nodal quantities. Assuming certain basic numerical requirements and standards of practice are satisfied, the solution obtained from the FEA estimates the exact physical solution.
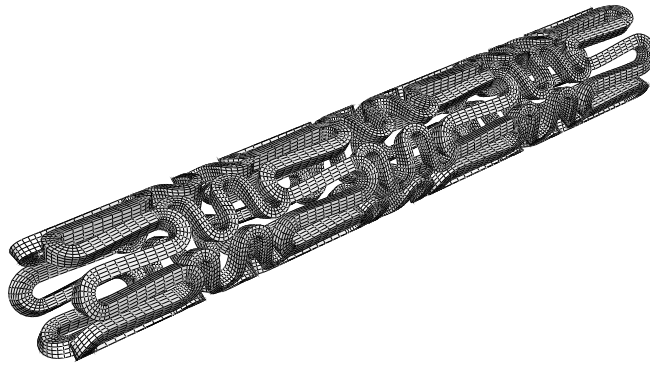
Figure 2.1: Approximate CAD model of *Cypher* stent with its finite element discretization.

2.2.2 Geometrical design and approximation

Commercially available stent geometries are often (if not always) subjected to very strict patent claims. For this reason, manufacturer's specific and detailed information regarding the stent geometry is usually not available in the public domain. As typical dimensions of (coronary) stent struts are in the order of magnitude of $100\,\mu$m, an accurate geometrical representation

of the stent can (only) be acquired using a microscope or micro-Computer Tomography [60]. The advantage of the micro-CT strategy is the possibility to build a precise three-dimensional (3D) reconstruction of both the stent (Figure 2.2) and balloon (Figure 2.3) directly from the CT-scans. The main stent dimensions can be measured and used to build a 3D CAD model of the (crimped) shape of the stent (Figure 2.1).
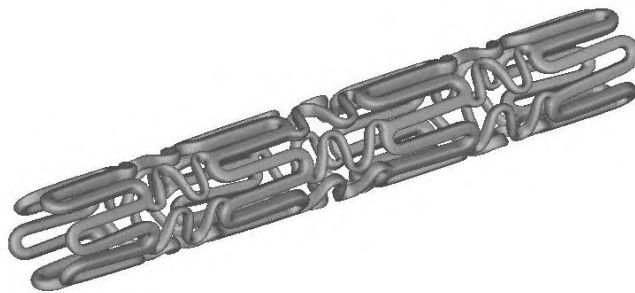
Figure 2.2: CT-image reconstruction of the *Cypher* stent.

Figure 2.3: CT-image reconstruction of a tri-folded angioplasty balloon. The image corresponds to a balloon cross-section just distal to one of the stent ends.

2.2.3 Material properties

Angioplasty balloons are generally manufactured from either PolyEthylene Terephthalate (PET) or Polyamide (nylon) [61]. PET balloons are usually stronger and have a lower compliance than nylon balloons. Based on in vitro testing the change in balloon diameter as a function of inflation pressure is determined by the manufacturer and summarized in a compliance chart in the directions for use.

For balloon expandable stents that undergo plastic deformation during stent deployment, metallic materials (e.g. (coated) medical grade stainless steel, cobalt chromium, etc.) are required. An extensive review regarding the suitability of different biomaterials as coronary stents has recently been given by Mani and his colleagues [62]. The most widely used material for such balloon expanding stents is the low carbon 316L stainless steel. As the constitutive behavior of a material is dependent on its pre-treatment (e.g. hot rolling, cold finishing, annealing, etc.), the material properties should (ideally) be obtained from tensile tests on specimens extracted from batches that are eventually used to create the stent structure. Such experimentally obtained stress and strain values (e.g. reported by Murphy et al. [63]) can be implemented in the finite element model.

2.2.4 Loading and boundary conditions

A finite element model should be subjected to loading and boundary conditions that represent the actual loading history of the stent. Depending on the aim of the study, the model should incorporate conditions that simulate the real-life loading on the stent during manufacturing, catheter loading (crimping and recoil after crimping) and deployment (tortuous path, expansion, interaction with the blood vessel tissue and recoil after expansion). In general, the stent expansion can be modeled as a pressure-driven process (e.g. applying an increasing pressure on the stent or balloon) or a displacement driven process (e.g. enforcing radial displacements on the stent or balloon).

2.2.5 Finite element stent design

The 'ideal' stent is inexpensive to manufacture, easy to deliver and deploy, sufficiently rigid to provide support and able to deliver therapeutic agents. Some of these design requirements (described by Lally et al. [43]) to optimize the mechanical properties of a stent can be examined in a virtual design space. This design space can be used to improve the stent characteristics in its crimped state and its expanding (and expanded) state.

2.2.5.1 Crimped stent requirements

Good flexibility: The stent, crimped on the delivery catheter, must be advanced through the vascular tree, which can include narrow, tortuous passages, to reach the targeted site. Therefore, the crimped stent (on the delivery catheter) must be flexible. Furthermore, a high dislodgment resistance is required to avoid stent loss from the unexpanded balloon in clinical use.

2.2.5.2   Expanding (Expanded) stent requirements

Uniformity: The implantation of a stent, in particular during and post deployment, may induce vascular injuries. The manner in which stents are implanted is a critical determinant of the degree of injury they cause [35]. The (transitory) nonuniform in vivo expansion, frequently in end-first manner (i.e. dogboning), is one of the (possible) reasons for the acute vascular injuries observed surrounding the edges of the stent. This dogboning phenomenon is directly dependent on both the balloon length and the stent design. Furthermore, depending on the stent design, the length of the stent may shorten during radial expansion. This foreshortening affects the precise stent positioning and the friction between the stent and the arterial wall can injure the endothelium (i.e. vascular inner lining). Both the dogboning and the foreshortening phenomenon should be reduced to a minimum.

High radial strength: A stent should be designed as a mechanical scaffold to support the vessel lumen by minimizing post-stenting vessel recoil. The radial support is both design and material dependent.

Low elastic recoil: To achieve a final lumen diameter consistent with the targeted vessel diameter, knowledge of the degree of elastic radial recoil of the stent must be factored into the expansion of the stent during deployment. To minimize the 'inevitable' over-expansion, the material and design dependent radial recoil should be reduced to the absolute minimum. In addition to foreshortening, undesirable shearing along the arterial walls may also be caused by longitudinal recoil after the balloon is deflated and this phenomenon should be minimized.

Good Flexibility: The expanded stent must conform to the tortuous vessel geometry and should not straighten the vessel, as that would induce significant injuries to the vessel wall.

Optimal Scaffolding: To ensure vessel tissue not to prolapse between the stent struts, the stent should provide optimum (uniform) vessel coverage. In addition, a uniform strut distribution is beneficial to avoid local drug concentration and gradients in DES [36]. However, a low artery-stent contact surface area should also be maintained, because the body-foreign material of the stent can initiate an aggressive thrombotic response.

2.2.6   Effective use of FEA

The correlation between finite element approximations and the physical reality is directly related to the ability of the scientist to accurately define the geometry, material behavior and loading environment of the device. While simplifying assumptions are often (if not always) inevitable, there is a risk that significant simplifications considerably alter the analysis of the problem. Therefore, the influence of the simplifications on the solution of the

original problem must always be evaluated. Consequently, the numerical results should be validated by (targeted) experiments under similar conditions.

2.3 Survey of the state of the art in stent modeling

When reviewing literature regarding finite element models of the (free) expansion of balloon expandable stents, two possible ways to simulate the inflation of the balloon are reported up to date: (i) neglecting the presence of the balloon and applying an increasing pressure on the inner surface of the stent or (ii) assuming the balloon to have a cylindrical shape (Figure 2.4). When modeling the vessel reaction to stenting, the geometry of the stenosis can be simplified (symmetric and asymmetric stenosis) or patient specific. The reviewed manuscripts are categorized chronologically (up to the summer of 2007) in the subsequent paragraphs according to the applied stent expansion methodology. This chronological order clearly illustrates the rapid (r)evolution which this research domain has undergone since the reported results of the pioneers.
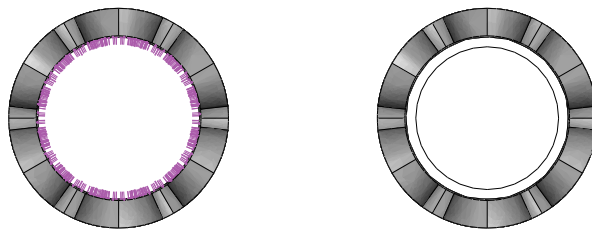
Figure 2.4: Stent expansion strategies: no balloon (left) and cylindrical balloon (right).

2.3.1 Neglect of the balloon

In the year 2000, Dumoulin et al. [64] evaluated and characterized some mechanical properties (shortening percentage on expansion, radial and longitudinal recoil, resistance to crushing under external pressure and fatigue) of balloon expandable *P308 Palmaz* stents (Johnson&Johnson) using the finite element method. The balloon is discarded from the numerical simulations and (a generic part of) the stent is expanded by applying a uniform pressure on the inner surface of the stent. This assumption is well motivated
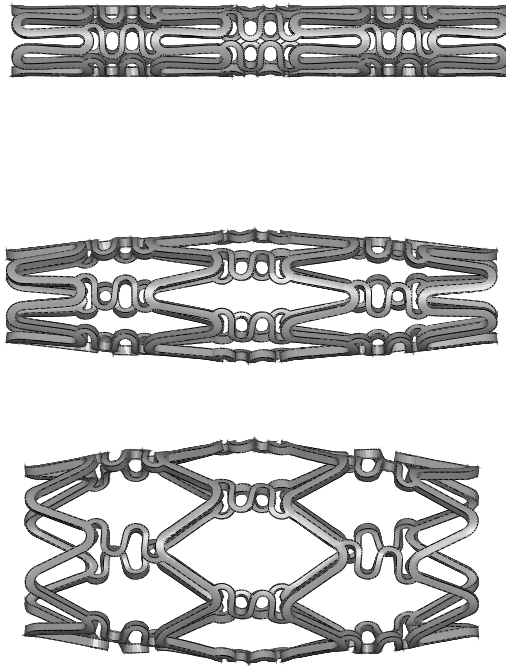
Figure 2.5: Illustration of pressure driven *Cypher* stent expansion (Neglect of the balloon). Top: no pressure; Middle: low pressure range; and Bottom: high pressure range.

by the authors and is stated as valid for the central part of the stent. The assumption is based on a careful examination of an in vitro experiment of the free expansion of the investigated stent. Furthermore, the mechanical properties are described in terms of diameters instead of internal pressures. The numerical model is validated by comparing the expansion size (i.e. stent length) with data provided by the manufacturer and a good correspondence is found. Dumoulin et al. clearly demonstrate that under certain specific conditions it is possible to investigate certain mechanical properties of balloon expandable stents with the presence of the balloon discarded in the numerical models.

In the finite element stent study of Auricchio and his colleagues [1], reported in 2001, the expansion behavior of a stent with a rectangular slotted tube design, i.e. *Palmaz-Schatz* (Johnson&Johnson) like, is investigated. Both the stent free expansion and the vessel reaction to the stent expansion are

studied and the stent design is modified in order to reach a more uniform expansion. Some typical stenting parameters (i.e. elastic recoil, foreshortening, ...) are computed and presented. The authors stated that it is reasonable to neglect the balloon, because of its lower stiffness compared to the stiffness of the stent. This hypothesis permits the possibility of discarding the presence of the balloon in the analysis by applying the internal pressure, which normally acts on the balloon, directly to the inner surface of the stent. Hence, the stent is loaded by an internal uniform radial pressure varying linearly from zero to $1.3\,\mathrm{N/mm^2}$ (inflation) and then again linearly back to zero (deflation). The numerical results for some mechanical properties (elastic recoil, foreshortening, metal-artery ratio) correspond with values available in literature for the non-modified stent design. Though, the validation of the stent expansion behavior is rather limited. To investigate the revascularization a symmetric three-dimensional model of the plaque and artery is developed (see Figure 2.6). The idealized 'symmetric stenosis' is characterized by a straight artery segment and a plaque with a parabolic longitudinal profile and the constitutive material behavior is adopted from literature. This pioneering work clearly shows the enormous potential of the finite element method in this research domain, both on stent design and procedural level.
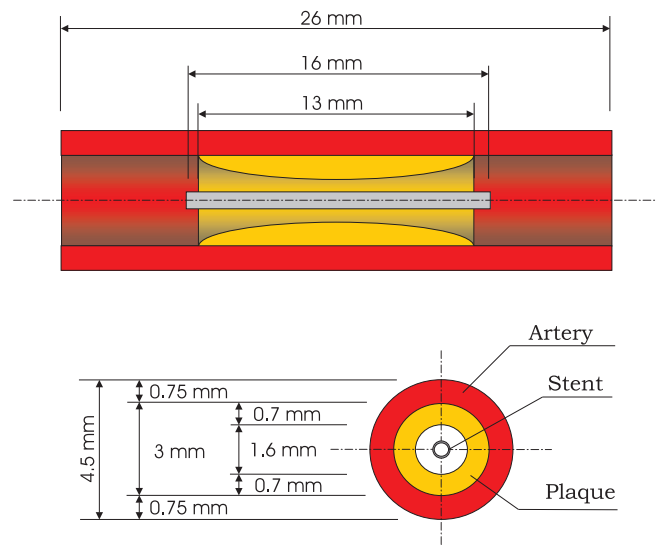
Figure 2.6: Pictorial description of the complete system (stent, artery, plaque) before the stent apposition and indications on the dimensions of the considered model [1].

In the same period, Etave et al. [65] used a finite element analysis to determine the 'exact' mechanical characteristics of tubular (*Palmaz-Schatz*,

Johnson&Johnson) and coil (*Freedom*, Global Therapeutics Inc.) stents. Seven mechanical properties were studied numerically with determination of: (1) stent deployment pressure, (2) intrinsic elastic recoil of the material used, (3) resistance of the stent to external compressive forces, (4) stent foreshortening, (5) stent coverage area, (6) stent flexibility, and (7) the stress maps. The balloon is ignored in the numerical simulations and the stents were expanded by a radial displacement driven process, forcing the stent to expand as a cylinder during the complete expansion (i.e. dogboning is excluded from the analysis). This numerical study shows the possibility of studying several important mechanical characteristics of different stent designs, but no experimental validation of the numerical results is reported.

One year later, in 2002, Migliavacca et al. [3] investigated the mechanical behavior of coronary stents by means of the finite element method. Finite element analyses were applied (i) to understand the effects of different geometrical parameters (thickness, metal-to-artery surface ratio, longitudinal and radial cut lengths of a *Palmaz-Schatz* like stent) of a typical diamond-shaped coronary stent on the device mechanical performance, (ii) to compare the response of different next generation stent models (*Multi-Link Tetra*, Guidant and *Carbostent*, Sorin Biomedica) when loaded by internal pressure (see Figure 2.7) and (iii) to collect suggestions for optimizing the device shape and performance. The presence of the balloon is discarded in the analysis and the internal pressure on the balloon is directly applied to the inner surface of the stent corresponding with the expansion strategy proposed by Auricchio et al. [1]. The introduction of new generation stent geometries opens the door to study stent designs currently used in the clinical practice. Experimental evidence of the numerical results would certainly create a more solid base for the proposed design optimization.
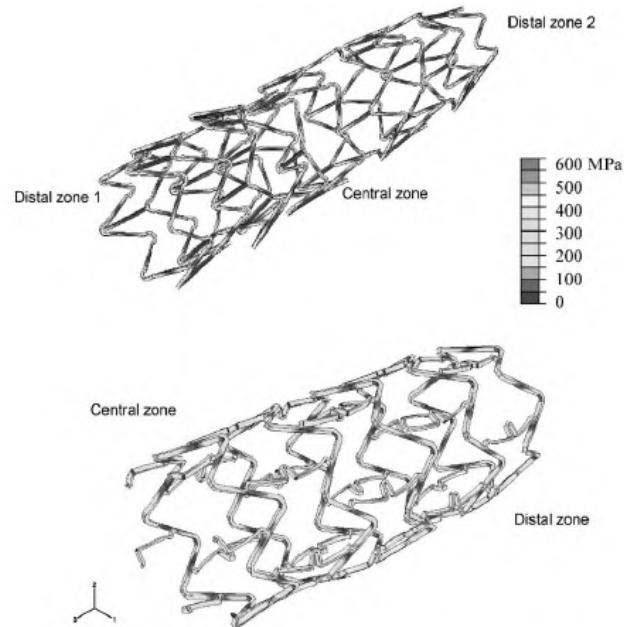
Figure 2.7: von Mises stress contours in the expanded *Multi-Link Tetra* and *Carbostent* [3].

More recently, in 2004, McGarry et al. [66] examined the mechanical behavior of a stainless steel balloon expandable stent design using computational micromechanics in the context of the finite element method. Stent deployment and cardiac pulsing loading conditions were considered. As the typical dimensions of stent struts (e.g. $100\,\mu$m for coronary stents) are of a similar order of magnitude as the average grain size in medical grade stainless steel (i.e. $25\,\mu$m), continuum approaches relying on macroscopic material properties may be regarded as somewhat questionable, and alternative numerical analysis, based on crystal plasticity for example, may need to be used. McGarry and colleagues used classical phenomenological plasticity theory (J_2 flow theory) and physically based crystal plasticity theory to describe the stent material behavior. Important stent deployment characteristics such as recoil and foreshortening were determined using a two-dimensional (2D) model of a unit cell (i.e. characteristic pattern which is repeated both circumferentially and longitudinally) of the *NIR* stent (Medinol/Boston Scientific). The deployment of the 2D unit stent cell was modeled using applied displacements. Furthermore, elementary fatigue factors of safety were determined by plotting Goodman diagrams to compare both material models, leading to a lower (and thus conservative) factor of safety for the classical plasticity theory in comparison to the crystal plasticity model. The numer-

ical results in terms of average hydrostatic stresses are in the correct order of magnitude relative to experimental data reported in literature. McGarry et al. clearly demonstrate that under specific conditions it is possible to investigate certain mechanical properties of balloon expandable stents (e.g. recoil, foreshortening, etcetera) with the presence of the balloon discarded in the numerical models and that the micromechanical approach seems to have the potential of describing the stent mechanical properties (e.g. recoil) more accurately as compared to the classical continuum approach. Nevertheless, (experimentally validated) full 3D stent modeling should be performed in order to improve the accuracy according to McGarry and colleagues.

Gu and his colleagues [67] performed finite element analyses of covered microstents (i.e. bare-metal stents with ultra thin tubular coverings to treat for example wide-necked intracranial aneurysms) to assist in the design of stent coverings and to select materials for the cover in 2005. The primary objective of this study was to determine the mechanical properties of the covered microstent (e.g. longitudinal shortening, elastic recoil, ...) and investigate the effects of the covering on the mechanical behavior of the stent (e.g. deployment pressure vs. covering thickness). Careful observation of in vivo stenting experiments showed an almost uniformly inflated balloon except at its two ends, and the central portion of the stent is expanded by the uniformly inflated part of the balloon. Therefore, the authors decided to expand the stents in the model by a uniform internal pressure that was applied in small increments on the internal surface of the covered microstent. During loading, pressure was increased until the final diameter of the stent reached a certain value and then the pressure was decreased to study recoil. Although a simple non-specified in vitro experiment was performed to study the expansion of the stent, surprisingly no quantitative validation of the numerical results was presented in terms of the recorded deployment pressure-diameter data. Consequently, the accuracy of the proposed methodology has not been confirmed quantitatively.

A computational methodology that allows a set of stent parameters to be varied, with the aim of evaluating the difference in the mechanical environment within the arterial wall before and after angioplasty with stenting is proposed in the same period by Holzapfel et al. [68]. This methodology is applied to an image-based three-dimensional geometrical model of a post-mortem specimen of a human iliac artery with a stenosis. Three-dimensional stent models are parameterized in order to enable new designs to be generated simply with regard to variations in their geometric structure. The following parameters are altered to analyze their inter-relationship: (i) the type of stent cells, similar to three commercial products (*Multi-Link Tetra*, Guidant; *Niroyal-Elite*, Boston Scientific and *Inflow-Gold-Flex*, InFlow Dynamics), (ii) the geometry of stent struts, (iii) the radial mismatch between the smallest lumen diameter in the stenosis and the expanded stent diameter (nominal stent diameter). Furthermore, the numerical simulations

allowed to characterize the following indicators: (i) the change of the intimal pressure caused by the struts of the stent, (ii) the stress change within the arterial wall caused by the stent (see Figure 2.8), and (iii) the luminal change due to angioplasty. The obtained numerical results are interpreted in terms of restenosis rates reported in clinical studies. This approach allows the analysis of the 3D interaction between the stent models and patient specific wall models, the quantification of change in the mechanical environment which occurs during stent placement, and the comparison of effects of different parameters to identify optimal stent designs. In the numerical simulations the balloon is ignored and the (deformation dependent) pressure load is applied directly on the stent struts. This groundbreaking work combines parametric modeling of new stent designs with the possibility to study the interaction of these designs with a patient specific stenosis.
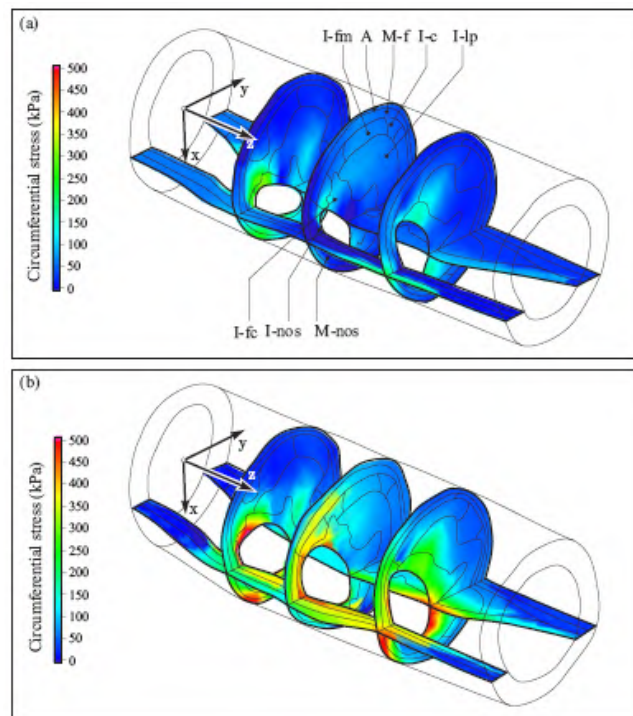
Figure 2.8: Circumferential Cauchy stress distributions in the arterial wall before (a), and after stenting [68].

Also in 2005, Migliavacca et al. [5] applied the Finite Element Method to study the mechanical behavior of a new generation coronary stent (*BX Velocity*, Cordis). The results from the computations were compared with those from a laboratory experiment in terms of radial expansion and elastic

recoil. Furthermore, Migliavacca and his colleagues were the first to compare the compliance of the stent in their simulations with the compliance chart of the manufacturer (see Figure 2.9). The presence of the balloon is discarded in the analysis and a uniform linearly increasing radial pressure was applied to the internal surface of the stent to mimic the free expansion of the stent. In addition, to investigate the mechanical properties of the stent after the load removal, the stent was unloaded decreasing the internal pressure back to zero. The authors state that the absence of any balloon model is the real decisive element in interpreting the discrepancies between the experimental and the computational tests. Therefore, the development of more realistic computational models accounting for the presence of the balloon (in its actual folded shape and with a correct constitutive description) is required.
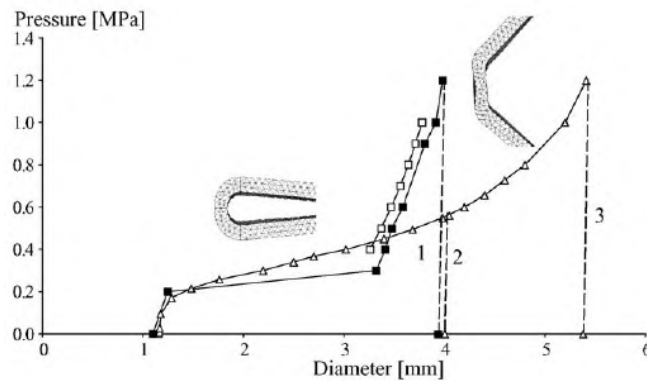
Figure 2.9: Results from the FEM analysis (empty triangle), from the experimental test (solid squares) and data provided by the company (empty squares) [3].

One year later and in order to reduce the dogboning to a minimum, De Beule and his colleagues [69] exploited the finite element method to investigate and compare the expansion of different designs of a first-generation *Palmaz-Schatz* stent. The stent expansion is studied by applying a uniformly distributed internal pressure directly to the inner surface of the stent as proposed by Auricchio [1]. The dogboning effect even vanished when altering the original symmetric stent design to an asymmetric design. Thus taking asymmetry into account in the design seems very promising, at least from the point of view of dogboning. However, no experimental validation of the numerical results has been performed and the authors acknowledge that more realistic balloon-stent interactions should be taken into account in future studies as the stent expansion behavior might be governed by the unfolding and expansion of the balloon.

Finally, it was in 2006 that Bedoya and co-workers [70] devoted a numer-

ical study to the effects of stent design parameters on the stress field induced in the normal artery wall and to the radial displacement achieved by the stent during systole and diastole. Each stent was positioned in a straight homogeneous cylindrical artery model with nonlinear hyperelastic mechanical properties. These mechanical properties were obtained from pressure-diameter and force-elongation tests on a porcine artery specimen. The study indicated that stent designs (consisting of concentric rings of sinusoid like curves linked by straight bars of various lengths) incorporating large axial strut spacing, blunted corners at bends, and high axial ring segment amplitudes exposed smaller regions of the artery to high stresses, while maintaining an adequate radial displacement. Timmins et al. [4] extended the work of Bedoya by developing an algorithm to optimize stent design, allowing for consideration of wall stress, lumen gain and cyclic deflection. The stent strut configuration was refined, via varying specific design parameters, to optimize stent performance. This innovative study demonstrates the feasibility of medical device design optimization under complex circumstances. Analogous to the methodology developed by Lally and her colleagues [71], the stent expansion process is not taken into account in both studies and the stent was initially a straight cylinder with a constant diameter (larger than the systolic arterial diameter). Therefore, the proposed design guidelines might alter when studying the real expansion in a patient specific stenosis, a logical topic for further investigation.

2.3.2 Cylindrical balloon

Rogers et al. [28] were the first (in 1999) to report an innovative experimental and numerical study on the balloon-artery interactions during stent placement, hypothesizing that balloon-artery interaction is a mechanism of vascular injury during stent deployment. Therefore, a two-dimensional finite element model was made to investigate how balloon-artery contact stress and area depend on stent-strut geometry, balloon compliance, and inflation pressure. The model assumed a linear elastic balloon membrane under pressure loading conditions to study balloon extrusion between struts. The constitutive behavior of the arterial wall was also considered to be linear elastic, based on previously published studies. The study demonstrates the influence of balloon compliance, stent geometry and pressure load on contact pressure and surface.

One year later, Holzapfel et al. [2] studied the solid mechanics of angioplasty with and without stenting to provide essential insight in the mechanisms of angioplasty such as overstretching the disease-free tissue, plaque disruption or dissection, redistribution inside the wall and lipid extrusion etc. High resolution Magnetic Resonance Imaging (MRI) was used to obtain accurate geometrical data for the vessel wall and plaque architecture and to identify different types of soft (biological) tissues and calcifications
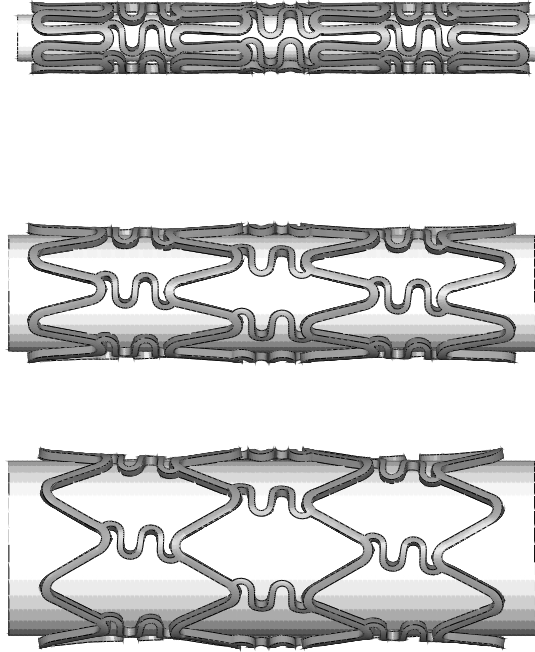
Figure 2.10: Illustration of displacement driven *Cypher* stent expansion (Cylindrical balloon) (Color Key: balloon - white, stent - gray).

(see Figure 2.11). New experimental results showing strong nonlinearity and anisotropy were presented based on a sample of a human iliac artery with eccentric stenosis. The numerical model - to study both angioplasty procedures with and without the *Palmaz-Schatz* stent (Johnson&Johnson) - assumed a cylindrical balloon with pressure loading in the balloon. Their nonlinear numerical analysis showed that for this type of stenosis, with the presence of a complete collagenous cap, the disease-free segments of the vessel wall were overstretched, i.e. loaded beyond the elastic limit, while the plaque region was relatively unstretched. This (over)stretch leads to gains of the cross-sectional lumen area, which turns out to be a major mechanism of angioplasty for this type of stenosis as also suggested by other scientists. Subsequently, Holzapfel and his colleagues [72] analyzed the 3D stress states of the investigated artery during balloon expansion and stent deployment. Changes of 3D stress state due to model simplifications, which are characterized by neglecting axial in situ prestretch, assuming plane strain states and isotropic material responses, were studied. These simplifications lead

to maximum stress deviations of up to 600 % and are thus in general inappropriate. The (fully inflated) balloon is modeled as a rigid cylinder-shaped structure and both the balloon inflation and the stent expansion are modeled as displacement-driven processes. The authors state that the assumption of a rigid cylinder is justified by the fact that fully inflated angioplasty balloons behave as non-compliant tubular structures, though this assumption has not been validated. The work by Holzapfel and his colleagues is groundbreaking on the basis of the simulation of the stenosed artery, taking into account realistic non linear, anisotropic and eccentric characteristics.
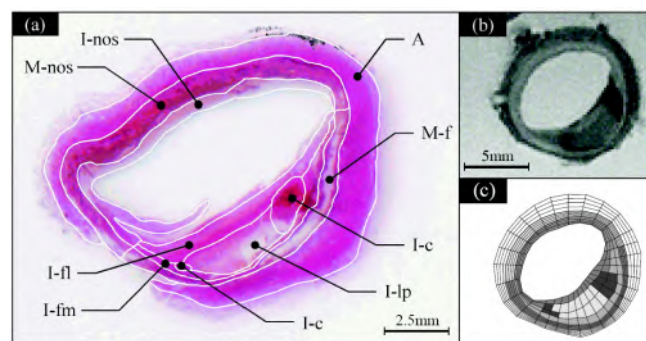
Figure 2.11: Histology (a), MRI (b) and FE-mesh (c) of a typical section excised an external iliac artery with an eccentric stenosis [2].

Recently, in 2005, Liang and co-workers [73] investigated the biomechanical characteristics of intracoronary stent implantation by developing a three-dimensional model of the complete stenting system and self-defined constitutive models for the plaque, the arterial wall and the balloon. The stress concentrations in the contacting areas between stent and plaque, and the recoil ratios were examined. The artery and plaque were modeled as two symmetrical concentric cylindrical tubes. Due to the model symmetry, only a 120° segment was considered in this work. Uniaxial and biaxial experiments on human arteries were used to develop a hyperelastic constitutive model for the artery. In order to characterize the non-recoverable deformations of the interlining between plaques and arteries, a visco-plastic material model was established for the plaque. The authors state that this is a clearly limiting and somewhat unrealistic assumption due to the lack of experimental data. The balloon was modeled as a cylindrical shell with a fictitiously adopted hyperelastic material model in order to try to capture the unfolding of the balloon. This is an interesting approximative methodology, but unfortunately not validated.

Even more recently, in 2006 Ballyk [74] evaluated the impact of stent oversizing on resulting arterial wall stress concentrations and examined the

concept of a 'stress threshold' for neointimal hyperplasia development. A three-dimensional large-strain hyperelastic numerical model was used to examine the nonlinear isotropic behavior of a 6 mm diameter straight cylindrical artery during stent deployment. In a fashion similar to that used by Holzapfel [2] a *Palmaz-Schatz* stent was deployed to a diameter 30 % greater than that of the native artery by a displacement driven process. Ballyk found that the order in which location-specific peak stresses exceeded a predetermined stress threshold was constant: the threshold was first surpassed at the stent ends, followed by the stent cross-links, then the stent struts and finally the bare (non-stent-covered) area between the stent struts. According to several (experimental) studies, these locations corresponded to the most common locations of intimal proliferation after stent deployment. Furthermore an exponential relationship between peak stress concentration and percent stent inflation was formulated. These considerations provide a rationale for a stent design strategy aimed at minimizing vascular injury by optimizing rather than maximizing balloon inflation pressure and diameter. This interesting study is mainly limited by the absence of a realistic balloon, which will induce additional vessel stresses when protruding the bare (non-stent-covered) area between the stent struts (as shown by Rogers [28]) and might also have an impact on the order in which the threshold is exceeded by the peak stresses. These findings could be supported by targeted (e.g. in vitro) experiments.

Also in 2006, a new methodology for quantitatively predicting the fatigue life of cobalt-chromium stents was presented by Marrey et al. [75]. In addition, fracture mechanics analysis was used to evaluate the role of pre-existing microstructural flaws. Therefore the severity of such flaws observed on expanded stents were assessed quantitatively in terms of the propensity of the flaw to propagate and lead to in vivo failure of the stent when subjected to cyclic systolic/diastolic pressure loads within the implanted artery. An interesting submodeling capability of the ABAQUS finite-element analysis program was utilized, which allowed for a localized region of the stent structure to be modeled in a greater level of detail based on the numerical results from the entire stent analysis. The loading on the stents was modeled in terms of four discrete phases that are experienced in service, namely (i) assembly onto the balloon catheter (i.e. crimping), (ii) balloon-inflation, (iii) recoil, and (iv) physiological loading within the artery (see Figure 2.12). At the end of the crimping phase, a semi-rigid expansion cylinder was used to expand the stent into a hyperelastic tube, simulating the controlled inflation of the balloon. The symmetric hyperelastic tube represented the section of the coronary artery into which the stent is implanted. The material constants of the hyperelastic tube were numerically calibrated to exhibit a physiologically relevant coronary arterial distension. Marrey et al. clearly demonstrate that under certain specific conditions it is possible to investigate the mechanical properties of balloon expandable

stents with the presence of the actual folded balloon shape discarded in the numerical models.
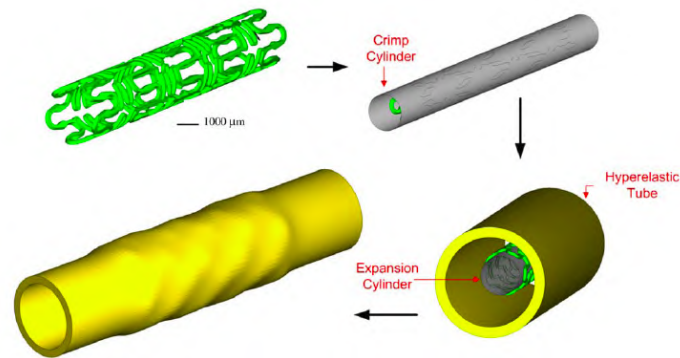
Figure 2.12: Schematic of the sequence used to assemble and deploy the stent involving the crimp and expansion steps modeled by the stress analysis [75].

In the same period, an interesting comparison of element technologies for modeling stent expansion was published by Hall and Kasper [76]. The computational efficiency and results achieved using continuum solid, shell and beam elements were compared and the study showed that all of the element formulations provide (asymptotically) a similar response in the context of stent deployment simulations. Among the element choices, the beam formulation is computationally most efficient by a significant factor with regard to problem size, time and memory requirements. Furthermore, the beam simulations predict nearly the same extreme values of stress, strain, and equivalent plastic strain at identical locations on the stent. Hall and Kasper clearly showed that beam discretization of stents might be very useful to speed up some aspects of the design phase. However, modeling the vascular reaction to stenting and the consequent flow disturbance might be more challenging using beam elements.

Next, Wang et al. [77] applied the finite element method to simulate the transient expansion phase of a stent/balloon system with different stent structures and balloon lengths under internal pressure loading conditions. Two types of stents (with length equal to 9.8 mm and six collocations of stent and balloon were modeled to investigate the reduction (elimination) of the dogboning phenomenon by decreasing the balloon (over)length and increasing the stent-end stiffness (i.e. increased strut width). The authors state that a 'virtual' linear elastic material - designed to imitate the behavior of the real balloon with a simple cylindrical model - does not notably affect the transient deformation of a stent. The finite element results were validated *qualitatively* by recording the transient stent (with length 17 mm) expansion process and by measuring the outer diameter and stent length at

different inflating pressures (providing pressure-diameter curves). Although this methodology has several interesting features, certain limitations in the approach need to be addressed. Firstly, the discrepancy between the stent length in the numerical and experimental models is not motivated and secondly, the numerical results are not validated quantitatively, whereas the proposed methodology seems to provide both numerical and experimental pressure-diameter information (see Figure 2.13). Therefore, the accuracy of the 'virtual' cylindrical balloon hypothesis has still to be demonstrated.
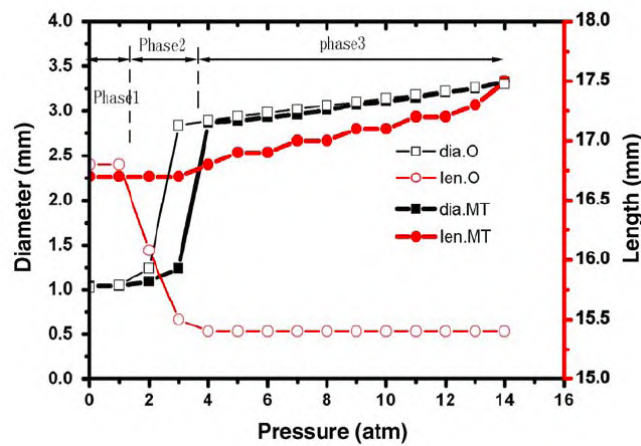
Figure 2.13: Comparison of the experimentally obtained expansion characteristics of two selected stents: dia.O represents the diameter of unmodified type-one stent, len.O the length of unmodified type-one stent, dia.MT the diameter of modified type-two stent and len.MT the length of modified type-two stent [77].

Takashima et al. [78] characterized the stress distribution at the contacts between the stent and the artery using mathematical and experimental modeling in 2007. Comparison of the experimental with the finite element results revealed that the contact area between the stent (with a high number of cells and links) and the artery model was distributed over the total surface of the stent. The stents are expanded 'in numero' by the inflation of a very stiff cylindrical balloon (Young's modulus of 400 GPa) controlling the displacement of the stent. The finite element results (in terms of contact area ratio) were validated both qualitatively and quantitatively and the contact areas of the stents corresponded to the areas of high radial compressive stress. The contact area ratios were (much) larger in the experimental model than in the finite element analysis. The authors suggest that this discrepancy may be the result of several factors (contact surface area calculation, problem non-linearity, material parameters, mesh size), which are all variables that can (easily) be examined by extending the numerical model. However,

the main limitations seem to be the discrepancy between the geometry and the loading conditions of both the numerical model (length of vessel and plaque: 18 and 7 mm; vessel outer diameter 3.6 mm; displacement driven process) and the experiment (length of vessel and plaque: 50 and 30 mm; vessel outer diameter 4 mm; pressure driven process). Consequently, simulating the exact experiment could surely reduce the variation in the contact area ratios.

Finally, Wu and his colleagues [79] proposed a finite element based methodology to study the stent expansion in both a straight and a curved vessel. The stent expansion in the curved vessel was simplified as follows: firstly the vessel was expanded by applying a pressure on the inner surface of the tissue. Subsequently the stent was expanded with a straight semi-rigid balloon and the pressure on the vessel was reduced. Lastly the balloon diameter was reduced to its original shape. Their results show a hinge effect at the stent extremities and a straightening of the curved vessel by stenting. Furthermore, the maximum tissue prolapse was more severe, the minimum lumen area decreased and the tissue stress levels were higher for the curved vessel model when compared to the straight vessel model. The proposed methodology is one of the first to investigate the stenting procedure of curved vessels, but (some) of the results and conclusions should be interpreted skeptically as the validation is limited. The main limitation seems not to be the absence of the fluid dynamical aspect (i.e. study of the flow disruption in the stented vessel), but the applied stent expansion methodology which might influence tissue prolapse, minimum lumen area and tissue stress levels. Therefore, experimental evidence seems necessary to show whether the actual stent expansion might be simplified as proposed by the authors. Furthermore, the real non-recoverable deformations of the tissue during a stenting procedure (which can not be captured by the applied hyperelastic constitutive behavior for the vessel and plaque) will influence the tissue stress levels, as already mentioned by Holzapfel [72], and probably also influence the interaction between the stent and the vessel wall.

2.3.3 Summary

For each of the above mentioned studies; the aim, the balloon inflation methodology and the validation strategy are briefly summarized in Table 2.2.

Table 2.1: Reported material properties for Stainless Steel SS316L

Group	Young modulus (N/mm^2)	yield stress (N/mm^2)	material reference
Auricchio [1]	196000	205	Metals handbook (American Society for Metals)
Etave [65]	190000	-	Standard stress/strain curve for annealed material
Migliavacca [3]	196000	205	Auricchio [1]
McGarry [66]	209000	264	Uniaxial tensile test
Gu [67]	196000	205	Auricchio [1]
Migliavacca [5]	196000	105	Kinematic hardening yield stress reduction (crimping)
Liang [73]	201000	330	Tensile tests on wires
Hall [76]	196000	290	-
Wang [77]	201000	-	Tensile test on annealed wire
Bedoya [70, 4]	200000	-	-
De Beule [69]	196000	205	Auricchio [1]
Wu [79]	201000	280	Standard true stress/strain curve for annealed material
Takashima [78]	200000	315	-

Table 2.2: Chronological overview of balloon expandable stent modeling

Year	Group	Research	Balloon	Validation
1999	Rogers [28]	2D balloon/artery interaction analysis. Contact pressure and surface dependent on balloon compliance, stent geometry and pressure load.	Linear elastic membrane	In-vivo and in-vitro experiments (qualitatively)
2000	Dumoulin [64]	Free stent expansion: evaluation and characterization of some mechanical stent properties.	No balloon	Examination of in vitro experiment
2000	Holzapfel [2]	Mechanisms of angioplasty.	Elastic cylinder	Literature (principle of luminal gain)
2001	Auricchio [1]	Vascular reaction to *Palmaz-Schatz* stent expansion: influence of modified stent geometry.	No balloon	Literature (stent mechanical properties)
2001	Etave [65]	Seven mechanical characteristics of *Palmaz-Schatz* and *Freedom* stent.	Theoretical analysis	Not reported
2002	Migliavacca [3]	Mechanical behavior of *Palmaz-Schatz* stent: modification of stent design. Comparison Carbostent and Multi-Link Tetra stent.	No balloon	None
2002	Holzapfel [72]	3D stress state in patient specific stenosis with anisotropic material properties during balloon expansion and stent deployment: influence of constitutive material model simplifications.	Rigid cylinder	None (proposes appropriate in vitro bench-mark test)

Table 2.2: Chronological overview of balloon expandable stent modeling

Year	Group	Research	Balloon	Validation
2004	McGarry [66]	Deployment characteristics (recoil, foreshortening and fatigue safety factor) of *NIR* stent using a 2D model of a unit cell (recoil, foreshortening) based on micromechanical modeling. Stent material behavior described by classical and crystal plasticity theory.	No balloon	Literature (non-uniform grain level deformation and residual stresses)
2005	Gu [67]	Mechanical performance of the covered *Palmaz-Schatz* microstent (e.g. longitudinal shortening, elastic recoil, deployment pressure vs. covering thickness, ...).	No balloon	In vivo and in vitro experiments (qualitatively)
2005	Holzapfel [68]	3D interaction between different stent models (*Multi-Link Tetra, Niroyal-Elite* and *Inflow-Gold-Flex*) and a patient specific wall model with anisotropic material properties. Quantification of the change in the mechanical vascular environment during stent placement and comparison of the effects of different parameters to identify optimal stent designs. Linked to restenosis.	No balloon	Literature (degree of restenosis)
2005	Migliavacca [5]	Mechanical behavior of *BX Velocity* coronary stent.	No balloon	Data manufacturer and experimental test.

Table 2.2: Chronological overview of balloon expandable stent modeling

Year	Group	Research	Balloon	Validation
2005	Liang [73]	Simulation of balloon driven stent expansion in stenosed artery.	Hyperelastic cylinder	None
2006	Ballyk [74]	Evaluation of the impact of stent oversizing on resultant arterial wall stress concentrations and examination of the concept of a 'stress threshold' for neointimal hyperplasia development.	Rigid cylinder	Literature (locations of intimal proliferation after stent deployment)
2006	De Beule [69]	Introduction of asymmetry in the *Palmaz-Schatz* stent design to avoid dogboning.	No balloon	None
2006	Marrey [75]	New methodology for quantitative prediction of the fatigue life of cobalt-chromium stents.	Semi-rigid cylinder	Experimental tests on stent(wire) specimens
2006	Hall [76]	Comparison of element technologies for modeling stent expansion.	Semi-rigid cylindrical surface	None
2006	Wang [77]	Transient expansion behavior and design optimization of coronary stents: reduction of dogboning by adapting stent geometry and balloon length.	Linear elastic cylinder	In vitro experiments (qualitatively)

Table 2.2: Chronological overview of balloon expandable stent modeling

Year	Group	Research	Balloon	Validation
2006	Bedoya [70]	Monitoring of the radial displacements achieved by the stent during systole and diastole and the stress levels within a symmetric artery provoked by different stent designs. Linked to restenosis	No balloon	None
2007	Wu [79]	Stent expansion in both straight and curved vessel.	Rigid cylinder	None
2007	Timmins [4]	Development of an algorithm to optimize stent design, allowing for consideration of competing wall stress, lumen gain and cyclic deflection.	No balloon	None
2007	Takashima [78]	Simulation and experimental observation of contact conditions between stents and artery models.	Elastic cylinder	Qualitative and quantitative (contact area ratio)
2008	De Beule [80]	Comparison of different modeling strategies for a new generation balloon-expandable coronary stent (see Section 3.2.1).	Elastic trifolded balloon	Qualitative and quantitative (data manufacturer)

2.4 Alternative methods for biomechanical modeling of stents

As stated in the introduction, this review focuses on Finite Element Method (FEM) based studies dealing with the mechanical behavior of (balloon expanding / expanded) stents. The study of the mechanical properties of the *Palmaz-Schatz* and *Freedom* stents by Tan and his colleagues [81] was not included in the survey as the expansion methodology is not described. In addition, the FEM can be applied to study other important mechanical stent characteristics, such as tissue prolapse, flexibility, strut micromechanics and also self expandable stents. Furthermore, the impact of the stent design (e.g. strut shape, interstrut distance, ...) on the blood flow patterns can be examined using Computational Fluid Dynamics (CFD). Finally, the kinetics of the drug release - in the case of DES - can also be examined numerically. Some studies dealing with these issues are summarized below.

2.4.1 FEM - Prolapse, flexibility and strut micromechanics

To analyze tissue prolapse in cardiovascular stents, Prendergast et al. [82] performed uni- and biaxial experiments on human femoral artery and porcine aortic vascular tissue to develop a hyperelastic constitutive model of vascular tissue suitable for implementation in a finite element model. To study the deflection of tissue between the struts of the stent (i.e. prolapse), four stent designs (*BeStent 2*, Medtronic AVE; *Niroyal*, Boston Scientific; *Velocity*, Cordis; *Tetra*, Guidant) were expanded in vitro to determine their repeating-unit dimensions. This geometrical information was used to generate a finite element model of the vascular tissue supported within a repeating-unit of the stent. This methodology is proposed as a way to compare stents relative to their potential for restenosis and as a basis for a biomechanical design of a stent repeating-unit that would minimize restenosis. The stent measurements were obtained by taking pictures of the fully expanded stent under a microscope and the images were then projected onto a 3.5 mm cylinder to define the geometry of one repeating unit of each stent design. Consequently, the blood vessel is modeled as a symmetric concentric cylindrical tube. The most important simplification made by the authors is that the prolapse is not investigated by taking the stent expansion process into account. Furthermore, the effect on the prolapse of taking a realistic (patient-specific) artery with a stenosis into account is not (yet) examined. Subsequently, in the same year, Lally et al. [71] analyzed the stress levels within a symmetric atherosclerotic artery provoked by two different stent designs (*S7*, Medtronic AVE and *NIR*, Boston Scientific). These stress levels are linked to possible vascular injury and thus, to the degree of

restenosis reported in clinical studies. The developed methodology consists of two steps: in the first step the vessel was expanded to a diameter greater than that of the 'idealized' expanded stent by applying a sufficient internal pressure to the vessel and secondly the pressure on the inner lumen of the artery was gradually reduced. The arterial tissue material model was determined by data from uniaxial and equibiaxial tension tests of human femoral arterial tissue. The hyperelastic constitutive model used to characterize the plaque tissue was determined by fitting to published data for human calcified plaques. Due to the elastic nature of the hyperelastic arterial tissue the vessel contracted around the scaffolding stent (see Figure 2.14). The main limitations of this interesting study are, according to the authors, the idealized representation of the arteries in which the stents are implanted and the absence of the stent expansion process. Therefore, the influence of the stenosis on the stent expansion and the influence of the shear force during the expansion remain unstudied.
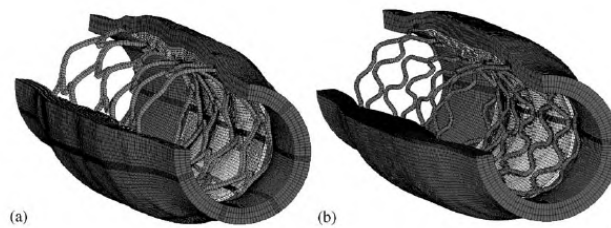
Figure 2.14: The deformation of the artery, stenotic material and stent for (a) the *NIR* stent and (b) the *S7* stent (one quarter of the artery and stenosis removed for viewing) [71].

Both Petrini and her colleagues [83] and Mori and co-workers [84] explored the advantages of the finite element method in order to investigate stent performance in terms of flexibility. Petrini et al. considered two three-dimensional models resembling two new generation coronary stents (*BX Velocity*, Cordis and *Carbostent*, Sorin Biomedica), both in the expanded and unexpanded configuration. The analyses were performed under displacement control: the extremes of the models sketched in Figure 2.15 were rotated at a fixed angle φ. The main limitations of the work are the absence of an experimental validation and the absence of the delivery system during the flexibility analysis in the unexpanded configuration. Mori et al. applied the four-points bending test to evaluate stent flexibility, and employed the finite element method to assess the effect of stent structure on flexibility in stents with differing link structures under compressive loading conditions. The flexibility predicted from their simplified 2D finite element analysis correlated with the bending stiffness of the stents. The main limitation of this study is that the flexibility is examined only in the stent's

expanded configuration, where the stent also should possess flexibility for maneuverability through tortuous vasculature to the site of occlusion in the unexpanded configuration.
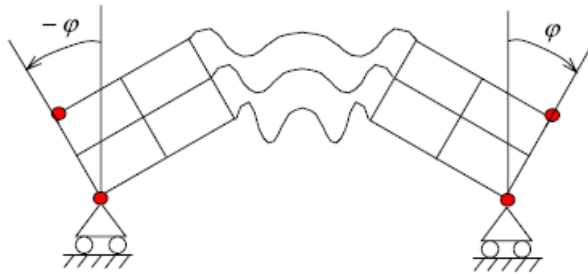

Figure 2.15: Sketches of the stent unit with angle of rotation φ [83].

The use of finite element analysis to predict the mechanical failure of stent struts was investigated by Savage et al. [85]. A 2D computational micromechanics approach was considered involving an explicit representation of the grain structure in the steel struts to accurately represent the constitutive behavior of the material, as question arises as to the suitability of using bulk material properties at the size scale of stent struts. The predictions of the failure strains in virtual uniaxial tensile tests on strut specimens are in good qualitative agreement with the experimental results of Murphy and his colleagues [63], i.e. the observation of a similar trend in the variation of the failure strain with strut thickness. In order to produce better quantitative results, full 3D models and models with an explicit damage mechanism seem necessary before even thinking of studying the (micro)mechanical behavior of entire stents in their natural environment. Furthermore these extended models might require very high computational times as already stated by the authors.

2.4.2 FEM - Self expandable stents

The first one to report a numerical study on the behavior of self expandable stent structures was Whitcher [86], who estimated the in vivo structural behavior and fatigue properties of nitinol stents in 1997. Migliavacca and colleagues [87] analyzed the stress state induced on the vascular wall, by the expansion of both balloon- and self-expandable stents using the finite element method, as the modified mechanical stress state is in part responsible for the restenosis process. Comparing the stainless steel balloon expandable stent with the shape memory alloy (Nitinol) self expandable one, the latter induces lower stresses, but on the other hand, its lower stiffness induces a

lower capability to restore artery lumen and to counteract arterial elastic recoil. However, because of the strong dependency of the material properties on the shape memory alloy composition and thermomechanical treatment, this study does not make any attempt to give quantitative indications. In a more general computational study of the shape memory alloy (SMA) behavior in biomedical applications, Petrini and her colleagues [88] performed an experimental and virtual stent crush test. Again, the exact knowledge of the real characteristic material properties is missing, but the observed agreement between the experimental and numerical results is encouraging and shows the capability of the implemented material model to describe the fully three-dimensional behavior of SMA devices. A novel and interesting concept of progressively expanding shape memory stents was proposed and studied by Thériault et al. [89]. Restenosis is hypothesized to be caused by intimal hyperplasia, related to arterial wall injury due to the violent penetration of the stent structure. This study proposes a nitinol self expanding stent with a progressive expansion system activated by the creep effect of polyethylene rings to prevent restenosis. This device will impose a smooth and gradual contact between the stent and the endothelium, giving the artery the opportunity to adapt to the presence of the device. A modeling strategy was proposed to obtain the final geometry of the stent laser cut from a small tube and to examine the behavior of the prosthesis during surgery and over the 4 weeks following the operation. The numerical results demonstrate that a compromise can be reached between a limited expansion prior to the inflation of an expandable balloon and a significant expansion by creep of the polymer rings. However, experimental validation of the mechanical behavior of the prosthesis is missing and the interaction of the device with a (patient specific) stenosis has not yet been investigated. In a virtual study by Wu and colleagues [90], two superelastic stents (S_{ori} and S_{mod}) were delivered into a stenotic carotid bifurcation through a sheath and self-expanded in the internal and common carotid artery. The stent with shorter struts had less malapposition areas, a higher luminal gain, caused more tortuosity changes and induced higher maximum vessel stresses. The actual stent release from the catheter is simplified by assuming a uniform diameter increase of the sheath and contact between the stent struts during compression of the stent in the sheath is neglected. Furthermore, only one kind of nitinol material properties was modeled, whereas the actual (and highly adaptable) nitinol properties can influence the stent mechanical properties greatly. The above mentioned assumptions can (only) be justified through a missing targeted experimental validation.
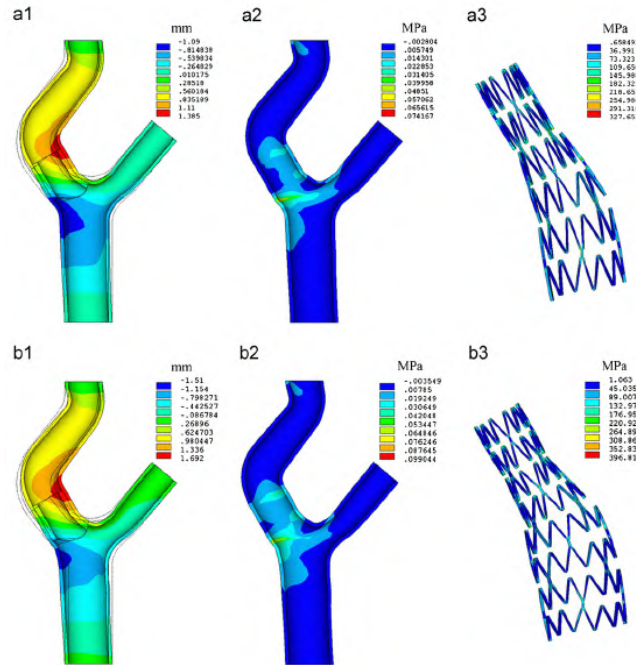
Figure 2.16: (a1) and (b1) Displacement in the global X direction of the tissue deformed by the S_{ori} and S_{mod}, respectively. The original shape edge is also shown for comparison. (a2) and (b2) The first principle stresses of the vessel caused by the interaction with the S_{ori} and S_{mod}, respectively. (a3) and (b3) Von Mises stress distribution of the S_{ori} and S_{mod} after stent release, respectively [79].

As summarized above, the studies in engineering literature dedicated to the analysis of the mechanical properties of nitinol self-expanding stents and to their interaction with the vessel wall focus on tubular stents. In contrast, the number of virtual studies related to wire stents is rather limited. This is surprising because of the wide application field of these devices [46, 91, 47, 92]. Jedwab and Clerc [93] developed an experimentally validated theoretical model of a self-expanding metallic wire stent with the aim of predicting the various mechanical properties of the stent. Wang and Ravi-Chandar [94, 45] developed a mathematically rigorous model, based on the theory of slender rods, that describes the response to internal and external loading conditions of a metallic braided wire stent and the obtained results were validated with experimental data. In addition, Canic et al. [95] performed an analytical study in order to analyze the mechanical properties of two bare-metal braided stent grafts and to compare their response to hemodynamic forces. Furthermore, Brand and his colleagues [96] developed an analytical approach for the mechanical interaction of the self-expanding

Cardiocoil (Medtronic InStent) stent with the stenosed artery. All these studies show good results, but at the same time they demonstrate the necessity to build complex analytical models to examine the mechanical behavior of wire stents. Furthermore, these analytical models seem challenging to analyze the expansion of wire stents in patient-specific anatomical geometries and seem unable to capture the mechanical behavior of innovative bioabsorbable braided stents [97]. In an attempt to partially justify the lack of finite element based wire stent studies, one should consider the complexity of building the geometrical model of such a wire stent using classical CAD methodologies and subsequent (numerical) analysis of this family of stents.

2.4.3 CFD, Drug Elution and Immersed FEM

Frank and his colleagues [29] have given a brief overview of Computational Fluid Dynamics (CFD) research studies dealing with stent design. CFD approaches are well suited to obtain detailed information on stent flow patterns and the strong dependence of flow stagnation (possibly related to restenosis) on stent strut spacing has clearly been demonstrated. He and co-workers [98] examined detailed flow characteristics by estimating the Wall Shear Stress (WSS) in the near-strut region of realistic stent designs using three-dimensional CFD. Their results also indicated that stent design is crucial in determining the fluid mechanical environment in an artery. The results of the 3D CFD study of LaDisa et al. [99] supported the hypothesis that circumferential vascular deformation after stent implantation imparts distinctive alterations in WSS that are not detected by using a standard circular model of the vascular cross section. In addition, Benard and his colleagues [100] investigated the effects of blood (rheological) properties on changes in intra-stent flow with a three-dimensional CFD model. Balakrishnan et al. [101] coupled computational fluid dynamics and a mass transfer model to predict drug deposition for single and overlapping drug eluting stents. The simulations correlated with in vivo effects and revealed that drug deposition occurs not only beneath regions of arterial contact with the stent strut, but surprisingly also beneath standing drug pools created by strut disruption of flow. Also, recently Balossino [40] investigated the fluid dynamic changes, in terms of WSS and velocity field, in the presence of commercial bare-metal stents and studied the mass transport accross the arterial wall of Paclitaxel eluting stents. Finally, the mechanical behavior of stents during and after implantation were studied by Gay et al. [102] using a fluid-structure interaction computational technique. This complex fluid and deformable structure interaction problem was tackled using an Immersed Finite Element Method (IFEM) and allows to study the flow patterns during the deployment of a stent. However, the proposed modeling strategy is not (yet) validated and the effect of realistic stent expansion by balloon unfolding on the flow patterns remains unknown.

2.5 Future prospects

Future developments in stent modeling will most likely include further integration of innovative (braided and tubular) stent designs and materials in realistic patient specific stenosis models. Such integrated models may even further raise its share in the stent design phase and eventually enter the clinical practice to optimize the coronary revascularization procedure for a specific patient (e.g. as a presurgical planning tool).

In the 'hunt' for the ideal stent, new stent materials (e.g. cobalt-chromium, superelastic shape-memory alloys, (biodegradable) polymers, magnesium, etc.) are emerging. Each of these materials has a specific constitutive behavior and consequently requires a specific innovative stent design. These inventive stent designs and materials can and will further be tested and evaluated 'in numero' [75, 88, 103].

The current (r)evolution in medical imaging, providing scientists with even more detailed and accurate geometrical information for the vessel wall and plaque architecture, in combination with new insights in the constitutive material behavior of soft (biological) tissues and calcifications will allow further optimization of the strategy proposed by Holzapfel and his colleagues [2]. In addition, the recent advances in both image reconstruction, allowing to transfer these detailed medical images and material data into an accurate mathematical model, and simulation tools (e.g. complex contact definitions and innovative geometrical modeling frameworks) will only speed-up this optimization. Furthermore, validation of these numerical results with innovative (targeted) experiments [78] will only encourage the use of the 'in numero' strategy. Therefore, the idea of a surgeon implanting a patient specific stent, selected by means of a numerical presurgical planning tool, no longer seems science fiction.

2.6 Conclusion

From this review, it is obvious that the finite element method offers numerous possibilities in the optimization of (coronary) revascularization procedures.

- The application of such a numerical approach in this specific biomechanical research domain is quite recent (1997) and has known an enormous evolution the last few years. Undoubtedly, all previously mentioned papers have contributed to the current level of understanding the mechanics of both stent designs and angioplasty procedures and the quality of these studies should be evaluated taking into account the available prescience and computational facilities (at the moment of publication). In the early years, numerical simulations were based on

Palmaz-Schatz (Johnson&Johnson) like stents and simplified symmetrical stenosed arteries, mainly due to their straightforward geometry (e.g. the pioneering study published by Auricchio [1]). Furthermore, the *Palmaz-Schatz* stent was the only stent used in a multitude of large clinical studies at that time. Since then this numerical (r)evolution has been characterized by some important milestones, such as (i) the introduction of patient-specific stenosis models by Holzapfel and co-workers in 2000 [2], (ii) the introduction of next generation stent geometries by Migliavacca et al. in 2002 [3] and the introduction of stent design optimization techniques by Timmins and his colleagues [4].

- An astonishing observed fact in numerous studies is the lack of experimental evidence for the obtained numerical results, creating a missing-link with reality and provoking an (understandable) skepticism with respect to numerical models and to the conclusions drawn from them. The little validation that is performed is often merely qualitative, and thus not always applicable to interpret and verify the numerical results. The only consistent quantitative validation regarding the stent free expansion is from Migliavacca et al. [5], showing the considerable discrepancy between numerical results and reality when discarding the presence of the balloon. Regarding the vascular reaction to stent deployment, it should be nuanced that measuring the - by the stent (expansion) induced - stresses in the vessel wall in an experimental setup is a huge challenge. For such specific numerical studies, it makes sense to compare the results with clinical findings in literature (e.g. restenosis rates). Nevertheless, caution should be paid to the adopted methodology of the cited clinical trials (i.e. investigated stent designs, patient recruitment, ...) and specifically designed new clinical follow-ups could be required for thorough validation of the developed hypotheses from the numerical results. In addition, it should be feasible to examine the deployment characteristics of a stent using for example X-ray (Nano) Microtomography [104]. Furthermore, the impact of the assumptions that were made (e.g. balloon neglect or simplification, applied constitutive material models, ...) on the obtained results, should be investigated thoroughly, as already indicated by Holzapfel et al. [72].

- The development of an experimentally validated virtual framework to study the mechanics of stents, both applicable to tubular and braided designs in a variety of materials, seems a challenging though logic first step to meet the above mentioned future prospects. Such a modeling tool should be able to accurately predict the most important stent characteristics (e.g. expansion, recoil, dogboning, foreshortening, flexibility, stiffness, etc.) and is presented in this work.

Chapter 3

Balloon expandable stent design

BALLOON expandable stents are currently manufactured in a wide range of materials (e.g. stainless steel, cobalt-chromium, magnesium, (biodegradable) polymers, etc.) and the vast majority of them are fabricated by precise laser cutting. The cutting pattern (and consequently the resulting stent design) can be chosen in such a way to combine a high flexibility with a sufficient radial strength, without excessive foreshortening, recoil and dogboning phenomena (see stent requirements in Section 2.2.5). However, the variation from existing designs is also a predominant factor in the quest for the 'ideal' stent design, at least from a patent or marketing point of view and consequently, physicians are confronted with over hundred different stent designs for vascular and non-vascular indications in current clinical practice [105].

Despite this overflow in stent choice, restenosis remains the achilles heel of stenting procedures (even in the Drug Eluting Stent (DES) era [106]). Clinical evidence shows that restenosis is partly related to vascular injury and non-uniformity of stent strut distribution. Basically, vascular injury is due to a combination of stent-artery and balloon-artery interactions, both of which depend among other things on the stent design [33, 28]. Examination of the patterns of endothelial damage shows a higher incidence of injured regions at the stent ends [34, 35]. This observation has been explained by Squire [35] as the result of three facts: (i) the stent expands in a non-uniform ends-first manner (dogboning), causing high local contact stresses, (ii) an axial contraction of the geometry during the stent expansion (foreshortening) and (iii) contact between the balloon, which is longer

than the stent, and the artery. Furthermore, it was suggested in literature that restenosis after DES implantation may be partially related to non-uniform stent strut distribution [36]. This observation can be explained by the local drug concentrations and gradients, resulting from inhomogeneous strut placement [37]. Therefore (and also for minimizing the tissue prolapse) efforts should be made to optimize the uniformity of the stent strut distribution.

As stated in Chapter 2, most of the design requirements to optimize the mechanical properties of a stent can be examined in a virtual design space, provided that the virtual bench-mark tests capture the actual physical stent behavior. Thus, such validated bench-marks are extremely useful from a manufacturer point of view. In addition, subjecting different stent designs (e.g. from different manufacturers) to exactly the same virtual tests offers physicians an objective comparison of the mechanical behavior of the investigated designs, providing them with extra information to decide which stent to use for which patient. In this chapter several numerical bench-mark tests are described to study the (mechanical) performance of balloon expandable stents. First, a realistic and validated model is developed to study the expansion of folded angioplasty balloons based on the manufacturer's compliance chart. Subsequently, different expansion modeling strategies are studied and compared for a new generation balloon expandable coronary stent. The methodology taking into account the interaction between the trifolded balloon and the stent shows very good quantitative and qualtitative agreement with respectively manufacturer's data and experiments. In addition, the impact of balloon length, folding pattern and stent positioning on the stent expansion is examined in the proposed virtual design space. Finally, a computational stent design platform, combining parametric geometrical modeling with different finite element bench-mark tests to study stent flexibility, expansion and radial strength is presented.

3.1   Balloon expansion

An essential prerequisite in the quest for a realistic model to study the expansion of balloon expandable stents is (logically) a realistic and validated balloon model. Determining characteristics of such an angioplasty balloon catheter are the folding pattern (to have a low profile for deliverability and lesion access), the overall dimensions (length, diameter) and the material properties.

3.1.1   Introduction

Although several numerical studies can be found in literature dedicated to balloon expandable stents and balloon angioplasty, none of them include the

balloon itself in its actual folded shape and with an appropriate material description. Either the balloon is discarded from the analysis and replaced with a uniform pressure distribution or the balloon is simulated as a non-folded cylinder as summarized in Section 2.3. This study exploits the Finite Element Method (FEM) to investigate the free expansion of the commercially available trifolded semi-compliant *Raptor* (Cordis) angioplasty balloon. A methodology is proposed to derive a realistic constitutive balloon material model directly from the manufacturer's compliance chart. Since the fundamental constituent in every angioplasty procedure is a folded balloon, our approach could be the basis for new generation realistic computational models of such procedures and might play an important role in the design of new devices.

3.1.2 Materials and methods

The free expansion of the *Raptor* coronary dilatation catheter is simulated and validated through comparison with the manufacturer's compliance chart. Such a chart is at the disposal of the physicians[1] and describes the relationship between the inflation pressure and the corresponding diameter of the balloon.

Model geometry

The compliance chart is provided by the manufacturer for pressures p higher than $0.2\,\text{N/mm}^2$ (i.e. $0.2\,\text{MPa}$) and up to approximately $2\,\text{N/mm}^2$ for the *Raptor* balloon. Extrapolating the balloon diameter D_b from the compliance chart to $0\,\text{N/mm}^2$ leads to an initial diameter D_{b0} of $2.85\,\text{mm}$. The cylindrical *Raptor* balloon model, including the tapered heads, is depicted in the left panel of Figures 3.1 and 3.2 and the length of the non-tapered cylindrical part is $10.5\,\text{mm}$. The complete balloon measures $13.5\,\text{mm}$ from proximal to distal balloon tip.

The realistic folding pattern of the *Raptor* balloon (depicted in Figure 2.3) is geometrically approximated by folding the deflated balloon (around a cylindrical inner member) which decreases the diameter to $0.88\,\text{mm}$ as shown in the right panel of Figures 3.1 and 3.2. In view of the longitudinal symmetry of the model, only a segment with length $0.4\,\text{mm}$ is considered for the numerical simulations in this paragraph as depicted in the right panel of Figure 3.1. The uniform balloon thickness t_b and the cylindrical catheter shaft diameter D_c are assumed to be $0.02\,\text{mm}$ and $0.6\,\text{mm}$, respectively.

---

[1]Manufacturers are recommended (e.g. by the FDA) to label their devices with such a compliance chart as this information guides the selection of the balloon size to fit the target lesion.
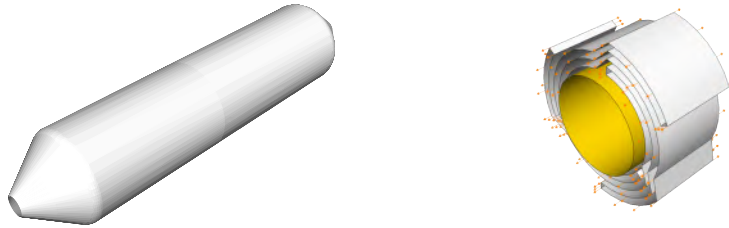
Figure 3.1: Geometrical model of the non-pressurized cylindrical shape with tapered heads (left panel) and the trifolded shape without tapering (right panel) of the *Raptor* balloon catheter. In the latter model, the effect of the tapered heads is included by imposing appropriate boundary conditions (orange arrows).
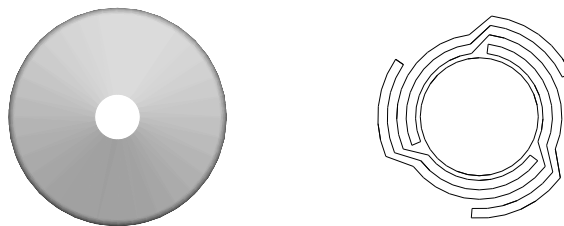

Figure 3.2: Detailed cross section of the cylindrical (left panel) and segment of the trifolded (right panel) *Raptor* balloon catheter model.

Material properties

The semi-compliant *Raptor* balloon is fabricated from nylon based Duralyn and the constitutive material behavior is derived from the compliance data (see Figure 3.5) based on thin shell membrane theory [107] under the following assumptions:

- the balloon material is linear elastic, isotropic and homogeneous

- the balloon material is in a state of plane stress

- $\frac{D_b}{t_b} \geqslant 5$ with t_b being uniform and constant

- the presence of the connection to the catheter shaft influences the axial stress state

The nominal circumferential (or hoop) strain $\epsilon_{\theta,\text{nom}}$ and stress $\sigma_{\theta,\text{nom}}$ components and the nominal axial stress $\sigma_{z,\text{nom}}$ are defined as:

$$\epsilon_{\theta,\text{nom}} = \frac{D_b - D_{b0}}{D_{b0}} \tag{3.1}$$

$$\sigma_{\theta,\text{nom}} = \frac{pD_b}{2t_b} \tag{3.2}$$

$$\sigma_{z,\text{nom}} = \frac{p(D_b^2 - D_c^2)}{4t_b D_b} \tag{3.3}$$

Since the balloon has closed ends, both axial and hoop stresses appear together when the balloon is inflated. Therefore, the balloon diameter variation is function of both the balloon material and its geometrical constraints (fixation to the catheter) and the constitutive law describing the balloon material must include these effects since the strain in any given direction is influenced not only by the stress in that direction, but also by the Poisson strains contributed by the stresses in the other direction. Consequently, the constitutive behavior of the assumed elastic material is given by:

$$\epsilon_{\theta,\text{nom}} = \frac{1}{E}\left(\sigma_{\theta,\text{nom}} - \nu\sigma_{z,\text{nom}}\right) \tag{3.4}$$

with E and ν respectively Young's modulus and Poisson's ratio.

To approximate the balloon by an elastic material, the (unknown) modulus of Young can be determined by plotting the true strain ϵ_{true} in function of the true stress σ_{true} components[2] as large deformations can be expected from a geometrical point of view. Therefore, the constitutive behavior is implemented in ABAQUS based on the true stresses and strains, instead of the nominal values (which is generally used with linear geometrical and material behavior).

Assuming nominal stress-strain data for a uniaxial test are available and the material is isotropic, a simple conversion to true stress and true (or logarithmic) strain is

$$\sigma_{\text{true}} = \sigma_{\text{nom}}(1 + \epsilon_{\text{nom}}) \tag{3.5}$$

---

[2]Nominal (or engineering) stress and strain measures incorporate fixed reference quantities. In this case, the undeformed cross-sectional area and length are used. True stress and strain measures account for changes in cross-sectional area and length by using the instantaneous values for area and length, giving more accurate measurements for events characterized by large deformations.

$$\epsilon_{\text{true}} = \ln(1 + \epsilon_{\text{nom}}) \tag{3.6}$$

An approximation for the two-dimensional stress state in the elastic balloon membrane can be obtained by combining Hooke's law (Equation 3.4) with Equation 3.5 leading to the following expression for the true stress $\sigma_{\theta,\text{true}}$

$$\sigma_{\theta,\text{true}} = (\sigma_{\theta,\text{nom}} - \nu\sigma_{z,\text{nom}})(1 + \epsilon_{\theta,\text{nom}}) \tag{3.7}$$

and based on Equation 3.6 the true circumferential strain $\epsilon_{\theta,\text{true}}$ is defined as

$$\epsilon_{\theta,\text{true}} = \ln(1 + \epsilon_{\theta,\text{nom}}) \tag{3.8}$$

The true strain and stress components are plotted in Figure 3.3 (crosses) and the balloon material is approximated by an elastic model (line), characterized by a Young's modulus of $920\,\text{N/mm}^2$. The adopted values for the (nylon) balloon material density and the Poisson's ratio are respectively $1100\,\text{kg/m}^3$ and 0.4 [108].

Numerical aspects

The cylindrical reference model is discretized by 2304 4-node quadrilateral membrane elements with reduced integration (M3D4R) and the fixation to the catheter shaft is modeled by constraining the displacements in each direction of the proximal and distal balloon tips. During virtual inflation up to a pressure of $20\,\text{atm}$ or $2.026\,\text{N/mm}^2$, the displacements in the radial and longitudinal direction are monitored in two reference points at a distance of respectively $0.5\,\text{mm}$ and $2\,\text{mm}$ from the longitudinal symmetry plane.

The complex geometry of the folded balloon is approximated by a finite element mesh consisting of 2220 (equal-sized) 4-node quadrilateral membrane elements with reduced integration (M3D4R) and the relatively stiff (as compared to the flexible balloon) inner cylindrical shaft is simulated with 154 4-node bilinear rigid quadrilateral elements (R3D4). Rigid body motion of the catheter shaft is prevented and the axial stress state - resulting from the proximal and distal fixation of the balloon to the inner member - is taken into account by imposing a (pressure dependent) axial displacement field to both balloon ends. This axial displacement field is assumed to vary
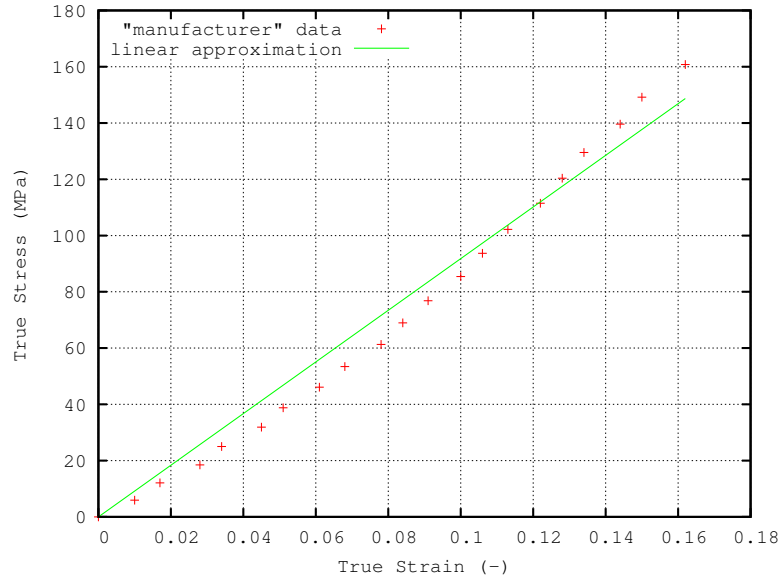
Figure 3.3: *Raptor* balloon constitutive material behavior: true strain and stress derived (Equations 3.8 and 3.7) from manufacturer compliance chart and linear elastic approximation.

linearly across the balloon length[3]. Consequently the prescribed displacements for the folded balloon model are obtained by multiplication of the values from the reference simulation obtained at 0.5 mm with the length of the folded balloon model (see Figure 3.4)[4]. The key features of the analysis are the presence of non-linearities due to large deformations and (self) contact. This complex contact problem of the balloon interacting with itself and the catheter is implemented by a stable general contact algorithm and the frictional behavior is described by a Coulomb friction model with a friction coefficient of 0.2 (nylon-nylon). Similar to the reference balloon inflation, the internal pressure is applied uniformly over the balloon's inner surface and is assumed to increase from 0 to 2.026 N/mm^2.

In general, ABAQUS/Explicit is ideally suited for the solution of complex non-linear dynamic and quasi-static problems, especially those involving extremely complex contact conditions. As inertia is assumed to have negligible effect on the expansion of an angioplasty balloon, both balloon ex-

---

[3]This linear approximation is confirmed by comparing the longitudinal displacements at 0.5 mm and 2 mm in the reference simulation, leading to increased axial displacements with factor 4 (e.g. at a pressure of 1 MPa, the longitudinal displacements are 2.59 μm and 10.38 μm at respectively 0.5 mm and 2 mm in the reference simulation).

[4]The proposed methodology allows for easy determination of the boundary conditions of balloons with different lengths
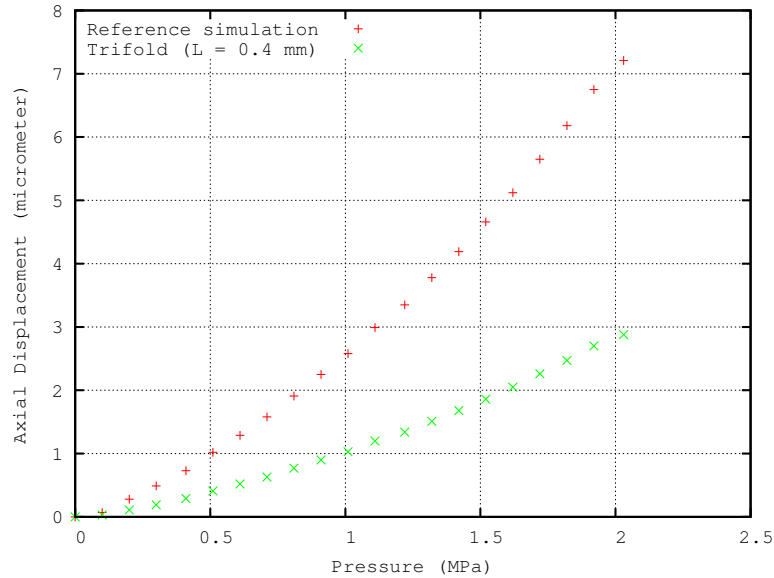
Figure 3.4: Axial displacement field obtained from the cylindrical reference *Raptor* balloon model (at 0.5 mm) and approximated for the folded balloon model with length 0.4 mm. As the axial displacement field will be implemented at both balloon ends, the axial displacements are determined by multiplying the reference values with the length of the folded balloon model (e.g. at a pressure of 1 MPa, the longitudinal displacements are 2.59 μm and 1.03 μm for respectively the 0.5 mm and 0.4 mm model).

pansions are modeled as quasi-static ABAQUS/Explicit procedures. To avoid unrealistic diameter fluctuations during the expansion of the trifolded model, mass-proportional Rayleigh damping is added to the model ($\alpha_R = 8000$, corresponding to 50 % of the critical damping ξ) as an energy dissipation mechanism. This mass-proportional damping simulates the idea of the model moving through a viscous 'ether' (a permeating, still fluid), which corresponds (qualitatively) to some extent to the natural habitat of an angioplasty balloon (even during submerged in vitro non-clinical testing for labeling).

3.1.3   Results and discussion

A very close agreement in compliance between the results from both analyses and data provided by the manufacturer reveals the potential of the proposed approach.

Reference simulation

The results of the reference simulation (cylindrical balloon) in terms of pressure p and balloon diameter D_b are summarized in Figure 3.5. The maximum percent difference occurs at $0.9\,\text{N/mm}^2$ and is an underestimation of only 1.3% of the balloon diameter as compared to the compliance data of the manufacturer (i.e. $3.04\,\text{mm}$ instead of $3.08\,\text{mm}$). As the international standard (ISO/DIS 25539-2) for cardiovascular implants and endovascular devices proposes an accuracy of $1\,\%$ in diameter measurements and $5\,\%$ in pressure measurements for vascular stents, the numerical results seem more than acceptable.
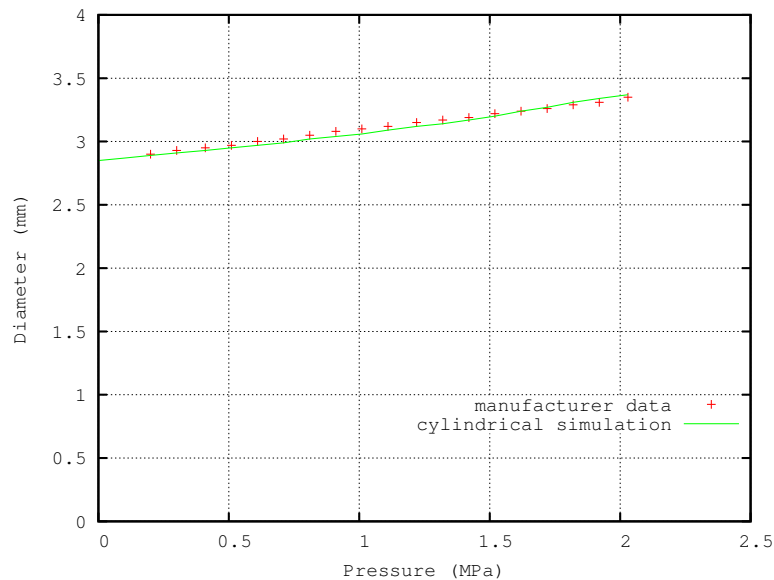

Figure 3.5: The cylindrical *Raptor* balloon model shows a very good agreement with the manufacturer compliance chart.

Trifolded simulation

The free expansion of the folded angioplasty balloon is characterized by a rapid unfolding at low pressures followed by an increase of diameter of the cylindrical shape at higher pressures, as shown in Figure 3.6. A close agreement in compliance between the results from the FE analysis and data provided by the manufacturer is established (see Figure 3.7). Adding mass-proportional damping to the model clearly reduces the diameter fluctuations without altering the overall expansion behavior significantly. As a result, the maximum percent difference between simulation and manufacturer data

reduces from 9.8% at a pressure of $0.3\,\text{N/mm}^2$ to 2.3% at a pressure of $0.3\,\text{N/mm}^2$ when taking damping into account. Furthermore, Figure 3.7 clearly illustrates still some minor diameter fluctuation in the low pressure range (i.e. pressure $\leqslant 0.4$) for the damping scenario. Ignoring these small fluctuations when comparing the numerical results with the compliance chart leads to a maximum percent difference of 1.2% at a pressure of $0.9\,\text{N/mm}^2$, showing the excellent agreement between the cylindrical model with tapered heads, the folded model and the compliance chart provided by the manufacturer.
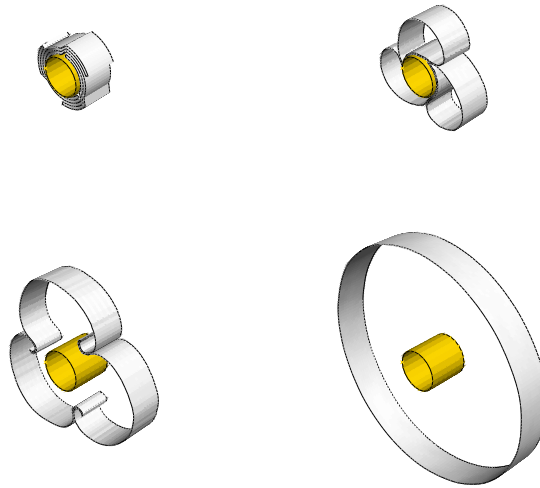

Figure 3.6: Expansion process of trifolded *Raptor* balloon characterized by balloon unfolding followed by gradual cylindrical expansion.

3.1.4 Limitations

With regards to the balloon thickness no data were available, so a general methodology is proposed to derive the constitutive behavior from the balloon compliance chart. The assumed balloon thickness of $0.02\,\text{mm}$ (corresponding with poly-urethane angioplasty balloons) influences the constitutive material behavior, but has no significant impact on the balloon compliance (e.g. a balloon with a greater thickness will generate a lower stiffness and consequently will lead to approximately the same diameter at a certain pressure as compared to a balloon with a smaller thickness). Furthermore, in clinical practice the balloon is expanded by gradual inflation via external
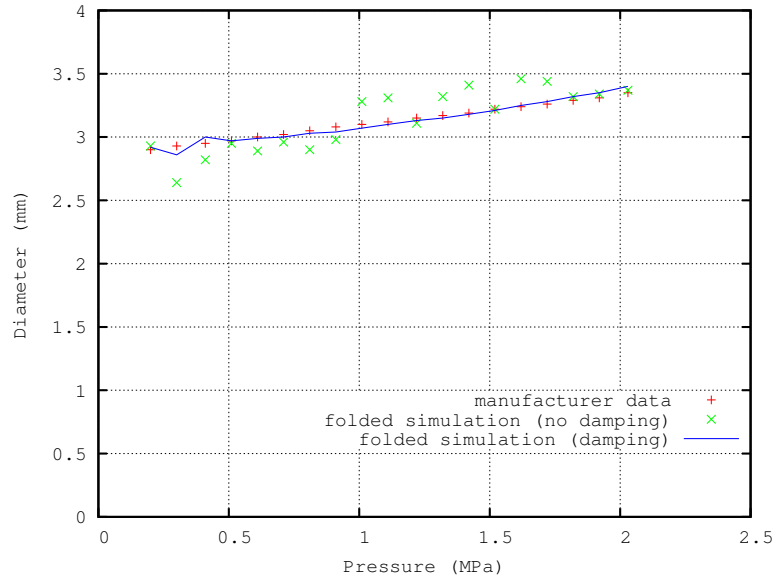
Figure 3.7: The folded *Raptor* balloon model (with damping) shows a very good agreement with the manufacturer compliance chart.

manually applied hydraulic pressurization (i.e. inserting a certain volume of liquid into the balloon). An extremely complex Fluid-Structure Interaction (FSI) problem needs to be solved to capture this balloon filling, as the computational grid is required to adapt significantly when the balloon transforms from its folded shape to the cylindrical shape. Such a detailed investigation is beyond the scope of this study. Therefore the balloon filling is modeled as an increasingly uniform pressure on the inner surface of the trifolded balloon.

3.1.5   Conclusions

The finite element method has proven to be a useful tool in simulating the free expansion of a commercially available trifolded angioplasty balloon and numerical results correspond very well with data provided by the manufacturer. The proposed methodology allows to determine approximate balloon material properties and appropriate boundary conditions (which mimic the balloon tapering) based solely on the manufacturer compliance chart. Consequently, our approach can easily be applied to most dilatation catheters[5] and could be the basis for new generation realistic computational models

---

[5]For compliant balloons, a hyperelastic approximation based on the nominal strain and stress values (Equations 3.1 to 3.4) might be more appropriate.

of angioplasty procedures. Such numerical models will offer interesting insights in the mechanical aspects of such procedures and play an important role in the design of new devices (e.g. dilatation catheters, stents, etc.).

3.2   Stent expansion

At present, the deployment of an intravascular stent has become a common and widely-used minimally invasive treatment for coronary heart disease. To improve these coronary revascularization procedures (e.g. reduce in-stent restenosis rates) the optimal strategy lies in the further development of stent design, material and coatings. In the context of optimizing the stent design, computational models can provide an excellent research tool.

3.2.1   Expansion modeling strategies

In this section, the hypothesis that the free expansion of a stent is determined by the unfolding and expansion of the balloon is examined. Different expansion modeling strategies are studied and compared for a new generation balloon expandable coronary stent. The trifolded balloon methodology presented here shows very good quantitative and qualitative agreement with respectively manufacturer's data and experiments. Therefore, the proposed numerical expansion strategy appears to be a very promising optimization methodology in stent design.

3.2.1.1   Introduction

The free expansion of a new generation balloon expandable coronary stent is investigated numerically following three scenarios: (i) ignoring the balloon and applying an increasing uniform pressure directly on the stent inner surface, (ii) accounting for balloon-stent interaction and enforcing a radial displacement-driven process on a cylindrical balloon and (iii) accounting for balloon-stent interaction by applying an increasingly uniform pressure on the inner surface of a trifolded balloon. The numerical results are validated quantitatively through a comparison with the reference pressure-diameter relationship (provided by the manufacturer). The proposed approach permits to evaluate and compare these different methodologies to model the free expansion of a balloon expandable stent and can be easily applied to most (coronary) stent designs. Consequently, this study allows assessing the optimal free expansion methodology for finite element based stent design.

3.2.1.2 Materials and methods

In general, a finite element model is defined by its geometry, material properties and some specific numerical aspects (e.g. appropriate loading and boundary conditions). To simulate the free expansion of balloon expandable stents, these prerequisites are described below.

Model geometry of stent/balloon

The investigated stent resembles the *Cypher* coronary stent (nominal length 8 mm, nominal diameter 3 mm; Cordis), crimped on a trifolded *Raptor* balloon (nominal diameter 3 mm; Cordis). The main stent dimensions are obtained from micro-Computer Tomography (micro-CT images [60]) and were used to build the geometrical model of the stent device by means of the graphical finite element preprocessor ABAQUS/CAE (Simulia, Inc.). The length, inner and outer diameter of the crimped stent are 8.5 mm, 0.9 mm and 1.2 mm respectively. The resulting strut thickness of 0.15 mm is also confirmed by the directions for use of the stent (provided by the manufacturer), stating that the stent outer diameter is 0.3 mm larger than the inner diameter. The non-tapered ,stent protruding, part of the balloon is both proximal and distal 1 mm in length. The trifolded pattern of the balloon was confirmed by micro-CT based image reconstruction of this part of the balloon (see Figure 2.3) and an idealized geometrical model of the folded balloon was built using ABAQUS/CAE (see Section 3.1). The uniform balloon thickness and the cylindrical catheter shaft diameter are assumed to be 0.02 mm and 0.6 mm, respectively. The complete model of the stent device is depicted in Figure 3.8.

Material properties

The balloon expandable *Cypher* stent is manufactured in 316L stainless steel. As the constitutive behavior of a material is dependent of its pretreatment (e.g. hot rolling, cold finishing, annealing, etc.), the material properties should be obtained from tensile tests on specimens extracted from batches that are eventually used to create the stent structure. For this reason, small 316L stainless steel strut specimens (60-500 μm) were examined under uniaxial tensile loading in an experimental study [63]. Therefore, the mechanical properties to describe and implement the inelastic behavior are based on this experimental study. The inelastic constitutive response is described through a von Mises plasticity model with isotropic hardening. The Young's modulus, the Poisson's ratio and the yield stress are 196000 N/mm^2, 0.3, and 375 N/mm^2 respectively [63]. As derived from the compliance chart in Section 3.1, the semi-compliant *Raptor* balloon material is approximated by an elastic model (line), characterized by a Young's
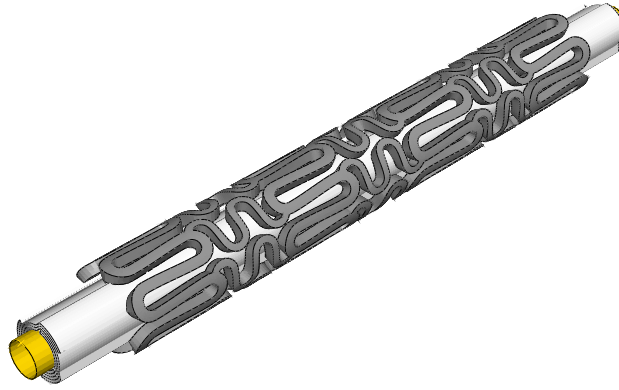
Figure 3.8: Geometrical model of the *Cypher* stent and part of the delivery system (inner shaft and non-tapered part of the folded balloon).

modulus of $920\,\mathrm{N/mm^2}$ and a Poisson's ratio of 0.4. The relatively stiff (as compared to the flexible balloon) inner shaft is modeled as a rigid cylinder. The adopted values for the material densities of the stent and the balloon are $7800\,\mathrm{kg/m^3}$ and $1100\,\mathrm{kg/m^3}$ respectively.

Numerical aspects

The stent is modeled with three-dimensional 8-node brick 'reduced-integration' elements (C3D8R) using ABAQUS finite element code. To keep the analysis run-time reasonable, a finite element mesh consisting of 30112 elements was used for the stent. The balloon was meshed with 58386 4-node quadrilateral membrane elements with reduced integration (M3D4R) and the rigid inner cylindrical shaft was simulated with 3410 4-node bilinear rigid quadrilateral elements (R3D4). Comparing these mesh densities to finer meshes for this specific stent delivery system design (i.e., stent: 53655, balloon: 103950 and catheter: 7040 elements) showed negligible divergence (i.e. difference in maximum radial displacement smaller than $1\,\%$). To simulate the free expansion of the stent, a large deformation analysis was performed following three scenarios: (i) ignoring the balloon and applying an increasing uniform pressure up to $2.1\,\mathrm{N/mm^2}$ directly on the stent inner surface, (ii) accounting for balloon-stent interaction and enforcing a radial displacement-driven process on a cylindrical balloon (to reach a nominal inner stent diameter of $3\,\mathrm{mm}$) and (iii) accounting for balloon-stent inter-

action and applying an increasing uniform pressure up to $1.5\,\text{N/mm}^2$ on the inner surface of a trifolded balloon. The key features of the analyses performed are the presence of non-linearities, large deformations and (self) contact. All numerical simulations were performed on an in-house built low-cost, high performance computing cluster [109] and for all three scenarios, the (final) numerical results were obtained within 48 hours after launching the computations. During expansion, the folded balloon is subjected to axial stresses resulting from the proximal and distal fixation of the balloon to the inner shaft as explained in Section 3.1. With regard to the stent modeling, boundary conditions are applied which constrain six nodes in the medial cross section of the stent itself in both the longitudinal and tangential directions. Inertia is assumed to have negligible effect on the expansion of a stent. Therefore, the stent expansion scenarios are modeled as quasi-static ABAQUS/Explicit procedures. Increasing the physical loading rate is often required to obtain a (computationally) economical solution with such an explicit dynamic procedure. Consequently, the actual duration of the numerical stent expansion is reduced artificially by increasing the rate at which the load is applied in the simulations. However, as the stent expansion is accelerated, inertia forces may become dominant. Therefore, a time-(in)dependency study was performed for all three scenarios to determine the loading rates at which inertial forces remain insignificant. The third expansion scenario is characterized by a complex contact problem as the balloon interacts with the catheter, the balloon-itself and the stent. This interaction problem is implemented by a stable general contact algorithm and the frictional behavior is described by a Coulomb friction model with a static friction coefficient of 0.2 (valid for a nylon-nylon and a nylon-steel friction couple under clean conditions [110]). These contact specifications allow avoiding numerical instabilities in the simulation of the interactions and are also implemented in the second expansion scenario.

3.2.1.3 Results and discussion

Simulation results

Figure 3.9 shows the stent deployment patterns for all three scenarios prior to, during and after the transient expansion phase (more specifically, when the inner diameter of the central zone of the stent reaches its nominal diameter of 3 mm). The stent shape during the transient expansion is highly dependent on the applied methodology to model the stent free expansion. Ignoring the presence of the balloon (scenario (i)) leads to a fusiform stent shape, characterized by larger radial displacements in the central zone as compared to the stent ends. The model incorporating the actual folded shape of the balloon (scenario (iii)) shows a completely opposite behavior, driven by the unfolding of the balloon. The expansion of the distal zone is

stronger with respect to the central zone and such a behavior is often referred to as 'dogboning'. An interesting observable fact is the longitudinal asymmetry[6] in the dogbone-shape, presumably related to the balloon folding pattern. Since the second scenario is characterized by a radial displacement-driven process, neither the fusiforming, nor the dogboning phenomena are observed and the stent shape remains cylindrical. After the transient expansion phase, the cylindrical stent shape when reaching its nominal diameter shows very good agreement for the second and third scenario. Though, the stent shape remains fusiform for the first scenario.

Validation

As a compliance chart is provided by the manufacturer for every commercially available stent, the numerical results regarding the free expansion of a stent can easily be validated quantitatively. Therefore, the results of both pressure-driven scenarios in terms of pressure and inner diameter D are summarized in Figure 3.10. Such a graphical interpretation of the numerical results is impossible for the second scenario since it is displacement-driven. Accounting for the presence of the folded balloon reveals a particular deployment pattern in the low pressure range ($< 0.4\,\mathrm{N/mm^2}$ or approximately $4\,\mathrm{atm}$) driven by the unfolding of the balloon and ensures a very close agreement between the simulated and reference pressure-diameter relationship. The maximum percent difference in diameter occurs at a pressure of $1.4\,\mathrm{N/mm^2}$ and is an underestimation of $4.1\,\%$ compared to the manufacturer data (i.e. $3\,\mathrm{mm}$ instead of $3.13\,\mathrm{mm}$). Discarding the balloon from the analysis reveals again a totally different deployment pattern and allows no reasonable comparison with the manufacturer data in function of pressure and diameter. It should be noted that the pressure to expand the stent to its nominal diameter for the 'no balloon' scenario (i.e. $2.1\,\mathrm{N/mm^2}$) is much higher compared to the pressure for the 'trifolded balloon' scenario (i.e. $1.4\,\mathrm{N/mm^2}$). On the one hand, this difference is related to the surface to which the pressure is applied, since the resulting radial force to expand the stent should be of the same order of magnitude for both scenarios. As the area of the inner surface of the trifolded balloon is much larger than the stent inner surface, a much lower pressure is required to expand the stent when taking the balloon into account in the model. On the other hand, the stent diameter is strongly related to the balloon compliance when reaching its cylindrical shape. As of that moment, part of the applied pressure is transferred into energy stored in the balloon membrane.

In addition to the good quantitative agreement with the manufacturer data, the numerical results of the third scenario correspond well with a qualitative experiment to visualize the expansion of the *Cypher* stent. The stent

---

[6]The difference in diameter between the distal and the proximal end during the transient deployment phase.
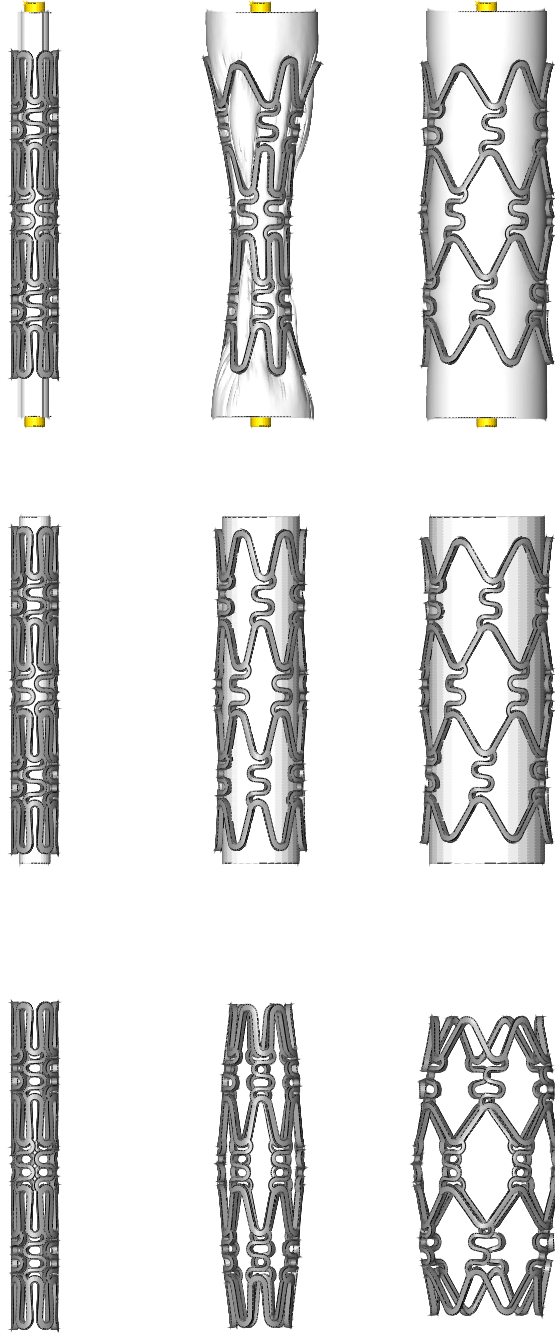
Figure 3.9: Stent deployment patterns resulting from (i) 'no balloon' scenario (left), (ii) 'cylindrical balloon' scenario (middle) and (iii) 'trifolded balloon' scenario (right) prior to (top), during (centre) and after (bottom) the transient expansion phase.
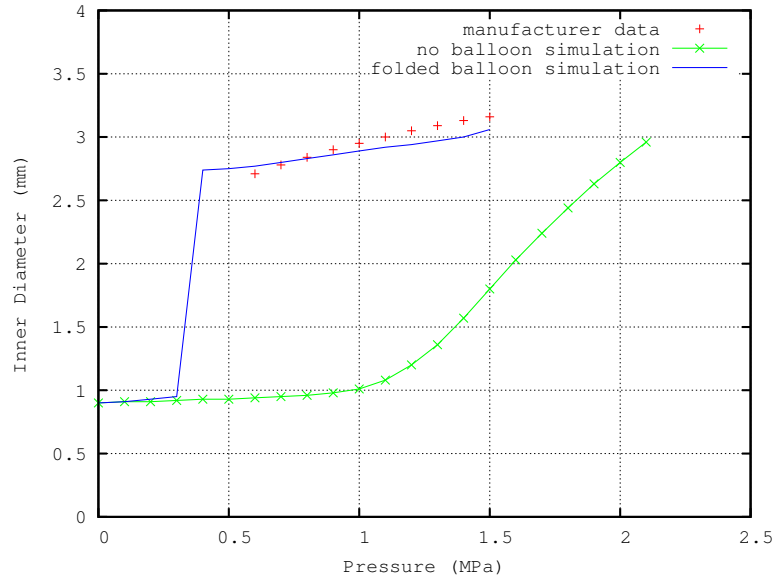
Figure 3.10: Results from the pressure-driven FEM analysis (scenario (i): no balloon; scenario (iii): trifolded balloon) and data provided by the manufacturer.

expansion, as acquired by an innovative μ-CT set-up [60], shows good agreement with the stent deployment pattern of the third scenario as depicted in Figure 3.11. Furthermore, the particular deployment pattern in the low pressure range (i.e. the rapid increase in diameter when the inflating pressure reaches a certain value) and the dogbone shape were also observed experimentally.

Discussion

Generally, the design of a new stent can be divided into two separate phases. At first, the designer is mainly interested in the global behavior of the stent (e.g. the stent shape when reaching its nominal diameter) and whether the design fulfills the prerequisites of the stent material (e.g. the strains are not exceeding the failure strain). The radial displacement driven cylindrical balloon expansion method provides useful and (relatively) accurate information regarding the stent shape (and thus, the stresses and strains the stent is subjected to) when reaching its nominal diameter. Therefore, the second expansion scenario is the optimal choice as it is computationally less expensive compared to the third scenario. However, to further optimize the transient expansion of the new stent, a model is required which shows good agreement with both qualitative and quantitative experiments. Con-
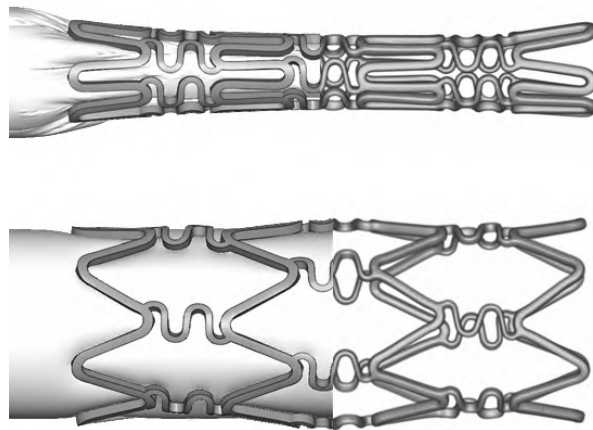
Figure 3.11: Results from the pressure-driven FEM analysis (scenario (iii): tri-folded balloon - left) and µ-CT visualization of stent expansion (right).

sequently, the third scenario is a very promising expansion strategy in this part of the design phase. Moreover, taking the folded balloon into account will provide designers the possibility to examine the effect of the balloon length, balloon folding pattern and the stent positioning on the stent expansion behavior. As both the deployment pattern of the stent and the stent shape at the end of the expansion do not correspond with reality, the first expansion strategy seems not the appropriate way for stent design purposes. Interesting alternative expansion strategies have been proposed in literature recently. To expand the stent, an increasing pressure is applied on a simple, non-folded cylinder with 'virtual' elastic [77] and hyperelastic [73] material properties. However, the accuracy of these assumptions remains unknown, as the validation is purely qualitative (e.g. the numerical simulations are not compared with the experimentally obtained pressure/diameter data) or even absent. Nevertheless, these approaches seem promising, because the computational cost can be reduced. Therefore it seems interesting to compare the results obtained by using the trifolded balloon expansion strategy with the outcome of these simplified approaches. Such a study will answer the question whether it is possible to obtain similar (accurate) results with a simplified balloon shape. Furthermore, the proposed model could be at the basis of studies to understand the impact of balloon unfolding on drug coatings and might have implications for delivery of other kinds of bioactive agents with the stent as a carrier. Finally, as the non-uniform transient stent expansion (i.e. dogboning) might influence the arterial injury, the interaction between balloon/stent and artery will be addressed in future numerical studies.

3.2.1.4 Limitations

The simulation of the free expansion of the *Cypher* stent presented in this study has several important features. The realistic folded geometry of the balloon and both the quantitative and qualitative validation of the numerical results make it a unique model. However, we must recognize remaining limitations in the proposed approach in order to further reduce the (rather small) discrepancies observed between simulations and experiments. These limitations primarily pertain to the balloon and stent geometry, the balloon inflation methodology, and the friction between the stent and the balloon. For numerical reasons (i.e. to enhance the element-choice of the finite element stent mesh), the stent mesh was not reconstructed directly from the CT-scans. Instead, the stent reconstruction was used to measure the main stent dimensions, which allowed building the geometrical model of the stent. This approach permits to neglect the small rounding of the stent struts. We believe that it does not have a significant impact on the stent compliance, and consequently smoothes the progress of the meshing. Furthermore, the use of a (general) static friction coefficient to describe the interaction between the distinct parts of the stent delivery system is a simplification of reality. A dynamic friction coefficient (e.g. function of the specific materials, surface finish, rate of relative movement) would probably be a better approximation of reality, and will be addressed in further research. Finally, clinically, it should be kept in mind that the final expansion diameter reached by a stent is far beyond the nominal diameter given by a compliance chart derived from free expansion in water [111] and that more complex interaction between the stent and the vessel wall must be taken into account [71, 68, 70].

3.2.1.5 Conclusions

The proposed approach allows evaluating and comparing different methodologies to model the free expansion of a balloon expandable stent. In the early stent-design phase, the radial displacement driven cylindrical balloon expansion method can provide useful and (relatively) accurate information regarding the stent shape (and thus, the stresses and strains the stent is subjected to) when reaching its nominal diameter. However, to further optimize the stent design and its expansion, this study shows the advantages of using the trifolded balloon methodology, since the free expansion of a stent is governed by the unfolding and expansion of the balloon. Moreover, the trifolded balloon expansion methodology shows good quantitative and qualitative agreement with respectively manufacturer data and in-house experiments.

3.2.2 The impact of balloon length, folding pattern and stent positioning

In this section, the impact of several parameters such as balloon length, folding pattern and relative position of the stent with respect to the balloon catheter on the free stent expansion are investigated. As the quantitatively validated trifolded modeling strategy shows excellent agreement with data provided by the manufacturer (see Section 3.2.1), this model serves as a solid basis for further investigations. The parametric analyses show that the balloon length and the folding pattern have a considerable influence on the uniformity and symmetry of the transient stent expansion. Consequently, this approach can be used to select the most appropriate balloon length and folding pattern for a particular stent design in order to optimize the stent deployment. Furthermore, it was demonstrated that small positioning inaccuracies may change the expansion behavior of a stent. Therefore, the placement of the stent on the balloon catheter should be carried out accurately, in order to (possibly) decrease endothelial damage.

3.2.2.1 Introduction

Computer simulation (e.g. finite element analysis, FEA) can be a very useful tool to study and optimize the stent expansion [64, 81, 71, 68]. Several numerical studies discuss non-uniform stent expansion without simulating the balloon [1, 5, 69], although it has been experimentally shown by Squire [35] that non-uniform stent expansion is related to both stent design and balloon length. The same conclusion was drawn by Wang et al. [77] based on experiments and FEA. Their simulations were performed by using a cylindrical (non-folded) balloon and were qualitatively validated. Furthermore, Narracott [51] clearly demonstrated experimentally the correlation between the (non-)uniform stent strut distribution and the balloon folding pattern. As stated in the literature survey (Chapter 2), all the published numerical studies concerning stent expansions ignore the folding pattern of the balloon and, consequently, the impact of the folding pattern on the uniformity of the stent expansion remains unknown. Furthermore, dogboning has always been considered at one specific moment in time, although this phenomenon changes during the deployment of a stent.

Keeping the previous considerations in mind, the phenomenon of non-uniform stent expansion is examined numerically at each moment during the deployment. More precisely, the consequences of combining different realistic folded balloon catheters with a particular balloon expandable coronary stent were investigated. Catheters with different balloon lengths and folding patterns were used in the simulations and consequently, this study allows choosing the optimal balloon catheter for this specific new generation stent design. Furthermore, the proposed methodology to obtain a uniform

stent expansion by selecting the most favourable balloon can easily be applied to all balloon expandable stents. Finally, attention has been paid to the impact of relatively small positioning inaccuracies during the crimping process on the expansion behavior. The crimping itself has not been incorporated in the simulations, as we have shown that including the crimping procedure has only a minor influence on the overall stent expansion behavior [112].

3.2.2.2 Materials and methods

Several numerical simulations are carried out to investigate the impact of combining different realistic balloon catheters with the *Cypher* stent geometry. The simulation which incorporates the correct balloon length (i.e. 10.5 mm) and folding pattern (i.e. trifolded), described in Section 3.2.1, is termed reference simulation. The obtained results from this reference simulation serve as a basis for the analysis of subsequent numerical calculations (see Table 3.1). Simulations A to J concentrated on the influence of the balloon length on the uniformity of the stent expansion, while keeping the folding pattern of the balloon. Then, simulation K was carried out to examine the influence of altering the folded shape from a trifolded to a sixfolded balloon as shown in Figure 3.12. In accordance with the trifolded balloon, the sixfolded balloon has been developed consistent with the initial balloon diameter, the stent inner diameter, the balloon thickness and the diameter of the cylindrical catheter tube. Finally, the influence of positioning inaccuracies was studied in the simulations L and M by axially translating the previously centrally placed stent over 0.1 mm.
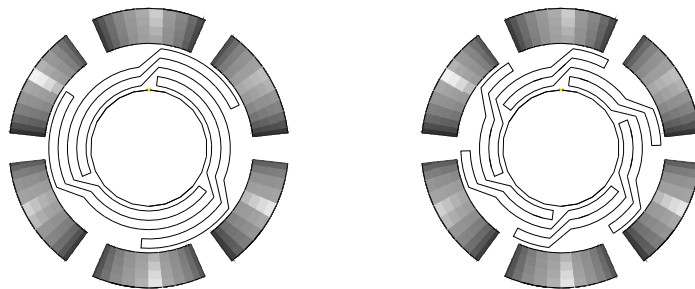
Figure 3.12: Comparison of a trifolded (left) and a sixfolded balloon (right). Both folding patterns are based on the same initial balloon diameter, namely $D_{b0} = 2.85$ mm.

With the aim of quantifying the uniformity of the stent expansion during inflation, the following dogboning (DB) and asymmetry (AS) coefficients

Table 3.1: Balloon length, folding pattern and stent positioning (non-central corresponds with a 0.1 mm axial translation).

Simulation	Balloon length (mm)	Folding pattern	Axial stent position
Reference	10.5	trifold	central
A	10.3	trifold	central
B	10.1	trifold	central
C	9.9	trifold	central
D	9.7	trifold	central
E	9.5	trifold	central
F	9.3	trifold	central
G	9.1	trifold	central
H	8.9	trifold	central
I	8.7	trifold	central
J	8.5	trifold	central
K	10.5	sixfold	central
L	10.5	trifold	non-central
M	10.5	sixfold	non-central

are introduced:

$$\text{DB} = \frac{R_{\max(\text{distal,proximal})} - R_{\text{central}}}{R_{\max(\text{distal,proximal})}} \tag{3.9}$$

$$\text{AS} = \frac{R_{\max(\text{distal,proximal})} - R_{\min(\text{distal,proximal})}}{R_{\max(\text{distal,proximal})}} \tag{3.10}$$

$R_{\max(\text{distal,proximal})}$ and $R_{\min(\text{distal,proximal})}$ stand respectively for the maximal and the minimal value of the two end radii of the stent measured at the inner surface at a specific moment during the inflation. This can be the distal or the proximal radius. This distinction is necessary as the stent ends may not have the same radii at the same moment during the stent expansion. R_{central} is the inner radius of the stents midsection at these moments.

3.2.2.3   Results and discussion

Influence of the balloon length

The stent geometry during the transient expansion phase for simulations E, J and the reference model is shown in Figure 3.13. In contrast to the

reference simulation, the stent model J with the shorter balloon length (8.5 mm) does not open in an ends-first manner. For the model E with the intermediate balloon length, the diameters of the stent ends during the transient phase are only slightly larger than the central diameter, but this phenomenon is less pronounced compared to the reference model. The dog-boning coefficient - whose value changes during the expansion of a stent - is an appropriate parameter to quantify these observations. For the reference simulation, this coefficient is 0 % at the start of the inflation (Figure 3.9, top right, cylindrical shape), reaches a maximum of 59 % during the short transient expansion phase (Fig 3.9, center right) after which it decreases again and finally becomes approximately 2 % at high pressures (Fig 3.9, bottom right, cylindrical shape). In order to obtain a uniform stent deployment, the maximum value of this dogboning coefficient during inflation should be kept as low as possible. Therefore, these maxima have also been determined for models A to J and are visualized in Figure 3.14, which shows a strong relation between the balloon length and the maximum observed dogboning coefficient during the different stent expansions. The non-smooth transition between the maxima might be explained by aliasing in the different simulations due to the maxima occuring at different moments and locations. These results can be used to determine the maximum balloon length that should be combined with a particular stent design in order to avoid dogboning.

As stated in the literature survey 2.3, Wang et al. [77] have also investigated the relationship between balloon length and dogboning by finite element modeling. However, they apply an increasing pressure on the stent by using a cylindrical balloon with 'virtual' material properties. The accuracy of this approximation is still unknown, as the validation is purely qualitative, whereas the model proposed in this study has been quantitatively validated. Furthermore, examining the impact of using a different number of folds is not possible when discarding the folding pattern. Nevertheless, this approach remains interesting for balloon length investigation, because the computational effort can be reduced.

Besides the impact of the balloon length on the vascular injury by dogboning, the balloon itself can cause endothelial damage by direct balloon-artery interactions [28, 35]. As a result, the balloon overlength should be reduced in order to decrease the balloon-artery contact area at the stent ends. Luckily, these two causes of vascular injury (dogboning and balloon-artery contact) result in the same guideline for the balloon length, namely that this length should be kept as small as possible. If a reduction of the balloon length fails to eliminate dogboning, the stent geometry should be modified, as dogboning also depends on this geometry [1, 5, 69, 77]. In particular, the stiffness of the stent ends has to be increased. However, too large an increase will result in an opposite (unwanted) effect (i.e. larger diameter of the central part of the stent compared with the diameter of the stent ends). Therefore, the modification of the stiffness should be done with great care.
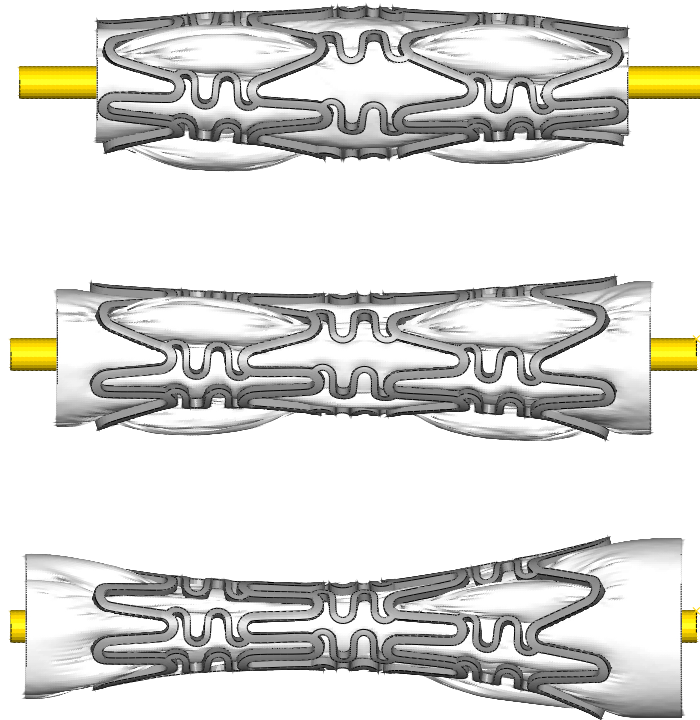
Figure 3.13: Transient expansion shape for model J (top), model E (center), and the reference model (bottom). A shorter balloon length results in a decreased dogbone effect.

Influence of the folding pattern

A comparison of the results from the reference model with those obtained from simulation K is shown in Figure 3.15. This comparison allows the identification of the impact of the folding pattern, as all the other variable parameters (e.g. balloon length, stent position) remain unchanged. During the transient stent expansion, one can observe that the balloon bulges out through some of the stent cells, as shown in Figure 3.13. In order to study the effect of this phenomenon on the stent strut distribution, a cross section of the model was further investigated. As can be seen in Figure 3.15 (left panel), using a trifolded balloon causes large balloon protrusions in three of the six stent cells in that cross section. These strongly protruding parts of the balloon result in larger stent openings at the locations of the protrusions
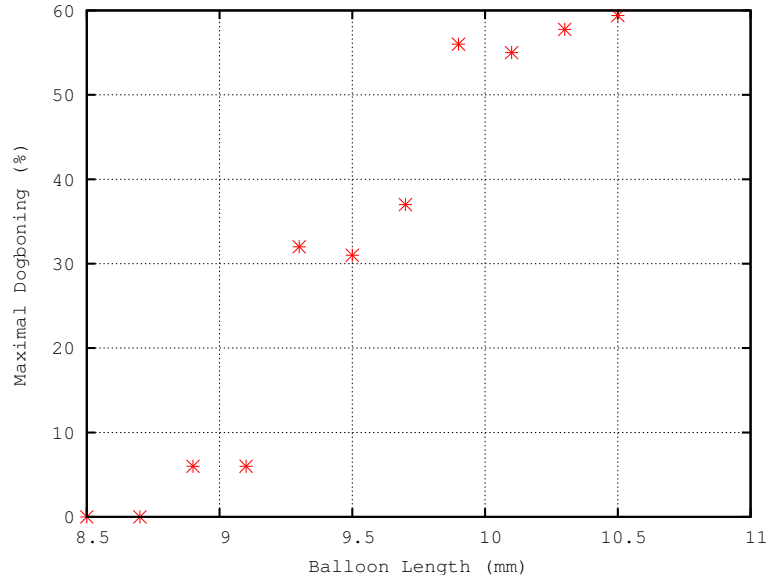
Figure 3.14: Relationship between the balloon length and the maximum of the dogboning coefficient during the expansion phase. A more uniform expansion is obtained by decreasing the balloon length.

and consequently, in a non-uniform stent strut distribution (the maximal angle between two struts is 71 °, a uniform stent strut distribution corresponds with an angle of 60 °). This non-uniform strut distribution was also observed experimentally with μCT at the end of the transient expansion phase (see Figure 3.15 (center panel)). As the number of balloon bulges (3) corresponds with the number of balloon folds (3), one should expect that using a sixfolded balloon would result in a more uniform strut distribution. Indeed, Figure 3.15 (right panel) shows the uniform strut distribution obtained by using a sixfolded balloon.

Influence of small positioning inaccuracies

The results of model L and M are shown in Figure 3.16. Moving the stent over a small distance (i.e. 0.1 mm) in the longitudinal direction results in a totally different deployment pattern during the transient phase. Such an axial translation can be due to positioning inaccuracies during the crimping process. The stent end corresponding with the longest free balloon end opens first, because at that end, the same pressure acts on a larger balloon surface. Results are summarized in Table 3.2 in terms of dogboning (DB) coefficients and coefficients of asymmetry (AS).

Figure 3.15: Cross section at the end of the transient stent expansion, showing that a trifolded balloon causes a non-uniform strut distribution (left panel: simulation; center panel: experiment), whereas a sixfolded balloon (right panel: simulation) results in a homogeneous strut placement.

The coefficient of asymmetry is strongly related to the position of the stent on the balloon catheter. For the trifolded balloon, the already existing asymmetric expansion of a centrally placed stent is reinforced by a small axial translation of the stent (coefficient changes from 34 % to 64 %). This difference is more pronounced in the case of a sixfolded balloon. A central stent position causes an approximately symmetric deployment (7 %), while a non-central placement leads to severe asymmetry (47 %). Consequently, minor positioning inaccuracies of the stent should be avoided, as this leads to asymmetric stent expansions. In future, more advanced computer models taking into account the exact stent geometry and incorporating the balloon ends could be used to tune manufacturing processes. More precisely, for a given balloon-stent combination and an allowed asymmetric expansion value, the maximum balloon eccentricity could be calculated.

Table 3.2: Influence of small positioning inaccuracies on the uniformity of the expansion.

Simulation	Folding pattern	Axial stent position	DB (%)	AS (%)
Reference	trifold	central	59	34
K	sixfold	central	54	7
L	trifold	non-central	60	64
M	sixfold	non-central	58	47

3.2.2.4 Limitations

In this study, the balloon ends were discarded from the model. Creating a balloon model that takes into account both the folding pattern and the bal-
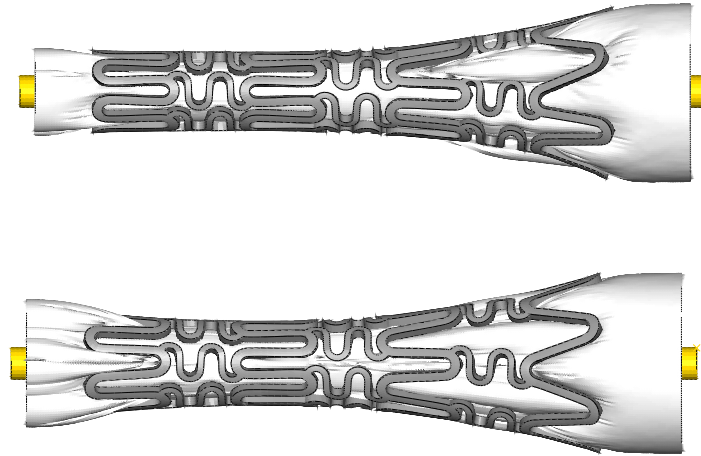
Figure 3.16: Transient expansion shape for model L (top) and M (bottom). A non-centrally placed stent results for both folding patterns in a strongly asymmetric expansion.

loon ends is a very complex problem. One way to overcome this limitation is to directly use a CT based 3D reconstruction of the folded balloon. The feasibility of this approach will be investigated in future work.

It has been shown that both the folding pattern and the longitudinal position of the stent on the balloon catheter have a considerable impact on the symmetry of the expansion, but the clinical consequences of these observations are still unknown. Therefore, future numerical models will incorporate the artery and this will allow to study the resulting strut distribution and stresses in the vessel wall. Including the artery in the simulation models can also be useful to investigate the impact of the presence of the artery on the obtained stent diameters, since it has been observed using intravascular ultrasound that in clinical practice the stents will only reach on average 75 % of the predicted diameter [111], as a consequence of complex interactions with the atherosclerotic plaque forming the coronary stenosis.

3.2.2.5 Conclusions

The validated numerical model described in Section 3.2.1 has been used as a basis for further investigation of several parameters, such as balloon length, folding pattern and relative position of the stent with respect to the balloon catheter. It was shown that changing these parameters can have an enor-

mous influence on the transient stent expansion behavior. Therefore, the proposed methodology can be used to select the most appropriate balloon length and folding pattern for a particular stent design. Furthermore, it has been shown that small positioning inaccuracies (e.g. during the crimping process) can considerably modify the stent deployment. Consequently, the positioning of the stent on the balloon catheter should be done with the greatest care and accuracy.

3.3 Parametric stent design, flexibility and radial strength

A virtual stent design platform, combining parametric geometrical design with different finite element bench-mark tests to study stent flexibility, expansion and radial strength, is presented in this section. These characteristics are examined for the reference *Cypher* (Cordis) stent design and for both a material and a geometrical variation.

3.3.1 Materials and methods

Model geometry and material

To allow parametric variation, the approximate three-dimensional geometry of the original (and thus reference) *Cypher* stent (nominal length 8 mm, nominal diameter 3 mm, strut thickness 150 µm) is created with an in-house script-based geometrical and finite element preprocessor, called pyFormex[7]. The stent design is characterized by ring elements linked by connectors. As stated by Petrini and her colleagues [83], the tubular-like ring elements mainly function to sustain the vessel after the stent expansion whereas the connecting links allow to advance these ring elements in a flexible way during the delivery process. It was shown by Petrini et al. that the flexibility of the considered design can be studied by observing only a portion of the complete stent model composed of two rings and the links between them (see Figure 3.17). The reference *Cypher* stent is made of 316L stainless steel, described by a Young's modulus, a Poisson's ratio and a yield stress of $196000 \, \text{N/mm}^2$, 0.3, and $375 \, \text{N/mm}^2$ respectively [63]. The first material variant corresponds geometrically to the original *Cypher* stent, though the stent is assumed to be made of high-strength L-605 cobalt-chromium. This cobalt-based alloy is implemented as a Hookean elastoplastic material, characterized by a Young's modulus of $243000 \, \text{N/mm}^2$, a yield strength of

---

[7]pyFormex, currently under development at Ghent University, is a tool for generating, manipulating and operating on large geometrical models of 3D structures by sequences of mathematical transformations [56].

$629\,\mathrm{N/mm^2}$ and a Poisson's ratio of 0.3 [113]. The impact of changing the geometry is examined by reducing the number of bends from six to five in both ring elements as depicted in Figure 3.17. Both the width and the height of the stent struts (in the bends and the connectors) remain unaltered.

Table 3.3: Overview of material and geometry of considered stent designs.

	Cypher (reference)	Δmaterial	Δgeometry
material	SS316L	L605 CoCr	SS316L
number of bends	6	6	5
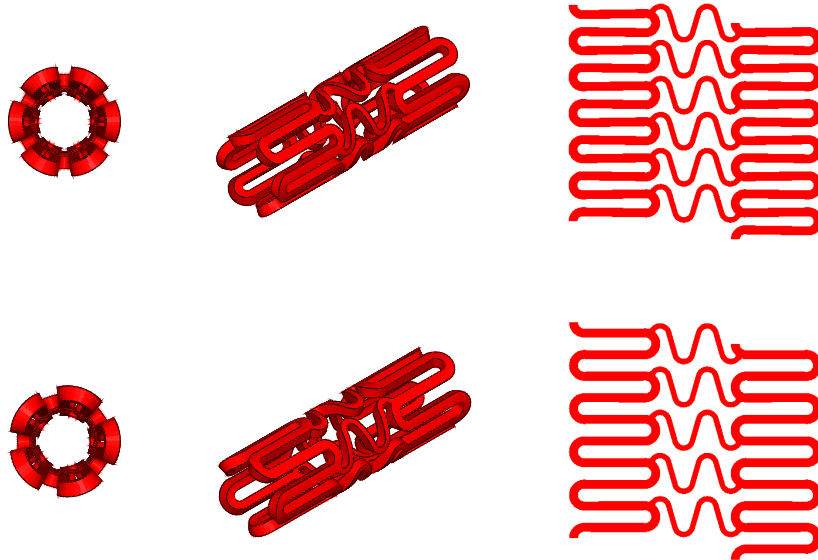
Figure 3.17: Geometry of a unit cell of the original (reference) *Cypher* stent (top) consisting of six bends per ring element and the geometrical design variant with five bends per ring (bottom).

Flexibility

The first bench-mark test is built according to the guidelines by Petrini [83] to evaluate the stent flexibility in the unexpanded state. The flexibility is measured by imposing a bending deformation on the repetitive unit of the stent and computing the corresponding bending loading. This (angular

displacement driven) loading scheme is implemented in ABAQUS/Standard and possible interactions between specific portions of the stent model are taken into account.

Expansion and radial strength

To examine the stent radial strength, a second virtual test is developed in which all stents are subjected to the following three-step loading scenario: (i) radial displacement driven expansion of a cylindrical balloon[8] revealing the expanded stent shape and the foreshortening (ii) reduction of the diameter of the cylindrical balloon revealing the elastic radial recoil of the stent and (iii) increasing external radial pressure on the stent outer surface. The elastic recoil and the foreshortening are defined by Migliavacca et al. [3] as:

$$\text{Radial recoil} = \frac{R_{\text{load}} - R_{\text{unload}}}{R_{\text{load}}} \tag{3.11}$$

$$\text{Foreshortening} = \frac{L - L_{\text{load}}}{L} \tag{3.12}$$

where R_{load} and R_{unload} are respectively the central stent radius when reaching the stent's nominal diameter and after balloon deflation. Expanding the stent to its nominal size (possibly) alters the original stent length[9] from L to L_{load}.

As the investigated stent design variants have a different surface area, the external pressure in the third step is normalized to a force per unit of length (by multiplying the pressure with the stent surface and dividing this product by the stent length L)[10].

3.3.2 Results and discussion

Flexibility

The results of the virtual flexibility tests are shown in Figure 3.18. The geometrically altered design demonstrates a higher flexibility compared to the reference *Cypher* stent and a much higher flexibility as compared to the cobalt-chromium design, because a lower reaction moment needed to obtain

---

[8]As stated in Section 3.2.1, this computationally efficient loading scenario provides an accurate approximation of the stent in the expanded state.

[9]For self expandable stents, the foreshortening is defined in a different way as these types of stents are not loaded externally to obtain their target diameter.

[10]Consequently, the proposed methodology is also applicable to study stents with different lengths.

high curvature values corresponds with a more flexible structure. Furthermore, self-contact of single connecting links takes place in both the reference *Cypher* stent and the CoCr design at a curvature of about 0.14 rad/mm, characterized by a discontinuity in the 'Curvature'/'Moment' curve and an increment in the slopes (see Figure 3.18).
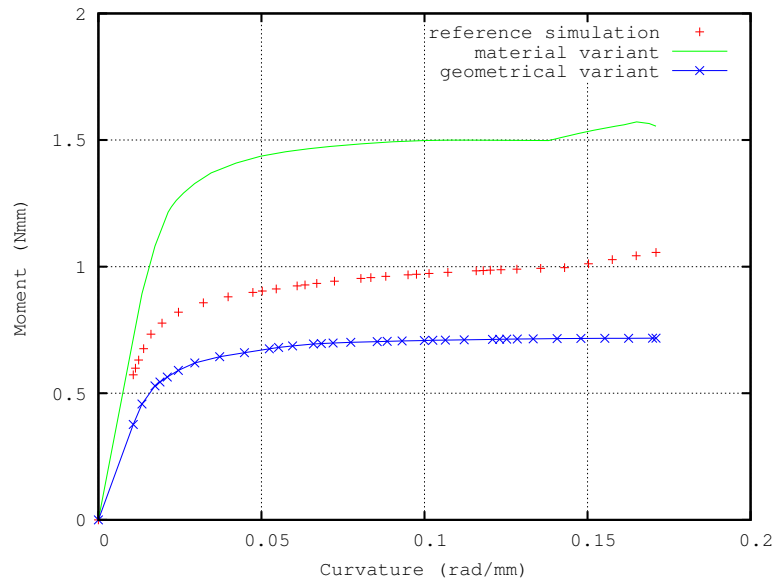
Figure 3.18: Fabricating the reference *Cypher* stent geometry from cobalt-chromium decreases the flexibility (material variant), whereas the flexibility is increased by reducing the number of bends from six to five (geometrical variant).

In order to understand these observations, one needs to be aware of the different parameters influencing stent flexibility: (1) material properties, (2) contact between different stent parts reducing the stent bending capacities [83], (3) the number of connections between two adjacent ring elements: more connections lead to a stiffer geometry, (4) the shape of the connectors [84] allowing compression and extension or not (see Figure 3.19) and (5) the cross-sectional area of the connectors. Keeping the previous considerations in mind, the differences in flexibility can easily be explained (as summarized in Table 3.4). The stiffer behavior of the CoCr design is obviously a consequence of the stiffer material. In contrast to the reference *Cypher* stent and the material variant, the geometrical variant (characterized by five bends and no early contact during bending) performs well on most of the previously described flexibility criteria.

When comparing the obtained flexibility curve for the reference model with the results of Petrini et al. [83], who numerically investigated the flexibil-

Table 3.4: Flexibility parameters.

	Cypher (reference)	Δmaterial	Δgeometry
material	SS316L	L605 CoCr	SS316L
contact during bending	yes	yes	no
number of bends	6	6	5
resulting flexibility	medium	low	high
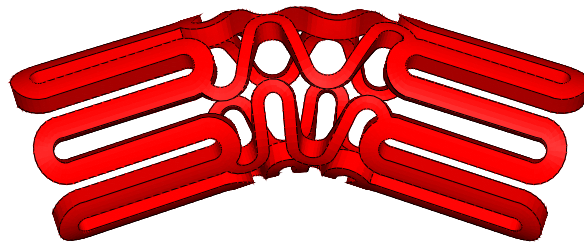
Figure 3.19: View of the reference *Cypher* stent at the end of the loading step indicating clearly the extension and compression of the linking members.

ity of the *BX Velocity* stent (i.e. bare-metal version of the *Cypher* stent), a rather large difference can be noticed (Petrini found a quasi horizontal plateau in the 'Curvature'/'Moment' curve at approximatly 0.25 Nmm). Firstly, these differing results are caused by the stent geometry that is not exactly the same in both numerical tests. The geometry used by Petrini et al. has connection elements with a smaller cross-sectional area, resulting in a lower stiffness of the structure. Secondly, the constitutive properties for SS316L applied by Petrini et al. are characterized by a yield stress of $205\,\mathrm{N/mm^2}$, which is significantly lower than the yield stress value of $375\,\mathrm{N/mm^2}$ used in this study. In order to verify these statements, a simulation was carried out in which the constitutive law used by Petrini et al. was applied. In addition, the geometrical properties of the stent were slightly modified and a simulation incorporating these alterations resulted in a flexibility curve, nearly identical to the one obtained by Petrini et al.

Foreshortening and recoil

The foreshortening of the three stent units can be determined by measuring the initial and the final stent length and for the original *Cypher* stent, the material and geometrical variant, the foreshortening is respectively 12.6 %, 13.3 % and 17.9 %. The increased foreshortening value of the geometrical

variant can be explained by the fact that the reduced number of bends have to flex more to reach the nominal diameter of 3 mm as compared to the reference model. This phenomenon is visualized in Figure 3.20.
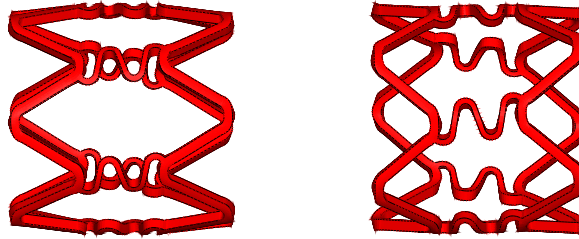
Figure 3.20: Expanded reference (left) and altered geometry (right), showing the higher flexion of the bends in the reduced bend geometry to reach the same nominal stent diameter.

Following to the expansion, the diameter of the inner cylinder is decreased in order to determine the elastic recoil of each stent design, leading to an elastic radial recoil of 3.7 % for the CoCr design, 2.5 % for the geometrical variant and 2.7 % for the *Cypher* stent. The obtained recoil value for the *Cypher* stent is in accordance with the value reported by Colombo et al. [114] (i.e. 2.5 %).

Radial strength

The radial strength for the three stents in terms of force per unit of length (as explained above) is depicted in Figure 3.21 and visualized in Figure 3.22. All three designs show a similar behavior when subjected to an externally applied pressure. The stents suddenly collapse (i.e. a rapid decrease of the stent radii) at an external force of approximately 1.7 N/mm for the reference geometry, 2.3 N/mm for the CoCr design and 2 N/mm for the five bend design.

Basically, the radial strength of a stent is related to four parameters: (1) the material properties, (2) the strut section (i.e. strut thickness and strut width), (3) the number of load bearing elements in the stent geometry (i.e. ring-elements) per unit length and (4) the orientation of the stent struts. Consequently, the higher radial strength of the altered designs as compared to the reference *Cypher* stent is obviously related to the stronger material properties of CoCr for the material variant and the orientation of the stent struts (of the bends) for the geometrically altered design. Figure 3.20 clearly illustrates that the stent struts of the geometrically modified design are oriented much more vertically as compared to the reference model, creating a higher resistance to the applied radial load.
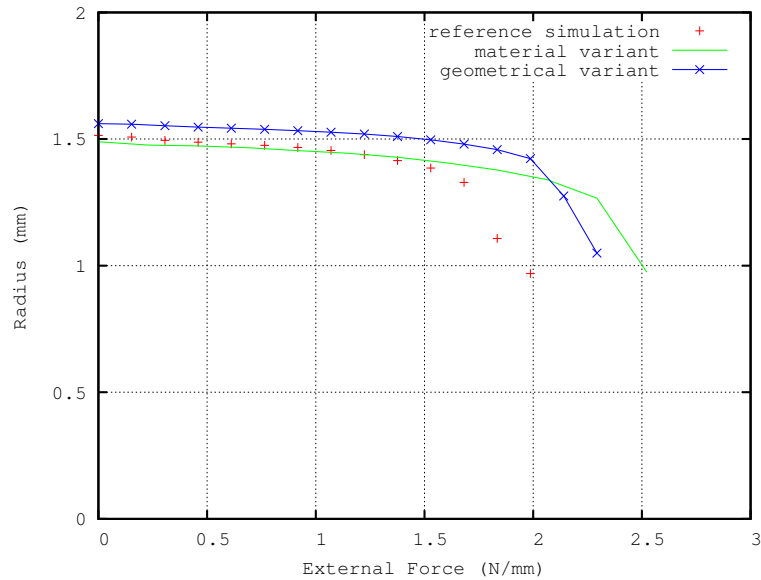
Figure 3.21: Fabricating the reference *Cypher* stent geometry from cobalt-chromium and modifying the geometry from six to five bends increases the radial strength.
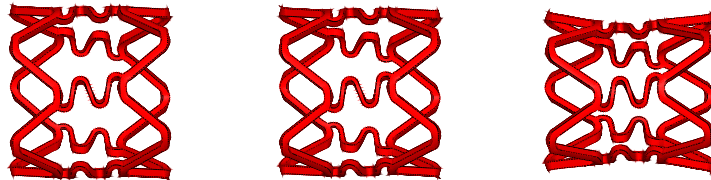
Figure 3.22: Radial compression analysis: expansion to nominal diameter (left), diameter reduction due to elastic radial recoil (center) and due to external compression (right).

The most important mechanical characteristics of the investigated stents are summarized in Table 3.5.

3.3.3 Limitations

The flexibility test, proposed by Petrini [83], is mainly limited by the absence of the delivery system (guidewire, catheter and balloon). Therefore, an interesting extension of the proposed methodology, beyond the scope of

Table 3.5: An overview of the mechanical properties obtained by virtual stent test procedures.

	Cypher (reference)	Δmaterial	Δgeometry
flexibility	medium	low	high
foreshortening (%)	12.6	13.3	17.9
recoil (%)	2.7	3.7	2.5
radial strength (N/mm)	1.7	2.3	2

this study, would take into account the contact between the guidewire, the catheter, the (folded) balloon and the stent. Such a study seems feasible with ABAQUS/Explicit, though requires accurate material and geometrical information of all components. Furthermore, the proposed radial strength test, although very useful for virtual comparison of different stent designs and materials, seems rather difficult to validate experimentally. In an experiment, the outer surface of the stent is subjected to the increasing radial pressure through a flexible membrane. Therefore, when material and geometrical data are available of such a membrane, it would be very interesting to implement them in the virtual bench-mark test (e.g. using the contact modalities of ABAQUS/Explicit). Alternatively, the experimentally validated crush test, compressing the stent between two parallel flat plates as proposed by Petrini et al. [88], is an interesting test to quantify the crush resistance. However, although similar, crush resistance with a radial applied load and using parallel plates measure different attributes of the stent.

3.3.4   Conclusions

A multitude of prerequisites are present in the quest for the 'ideal' stent, such as the stent flexibility, foreshortening, recoil and radial strength[11]. Therefore, a virtual stent design platform is developed which combines parametric stent design with dedicated virtual bench-mark tests. This powerful combination of virtual variation in stent geometry and material shortens the design process significantly and allows easy evaluation of the original design and its variations. The proposed virtual design tool is applied to the *Cypher* stent and reveals that both the flexibility and the radial strength can be increased by reducing the number of bends from six to five. However, this geometrical change increases the stent foreshortening and probably limits the use of the same stent geometry with larger balloon diameters.

---

[11]Of course, other stent characteristics are also of importance (e.g. critical stresses and strains, fatigue, uniformity of expansion, stent-vessel interaction).

3.4 Conclusion

A virtual design space is developed to investigate the mechanics of balloon expandable stents. The proposed validated bench-mark tests allow to study some of the most important stent design prerequisites (e.g. expansion, flexibility, radial strength, etc.) for a huge variety of (parametrically adaptable) stent designs and materials. Consequently, the proposed numerical framework has the potential to significantly speed-up the design phase and to provide physicians with additional information to compare different designs (from different manufacturers) in an objective manner. It can be concluded that:

- The proposed methodology to simulate the free expansion of folded angioplasty balloons allows to determine approximate balloon material properties and appropriate boundary conditions (which mimic the balloon tapering) based solely on the manufacturer's compliance chart. The numerical results in terms of pressure and diameter show very good agreement with data provided by the manufacturer and consequently the proposed balloon model seems a valuable tool to study realistic balloon/stent interactions.

- In the early stent-design phase, the radial displacement driven cylindrical balloon expansion method can provide useful and (relatively) accurate information regarding the stent shape when reaching its nominal diameter. However, to further optimize the stent design and its expansion, using the proposed trifolded balloon methodology seems to great advantage, since the free expansion of a stent is governed by the unfolding and expanding of the balloon. Moreover, the trifolded balloon expansion methodology shows very good quantitative and qualitative agreement with both manufacturer data and in-house experiments.

- Changing the balloon length and folding pattern can have an enormous influence on the transient stent expansion behavior. Therefore, the proposed methodology can be used to select the most appropriate balloon length and folding pattern for a particular stent design. Furthermore, small positioning inaccuracies of the stent with respect to the balloon catheter (e.g. during the crimping process) can considerably modify the stent deployment. Consequently, the positioning of the stent on the balloon catheter should be done with the greatest care and accuracy.

- The developed virtual stent design platform, combining parametric stent design with dedicated computational bench-mark tests can significantly shorten the design process and allows easy evaluation of the original design and its variations. Applying the proposed virtual

design tool to the *Cypher* stent reveals that both the flexibility and the radial strength can be increased by reducing the number of bends from six to five. However, this geometrical change increases the stent foreshortening and probably limits the use of the same stent geometry with larger balloon diameters.

Chapter 4

Self expandable wire stent design

Anything goes.
—M. Python

WIRE stents are a class of self-expandable stents braided from a set of fine wires and currently manufactured in a wide range of braiding patterns (single or multilayer) and materials (e.g. phynox, nitinol, (biodegradable) polymers). Braided stents tend to be very flexible, having the ability to be placed in tortuous anatomy while maintaining patency. Despite the promising clinical outcome of minimally invasive interventions with these braided wire stents [91, 46, 47, 49, 92], some drawbacks of this procedure still need further attention (e.g. restenosis, stent migration, artery straightening, side branch covering, etc.) [49, 50] and require additional investigation. As stated in the introduction, literature dedicated to the simulation of the mechanical behavior of braided wire stents is very scarce and often the stent(graft)s are simplified as virtual single sheets neglecting the actual wire stent composition. This lack of scientific efforts may partially be justified by considering the complexity of building the geometrical model of such a wire stent using classical CAD methodologies and subsequent (numerical) analysis of this family of stents.

Furthermore, the number of studies, in engineering literature, related to (the mechanical behavior of) wire stents is also very limited. Jedwab et al. [93] developed a mathematical model of a self-expanding metallic wire stent, based on the springs theory given by Wahl [115], with the aim of predicting various mechanical properties of the stent, and validated the analytical model with experimental data. Wang et al. [94, 45] developed a mathematically rigorous model, based on the theory of slender rods, that describes the

Wallstent (Boston Scientific Corporation, Massachusetts, USA) response to internal and external loading conditions and validated the obtained results with experimental data. In addition Canic et al. [95] performed an analytical study in order to analyze the mechanical properties of bare-metal *Wallstent* endoprostheses and *AneuRx* (Medtronic, Minneapolis, USA) stent grafts and to compare their response to hemodynamic forces. All these studies show excellent results, but at the same time they demonstrate the necessity to build complex analytical models to examine the mechanical behavior of wire stents. Furthermore, the proposed analytical models seem (unfortunately) not consistent, challenging to analyze the expansion of wire stents in patient-specific anatomical geometries and unable to capture the mechanical behavior of innovative bioabsorbable braided stents [97]. In fact, because of the larger fiber diameter of the bioabsorbable stents, the fibers can not freely deform when the stent diameter changes.

In this chapter a theoretical and numerical framework is described to study the mechanical behavior of braided wire stents under complex (though realistic) loading conditions. First, the fundamental concepts regarding the mechanics of wire stents are enlightened and a dedicated analytical model to describe their mechanical response is proposed, based on the theory of mechanical springs by Wahl [115] as suggested by Jedwab et al. [93]. Subsequently, an innovative pyFormex script-based approach for geometrical and finite element (parametric) modeling of wire stents is enlarged upon. This approach allows to study braided stents with arbitrary geometry, arbitrary material under complex loading conditions. In addition, the mechanical behavior of the *Urolume (Wall)stent* is studied in the developed framework, serving as a reference bench-mark, followed by analyzing geometrical variants. Next, the interaction of the wire stent with its constraining catheter is examined virtually and subsequently an optimization procedure is developed in the quest for a less shortening stent. Finally, the virtual design tool is applied to study the mechanical behavior of a promising new generation multilayer *3D structure stent* by reverse engineering.

4.1   Analytical modeling of wire stents

A braided wire stent does not require a balloon and expands by a spring mechanism triggered when the device is released from a constraining delivery catheter as depicted in Figure 4.1. The stent consists of a number of interwoven helical wires that impose a (chronic) outward radial force on the surrounding tissue. Therefore, the diameter of the stent in its unloaded state (optimally) should exceed the target lumen diameter. Consequently, the final diameter of the stent-vessel system is the result of the (elastic) equilibrium between the vessel's resistance and the stent's radial

strength. Logically, quantifying (analytically and/or numerically) the mechanical properties of such braided wire stents offers interesting insights to both stent designers and users (e.g. medical doctors). Furthermore, a correct analytical model is an excellent bench-mark for the validation of numerical results; particularly when experimental data are not available.
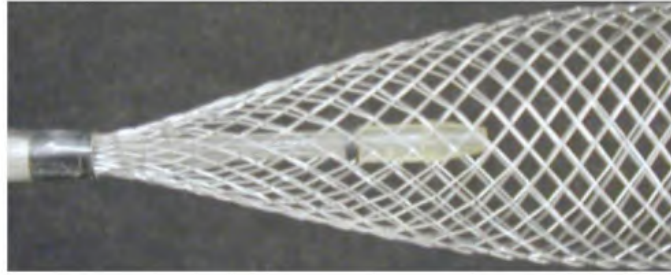
Figure 4.1: Shape of a wire stent exiting the catheter [45].

Following the methodology proposed by Jedwab [93], a mathematical model of a self-expanding metallic *Urolume Wallstent* is developed with the goal of computing several geometrical and mechanical braided stent properties. The theoretical model is based on four assumptions:

1. the stent is a combination of a number of open-coiled helical springs undergoing large deformations;

2. the extremities of the stent are not free to rotate about the axis of the spring(s) due to the friction between the stent wires in the crossing points;

3. the springs experience only elastic deformation;

4. the springs have a large ratio of stent diameter to wire diameter or D/d[1].

The previous assumptions are necessary to derive the model based on the spring theory given by Wahl [115]. In general, only five parameters are necessary to describe a braided stent geometry: the stent (external) diameter $D_{(e)}$ and length L, the wire diameter d, the number of wires n and the braiding or pitch angle[2] β. All relevant parameters to describe the stent

---

[1]Stresses and deformations due to direct shear may be neglected for high values of the spring index (i.e. $D/d > 10$) [116].

[2]The pitch angle β is defined as the angle between the tangent to a helical wire and a normal cross-section of the stent as depicted in Figure 4.2. In literature, the pitch angle is sometimes defined as the axially directed angle between two crossing wires.

geometrical and mechanical properties are summarized in Table 4.1 and a complete derivation of all formulas presented in this section is summarized in Appendix A.

Table 4.1: Geometrical and mechanical properties of a braided wire stent.

(D_0) D	(mm)	(initial) average stent diameter
(D_{e0}) D_e	(mm)	(initial) external stent diameter
(R_0) R	(mm)	(initial) average stent radius
d	(mm)	wire diameter
n	(-)	total number of wires
(β_0) β	(-)	(initial) pitch angle
(L_0) L	(mm)	(initial) stent length
c	(-)	number of coils
δ	(mm)	axial stent elongation
F	(N)	axial stent force
F'	(N)	axial wire force
M_0'	(Nmm)	end wire moment
p_{outer}	(N/mm^2)	outer radial pressure
K_L	(N/mm)	longitudinal stiffness
K_p	(N/mm^3)	radial stiffness

4.1.1   Axial elongation

When subjecting the stent to an axial force F, the stent undergoes a change in pitch angle so that the new pitch angle and stent average diameter are β and D, respectively. As a result, the stent has undergone an axial elongation δ and attains a new length L as depicted in Figure 4.2.

Based on Wahl's theory of springs with ends fixed against rotation, it may be shown that the load F acting on the stent is given by:

$$F = 2n \left[\frac{GI_p}{K_3} \left(\frac{2\sin\beta}{K_3} - K_1 \right) - \frac{EI\tan\beta}{K_3} \left(\frac{2\cos\beta}{K_3} - K_2 \right) \right] \qquad (4.1)$$

where K_1, K_2, K_3, I and I_p are constants given by:

$$K_1 = \frac{\sin 2\beta_0}{D_0} \qquad K_2 = \frac{2\cos^2\beta_0}{D_0} \qquad K_3 = \frac{D_0}{\cos\beta_0} \qquad (4.2a)$$
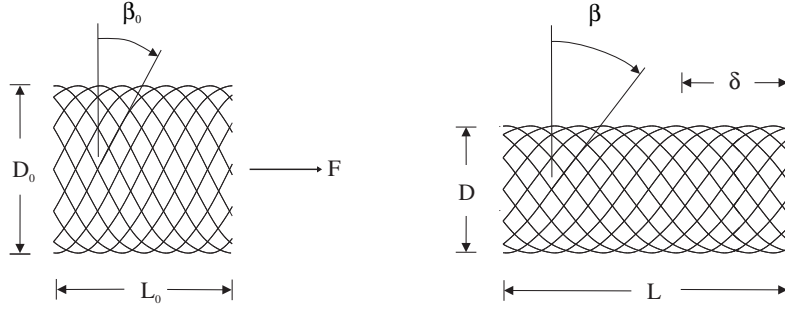
Figure 4.2: Increase of stent length L with increasing axial force F.

$$I = \frac{\pi\,d^4}{64} \qquad\qquad I_p = \frac{\pi\,d^4}{32} \qquad\qquad (4.2b)$$

I and I_p are the moment of inertia and polar moment of inertia of the wire, respectively, E is Young's modulus of elasticity, and G is the shear modulus.

The new stent length L can be written as an explicit function of the current pitch angle β:

$$L = L_0 + \frac{\pi c D_0}{\cos\beta_0}\left(\sin\beta - \sin\beta_0\right) \qquad\qquad (4.3)$$

and consequently the relation between the stent length L and the axial force F can be examined.

Furthermore, the longitudinal stiffness K_L is defined by:

$$K_L = \frac{\partial F}{\partial L} = \frac{2n}{K_3 \pi\,c\,\cos\beta}\left[\frac{GI_p}{K_3}\left(\frac{2\cos\beta}{K_3}\right) - \frac{EI}{K_3}\left(\frac{2\cos\beta}{K_3} - \frac{K_2}{\cos^2\beta}\right)\right] \quad (4.4)$$

In order to assess the validity of the model, Jedwab [93] compared the theoretical calculations with experimental data. The experimental and theoretical results for longitudinal load as a function of stent length are presented in Figure 4.3 and the geometrical and mechanical properties of the considered stent design are summarized in Table 4.2.
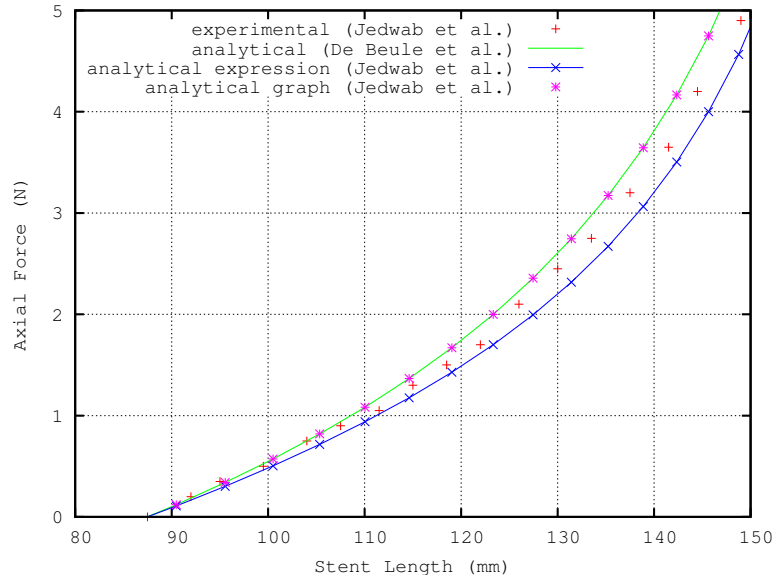
Figure 4.3: Increase of stent length L with increasing axial force F.

Table 4.2: Geometrical and mechanical parameters of the investigated *Urolume Wallstent.*

D_0	$16.71\,\text{mm}$
D_{e0}	$17.15\,\text{mm}$
d	$0.22\,\text{mm}$
n	24
β_0	$30.85\,°$
L_0	$87.5\,\text{mm}$
E	$206000\,\text{N/mm}^2$
G	$81500\,\text{N/mm}^2$

There is a close agreement between theory and experiment and all curves presented in Figure 4.3 show a monotonic increase of load F with stent length L. Consequently, the longitudinal stiffness of the stent K_L, defined as the slope at every point of the curve, also increases monotonically with the stent length. The slight difference between experiment and theory might be explained by a combination of experimental error and the effect of the (necessary) theoretical assumptions.

The discrepancy between the theoretical curves of Jedwab and De Beule can be explained by the difference in the proposed analytical expression for

the axial force F:

$$F_{\text{Jedwab}} = 2\,n\left[\frac{GI_p\,\cos\beta}{K_3}\left(\frac{2\,\sin\beta}{K_3}-K_1\right)-\frac{EI\,\tan\beta}{K_3}\left(\frac{2\,\cos\beta}{K_3}-K_2\right)\right] \quad (4.5)$$

Because of the extra $\cos\beta$ term in the numerator of the Jedwab expression for the axial force $F_{(\text{Jedwab})}$, a lower force is required to attain a certain stent length. As a consequence, the experimental length - load curve is underestimated by Jedwab's theoretical approximation. This is however inconsistent with graphical representation of the proposed analytical expression in Jedwab [93], where the experimental curve is overestimated and the theoretical curve corresponds with the author's analytical approximation in Figure 4.3. Moreover, the expression for the axial force F, derived by the author, is consistent with a similar expression - based on the same theory of elasticity - proposed by Wang et al. [94] to study the mechanical response of a stent subjected to internal or external pressure. Presumably, an erratum in Jedwab [93] is the cause of the revealed discrepancy. Unfortunately, this erratum has crept into the work of others (e.g. Nuutinen [97]). Furthermore, the length versus diameter data presented in Figure 4.4 show very good agreement between experiment and theory.
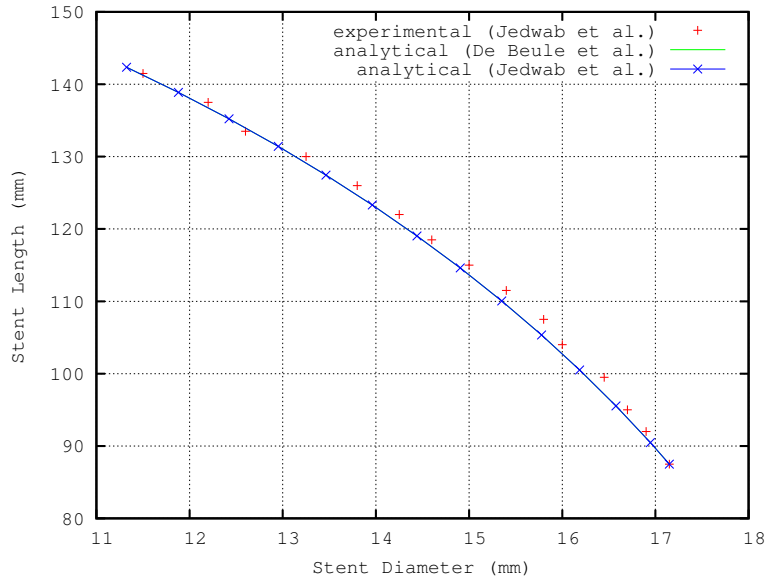
Figure 4.4: Increase of stent length L is accompanied by a corresponding decrease in diameter D. The coinciding analytical curves are a very good approximation of the experimental data.

It is necessary to keep in mind that the force acting on a single wire F' is given by F divided by the number of wires n. Based on Wahl's spring theory, the load F' and the moment M_0' acting on a single stent wire are defined as[3]:

$$F' = \frac{GI_p \cos\beta}{R}\left(\frac{\sin\beta\cos\beta}{R} - \frac{\sin\beta_0\cos\beta_0}{R_0}\right) - \frac{EI\sin\beta}{R}\left(\frac{\cos^2\beta}{R} - \frac{\cos^2\beta_0}{R_0}\right) \tag{4.6}$$

$$M_0' = GI_p\sin\beta\left(\frac{\sin\beta\cos\beta}{R} - \frac{\sin\beta_0\cos\beta_0}{R_0}\right) + EI\cos\beta\left(\frac{\cos^2\beta}{R} - \frac{\cos^2\beta_0}{R_0}\right) \tag{4.7}$$

Considering that the axial force F' and moment M_0' act simultaneously, the bending moment m_b and the twisting moment m_t acting on an elementary spring segment of length dS are:

$$m_b = M_0'\cos\beta - F'r\sin\beta = F_1' = EI\left(\frac{\cos^2\beta}{r} - \frac{\cos^2\beta_0}{r_0}\right) \tag{4.8}$$

$$m_t = M_0'\sin\beta + F'r\cos\beta = F_2' = GI_p\left(\frac{\sin\beta\cos\beta}{r} - \frac{\sin\beta_0\cos\beta_0}{r_0}\right) \tag{4.9}$$

Consequently, the maximum shear τ and bending stress σ [115] can be defined as:

$$\tau = \frac{16m_t}{\pi d^3} \tag{4.10}$$

$$\sigma = \frac{32m_b}{\pi d^3} \tag{4.11}$$

Combining these shear and bending stress components according to the von Mises yield criterion, the equivalent stress σ_e is given by:

$$\sigma_e = \sqrt{\sigma^2 + 3\tau^2} \tag{4.12}$$

---

[3]The complete derivation of the expressions for F' and M_0' is given in Appendix A.

4.1.2 Radial compression

Subjecting the virtual outer surface of the stent to a radial pressure p_{outer}, the stent undergoes also a change in pitch angle so that the new pitch angle and stent average diameter are β and D, respectively. As a result, the stent has undergone a similar axial elongation δ as in the axial load case and attains a new length L as depicted in the right panel of Figure 4.2. Based on the theory of virtual work, Jedwab et al. [93] show that the pressure p_{outer} acting on the stent is given by:

$$p_{outer} = -\frac{2\,F\,c}{D\,L\,\tan\beta} \tag{4.13}$$

The radial pressure exerted on the stent as a function of the stent diameter is presented in Figure 4.5. The experimental results are overestimated by those of the theoretical curve and the rather significant difference is thought to be principally due to the experimental set-up (friction, operator variability and mechanical properties) [93] without excluding possible errors induced by the theoretical model approximations.
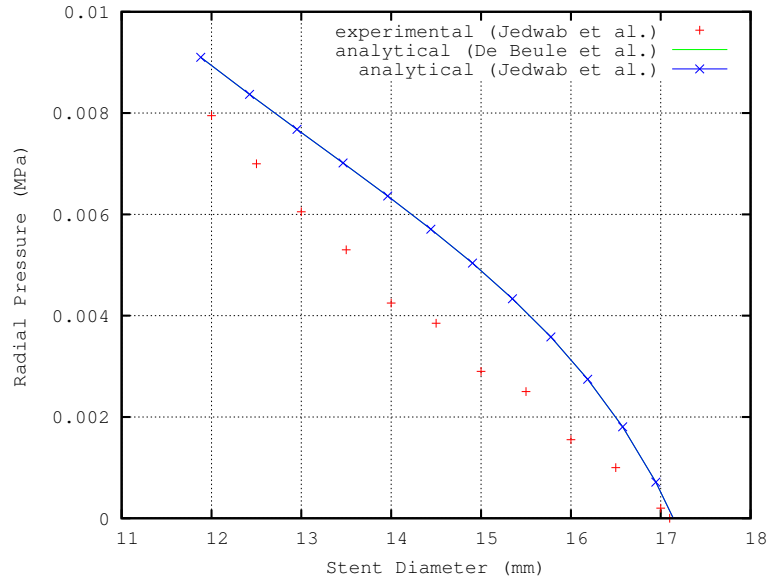
Figure 4.5: Decrease of stent diameter D with increasing radial pressure p. The coinciding analytical curves overestimate the experimental data.

The radial (pressure) stiffness K_p is defined by:

$$K_p = \frac{\partial p_{outer}}{\partial D} = \frac{2c}{K_3 \sin\beta \, (D\,L\,\tan\beta)^2} \left[2DLn\,\tan\beta \left(\frac{GI_p}{K_3} \left(\frac{2\cos\beta}{K_3} \right) - \right.\right.$$

$$\left.\frac{EI}{K_3} \left(\frac{2\cos\beta}{K_3} - K_2 \sec^2\beta \right) \right) - F \left(\frac{DL}{\cos^2\beta} + \right.$$

$$\left.\left. K_3 \sin\beta \, (\pi\,c\,D - L\,\tan\beta) \right) \right] \quad (4.14)$$

4.2 Geometrical modeling of wire stents with pyFormex

A condensed script (*WireStent.py*) was developed in pyFormex to build the geometrical model of a braided wire stent. pyFormex was (originally) intended by Verhegghe at Ghent University for the automated design of spatial structures and the generation of complex three-dimensional geometries by means of sequences of mathematical transformations [56]. Furthermore, pyFormex can be useful for (structural) analysis purposes, for operations on surface models or simply for generating illustrations. The development of pyFormex is an ongoing process, presented as an open source project: the program can be used, studied, modified and distributed under the conditions of the GNU General Public License (GPL) [117]. Currently, the program is already in use in both research and educational context. Future developments of this tool include interactive tools, surface and volume meshing, post-processing, distribution and installation. Originally developed in a Linux environment, pyFormex can be used, however, in a Windows environment as well. Being an implementation of Formex algebra in the programming language Python, the software is based on a script, from which a whole structure can be generated using only a limited number of command lines. Typical Formex operations used in the scripts are related to copying, translating, rotating, scaling, etcetera. The major advantage of this modus operandi is that parameters (e.g. dimensions, material properties, ...) can easily be changed and consequently a multitude of different configurations of the same geometry can be generated in a limited period of time. Also because of the scripting, there is virtually no limitation to the geometries that pyFormex can generate other than one's own imagination.

To explain the modus operandi of pyFormex, the *WireStent.py* script is parsed step by step. The full Demo version of the complete *WireStent.py* script can be found in Appendix B. To start, all required modules to run the *WireStent.py* script are imported (e.g. the math module to use the

mathematical constant π), as illustrated in script 4.1. Subsequently, the class DoubleHelixStent is defined which allows the simple use of the geometrical model in other scripts for e.g. parametric, optimization and finite element analyses of braided wire stents. Consequently, the latter scripts do not have to contain the wire stent geometry building and can be condensed and conveniently arranged. The definition of the class starts with a """documentation string""", explaining its aim and functioning.

Script 4.1: WireStent.py: **class DoubleHelixStent**

```
1   from formex import *
2
3   class DoubleHelixStent:
4       """Constructs a double helix wire stent.
5
6       A stent is a tubular shape such as used for opening
               obstructed
7       blood vessels. This stent is made from sets of wires
               spiraling
8       in two directions.
9       The geometry is defined by the following parameters:
10         L  : length of the stent
11         De : external diameter of the stent
12         D  : average stent diameter
13         d  : wire diameter
14         be : pitch angle (degrees)
15         p  : pitch
16        nx : number of wires in one spiral set
17        ny : number of modules in axial direction
18        ds : extra distance between the wires (default is 0.0
             for
19             touching wires)
20        dz : maximal distance of wire center to average
             cylinder
21        nb : number of elements in a strut (a part of a wire
             between two
22             crossings), default 4
23       The stent is created around the z-axis.
24       By default, there will be connectors between the wires
             at each
25       crossing. They can be switched off in the constructor.
26       The returned formex has one set of wires with property
             1, the
27       other with property 3. The connectors have property 2.
             The wire
28       set with property 1 is winding positively around the z-
             axis.
29       """
```

The constructor __init__ of the DoubleHelixStent class, defined in script 4.2, requires eigth arguments:

- stent external diameter D_e (mm).

- stent length L (mm).

- wire diameter d (mm).

- number of wires in one spiral set, i.e. wires with the same orientation, nx (-).

- pitch angle β (˚).

- extra radial distance between the crossing wires ds (mm). By default, ds is 0.0 mm for crossing wires, corresponding with a center line distance between two crossing wires of exactly d.

- number of elements in a strut, i.e. part of a wire between two crossings, nb (-). As every base element is a straight line, multiple elements are required to approximate the curvature of the stent wires. The default value of four elements in a strut has proven to be a good assumption.

- If connectors=True, extra elements are created at the positions where there is physical contact between the crossing wires. These elements are required to enable contact between these wires in finite element analyses.

The virtual construction of the wire stent structure is defined by the following sequence of four operations: (i) creation of a nearly planar base module of two crossing wires; (ii) extending the base module with a mirrored and translated copy; (iii) replicating the extended base module in both directions of the base plane and (iv) rolling the nearly planar grid into the cylindrical stent structure, which is easily parametric adaptable.

4.2.1 Creating the base module

Depending on the specified arguments in the constructor, the mean stent diameter D, the average stent radius r, the bump or curvature of the wires dz, the pitch p and the number of base modules in the axial direction ny are calculated in script 4.2. As the wire stent structure is obtained by braiding, the wires have an undulating course and the bump dz corresponds to the amplitude of the wave. If no extra distance ds is specified, there will be exactly one wire diameter between the centerlines of the crossing wires. The number of modules in the axial direction ny is an integer, therefore, the actual length of the stent model might differ slightly from the specified, desired length L[4]. However, this difference has a negligible impact on the numerical results.

Script 4.2: WireStent.py: stent geometrical properties

```
1       def __init__(self,De,L,d,nx,be,ds=0.0,nb=4,connectors=
            True):
2           """Create the Wire Stent."""
3           D = De − 2*d − ds
4           r = 0.5*D
5           dz = 0.5*(ds+d)
6           p = math.pi*D*tand(be)
```

---

[4]The actual (initial) stent length is underestimated by 1.5 % for the investigated *Urolume (Wall)stent*.

```
7              nx = int(nx)
8              ny = int(round(nx*L/p))   # The actual length may
                   differ a bit from L
```

All parameters to describe the stent geometry are specified and available to start the construction of the wire stent. Initially a simple Formex is created using the pattern()-function: a straight line segment of length 1 oriented along the X-axis. The replic ()-functionality replicates this line segment nb times with step 1 in the X-direction (0-direction). Subsequently, these nb line segments form a new Formex which is given a one-dimensional bump with the bump1()-function. The Formex undergoes a deformation in the Z-direction (2-direction), forced to the point [0,0, dz]. The bump intensity is specified by the quadratic bump_z function and varies along the X-axis (0-axis). The creation of this single bumped strut, oriented along the X-axis is summarized in script 4.3 and depicted in Figure 4.6.

Script 4.3: WireStent.py: Single bumped strut

```
1              # a single bumped strut, oriented along the x-axis
2              bump_z=lambda x: 1.-(x/nb)**2
3              base = Formex(pattern('1')).replic(nb,1.0).bump1
                   (2,[0.,0.,dz],bump_z,0)
```


(a)   (b)

Figure 4.6: Creation of single bumped strut (b) from a straight and replicated (a) line segment.

Script 4.4 rescales the single bumped strut (base) homothetically in the XY-plane to size one with the scale ()-function. Subsequently, the shear ()-functionality generates a new North East NE Formex by skewing the base Formex in the Y-direction (1-direction) with a skew factor of 1 in the XY-plane. As a result, the Y-coordinates of the base Formex are altered. Similarly a South East SE Formex is generated by a shear() operation on a mirrored copy of the base Formex. The base copy, mirrored in the direction of the XY-plane (perpendicular to the 2-axis), is obtained by the reflect () command. Both Formices are given a different property number by the setProp()-function, visualised by the different color codes in Figure 4.7. This number can be used as an entry in a database, which holds some sort of

property. The Formex and the database are two separate entities, only linked by the property numbers. The rosette ()-function creates a unit cell of crossing struts by two rotational replications with an angular step of 180° around the Z-axis (the original Formex is the first of the 2 replicas). If specified in the constructor, an additional Formex with property 2 connects the first points of the NE and SE Formices.

Script 4.4: WireStent.py: Nearly planar base module

```
1       # scale back to size 1.
2       base = base.scale([1./nb,1./nb,1.])
3       # NE and SE directed struts
4       NE = base.shear(1,0,1.)
5       SE = base.reflect(2).shear(1,0,-1.)
6       NE.setProp(1)
7       SE.setProp(3)
8       # a unit cell of crossing struts
9       cell1 = (NE+SE).rosette(2,180)
10      # add a connector between first points of NE and SE
11      if connectors:
12          cell1 += Formex([[NE[0][0],SE[0][0]]],2)
```


(a)   (b)

Figure 4.7: Creation of unit cell of crossing and connected struts (b) from a rescaled and mirrored, skewed (a) bumped strut.

4.2.2   Extending the base module

Subsequently, a mirrored copy of the base cell is generated in script 4.5. Both Formices are translated to their appropriate side by side position with the translate ()-option and form the complete extended base module with size 4 by 4 as depicted in Figure 4.8. Furthermore, both Formices are defined as an attribute of the DoubleHelixStent class by the self -statement, allowing their use after every DoubleHelixStent initialization. Such further use is impossible with local variables, such as for example the NE and SE Formices.

Script 4.5: WireStent.py: Extended base module

```
1       # and create its mirror
2       cell2 = cell1.reflect(2)
```

```
3        # and move both to appropriate place
4        self.cell1 = cell1.translate([1.,1.,0.])
5        self.cell2 = cell2.translate([−1.,−1.,0.])
6        # the base pattern cell1+cell2 now has size
                  [−2,−2]..[2,2]
```


(a)   (b)

Figure 4.8: Creation of the complete extended base module (b) from the original and mirrored (a) unit cell.

4.2.3 Full nearly planar pattern

The full nearly planar pattern is obtained by copying the base module in two directions and shown in Figure 4.9. replic2 () in script 4.5 generates this pattern with nx and ny replications with steps dx and dy in respectively, the default X- and Y-direction.

Script 4.6: WireStent.py: Full pattern by replication

```
1        # Create the full pattern by replication
2        dx = 4.
3        dy = 4.
4        F = (self.cell1+self.cell2).replic2(nx,ny,dx,dy)
```
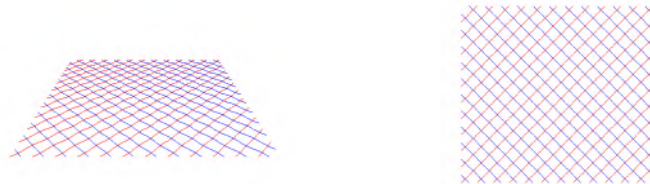

Figure 4.9: Creation of the full nearly planar pattern.

4.2.4   Cylindrical stent structure

Finally the full pattern is translated over the stent radius r in Z-direction and transformed to the cylindrical stent structure by a coordinate transformation in script 4.7 with the Z-coordinates as distance r, the X-coordinates as angle θ and the Y-coordinates as height z. The scale ()-operator rescales the stent structure to the correct circumference and length. The resulting stent geometry is depicted in Figure 4.10.

Script 4.7: WireStent.py: Rolling the nearly planar grid into a cylinder

```
1              # fold it into a cylinder
2              self.F = F.translate([0.,0.,r]).cylindrical(dir
                  =[2,0,1],scale=[1.,360./(nx*dx),p/nx/dy])
3              self.ny = ny
```


| (a)   (b) |

Figure 4.10: Creation of the cylindrical stent structure ((a) iso and (b) right view).

In addition to the stent initialization, the DoubleHelixStent class script contains a function all () representing the complete stent Formex. Consequently, the DoubleHelixStent class has four attributes: the Formices cell1 , cell2 and all ; and the number ny as specified in scripts 4.6, 4.7 and 4.8.

Script 4.8: WireStent.py: Complete Formex

```
1      def all(self):
2          """Return the Formex with all bar elements."""
3          return self.F
```

4.2.5 Parametric stent geometry

DHS (16,40,0.22,6,25)

DHS (16,40,0.22,6,50)

DHS (16,40,0.22,10,25)

DHS (16,40,0.22,10,50)

DHS (32,40,0.22,6,25)

DHS (32,40,0.22,6,50)

DHS (32,40,0.22,10,25)

DHS (32,40,0.22,10,50)
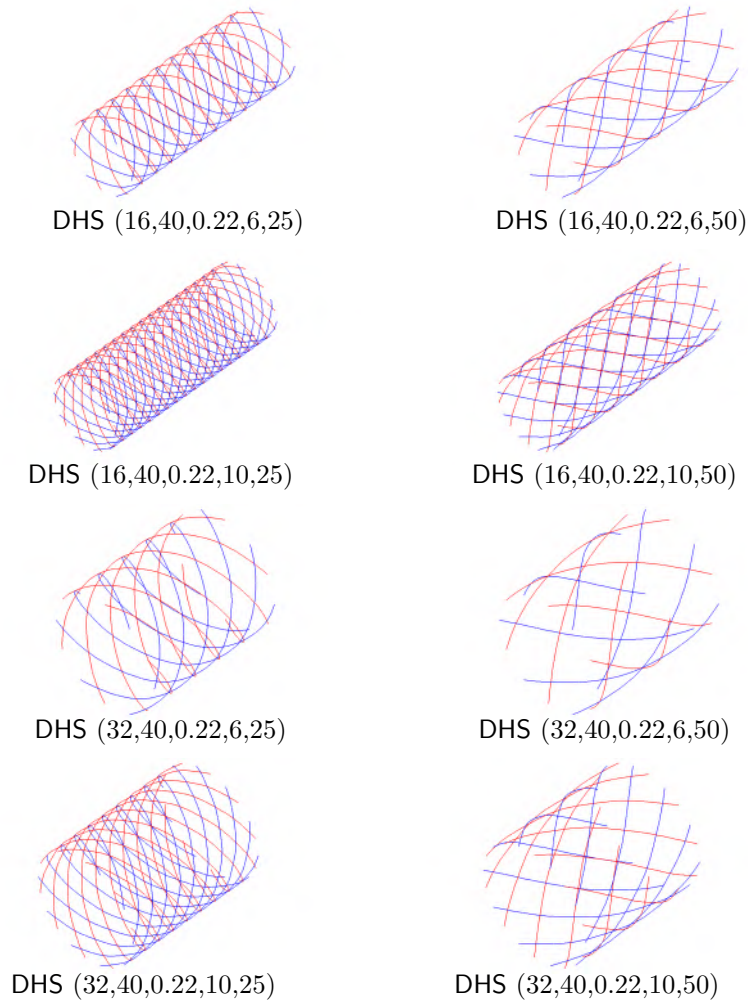
Figure 4.11: Variations on the wire stent geometry using the DoubleHelixStent(D_e, L, d, nx, β) (DHS ()) class.

An inherent feature of script-based modeling is the possibility of easily generating lots of variations on the original geometry. This is a huge advantage for parametric analyses and illustrated in Figure 4.11: these wire stents are all created with the same script 4.9, but with other values of the parameters D_e, nx and β. As the script for building the wire stent geometry is

defined as a DoubleHelixStent class in the *WireStent.py* script, it can easily be imported for e.g. this purpose.

Script 4.9: Example of parametrically generating wire stent geometrical variations

```
1   from examples.WireStent import DoubleHelixStent
2
3   for i in [16.,32]:
4       for j in [6,10]:
5           for k in [25,50]:
6               stent = DoubleHelixStent(i,40.,0.22,j,k).all()
7               draw(stent,view='iso')
8               pause()
9               clear()
```

Obviously, generating such parametric wire stent geometries with classical CAD methodologies is feasible, though probably (very) time consuming. However, as pyFormex provides a multitude of features (such as parametric modeling, finite element pre- and postprocessing, optimization strategies, etcetera) in one single consistent environment, it appears to be a promising way to go when studying the mechanical behavior of braided wire stents.

4.3 Numerical model of the Urolume Wallstent

Section 4.1.1 clearly illustrates the dependency of the mechanical behavior of braided stents on the stent geometry. For example, the axial force F is directly related to the wire diameter d, the number of wires n and the pitch angle β (see equation 4.1). Therefore, studying the influence of these parameters on the mechanical behavior is appropriate from design point of view. For this purpose, the modeling strategy of choice is non-linear finite element analysis, because a validated finite element model offers a solid base to study variations on the original design even in areas (far) beyond the limits of the proposed analytical models (e.g. for bioabsorbable and/or multilayer braided stents). Therefore, complementary to the condensed *WireStent.py* script, several dedicated Python scripts are developed for finite element pre- and postprocessing. The preprocessing scripts transform the geometrical model automatically into a finite element model by defining the material properties, the elements, the boundary conditions and load cases. Consequently, an input file for the commercial finite element solver ABAQUS[5] is generated and the discretized non-linear problem is analysed and solved by ABAQUS. Subsequently, the resulting data obtained from this simulation is automatically (post)processed and the desired graphs[6] are created

---

[5]Of course pyFormex is not limited to ABAQUS and is able to export finite element input files for probably every package available to date.

[6]All graphs in this chapter are automatically generated by such dedicated postprocessing scripts.

with (again) special purpose Python scripts. The flowchart of this virtual modeling strategy is illustrated in Figure 4.12 and applied to study the mechanical behavior of the experimentally and analytically studied *Urolume Wallstent* (see section 4.1). Finally, this validated bench-mark is used to analyze the impact of variation of the wire diameter d, the number of wires n and the pitch angle β on some of the most important design characteristics such as the axial stiffness, the radial stiffness and the foreshortening of braided stents. The stent stiffness (axial and radial) influences the compliance of the target lesion, altering the response to the forces exerted on the vessel (e.g. compression, bending, torsion, extension). The radial stiffness is an important design characteristic as an exceedingly compliant stent is vulnerable for weak anchoring and stent migration [95]. Furthermore, stent foreshortening has been reported as a technical challenge, related to difficulties during placement in clinical practice [118]. In case of a shortening stent, the final stent length is function of the average luminal diameter of the target segment after final stent dilatation. Misjudgment will result in an excessively short stent with an inadequate coverage of the diseased segment [119]. Stent misplacement and migration are both listed as potential adverse effects in the manufacturer's 'Instructions for use' of the *(Urolume) Wallstent.*
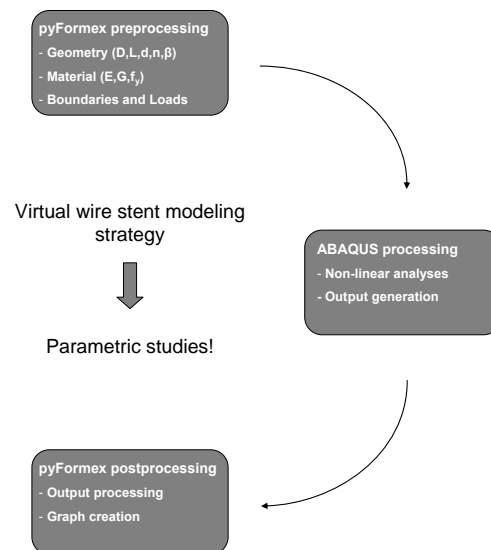
Figure 4.12: Flowchart of virtual wire stent modeling strategy.

4.3.1   Materials and methods

The investigated *Urolume Wallstent* (initial length L 87.5 mm, initial external diameter D_{e0} 17.15 mm) consists of double intertwined sets of 12 helical wires (initial pitch angle β_0 30.85° and wire diameter d 0.22 mm) made from phynox (see Table 4.2). The finite element mesh is created automatically by pyFormex and consists of 12672 Frame3D elements for the stent wires and 792 CONN3D2 (type JOIN) connector elements to model the contact between the crossing wires. The number of finite elements in each strut corresponds exactly to the number of elements that define the strut geometry nb and analogously, the finite element connectors correspond with the connectors defined in script 4.1. The element choice is dictated directly by the physical problem: Frame3D elements are well suited for one-dimensional approximations of three-dimensional continuums when the dimensions of the cross-section are small compared to the typical dimensions along the axis of the beam[7]. These frame elements are 2-node, initially straight, slender beam elements and operate directly in terms of axial force, bending moments, and torque at the element's end nodes. Consequently, when output in terms of stress is required, B31 Timoshenko beam elements are the way to go for wire stent modeling. JOIN connectors fix the (Cartesian) coordinates of both nodes of the crossing wires relatively to each other though rotational degrees of freedom are not constrained. As a result the pitch angle β is allowed to change when loading the stent as shown in Figure 4.2.

Different loading conditions on the stent are implemented in the pyFormex scripts: axial elongation and radial compression. These loads correspond to the physical experiments performed by Jedwab [93] and consequently allow (i) thorough validation of the proposed numerical model and (ii) easy evaluation of the stent stiffness and foreshortening. As already specified in section 2.2 both stent deformation states (stent diameter reduction through axial elongation or radial compression) can be obtained through force or displacement driven analyses. The reduction of the stent diameter is modeled by (i) applying an increasing axial force F' on the distal end of each stent wire (or alternatively impose axial displacements) or (ii) applying an increasing pressure p_{outer} on the virtual outer surface of the stent (or impose radial displacements), while the proximal end of the stent is constrained in both the axial and circumferential direction. These boundary conditions prevent rigid body motion and mimic the actual stent behavior as much as possible. Several sets of (finite element) nodes are automatically generated by pyFormex during the creation of the geometrical model. Three of them

---

[7]For beams made of uniform material, typical dimensions in the cross-section should be less than about 1/15 of typical axial distances for transverse shear flexibility to be negligible (Euler-Bernoulli (slender) beams). Shear flexible beam theory can provide useful results for cross-sectional dimensions up to 1/8 of typical axial distances (Timoshenko beams) [120].

are used for the automated implementation of the above specified loading
and boundary conditions (see Figure 4.13):

- loaded: Set of nodes in the cross-section of the distal end of the stent,
  used to impose the increasing axial force or displacements.

- fixed : The nodes in the cross-section of the proximal stent end to
  apply the constraining boundary conditions.

- outer: The node-set of the virtual outer surface of the stent for per-
  forming radial pressure or displacement driven simulations.
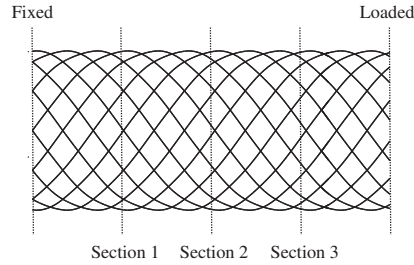
Figure 4.13: Automatically generated node sets of the braided stent model.

In case of displacement driven simulations the axial force and radial pressure
are derived from the reaction forces opposing to the imposed displacements
in the loaded or outer node-sets.

The stent mechanical behavior is characterised in terms of longitudinal or
axial stiffness, radial stiffness and foreshortening. The axial stiffness is de-
fined as the tangent to the 'Stent Length'/'Axial Force' curve (as defined
by equation 4.4. Correspondingly, the slope in the 'Stent Diameter'/'Radial
Pressure' curve defines the radial stiffness (see equation 4.14). The fore-
shortening defines the amount that the stent shortens during release from
the catheter:

$$\text{Foreshortening} = \frac{L_c - L}{L_c} \tag{4.15}$$

where L_c is the length of the stent inside the delivery catheter and L the
length of the stent when released in the target lesion.

Depending on the considered load case and desired output, the 'Stent
Length'/'Axial Force', 'Stent Diameter'/'Radial Pressure', 'Stent Diame-
ter'/'Stent Length' or 'Stent Diameter'/'Foreshortening' plots are automat-

ically generated. The output variables are averaged over multiple cross-sections to minimize the edge effect of the imposed boundary conditions. The stent length L is related to the initial length L_0 and the axial displacement u_3 as follows:

$$L = L_0 + \frac{L_0}{L_1} * (\overline{u}_3(\text{section } 3) - \overline{u}_3(\text{section } 1)) \qquad (4.16)$$

where L_1 is the longitudinal distance between the cross sections of the node-sets section 1 and section 3, located at approximately $25\,\%$ and $75\,\%$ of the stent length L (measured from the fixed set) as depicted in Figure 4.13. The axial displacement u_3 is averaged over all the nodes in the considered cross sections (denoted as $\overline{u}$).

The stent (external) diameter D_e, related to the initial average stent diameter D_0 and the radial displacement u_1, is defined as:

$$D_e = D_0 + 2d + \frac{1}{3}(\overline{u}_1(\text{section } 1) + \overline{u}_1(\text{section } 2) + \overline{u}_1(\text{section } 3) \qquad (4.17)$$

where d is the wire diameter and the node-set section 2 is located at $50\,\%$ of the stent length of the fixed set.

The parametric analysis investigates the impact of variation of the wire diameter d, the number of wires n and the pitch angle β in a realistic (thus manufacturable) design variable space. Consequently the wire diameter d is 0.17, 0.22 or $0.27\,\text{mm}$; the number of wires 24, 36 or 48 and the pitch angle β is 30.85, 35 or $40\,°$. As a result, the original *Urolume Wallstent* (of which the geometry falls into the considered design space: d $0.22\,\text{mm}$, n 24 and β $30.85\,°$) serves as a reference point for this parametric study. The design variable space is summarized in Table 4.3. To investigate the foreshortening of the stent, the catheter inner diameter D_c is $6\,\text{mm}$ as specified in the manufacturer's 'Instructions for use' of the *Urolume endoprosthesis*.

4.3.2   Results and discussion

4.3.2.1   Bench-mark model

Axial elongation

The results of the reference simulation are in close agreement with both the experimental data (provided by Jedwab [93]) and the proposed analytical approximation (see Figure 4.14). Over the whole range of loading, the

Table 4.3: Design variable space of the parametric study. The values for the reference *Urolume Wallstent* are in **bold**.

d (mm)	n	β (°)
0.17	24	30.85
0.22	**24**	**30.85**
0.27	24	30.85
0.22	36	30.85
0.22	48	30.85
0.22	24	35
0.22	24	40

simulation differs less than 3 % from both the analytical and experimental data[8]. Furthermore, the longitudinal stiffness of the stent increases with the stent length which is in line of expectations. As the load increases, the pitch angle increases and consequently, the wire direction corresponds more and more with the axial load orientation.

In the quest for a (probable) explanation for the small discrepancy between models and experiments - besides experimental error - the pitch angle β seems instinctively the predominant factor. Therefore, the original initial pitch angle is rounded off from 30.85 ° to 30 ° and the bench-mark simulation is repeated resulting in an almost perfect match between the experimental, analytical and numerical model (see Figure 4.15).

Figure 4.16 clearly shows the independency of the mechanical behavior of the numerical load implementation (force or displacement driven). Furthermore, the numerical model captures the geometrical changes during loading of the stent very well as the experimental data is closely approximated.

---

[8]The stent length predicted by the model underestimates the experimental length value by maximally 3 %.
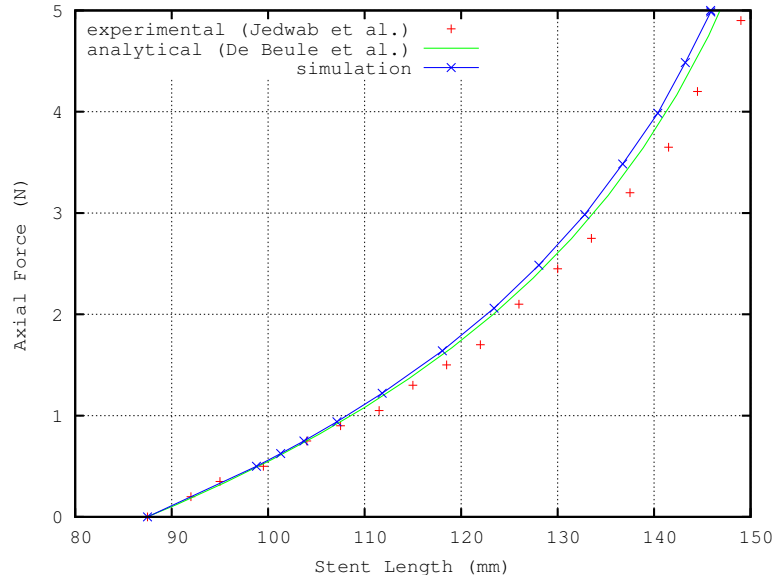
Figure 4.14: Validation of the numerical model with experimental and analytical data. Increase of longitudinal stiffness with increasing stent length.
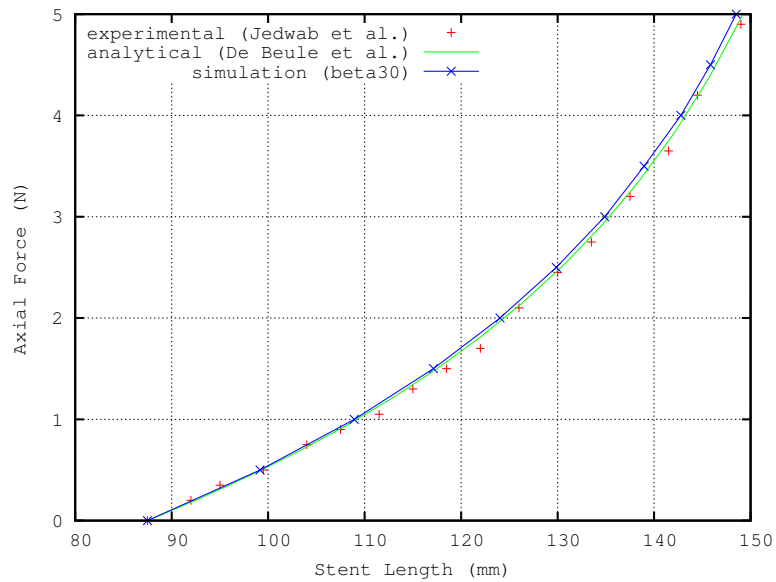
Figure 4.15: Changing the original pitch angle β from 30.85° to 30° results in an almost perfect match between experimental, analytical and numerical data.
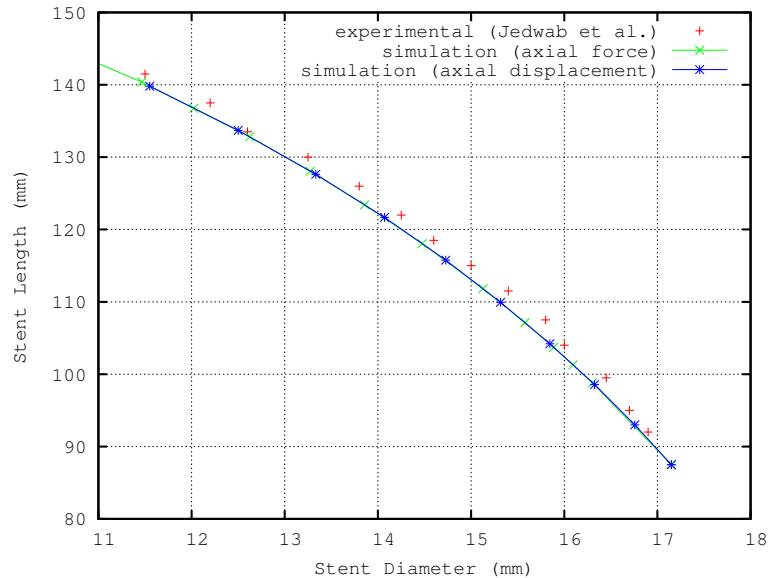
Figure 4.16: The mechanical behavior of the braided Wallstent is independent of the numerical load implementation as the axial force and displacement driven graphs coincide.

Radial compression

The radial pressure p_{outer} exerted on the stent as a function of the stent diameter D is presented in Figure 4.17. The non-linear 'Stent Diameter'/'Radial Pressure' relation suggests a radial stiffness increase with increasing stent diameter in the considered diameter range. This phenomenon is (yet again) related to the more and more similar orientation of both the radial load and the wires. The experimental results are overestimated by as well the analytical model as the numerical simulation, whereas the numerical model is a slightly better approximation. The hypothesis that the (still) rather significant difference is related to the experimental set-up (see section 4.1.2) is further corroborated by Figure 4.18. The (again corresponding) pressure and displacement driven simulations show a very good agreement with the experimental data (from the axial elongation test), suggesting the validity of the numerical model in both the axial elongation and radial compression load cases.
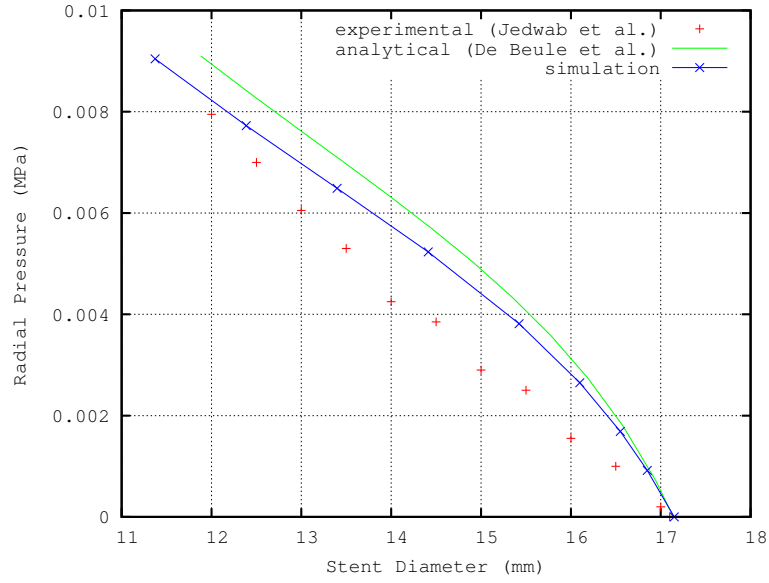
Figure 4.17: Validation of simulation with experimental and analytical data.
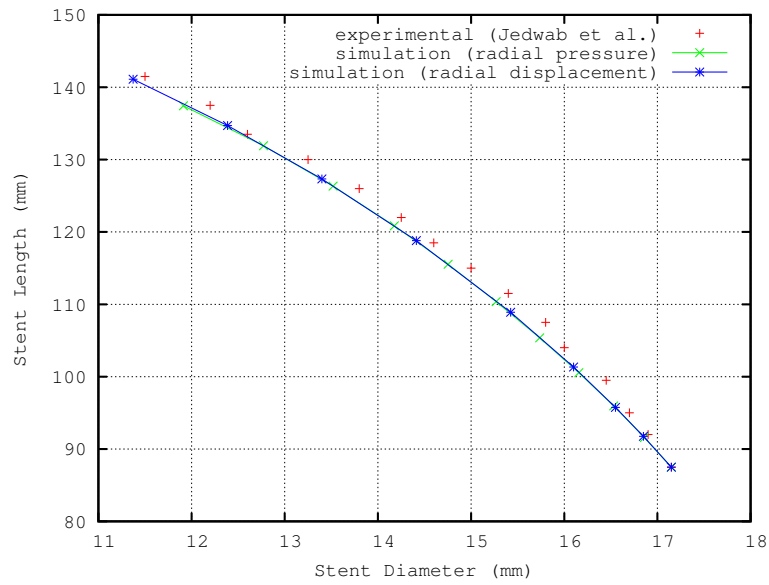
Figure 4.18: The mechanical behavior of the braided Wallstent is independent of the numerical load implementation as the radial pressure and displacement driven graphs coincide.

4.3.2.2 Parametric model

Axial elongation

An increase of the axial stiffness K_L is associated with an increase in wire thickness d (Figure 4.19), number of wires n (Figure 4.20) and/or pitch angle β (Figure 4.21). A basic (though logic) rule seems to be valid: 'the more material, the higher the stiffness'. However, the wire diameter seems a much more predominant impact factor than the number of wires which is explained by equation 4.4, as the longitudinal stiffness K_L is proportional to d^4 (through I and I_p) and n. The effect of the initial (design) pitch angle is again related to the correspondence between the wire direction and the applied loading.

Radial compression

Increasing the radial stiffness K_p of the stent is feasible by increasing the wire thickness d (Figure 4.22), increasing the number of wires n (Figure 4.23) and/or decreasing the value of the pitch angle β as shown in Figure 4.24. These phenomena are again explained by the same basic rule: 'more is more'. As also the radial stiffness K_p is proportional to d^4 and n (see equation 4.14), it is much more influenced by an increase in wire diameter as compared to an increase in number of wires. Furthermore, a similar orientation of both the radial load and the wires increases K_p, thus a stent design with a high radial strength can be achieved with a low initial design pitch angle.
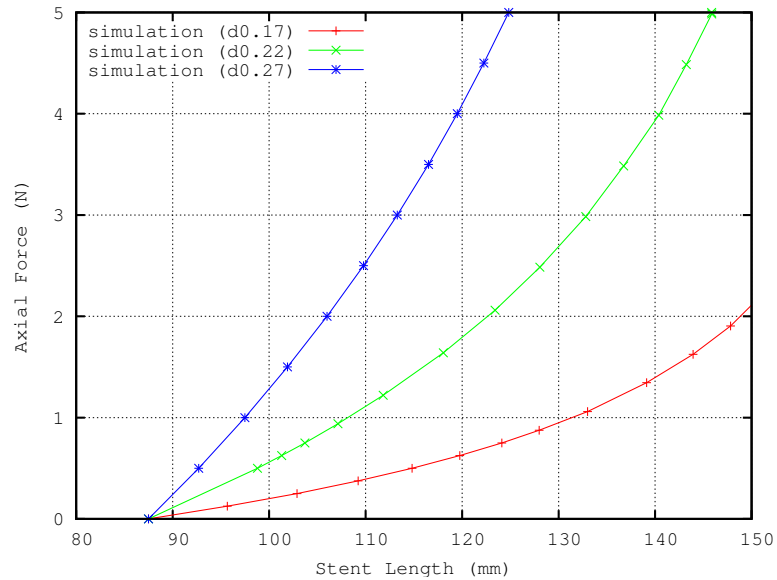
Figure 4.19: Increasing the wire thickness d results in a highly increased tangent to the 'Stent Length' / 'Axial Force' curve, defined as the axial stiffness.
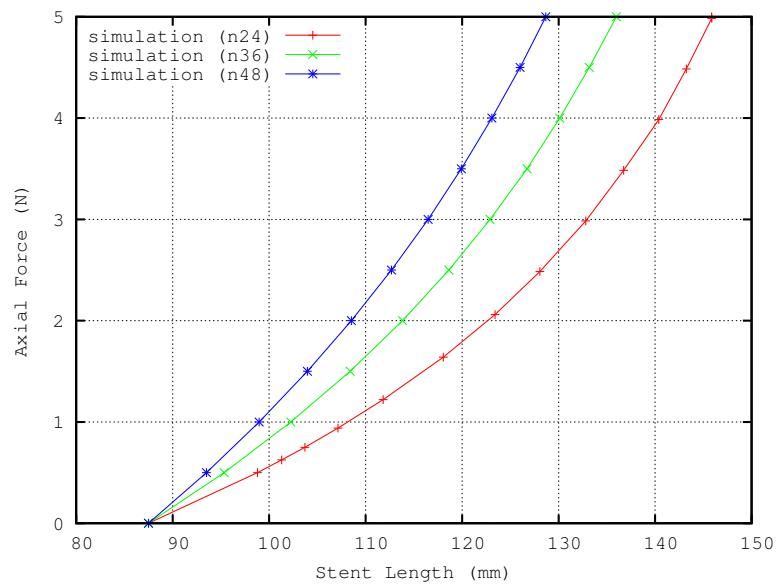
Figure 4.20: An increase in number of wires n causes an increase in axial stiffness.
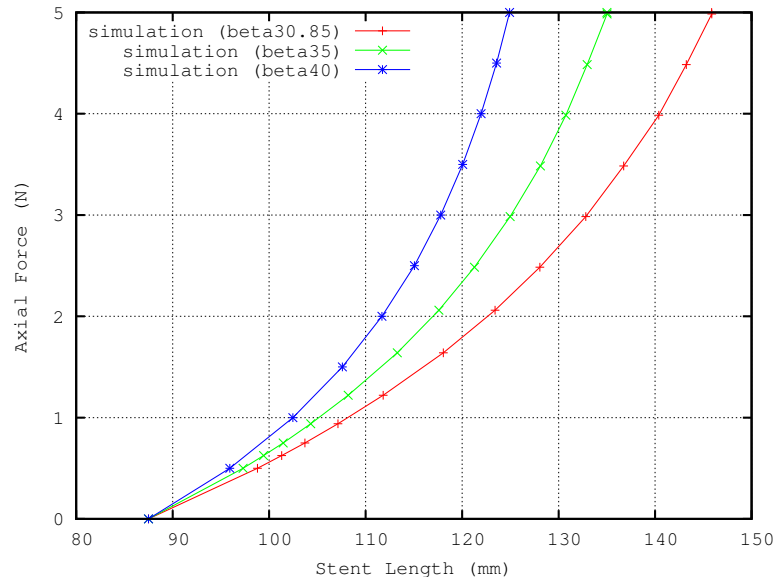
Figure 4.21: Increasing the pitch angle β increases the axial stiffness.
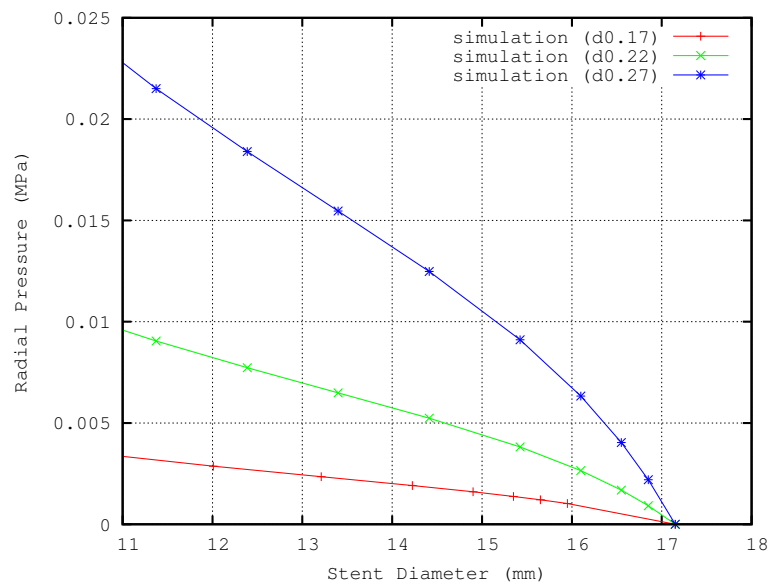
Figure 4.22: An increase in wire thickness d causes a highly increased radial stiffness (i.e. a higher slope of the 'Stent Diameter' / 'Radial Stiffness' curve).
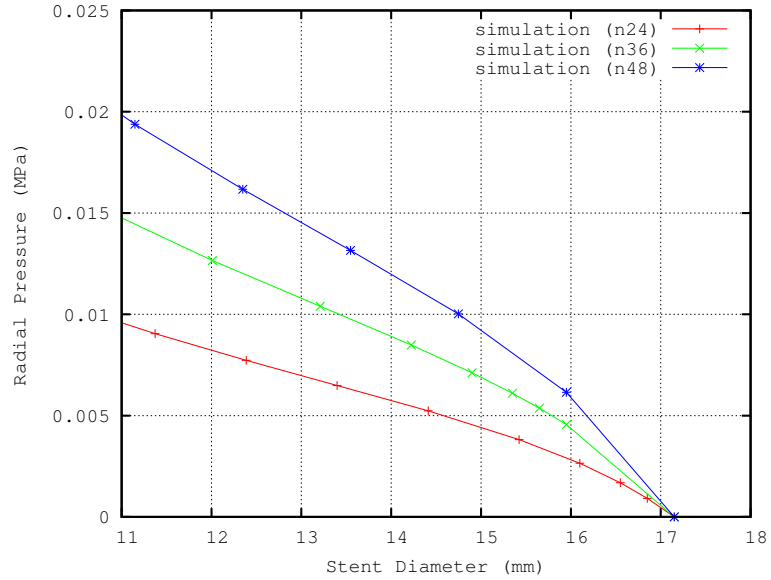
Figure 4.23: Increasing the number of wires n results in an increased radial stiffness.
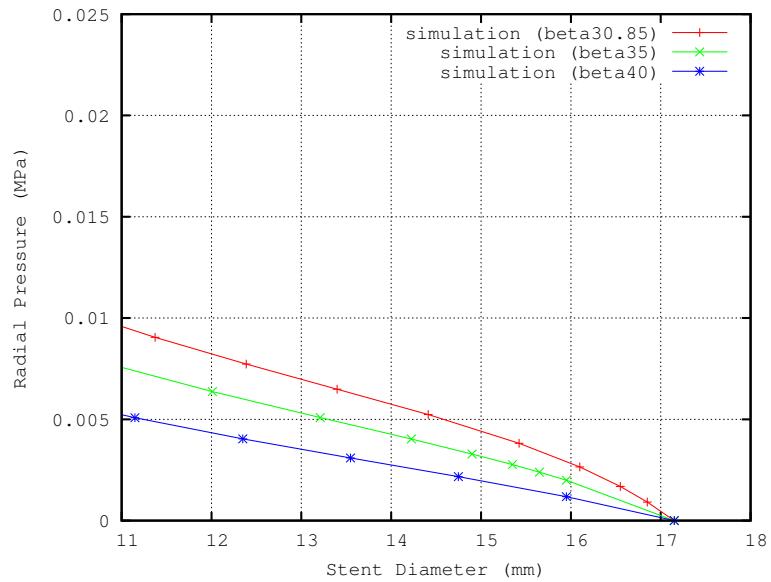
Figure 4.24: The radial stiffness is inversely proportional to the pitch angle β, decreasing the pitch angle increases the radial stiffness.

Foreshortening analysis

The foreshortening, defined by equation 4.15, is dependent only on the stent length L which is an explicit function of the pitch angle β (see equation 4.3). Logically a variation of the wire diameter d or the number of wires n has no influence at all on the stent shortening. Figures 4.25, 4.26 and 4.27 confirm these statements. Consequently, the pitch angle is the only braided wire stent design variable with the capacity of reducing the foreshortening. Though altering this pitch angle influences both the axial and radial stiffness as already described in the previous sections.
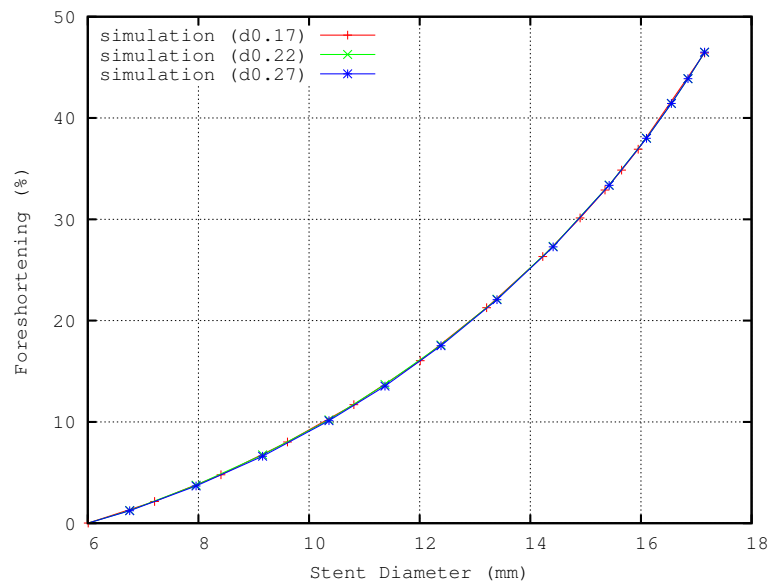
Figure 4.25: The foreshortening is independent of the wire diameter d.
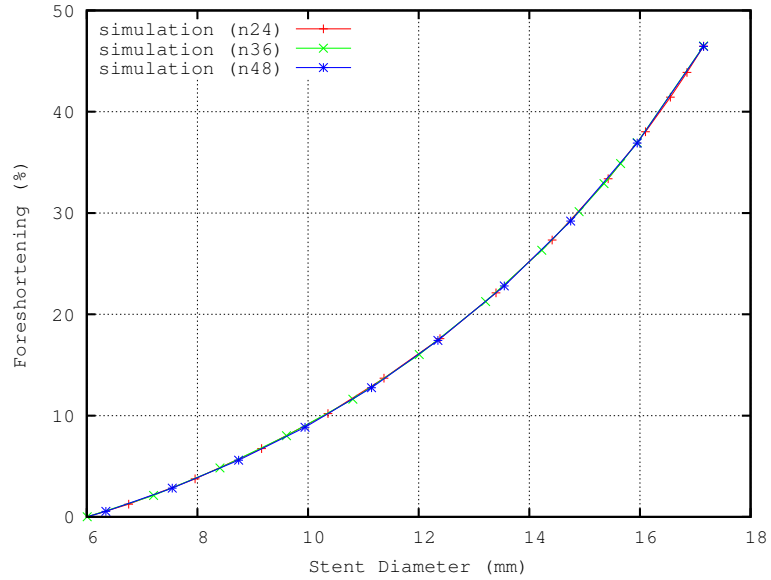
Figure 4.26: The foreshortening is independent of the number of wires n.
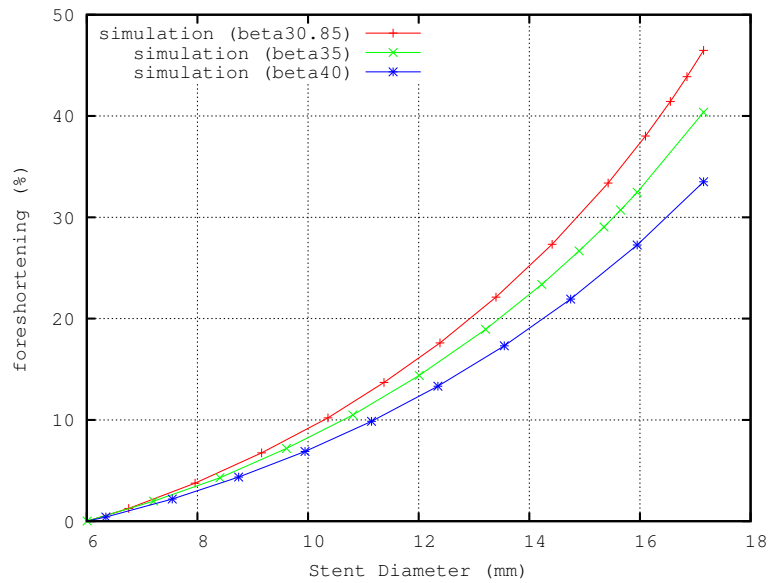
Figure 4.27: The foreshortening decreases with increasing pitch angle β.

4.3.3 Conclusions

Complex geometrical models of braided wire stents can quickly be built using the innovative **pyFormex** modeling paradigm. They can be used in finite element simulations for studying the mechanical behavior of the stent under complex mechanical loading conditions. Parametric modeling is an inherent feature of this paradigm and complex and extensive models can be generated from simple scripts. The results of the reference simulations of the *Urolume Wallstent* are in close agreement with both a newly proposed analytical approximation and experimental data.

The parametric study (varying the wire diameter d, the wire number n and the pitch angle β) shows an inversely proportional correlation between the radial stiffness of the stent and the pitch angle, whereas the axial stiffness is proportional to the pitch angle. Furthermore, both the longitudinal and radial stiffness are proportional to the wire diameter and the number of wires. The wire diameter is the most important impact factor for stiffness regulation. In addition, the shortening of the stent, independent of the wire diameter and the number of wires, is regulated (only) by the pitch angle.

Consequently, altering (increasing) only the initial design pitch angle reduces the foreshortening of the stent (to facilitate precise positioning), though decreases the radial stiffness. This behavior is observed, and thus confirmed in the commercially available 'standard braid' and 'less shortening braid' *Wallstent* [121, 122]. However, the parametric study clearly shows that this decrease in radial stiffness can be compensated (easily) by increasing the wire thickness and/or the number of wires. To find such optimal stent design configurations, optimization algorithms [4] seem a promising design strategy. Furthermore, providing the physicians with the relation between the 'Stent Diameter' and 'Stent Length' (see Figure 4.16)[9] could already be an important step forward to ease precise positioning of this type of devices.

The developed **pyFormex** modeling method is a solid base for further study of the mechanical behavior of braided wire stents in real life conditions (e.g. catheter / stent interaction, multilayer braided stents, ...) where simplified analytical approximations are no longer valid. Furthermore, other important design parameters (e.g. flexibility) could also be evaluated in the quest for the ideal prosthesis. Therefore, the use of finite element calculations combined with sophisticated **pyFormex**-based pre- and postprocessing techniques is a strong design tool for braided wire stent(graft)s.

---

[9]Analogously to the compliance chart of balloon expandable stents, the 'Instructions for Use' or even the 'packaging box' of the Wallstent seem very appropriate for this purpose. Of course the physician is supposed to have an idea of the (final) diameter of the stented vessel.

4.4   Wire stresses and catheter choice

In this section an analytically confirmed virtual bench-mark test is described to assess the stress state of the stent wires when the stent diameter of the bare-metal braided *Wallstent* is reduced for different catheter sizes. Subsequently, an original and experimentally validated methodology to analyze the free expanding stent exiting the catheter is developed. Our validated virtual bench-mark tests offer interesting possibilities to assess the coupled response of the stent and the blood vessel and may offer novel insights useful for improved prosthesis design.

4.4.1   Introduction

Based on the finite element wire stent models, a first virtual bench-mark test is developed in order to determine the minimal diameter of the wire stent that can be reached by applying an axial load without (unwanted) plastic deformations of the wires. Consequently, this analytically confirmed and therefore validated test is a useful tool to quantify the minimal diameter of the catheter that can be combined with a particular wire stent (material). Subsequently, a second bench-mark test is proposed to perform stable and accurate finite element simulations of the wire stent free expansion (i.e. when the stent is released from the catheter). Furthermore, the impact of combining the wire stent geometry with different materials (phynox, stainless steel and nitinol) is investigated. The numerical results have been validated by comparison with experimental data.

4.4.2   Materials and methods

In the non-deformed state the external diameter D_{e0} and the length L_0 of the investigated *Wallstent* are 20 mm and 80 mm, respectively. The stent consists of 36 wires, each of a diameter d of 0.17 mm, braided into a helical composition with 18 left-handed and 18 right-handed helices with an initial pitch angle β_0 of 34° [94]. The considered stent geometry is combined with three stent materials (stainless steel, high strength phynox and shape memory nitinol [123]) and the mechanical properties of these materials are reported in table 4.4. Only the super-elastic behavior of the nitinol alloy is taken into account, assuming that a temperature dependent shape memory effect is negligible in this context. This nitinol super-elastic behavior has been implemented numerically in the finite element solver ABAQUS [120] using the User Defined Material Model subroutine (UMAT, supposing a working temperature of 22 °C)[10]. The stent model is defined by 20160 2

---

[10]This temperature setting suposes the mounting of stents inside the catheter and in vitro deployment check at room temperature.

node linear beam elements (B31). All geometrically non-linear numerical simulations were performed on a single node of an in-house built low-cost, high performance computing cluster [109]. For both bench-mark tests, the (final) numerical results were obtained within 30 minutes after launching the computations. Consequently, the proposed modeling strategy is very time effective, even on a standard desktop computer.

Table 4.4: Material properties used in the simulations.

	stainless steel	
E	modulus of Young	$196000\,\mathrm{N/mm^2}$
ν	Poisson's ratio	0.3
σ_y	yield stress	$375\,\mathrm{N/mm^2}$
	phynox	
E	modulus of Young	$220000\,\mathrm{N/mm^2}$
ν	Poisson's ratio	0.33
σ_y	yield stress	$1578\,\mathrm{N/mm^2}$
	nitinol	
E_A	austenite elasticity	$35877\,\mathrm{N/mm^2}$
ν	Poisson's ratio	0.33
σ_L	start of transformation loading	$489\,\mathrm{N/mm^2}$

4.4.2.1   Equivalent stress state in the stent wires

The first objective of this section is to develop a virtual bench-mark test to assess the equivalent stress state of the stent wires when the diameter of the braided stent is reduced, simulating the insertion of the stent into the catheter. The reduction of the stent diameter is modeled by applying an increasing axial load nF' resulting in an equivalent axial force F' on each wire from 0 to $0.6\,\mathrm{N}$ on one end of the stent while the other end of the stent is constrained in both the tangential and axial direction (Figure 4.28). Consequently, this test permits to compare the current stent wire stress state with (i) the yield stress to see what diameter reduction introduces plastic (undesired) deformations of the phynox and stainless steel stent and (ii) the transformation loading stress to evaluate whether the super-elastic properties of the nitinol stent are actually exploited.
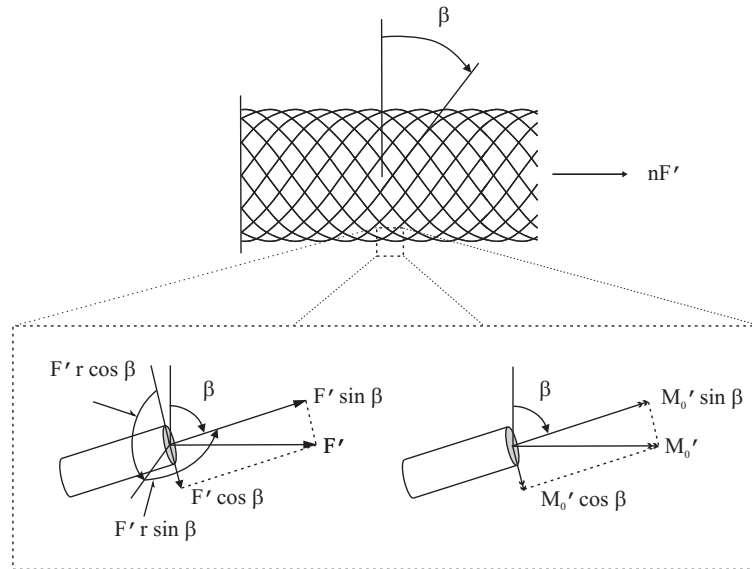
Figure 4.28: Axial force nF' applied to one end of the wire stent model (top panel) and resulting force F' and bending and twisting moments acting on the wire (bottom panel). Due to the fixation against rotation of the stent ends, the wires are subjected to additional bending and twisting provoked by the clamping moment M_0'.

The numerical results are compared with the analytical model described in section 4.1. With equation 4.12 it is possible to compute the maximum von Mises stress in the stent wires. It should not exceed the yield stress σ_y of the material in order to avoid plastic deformations (compromising the stent deployment performance).

4.4.2.2   Wire stent free expansion

The second objective of this section is to develop a stable modeling strategy to analyze the free expansion of the stent exiting the catheter. At first sight, the obvious way to simulate the stent deployment out of the catheter is to consider the actual interaction between the wire stent and the catheter. However, this strategy involves a very complex contact problem characterized by numerical instabilities and long (unpractical) simulation times. In order to avoid this computational problem the stent expansion is modeled as a displacement driven process mimicking reality. We thereby assume that the contact between the stent and the catheter takes place in the outer-nodes

of the stent model, i.e. the nodes in contact with an imaginary cylindrical surface that has the same diameter D_{e0}. During the generation of the finite element stent model with pyFormex, the outer nodes of the stent are automatically divided into several ($n = 68$) subsequent subsets. To study the variation of the stent radius as it exits the catheter, radial displacement boundary conditions (BC) were applied on these node subsets to first reduce the stent diameter to the catheter size (i.e. 10 French or 3.4 mm diameter) and subsequently release these boundary conditions set by set as shown in Figure 4.29.

The effect of the material (phynox, stainless steel and nitinol) properties on this expansion process are examined and the results of the numerical simulations are validated with experimental data reported by Wang [45].
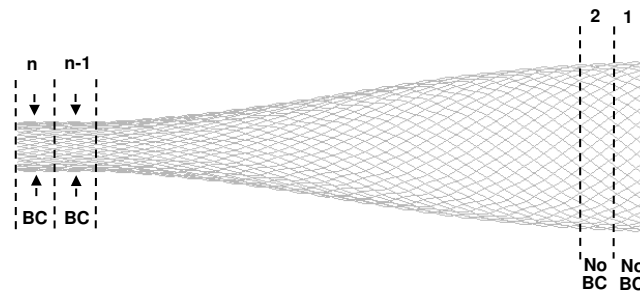
Figure 4.29: The outer nodes of the stent geometry are divided into several subsets as indicated by the dashed lines. Radial Boundary Conditions (BC) are imposed and released set by set.

4.4.3 Results and discussion

4.4.3.1 Equivalent stress state in the stent wires

The equivalent stress σ_e in the stent wires is computed analytically according to equation 4.12 and compared with the corresponding values of

the equivalent von Mises stresses obtained from the finite element computations for the phynox, stainless steel and nitinol stent. The proposed loading scheme causes a slightly non-uniform radial deformation and non-homogeneous stress distribution along the stent length. Therefore, the stress and diameter values are averaged over several nodes along this length.

Over the whole range of loading, the simulation corresponds well with the proposed analytical approximation for both the phynox and nitinol stent and offers an excellent approximation of the equivalent stress state (Figure 4.30). However, reducing the diameter of the stainless steel stent to a value less than 14 mm induces plastic deformations, logically not captured by the elastic analytical approximation. In the investigation of the equivalent stresses it is important to notice, when using phynox, the equivalent stress does not exceed the maximum stress allowed by the von Mises criterion: $\sigma_e < \sigma_y$. Consequently, it seems possible to reduce the actually used catheter size for the considered stent design and high strength material without plastic deformations of the stent. On the other hand, when using nitinol, it should be noted that the super-elastic properties are not exploited for the considered stent design and material properties as the transformation stress (i.e. $489 \, \mathrm{N/mm^2}$) is not reached during the stent diameter reduction.
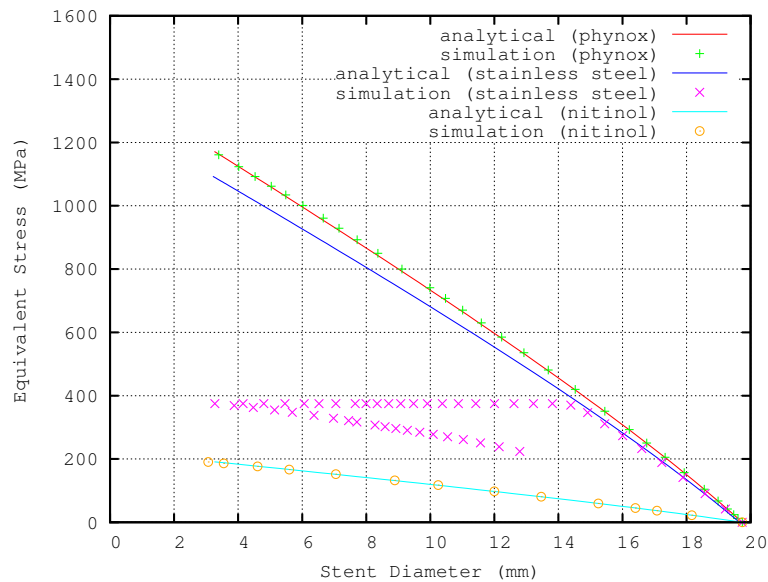
Figure 4.30: Comparison of analytically calculated and FEM based equivalent von Mises stress (distribution) in phynox, stainless steel and nitinol stent wire.

4.4.3.2 Wire stent free expansion

The simulations of the deployment of the wire stent have been performed using the methodology previously illustrated (Figure 4.29) and have been validated by comparison with experimental data reported by Wang [45]. Reducing the stent diameter to the catheter size by the applied boundary conditions provides a uniform radial deformation and a homogeneous stress distribution along the stent length. A comparison of the shape of the stent exiting the catheter as predicted by the numerical simulations with the shape measured from a photograph of the stent partially released from the catheter is depicted in Figure 4.31. The numerical simulations provide a very good representation of the deformability of the stent and clearly the mechanical (expansion) behavior of the stent is compromised by the effect of plastic deformation in the case of the stainless steel stent.

Furthermore, it can be noted that the material properties of phynox and nitinol seem to have limited influence on the stent expansion behavior. This phenomenon can be explained by the fact that the stent release can be considered as a linear elastic problem governed by imposed displacements.

In addition, the numerical simulations show an area of stress concentration at the tip of the catheter where the von Mises stress exceeds the yield stress for the phynox material during the expansion. This stress concentration is caused by the high gradient of radial deformation (radius out of the catheter = 10 mm and radius inside the catheter = 1.7 mm and is impossible to observe with the proposed analytical approach. However, this effect seems to have minor influence on the overall stent expansion behavior for the considered stent design and materials.
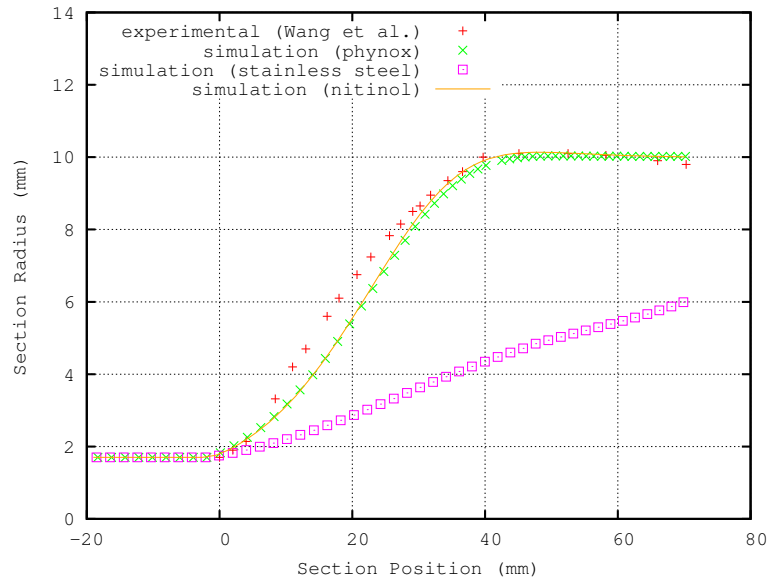
Figure 4.31: Comparison of expansion curves for phynox, stainless steel and nitinol stents. The plastic deformation of the stainless steel stent compromises the expansion behavior.

4.4.4   Limitations

It must be noted that in the proposed numerical model friction between (i) the stent wires and (ii) the stent wires and the catheter is not implemented. Also, the effect of a possible reduction of the catheter size on the actual stent performance (e.g. ease of delivery, flexibility,...) has not been examined. Further investigations in these directions - beyond the scope of this section - might allow capturing novel insights in the mechanical behavior of (bioabsorbable) braided stents and could deliver additional information useful for the quest for the optimal braided stent/catheter combination.

4.4.5   Conclusions

An analytically confirmed virtual bench-mark test is described to evaluate the stress state of the stent wires when the stent diameter of the braided *Wallstent* is reduced to several catheter sizes. It seems possible to reduce the actually used catheter size for the considered stent design and phynox material without plastically deforming the stent. Such a catheter size reduction would increase in-situ lesion access, but could decrease the ease of the actual stent delivery (i.e. higher force necessary to release the stent out

of the catheter). Furthermore, the use of high strength steels (i.e. characterized by high yield stress values) is required to avoid undesirable plastic deformation of the braided stent. Braiding the stent for example from 316L Stainless steel wires (characterized by a yield stress in the range of 205 to $375 \, \text{N/mm}^2$ and a modulus of Young comparable to the one of phynox) definitely induces such plastic deformations. Subsequently, an original and experimentally validated methodology to analyze the free expanding stent exiting the catheter is developed and shows that the elastic material properties (from phynox and nitinol) have limited influence on the stent expansion behavior.

4.5   Optimization

In this section a virtual procedure is described to seek optimized braided stent designs fulfilling specific design prerequisites. The proposed virtual optimization scheme is a time-effective, efficient and accurate technique in the quest for the ideal prosthesis.

4.5.1   Introduction

The precise positioning of the *Urolume (Wall)stent* (AMS, Minnesota, USA) is extremely important as an inappropriate position of the device in the external sphincter might lead to the patient's incontinence in the case of urethral strictures and prostatic obstructions [48]. Unfortunately, this precise positioning is complicated by the inherent characteristic of a braided stent: its significant foreshortening. Consequently, a less-shortening stent seems beneficial from a procedural point of view. However, reduction of radial stiffness has to be avoided as the prosthesis' radial stiffness is an essential characteristic to avoid device migration. Stent malpositioning and migration are both listed as potential adverse effects in the manufacturer's 'Instructions for use' of the *(Urolume) Wallstent*. Furthermore, if possible the wire mesh density (directly related to the amount of foreign body material) should be restricted. Of course equivalent braided stent design prerequisites are valid for other target vessels (e.g. carotid artery, colon, esophagus, ...).

When seeking a specific braided stent design to meet multiple (sometimes competing) prerequisites, different 'in silico' R&D strategies can be followed: (i) analytical modeling, (ii) parametric computational modeling and (iii) optimization computations. As the proposed analytical model of Jedwab [93] has a limited applicability (e.g. Nuutinen [97] showed the inability to analytically capture the mechanical behavior of biodegradable braided stents), a more general 'in silico' framework seems appropriate to study the mechanical behavior of braided stents, allowing for different materials and braiding

compositions (single and multilayer). However, while it is feasible to perform extensive parametric studies based on a validated bench-mark model, such a parametric approach is useful to understand the global mechanics of the device, though not very time-effective when searching for a specific optimized geometry due to the inherent high pre- and postprocessing effort to create these models and subsequently interpret the results. Therefore, an optimization scheme is the preferred design strategy as it has the potential to identify optimal geometries in a much more efficient manner. Timmins [4] recently developed such an optimization scheme, though limited to tubular stents.

In general, optimization problems are based on three basic components [124]:

- An objective function which the designer wants to minimize or maximize. Often, a number of different objectives are pursued which are frequently not compatible; the variables that optimize one objective may be far from optimal for the others. For instance, in the wire stent design process, reducing the foreshortening by increasing the pitch angle reduces automatically the radial stiffness. However, this loss of radial stiffness can be compensated by increasing the wire diameter and/or the number of wires. In practice, problems with multiple objectives can be reformulated as single-objective problems by forming a weighted combination of the different objectives.

- A set of unknowns or variables which affect the value of the objective function. The determinant geometrical variables in the braided stent design problem are the wire diameter d, the number of wires n and the pitch angle β.

- A set of constraints that allow the unknowns to take on certain values but exclude others. For the wire stent design problem, the variables are for example limited to a manufacturable design space.

Consequently, the optimization problem is then defined as to find values of the variables that minimize or maximize the objective function while satisfying the constraints.

4.5.2   Materials and methods

In the quest for the golden mean to reconcile the (at first sight) competing braided wire stent characteristics (e.g. radial stiffness and foreshortening), an optimization algorithm is implemented in pyFormex. The flowchart of this virtual optimization strategy is illustrated in Figure 4.32 and the value of the algorithm is confirmed by several optimization quests: (i) a bench-mark problem to search a stent design with the specific mechanical characteristics

of the *Urolume (Wall)stent* and (ii) a search for an optimized *Urolume stent* design with reduced foreshortening and unaltered radial stiffness (and wire surface ratio).
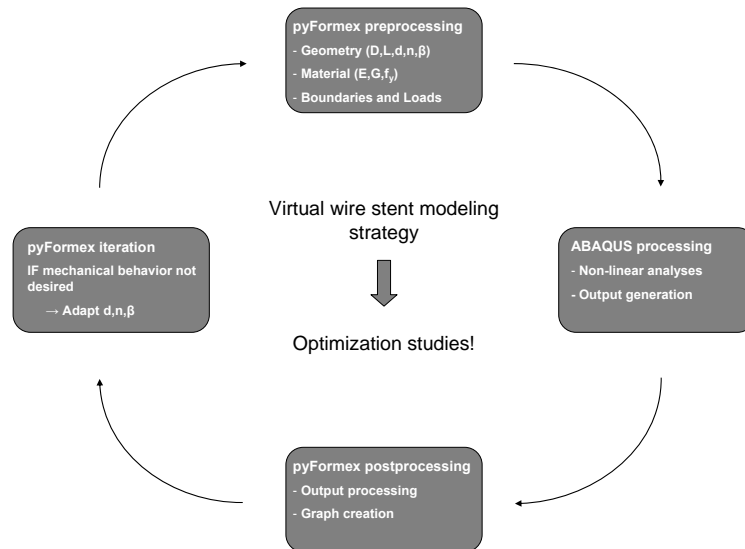
Figure 4.32: Flowchart of optimization modeling strategy.

4.5.2.1   Optimization algorithm

The Nelder-Mead 'simplex' method, attributed to J. A. Nelder and R. Mead (1965), is a widely used non-linear optimization algorithm [125]. It attempts to minimize a non-linear function of n real variables using only function values (no function derivatives are required) and uses the concept of a simplex, i.e. a polytope of $n + 1$ vertices in n dimensions: a line segment on a line, a triangle on a plane, a tetrahedron in a three-dimensional space and so forth. The method approximately finds a locally optimal solution when the objective function varies smoothly. Each iteration begins with a simplex, specified by its $n + 1$ vertices and the associated function values. Nelder-Mead generates a new test point by inter- and extrapolating the behavior of the objective function measured at each test point (i.e. the simplex vertices). The algorithm replaces one of the original test points with the new point and consequently the algorithm progresses as the $n + 1$ vertices of the new simplex are closer to the (local) minimum after every iteration. The algorithm is effective, computationally compact and implemented in Numerical Python by Oliphant [126].

4.5.2.2 Urolume endoprosthesis optimization

The mechanical behavior of the investigated *Urolume (Wall)stent* (see Table 4.2) is characterised by the following relevant design parameters (i) the radial stiffness, (ii) the axial stiffness, (iii) the foreshortening and (iv) the wire surface ratio. The determinant geometrical design variables - which influence these parameters - are the wire diameter d, the number of wires n and the pitch angle β. As depicted in Figure 4.5 and illustrated by equation 4.14, the radial stiffness alters with changing stent diameter. Therefore, the radial stiffness is quantified as K_{p0} for one characteristic point in the 'Stent Diameter' / 'Radial Pressure' curve, i.e. the initial stent diameter D_0. Analogously, K_{L0} is the quantification of the longitudinal stiffness defined at L_0 in the 'Stent Length' / 'Axial Force' curve. The foreshortening FS is defined as the amount that the stent shortens during unconfined free release from the catheter (see equation 4.15) and the ratio of wire area to the virtual cylinder surface[11] μ is chosen as a suitable criterion to quantify the wire mesh density and compare the effect of the geometrical changes (as this factor incorporates the three investigated design variables):

$$\mu = \frac{L_w d - \frac{N d^2}{\sin(2\beta)}}{\pi D L} \tag{4.18}$$

with L_w the total wire length and N the number of intersections.

The developed optimization tool is able to combine analytical and computational models. Both the radial and axial stiffness are obtained through numerical simulations, whereas the foreshortening and the wire surface ratio are analytically calculated for numerical stability (e.g. avoid round-off errors) and optimization efficacy reasons.

The relevant design parameters of the original (reference) *Urolume stent* design are summarized in Table 4.5 and this multiple objectives problem is defined as the following weighted single-objective function:

$$F(d, n, b) = W_{K_{p0}}(K_{p0} - K_{p0,desired})^2 + W_{K_{L0}}(K_{L0} - K_{L0,desired})^2 +$$
$$W_{FS}(FS - FS_{desired})^2 + W_{\mu}(\mu - \mu_{desired})^2 \tag{4.19}$$

The weighting coefficients represent the relative importance of the design parameters and allow for parameter exclusion ($W = 0$), inclusion ($W > 0$) and/or emphasis ($W >> 0$) in the optimum quest.

---

[11]This ratio is related to the area of the wire stent which is in contact with the target vessel and the complete derivation is given in Appendix A.

The user of the scripts is able to define the necessary constraints during the optimization process to assure the feasibility of the optimal geometry (e.g. from a manufacturing point of view). Consequently the wire diameter d, the number of wires n and the pitch angle β are for example constrained respectively to the $[0.17, 0.27]$mm, $[24, 48]$ and $[30, 40]$degrees ranges. These constraints are implemented by multiplying the objective function F value with a high penalty factor when one or more design variables exceed their design range. As a result, wire stent geometries outside the target design space will never result in a minimal function value. The principle of this penalty method is illustrated in Figure 4.33.
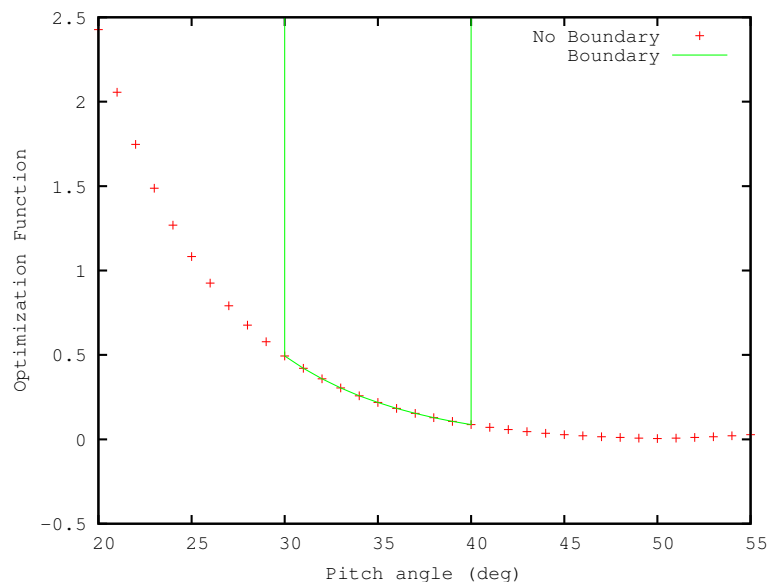
Figure 4.33: Example of implemented penalty function altering the proposed optimal pitch angle β from 50° in the unconstrained search to 40° in the quest with boundaries.

Running the optimization script without constraining boundaries results in an optimal geometry (i.e. minimal objective function value) with a pitch angle of 50°. However, seeking the same optimal geometry with the pitch angle constrained to the $[30, 40]$ interval results in a minimal function value at the design domain boundary, i.e. β equal to 40°.

Furthermore, as an odd number of wires is unpractical from a manufacturing point of view, odd wire numbers are automatically rounded off to even numbers by the algorithm.

To determine a good (operator independent) starting point for the optimiza-

tion quest, a Monte Carlo based algorithm is implemented in pyFormex[12].
Prior to the optimization launch, the objective function value F is deter-
mined for 10 at random combinations of possible design variables. The
combination with the lowest resulting function value is the starting point
(i.e. the original simplex) for the optimization quest. This methodology
is illustrated in Figure 4.34 where the simplex starting point is determined
after 10 at random approximations. Moreover, the resulting starting point
is a good first estimate of the final optimal geometry.
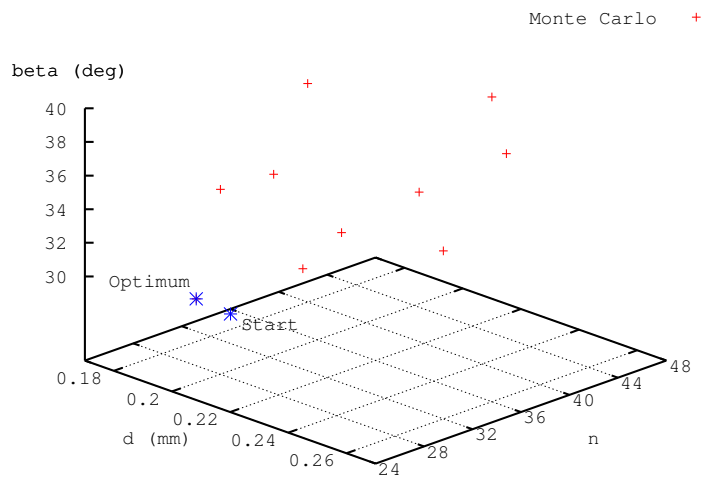
Figure 4.34: Monte Carlo based estimation of the starting point for the opti-
mization procedure.

The accuracy and efficacy of the proposed optimization strategy is tested
for two specific cases: (i) a bench-mark to search (from scratch) a stent de-
sign with the specific mechanical characteristics of the *Urolume (Wall)stent*
and (ii) a search for an optimized *Urolume stent* design with reduced
foreshortening and unaltered radial stiffness and wire surface ratio. The
starting points for all the optimization procedures are determined by 10
at random Monte Carlo based approximations. The bench-mark is initi-
ated by determining the mechanical properties of the reference *Urolume
(Wall)stent*, subsequently the optimization script searches for a specific ge-
ometry (within the specified design space) with similar mechanical prop-
erties with $W_{K_{p0}} = W_{K_{L0}} = W_{FS} = W_{\mu} = 1$. The second optimiza-

---

[12]A Monte Carlo method is a computational algorithm which relies on repeated random
sampling to compute its results [127].

tion process seeks two optimized geometries: (a) a stent geometry with a similar radial stiffness and a reduction of the foreshortening with 20 % ($W_{K_{p0}} = W_{FS} = 1; W_{K_{L0}} = W_\mu = 0$) and (b) a stent geometry with a similar radial stiffness and wire surface ratio and the same foreshortening reduction of 20 % ($W_{K_{p0}} = 1000; W_{FS} = W_\mu = 1; W_{K_{L0}} = 0$)[13].

All optimization simulations were performed on a single node (dual core) of an in-house built low-cost, high performance computing cluster [109]. For both cases, the (final) numerical results were obtained within four hours after launching the optimization scripts. Consequently, the proposed modeling strategy is very time effective, even on a standard desktop computer.

4.5.3 Results and discussion

The ability of the proposed optimization procedure to identify optimal geometries, satisfying the requested mechanical properties as much as possible in the constrained design variable space, is evidenced by both considered cases.

4.5.3.1 Optimization bench-mark

The optimization search for the *Urolume Wallstent* geometry is shown in Figure 4.35 (and the corresponding 2D plots are shown in Figures 4.36, 4.37 and 4.38) and summarized in Table 4.5. The outcome of the Monte Carlo approximation is a starting point characterised by a wire diameter $d = 0.20$ mm, $n = 26$ wires and a pitch angle of 30°. This starting geometry results in an underestimated stent stiffness and a slight overestimation of the foreshortening and wire surface ratio. Subsequently, the requested mechanical and geometrical stent properties are found by increasing the wire diameter to 0.22 mm and decreasing the number of wires and pitch angle to respectively 24 and 30.85°.

As clearly illustrated in Figures 4.36 and 4.37, the first part of the optimization procedure is dominated by a varying pitch angle. Due to this pitch angle change the foreshortening prerequisite is met because the shortening of the stent is independent of the wire diameter and number of wires. In the subsequent part of the optimization quest, the other design requirements are fulfilled by increasing the wire diameter and decreasing the number of wires (see Figure 4.38), while keeping the pitch angle at the desired constant value of 30.85°. At the end of the optimum search, when the number of wires

---

[13]The weight factor of the radial stiffness $W_{K_{p0}}$ is increased because a similar optimization quest with $W_{K_{p0}} = W_{FS} = W_\mu = 1; W_{K_{L0}} = 0$ results in a sub-optimal geometry with an insufficient radial stiffness of $0.0026\,\text{N/mm}^3$.

is rounded off to 24, a significant change in both wire diameter (0.22 mm - 0.23 mm) and pitch angle (32.4 ° - 29.3 °) is observed to find an (even more) optimal solution to compensate this rounding off (see Figure 4.36).
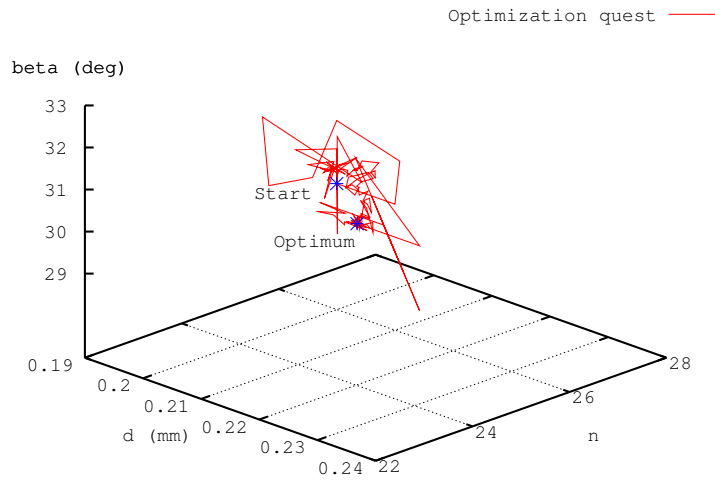
Figure 4.35: Quest for the *Urolume (Wall)stent* geometry ($W_{K_{p0}} = W_{K_{L0}} = W_{FS} = W_{\mu} = 1$) in 232 iterations.

Table 4.5: Geometrical and mechanical characteristics of the reference *Urolume Wallstent*, the starting and the optimal stent geometry.

		Geom_{ref}	$\text{Geom}_{\text{start}}$	Geom_{opt}
d	(mm)	0.22	0.20	0.22
n		24	26	24
β	(°)	30.85	30	30.85
K_{p0}	(N/mm³)	0.0031	0.0025	0.0031
K_{L0}	(N/mm)	0.0422	0.0302	0.0422
FS	(%)	46	47	46
μ		0.191	0.193	0.191
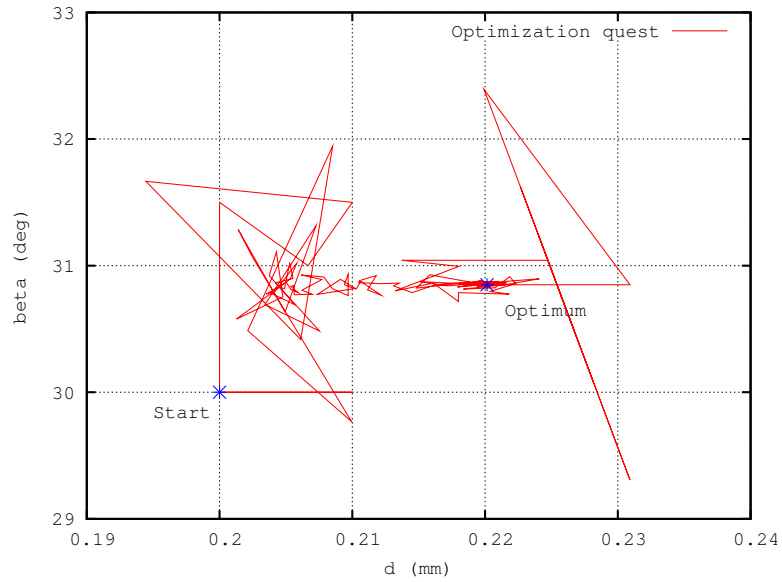
Figure 4.36: Wire diameter d and pitch angle β variation in the quest for the *Urolume stent* ($W_{K_{p0}} = W_{K_{L0}} = W_{FS} = W_{\mu} = 1$).
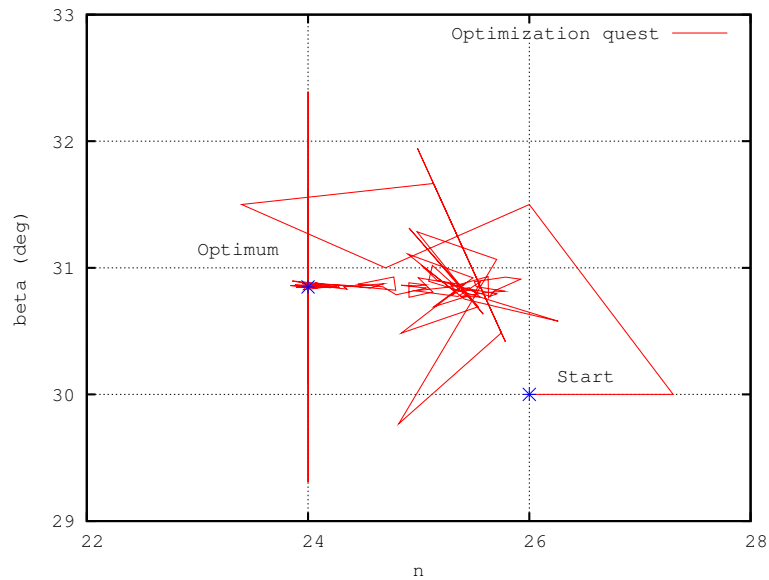
Figure 4.37: Variation of the number of wires n and the pitch angle β in the search for the *Urolume Wallstent* geometry ($W_{K_{p0}} = W_{K_{L0}} = W_{FS} = W_{\mu} = 1$).
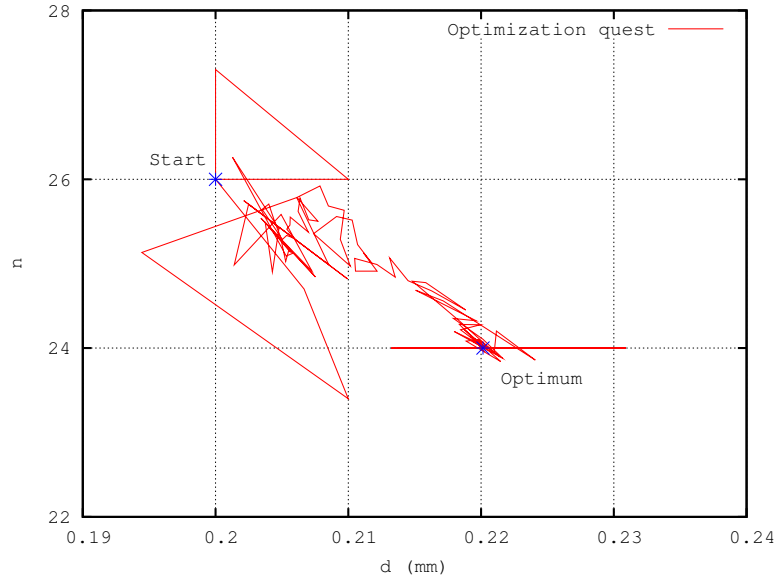
Figure 4.38: Increase of the wire diameter d compensating the wire number n reduction in the quest for the *Urolume endoprosthesis* ($W_{K_{p0}} = W_{K_{L0}} = W_{FS} = W_\mu = 1$).

4.5.3.2   Optimized foreshortening

The ability of the optimization procedure to identify a geometry with an unaltered radial stiffness and a 20 % foreshortening reduction as compared to the reference *Urolume Wallstent* is shown in Figure 4.39 and Table 4.6. The optimal geometry is found by increasing the wire diameter d, the number of wires n and the pitch angle β as compared to the *Urolume* reference geometry. The loss in radial stiffness induced by the pitch angle increase is compensated by the increase in both wire diameter and number. However, the increase of these factors influences the wire surface ratio considerably, resulting in a 36 % increase of μ. Furthermore, the cumulative effect on the axial stiffness K_{L0} of the wire diameter, wire number and pitch angle increase is significant (i.e. a 187 % increase). Presumably, a stiffness corresponding as good as possible to the target vessel and/or possible attached graft stiffness is the best option, though quantitative data regarding this design parameter is very scarce.
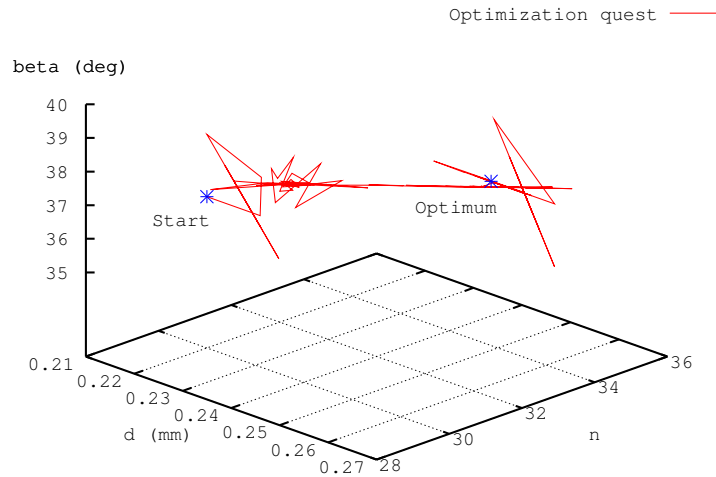
Figure 4.39: Quest (199 iterations) for a less foreshortening *Urolume stent* with $W_{K_{p0}} = W_{FS} = 1; W_{K_{L0}} = W_{\mu} = 0$.

Table 4.6: Geometrical and mechanical characteristics of the reference *Urolume endoprosthesis* and less shortening stent and their relative percentage differences.

		Geom_{ref}	$\text{Geom}_{\text{start}}$	Geom_{opt}	Diff (%)
d	(mm)	0.22	0.22	0.25	+14
n		24	30	34	+42
β	(°)	30.85	37	37.4	+21
K_{p0}	(N/mm^3)	0.0031	0.0017	0.0031	**0**
K_{L0}	(N/mm)	0.0422	0.063	0.121	+187
FS	(%)	46	37.3	36.8	**-20**
μ		0.191	0.203	0.259	+36

In an attempt to further optimize the previously obtained geometry, the optimization procedure is repeated with one additional request: maintaining the wire surface ratio μ of the reference *Wallstent*. This successful optimization quest is illustrated in Figure 4.40 and Table 4.7. Increasing the wire diameter d and pitch angle β significantly, while maintaining the number of wires n defines an optimal braided stent geometry. The increase in wire diameter compensates the decrease in radial stiffness (and the increase in wire surface ratio) related to the pitch angle increase. Again, the cumulative effect of the increase of the wire diameter and the pitch angle

on the axial stiffness is considerable (i.e. a 177 % increase). Furthermore, the resulting radial stiffness is slightly different from the requested value, because the wire diameter of 0.27 mm is limited by its constraint. Similarly, the wire surface ratio of the proposed optimal geometry is slightly higher than the reference value, most likely due to the limitations of the considered design space. Most probably the even integer constraint of the wire number is causing the discrepancy between the desired and obtained wire surface ratio.
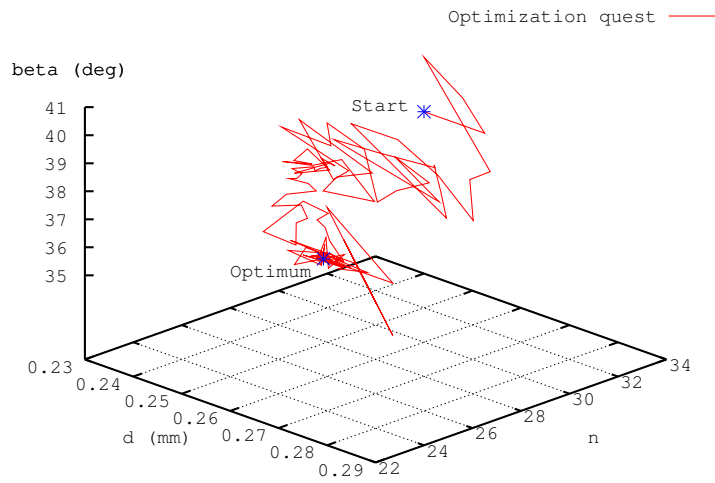
Figure 4.40: Optimization (FS reduction with μ constant) of the *Urolume (Wall)stent* with $W_{K_{p0}}=1000$ and $W_{FS}=W_\mu=1$ (in 288 iterations).

Table 4.7: Geometrical and mechanical characteristics of the reference *Urolume urethral stent*, the optimized less shortening stent and their relative percentage differences.

		$\mathrm{Geom_{ref}}$	$\mathrm{Geom_{start}}$	$\mathrm{Geom_{opt}}$	Diff (%)
d	(mm)	0.22	0.25	0.27	+23
n		24	32	24	0
β	(°)	30.85	39	37.4	+21
K_{p0}	(N/mm³)	0.0031	0.0025	0.0030	**-3**
K_{L0}	(N/mm)	0.0422	0.118	0.117	+177
FS	(%)	46	34.6	36.8	**-20**
μ		0.191	0.235	0.198	**+4**

4.5.4 Conclusions

This study demonstrates both the feasibility and the efficacy of braided stent design optimization with pyFormex. For this specific class of stents, the (at first sight) competing stent characteristics (e.g. radial stiffness and foreshortening) are reconcilable as illustrated in Table 4.6 by altering the relevant geometrical design variables (wire diameter d, wire number n and pitch angle β) in an intelligent way. Moreover, other important stent design requirements (e.g. axial stiffness and wire surface ratio) can be taken into account in the search for an optimal design as summarized in Tables 4.5 and 4.7. To facilitate precise positioning of the *Urolume (Wall)stent* by reducing the foreshortening with 20 %, while maintaining both the radial stiffness and the wire surface ratio, the design optimization algorithm proposes to increase the original wire diameter from 0.22 to 0.27 mm and the pitch angle from 30.85 ° to 37.4 °.

The developed stent design optimization tool presented in this study has several important features. However, we must recognize remaining limitations in the proposed approach in order to further improve this virtual design strategy. These limitations primarily pertain to the weighting coefficients choice, the analytical determination of foreshortening and the unicity of the optimization procedure ending point. Some degree of trial and error still exists in the determination of the most appropriate weighting coefficients. In general the best strategy appears to be to first equate all relevant coefficients and subsequently, increase those coefficients for the sub-optimal design parameters. An initial normalization of all relevant design objectives seems a logic step to overcome this empirical method, though rather complex since knowledge about the variation of these parameters through the complete design space is required. Furthermore, round-off errors seem to influence the foreshortening obtained through numerical simulation and finally, the method approximately finds a locally optimal solution, so no guarantee is given regarding the uniqueness of the solution.

However, besides trying to overcome these limitations, it is of course possible to extend the proposed wire stent design strategy by implementing other relevant design parameters, such as stent material, braiding composition and flexibility. Further investigations in these directions - beyond the scope of this study - might allow to capture novel insights in the mechanics of bioabsorbable and/or multilayer braided stents and could deliver additional information useful for the quest for the optimal braided stent design.

4.6 Multilayer braided wire stents

A promising new generation stent design to treat vascular diseases (both stenoses and aneurysms) has been developed recently by Cardiatis (Isnes,

Belgium [128]). This *3D structure stent* is made up of several layers braided together, creating a configuration of multiple interconnected layers. Preliminary in-vivo (animal) studies with this device have shown several benefits: immediate thrombosis and side branch patency of (saccular) aneurysms, no tissue ingrowth (thus cell proliferation prevention), etc. Consequently, this device seems promising to face the challenge of treating aneurysms (without covering) that involve arterial segments that contain essential branch arteries (both thoracic and cerebral).

To understand the underlying physical principles of this device behavior, an extensive research program has been set up at Ghent University, including in vitro experiments, computational simulations and animal studies. The experimental studies involve the quantification of the impact of the multilayer stent on the aneurysm and renal hemodynamics in a patient specific (anatomically correct) abdominal aortic aneurysm model. Computational fluid dynamical (CFD) models allow to examine the impact of the device on the flow and associated forces within the aneurysm (and side branches) and around the device wires. The biggest challenge associated with using CFD in this context is the enormous length scale disparity between the diameter of the parent vessel and the diameter of the individual endovascular device wires (i.e aneurysms 20 - 60 mm; stent wires 80 - 150 μm). Simultaneously, a finite element model is built to examine and characterise the (solid) mechanical behavior (e.g. the radial stiffness) of the device, meeting the challenge of modeling a braid of multiple wires in several layers. Finally, in vivo animal experiments, using a porcine aneurysm model, are conducted by dr. Frank Vermassen en dr. Lieven Maene to examine the prosthesis behavior in its natural habitat.

This section focuses on the solid mechanical aspects of the device. A validated (parametrically adaptable) finite element model is created through reverse engineering in pyFormex. This model allows to determine the (central) radial stiffness of the *3D structure stent* and consequently is an essential prerequisite for future studies (e.g. device optimization, stent / vessel interaction, etc.).

4.6.1   Materials and methods

The investigated multilayer *3D structure stent* (initial length L_0 60 mm, initial external diameter D_{e0} 8 mm) consists of several intertwined sets of in total 80 helical wires (initial pitch angle β_0 35 ° and wire diameter d 80 μm made from phynox (Young's modulus of elasticity E, and the shear modulus G, respectively equal to 220000 N/mm^2 and 82707 N/mm^2)). This braiding configuration is labeled as 320−80−01 below and depicted in Figure 4.41.
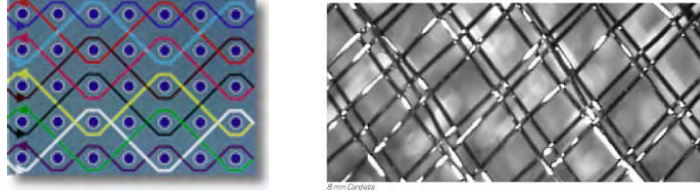
Figure 4.41: Multilayer braiding principle (left panel) and detail of braiding configuration of 320−80−01 stent (right panel).

4.6.1.1   Experimental set-up

To quantify the mechanical behavior of the 320−80−01 *3D structure stent* (in terms of (central) radial stiffness), a round wire (phynox, diameter 80 μm diameter) is placed around the circumference of the central part of the stent. Both ends of the wire are attached to the grips of a uniaxial tensile testing machine (Lloyd LFPlus, 50 N loadcell) and subsequently, the diameter of the stent is reduced by gradual increase of the distance between the grips. Both the intergrip distance change δ_{grip} and the force exerted on the wire T are monitored during the experiment and can be transformed in terms of external diameter D_e and radial line pressure q:

$$D_e = D_{e0} - \frac{\delta_{\text{grip}}}{\pi} \tag{4.20}$$

$$q = \frac{T}{D_e/2} \tag{4.21}$$

Consequently, the central radial stiffness of the stent structure is defined as the tangent to the 'Stent Diameter'/'Radial Line Pressure' curve (in accordance with the definition of the axial and radial stiffness defined in section 4.3).

4.6.1.2   Numerical model

The highly complex geometrical stent structure is accurately determined by importing the geometrical data directly from the stent fabrication software (used to operate the braiding machine in the manufacturing process) into pyFormex (see Figure 4.42).

Subsequently, dedicated pyFormex scripts unroll the cylindrical stent structure into a nearly planar full pattern and single out a base unit cell, as
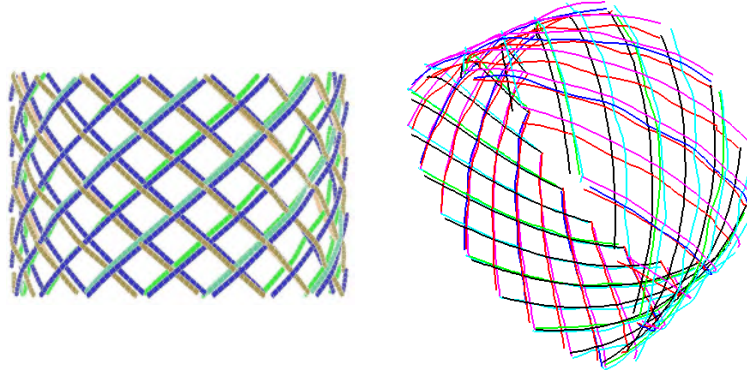
Figure 4.42: 3D representation of 320−80−01 stent in design software (left panel) and equivalent representation in pyFormex (right panel).

depicted in Figure 4.43. This base unit cell is approximated by an extended base module with inclusion of the appropriate connectors[14] to simulate contact between the wires in the finite element computations. The element choice (Frame3D) is again dictated directly by the dimensions of the wire cross-section, allowing for a one dimensional (thus computational efficient) approximation of the real three-dimensional structure.
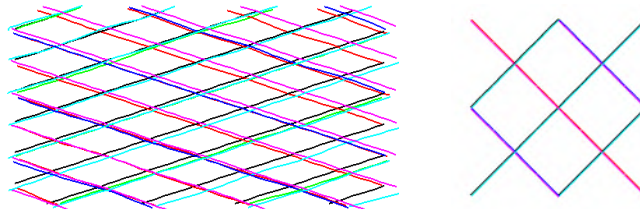
Figure 4.43: Unrolled pyFormex representation of 320−80−01 stent (left panel) and approximative pyFormex extended base module of crossing and connected wires (right panel).

Finally, the virtual 320−80−01 stent structure is defined by a sequence of operations similar to the pyFormex script to construct single layer braided wire stents (described in section 4.2). The resulting stent structure is a very good approximation of the real geometry (Figure 4.44) and is easily

---

[14]$JOIN$ connectors fix the coordinates of nodes of crossing wires from the same layer, whereas $SLIDE - PLANE$ connectors model the interaction between the interconnected layers constraining one node of the connectors to a plane while keeping the normal direction distance constant from the other node to the plane.

parametric adaptable (possible variation of wire diameter, wire number and pitch angle).
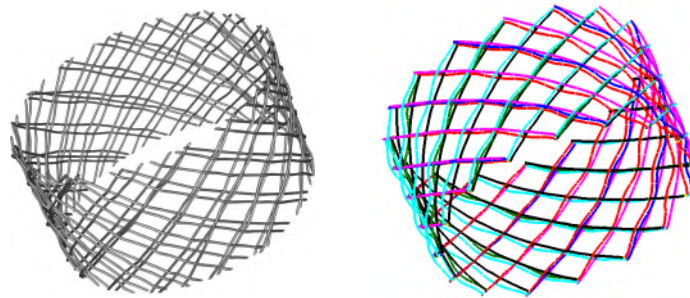
Figure 4.44: 3D reconstruction of µCT of multilayer braided stent (left panel) and equivalent pyFormex finite element model (right panel).

The physical loading on the stent, induced by the wire, is implemented by a radial displacement driven process. The central nodes of the finite element model are subjected to a radius reduction and the corresponding radial line pressure q is derived from the reaction forces opposing the imposed displacements in the central node-set. The discretized non-linear problem is analysed and solved by ABAQUS and subsequently post-processing is automated with pyFormex.

4.6.2 Results and discussion

The numerical model is a very good approximation of the experiment as depicted qualitatively in Figure 4.45 by the corresponding experimental and numerical stent shapes. Quantitatively, 'in vitro' and 'in numero' are compared in terms of the radial line pressure q exerted on the stent as a function of the stent diameter D (see Figure 4.46). The non-linear 'Stent Diameter'/'Radial Line Pressure' relation suggests an exponential (asymptotic) central radial stiffness increase with decreasing stent diameter. This phenomenon is governed by the decreasing interwire distance in the central region of the stent during the diameter reduction. Logically, this effect is more significant at small diameters, because the wires get more and more compacted, resulting in a very high stiffness at the end of the loading step. This stiffening behavior is observed in both the experimental and numerical results. The numerical model is a good approximation of the experiment in the 4 to 8 mm diameter range, however the discrepancy between the numerical and experimental results is more significant for diameters smaller than

4 mm.
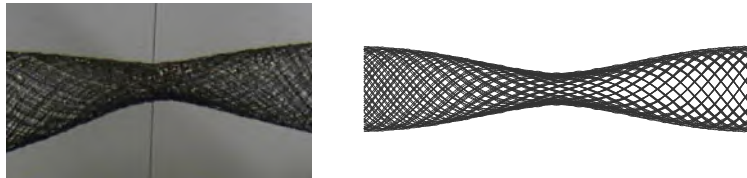
Figure 4.45: Central diameters reduction: experimental (left panel) and equivalent pyFormex finite element model (right panel).

This difference between experiment and simulation might be explained as follows: (i) only one experiment has been performed, therefore no data are available to reveal possible experimental scatter and (ii) the tensile wire is assumed not to elongate and to be perfectly perpendicular to the stent axis during the experiment. Furthermore, detailed information regarding the interaction between the braided wires during the stent diameter decrease might contribute to the model's accuracy (e.g. by a more accurate definition of the connectors). However, obtaining such detailed data regarding the wire interaction is far from trivial because of the wire diameter and the multilayer braiding pattern and is beyond the scope of this study.

4.6.3   Conclusions

The pyFormex pre- and postprocessing capabilities allow virtual examination of the mechanical behavior of new generation *3D structure stent* designs through reverse engineering. The complex geometrical structure is approximated directly from the manufacturing software, resulting in a parametrically adaptable accurate virtual model. Subsequently, the central radial stiffness of the stent structure is examined both experimentally and numerically and overall an acceptable correlation between 'in vitro' and 'in numero' results is obtained. An exponential increase in radial stiffness is observed with decreasing stent diameter, related to the increasing wire compaction. Consequently, this validated bench-mark is an essential prerequisite for future solid mechanical studies (e.g. device optimization, stent / vessel interaction, etc.) and is a step forward in the understanding of the mechanics of this promising prosthesis.
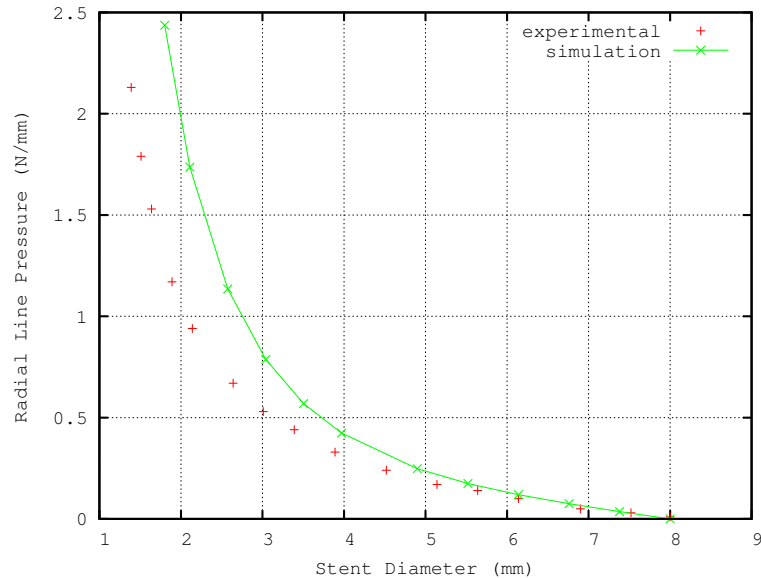
Figure 4.46: Diameter reduction caused by radial line pressure.

4.7 Conclusion

A theoretical and numerical framework was developed to study the mechanical behavior of braided wire stents under complex (though realistic) loading conditions. The validated virtual design space exceeds the analytical limitations, allowing a wide variety of materials (e.g. stainless steel, phynox, nitinol, etc.) and braiding patterns (single- and multilayer) to be considered in wire stent design. It can be concluded that:

- The revised analytical model provides useful information regarding wire stent mechanics for metallic (elastic) materials, simple braiding patterns and straightforward load cases. The theoretical predictions of the stent mechanical behavior under axial elongation and radial compression are experimentally confirmed and allow quantification of the stent axial and radial stiffness, the stent foreshortening, the wire surface ratio and the (von Mises) stresses in the stent wires.

- The innovative pyFormex modeling tool allows to quickly build complex geometrical and finite element models of wire stents, useful in finite element simulations for studying the mechanical behavior of wire stents with arbitrary geometry and arbitrary material under complex loading conditions. The proposed modeling strategy easily generates

lots of variations of the original geometry, an essential prerequisite for efficient stent design.

- The proposed virtual design tool is validated both analytically and experimentally, by examining the mechanics of the *Urolume (Wall)stent.* Parametrically adapting the original (bench-mark) geometry leads to the following design guidelines: (i) increasing the wire diameter and the number of wires augments the stent stiffness (axial and radial); (ii) increasing the pitch angle augments the axial, though decreases the radial stiffness; (iii) the wire diameter is the most important impact factor for stent stiffness regulation and (iv) the stent foreshortening, independent of the wire diameter and the number of wires, decreases with increasing pitch angle.

- Plastic deformation during stent insertion in the catheter should be avoided as it compromises the stent delivery and (mechanical) performance. The (experimentally validated) numerical modeling tool is able to predict these undesirable plastic deformations and thus, allows for both material and catheter size evaluation. The elastic material properties do not significantly influence the stent shape exiting the catheter.

- In addition to parametric modeling, the developed virtual wire stent design tool is extended with an efficient design optimization algorithm. Consequently it is feasible to reconcile competing stent characteristics in the quest for the 'perfect' stent by altering the relevant geometrical design variables (wire diameter, wire number and pitch angle). To facilitate precise positioning of the *Urolume endoprosthesis* by reducing the foreshortening with 20 %, while maintaining both the radial stiffness and the wire surface ratio, the algorithm automatically proposes to increase the original wire diameter from 0.22 to 0.27 mm and the pitch angle from 30.85 to 37.4 °.

- pyFormex is a suitable tool for reverse engineering of complex existing stent designs as it allows to create parametrically adaptable accurate virtual models (directly from the manufacturing software). As an example, the mechanical behavior of the multilayer *3D structure stent* is examined in terms of central radial stiffness. Overall a close correlation between numerical and experimental results is obtained and an exponential increase in radial stiffness is observed with decreasing stent diameter.

Chapter 5

Final remarks

The best is yet to come.
—Novastar

5.1 Conclusion

Within this thesis, we have created a validated virtual design space to investigate the mechanics and optimize the performance of stents using the finite element method. This design tool is applicable to both balloon and self expandable stents in a variety of materials (stainless steel, cobalt-chromium, nitinol, etc.) and configurations (laser-cut, braided).

From the review presented in **Chapter 2**, it is obvious that the finite element method offers numerous possibilities in the optimization of (coronary) revascularization procedures. The application of such a numerical approach in this specific biomechanical research domain is quite recent (1997) and has known an enormous evolution the last few years. Undoubtedly, all previously mentioned papers have contributed to the current level of understanding the mechanics of both stent designs and angioplasty procedures and the quality of these studies should be evaluated taking into account the available prescience and computational facilities (at the moment of publication). In the early years, numerical simulations were based on *Palmaz-Schatz* (Johnson&Johnson) like stents and simplified symmetrical stenosed arteries, mainly due to their straightforward geometry (e.g. the pioneering study published by Auricchio [1]). Furthermore, the *Palmaz-Schatz* stent was the only stent used in a multitude of large clinical studies at that time. Since then this numerical (r)evolution has been characterized by some important milestones, such as (i) the introduction of patient-specific stenosis models by Holzapfel and co-workers in 2000 [2], (ii) the introduction of

next generation stent geometries by Migliavacca et al. in 2002 [3] and the introduction of stent design optimization techniques by Timmins and his colleagues [4]. An astonishing observed fact in numerous studies is the lack of experimental evidence for the obtained numerical results, creating a missing-link with reality and provoking an (understandable) skepticism with respect to numerical models and to the conclusions drawn from them. The little validation that is performed is often merely qualitative, and thus not always applicable to interpret and verify the numerical results. The only consistent quantitative validation regarding the stent free expansion is from Migliavacca et al. [5], showing the considerable discrepancy between numerical results and reality when discarding the presence of the balloon. Regarding the vascular reaction to stent deployment, it should be nuanced that measuring the - by the stent (expansion) induced - stresses in the vessel wall in an experimental setup is a huge challenge. For such specific numerical studies, it makes sense to compare the results with clinical findings in literature (e.g. restenosis rates). Nevertheless, caution should be paid to the adopted methodology of the cited clinical trials (i.e. investigated stent designs, patient recruitment, etc.) and specifically designed new clinical follow-ups could be required for thorough validation of the developed hypotheses from the numerical results. Furthermore, the impact of the assumptions that were made (e.g. balloon neglect or simplification, applied constitutive material models, etc.) on the obtained results, should be investigated thoroughly, as already indicated by Holzapfel et al. [72].

The virtual design space to investigate the mechanics of balloon expandable stents is described in **Chapter 3**. The proposed methodology to simulate the free expansion of folded angioplasty balloons allows to determine approximate balloon material properties and appropriate boundary conditions (which mimic the balloon tapering) based solely on the manufacturer's compliance chart. The numerical results in terms of pressure and diameter show very good agreement with data provided by the manufacturer and consequently the proposed balloon model is an essential prerequisite to study realistic balloon/stent interactions. In the early stent-design phase, the radial displacement driven cylindrical balloon expansion method can provide useful and (relatively) accurate information regarding the stent shape when reaching its nominal diameter. However, to further optimize the stent design and its expansion, using the proposed trifolded balloon methodology seems to great advantage, since the free expansion of a stent is governed by the unfolding and expanding of the balloon. Moreover, the trifolded balloon expansion methodology shows very good quantitative and qualitative agreement with both manufacturer data and in-house experiments. Changing the balloon length and folding pattern can have an enormous influence on the transient stent expansion behavior. Therefore, the proposed methodology can be used to select the most appropriate balloon length and folding pattern for a particular stent design. Furthermore, small posi-

tioning inaccuracies of the stent with respect to the balloon catheter (e.g. during the crimping process) can considerably modify the stent deployment. Consequently, the positioning of the stent on the balloon catheter should be done with the greatest care and accuracy. The developed virtual stent design platform, combining parametric stent design with dedicated computational bench-mark tests can significantly shorten the design process and allows easy evaluation of the original design and its variations. Applying the proposed virtual design tool to the *Cypher* stent reveals that both the flexibility and the radial strength can be increased by reducing the number of bends from six to five. However, this geometrical change increases the stent foreshortening and probably limits the use of the same stent geometry with larger balloon diameters.

In **Chapter 4**, a theoretical and numerical framework is presented to study the mechanical behavior of braided wire stents under complex (though realistic) loading conditions. The validated virtual design space exceeds the analytical limitations, allowing a wide variety of materials (e.g. stainless steel, phynox, nitinol, etc.) and braiding patterns (single- and multilayer) to be considered in wire stent design. The revised analytical model provides useful information regarding wire stent mechanics for metallic (elastic) materials, simple braiding patterns and straightforward load cases. The theoretical predictions of the stent mechanical behavior under axial elongation and radial compression are experimentally confirmed and allow quantification of the stent axial and radial stiffness, the stent foreshortening, the wire surface ratio and the (von Mises) stresses in the stent wires. The innovative pyFormex modeling tool allows to quickly build complex geometrical and finite element models of wire stents, useful in finite element simulations for studying the mechanical behavior of wire stents with arbitrary geometry and arbitrary material under complex loading conditions. The proposed modeling strategy easily generates lots of variations of the original geometry, an essential prerequisite for efficient stent design. This virtual design tool is validated both analytically and experimentally, by examining the mechanics of the *Urolume (Wall)stent*. Parametrically adapting the original (bench-mark) geometry leads to the following design guidelines: (i) increasing the wire diameter and the number of wires augments the stent stiffness (axial and radial), (ii) increasing the pitch angle augments the axial, though decreases the radial stiffness, (iii) the wire diameter is the most important impact factor for stent stiffness regulation and (iv) the stent foreshortening, independent of the wire diameter and the number of wires, decreases with increasing pitch angle. Plastic deformation during stent insertion in the catheter should be avoided as it compromises the stent delivery and (mechanical) performance. The (experimentally validated) numerical modeling tool is able to predict these undesirable plastic deformations and thus, allows for both material and catheter size evaluation. The elastic material properties do not significantly influence the stent shape exiting the catheter.

In addition to parametric modeling, the developed virtual wire stent design tool is extended with an efficient design optimization algorithm. Consequently it is feasible to reconcile competing stent characteristics in the quest for the 'perfect' stent by altering only the relevant geometrical design variables (wire diameter, wire number and pitch angle). To facilitate precise positioning of the *Urolume endoprosthesis* by reducing the foreshortening with 20 %, while maintaining both the radial stiffness and the wire surface ratio, the algorithm automatically proposes to increase the original wire diameter from 0.22 to 0.27 mm and the pitch angle from 30.85 to 37.4 °. Furthermore, pyFormex is a suitable tool for reverse engineering of complex existing stent designs as it allows to create parametrically adaptable accurate virtual models (directly from the manufacturing software). As an example, the mechanical behavior of the multilayer *3D structure stent* is examined in terms of central radial stiffness. Overall a close correlation between numerical and experimental results is obtained and an exponential increase in radial stiffness is observed with decreasing stent diameter.

5.2 Future work

The findings of this thesis can be used as a starting point for further research topics. Some of the interesting ones are listed below. Several suggestions for improving the techniques and methodologies applied in this research are also outlined below.

An interesting extension to the survey reported in **Chapter 2** would be to include literature dedicated to modeling (diseased) arterial segments and a reflection with respect to functionality and patency of different stent designs. From a modeling perspective, the interaction of the stent with the vessel wall is of major importance to (try to) understand the outcome of stenting procedures. Depending on the context and aim of the study, one can choose to model the artery as an isotropic (hyper)elastic material [71] or take into account anisotropy, nonlinearity and prestretch [72]. Whereas the first approach might allow to capture phenomena such as stent deformation and/or tissue prolapse, the second approach seems more appropriate to study the stress distribution in the vessel wall.

The trifolded balloon expansion model (**Chapter 3**) has a large potential for stent design practice. However, some aspects of this methodology need further attention, e.g. the influence of the use of a (general) static friction coefficient to describe the interaction between the distinct parts of the stent delivery system. A dynamic friction coefficient (e.g. function of the specific materials, surface finish, rate of relative movement) would probably be a better approximation of reality, though seems to require an extensive and

accurately monitored experimental program. Moreover, a comparison between the current expansion method, based on the actual folded shape, and models taking the tapered ends of the balloon into account as recently presented by Holzapfel et al. [129], Capelli et al. [130] and Laroche et al. [131] seems very interesting, nevertheless is left for future work. Such a comparive study should take into account factors such as accuracy and (computational) efficacy, and should provide design guidelines to determine which modeling strategy to use in which circumstances. The current method can also be extended towards virtual revascularization procedures, taking into account the folded balloon, the stent and the target vessel. Future numerical models will allow to study the effect of the folding pattern on the resulting strut distribution and stresses in the vessel wall. Including the artery in the simulation models can also be useful to provide interesting insights in the mechanical aspects of the different interventional techniques proposed in literature (e.g. to treat bifurcation stenoses). Recently, Mortier et al. [132] proposed a numerical model to examine the opening of the side branch by balloon inflation after stenting the main branch (see Figure 5.1). The proposed virtual model will allow an objective comparison of different balloon and stent designs and/or interventional techniques to treat bifurcation lesions.

Figure 5.1: View into the main branch prior (left panel) and after (right panel) balloon inflation in the side branch (balloon not shown), showing the increased cell opening.

Since the outcome of a stenting procedure is highly dependent on the interaction of the stent with the artery it is expanded in, the ongoing numerical research needs thorough validation which is challenging due to many factors such as the size of the stent, the complex contact problems and the 3 dimensional type of problem. Recently Connolley et al. [133] succeeded in creating a 3D representation of stent deployment in a mock artery using synchrotron facilities, Auer and colleagues [134] were able to capture the arterial wall deformations during balloon angioplasty of in vitro samples with MRI and Van Loo et al. [135] created an in-house built setup, that permits 3D visualization during balloon and stent expansion using X-ray

microtomography, dedicated to create and validate numerical models (see Figure 5.2).
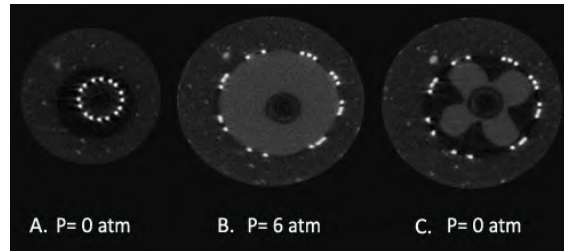
Figure 5.2: Cross-sections reconstructed from micro-CT scans before (A), during (B) and after (C) balloon inflation of a *Tenax* stent in a silicone artery.

The adopted flexibility test, proposed by Petrini et al. [83], is mainly limited by the absence of the delivery system (guidewire, catheter and balloon). Therefore, an interesting extension of the proposed methodology, beyond the scope of this work, would take into account the contact between the guidewire, the catheter, the (folded) balloon and the stent. Such a study seems feasible with ABAQUS/Explicit, though requires accurate material and geometrical information of all components. Furthermore, the proposed radial strength test, although very useful for virtual comparison of different stent designs and materials, seems rather difficult to validate experimentally. In an experiment, the outer surface of the stent is subjected to the increasing radial pressure through a flexible membrane. Therefore, when material and geometrical data of such a membrane are available, it would be very interesting to implement them in the virtual bench-mark test (e.g. using the contact modalities of ABAQUS/Explicit).

It would be worthwile to see whether the proposed finite element model to study the mechanics of braided wire stents (**Chapter 4**) can be fine-tuned further by accounting for friction between the stent wires as this could provide valuable insights in the mechanics of bioabsorbable braided stents. Friction can be taken into account in the proposed modeling strategy by choosing an appropriate connecting element between the crossing wires, although a complementary thorough experimental study would be (highly) recommended for validation purposes. Also, the effect of a possible reduction of the catheter size on the actual stent performance (e.g. ease of delivery, flexibility,...) seems a very interesting topic for future research, though again requires various stent samples for experimental validation purposes. Remaining limitations in the proposed optimization approach primarily pertain to the weighting coefficients choice, the analytical determination of foreshortening and the unicity of the optimization procedure ending point. Some degree of trial and error still exists in the determi-

nation of the most appropriate weighting coefficients. In general the best strategy appears to be to first equate all relevant coefficients and subsequently, increase those coefficients for the sub-optimal design parameters. An initial normalization of all relevant design objectives seems a logic step to overcome this empirical method, though this is rather complex since knowledge about the variation of these parameters through the complete design space is required. Furthermore, round-off errors seem to influence the foreshortening obtained through numerical simulation and finally, the method approximately finds a locally optimal solution, so no guarantee is given regarding the uniqueness of the solution. Even though the multilayer stent model was shown appropriate for characterising the radial stiffness, it can still be modified to obtain diameter / radial line pressure curves that better resemble in vitro results. Therefore, it would be valuable to perform a series of experiments monitoring the angle between the tensile wire and the stent axis and the interaction between the braided wires during the stent diameter decrease. However, obtaining such detailed data regarding the wire interaction is far from trivial because of the wire diameter and the multilayer braiding pattern.

Appendix A

Mechanical springs

J EDWAB and Clerc [93] described the geometrical and mechanical properties of self-expanding braided wire stents using the equations for open-coiled helical springs given by Wahl [115]. To revise these formulas, the basics of mechanical spring theory (as described by Wahl [115]) are repeated in this section, followed by extending this theoretical framework to wire stent structures.

A.1 Theoretical spring mechanics framework

Subjecting an open-coiled helical spring to an axial extension giving a large deflection, the coils tend to unwind; in other words there is a tendency of one end of the spring to rotate with respect to the other about the spring axis. For this reason, it is necessary to distinct two cases to study the mechanical spring behavior: (i) ends free to rotate, and (ii) ends fixed against rotation (e.g. due to friction or clamping). The cross section of the wire is assumed to be circular, the material elastic and the spring index D/d large. All relevant parameters to describe the stent (spring) geometrical and mechanical properties are summarized in Table A.1.

A.1.1 Springs with ends free to rotate

Assuming a helical spring axially loaded (with an axial force F') with the ends free to rotate, the spring wire is shown to change in wire curvature $\Delta\kappa$ and twist $\Delta\theta$ in the wire per unit length as the spring deflects from an initial pitch angle β_0 to a different pitch angle β. R_0 and R are respectively the initial and actual coil radius after deflection. In general, the wire curvature κ and the wire twist θ are:

Table A.1: Geometrical and mechanical properties of a braided wire stent.

(D_0) D	(mm)	(initial) average stent diameter
(D_{e0}) D_e	(mm)	(initial) external stent diameter
(R_0) R	(mm)	(initial) average stent radius
d	(mm)	wire diameter
n	(-)	total number of wires
(β_0) β	(-)	(initial) pitch angle
(L_0) L	(mm)	(initial) stent length
c	(-)	number of coils
δ	(mm)	axial stent elongation
F	(N)	axial stent force
F$'$	(N)	axial wire force
M_0'	(Nmm)	end wire moment
p_{outer}	(N/mm^2)	outer radial pressure
K_L	(N/mm)	longitudinal stiffness
K_p	(N/mm^3)	radial stiffness

$$\kappa = \frac{\cos^2 \beta}{R} \qquad\qquad \theta = \frac{\sin \beta \, \cos \beta}{R} \tag{A.1}$$

Varying the pitch angle from β_0 to β induces the following curvature and twist changes:

$$\Delta\kappa = \frac{\cos^2 \beta}{R} - \frac{\cos^2 \beta_0}{R_0} \tag{A.2}$$

$$\Delta\theta = \frac{\sin \beta \, \cos \beta}{R} - \frac{\sin \beta_0 \, \cos \beta_0}{R_0} \tag{A.3}$$

The bending moment acting on the wire m_b, equal to $F' R \sin \beta$ (see Figure A.1), induces the wire curvature change and consequently, the bending moment is quantified by multiplying this change in curvature $\Delta\kappa$ with the bending stiffness EI. Accordingly, the axial force F' is given by equation A.5

$$m_b = - F' R \sin \beta = -EI \left(\frac{\cos^2 \beta}{R} - \frac{\cos^2 \beta_0}{R_0} \right) \tag{A.4}$$

$$F' = F_b' = \frac{EI}{R \sin \beta} \left(\frac{\cos^2 \beta}{R} - \frac{\cos^2 \beta_0}{R_0} \right) \tag{A.5}$$
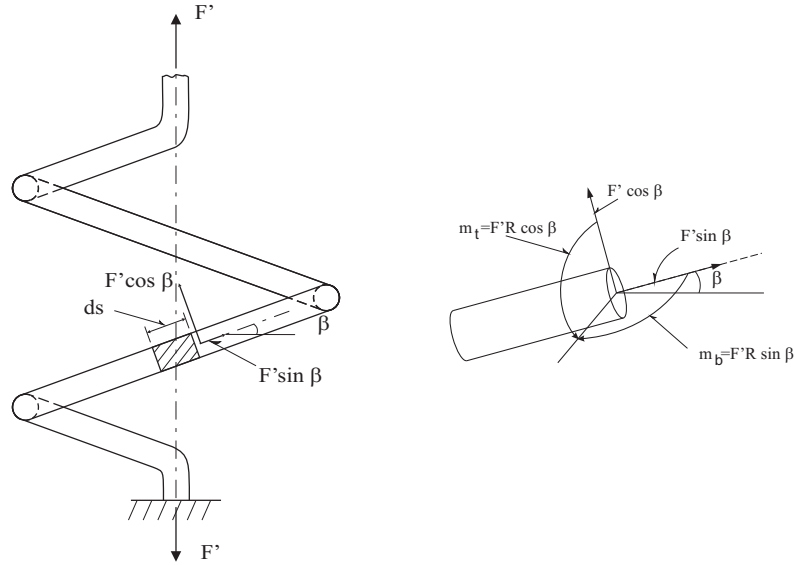
Figure A.1: Spring with ends free to rotate: Axial loaded open-coiled helical spring (left panel) and resulting forces and moments acting on wire part (right panel).

Likewise, the twisting moment m_t is equal to $F'\,R\cos\beta$. This twisting moment acting on the wire is quantified by multiplication of the wire twist change $\Delta\theta$ with the torsional rigidity GI_p.

$$m_t = F'\,R\cos\beta = GI_p \left(\frac{\sin\beta\,\cos\beta}{R} - \frac{\sin\beta_0\,\cos\beta_0}{R_0} \right) \qquad (A.6)$$

$$F' = F'_t = \frac{GI_p}{R\cos\beta} \left(\frac{\sin\beta\,\cos\beta}{R} - \frac{\sin\beta_0\,\cos\beta_0}{R_0} \right) \qquad (A.7)$$

The axial load induces an axial elongation δ of the spring in addition to the rotation of one spring end relative to the other. Assuming the active length of the spring l_{spring} remains constant (which is reasonable for springs with large index), the spring deflection δ can easily be determined from the geometry of Figures A.2 and A.3.

Figure A.2 (longitudinal spring axis horizontal) shows schematically the change in circumference and the corresponding pitch[1] change caused by the

---

[1] The pitch is defined as the axial distance covered by one revolution
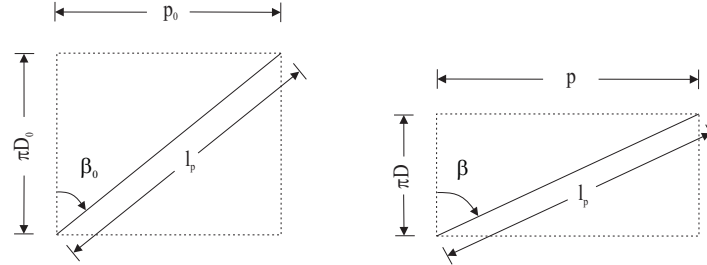
Figure A.2: Schematic representation of one unrolled revolution of a helical wire during spring elongation (longitudinal spring axis horizontal): unloaded (left panel) and loaded (right panel).

axial spring loading. The circumference alters from πD_0 in the unloaded state to πD when loaded, the pitch angle varies from β_0 to β and the pitch from p_0 to p. The developed spring length for one revolution is defined as l_p and is considered to be constant.

The wire length l_p of one revolution, the initial pitch length p_0, the number of (active) coils c, the wire length of the complete spring $l_{\text{w-spring}}$ and the total spring deflection δ are defined subsequently. Figure A.2 visualises the total wire length of one revolution l_p, quantified by

$$l_p = \frac{\pi\,D}{\cos\beta} \tag{A.8}$$

The pitch:

$$p_0 = \pi\,D_0\,\tan\beta_0 = l_p\,\sin\beta_0 \tag{A.9}$$

The number of (active) coils or revolutions is c, with L_0 the total length of the spring.

$$c = L_0\,/\,p_0 \tag{A.10}$$

As the total spring is defined by c coils, the total wire length of the spring $l_{\text{w-spring}}$ is:

$$l_{\text{w-spring}} = c\,l_{\text{p}} = \frac{c\,\pi\,D}{\cos\beta} \tag{A.11}$$
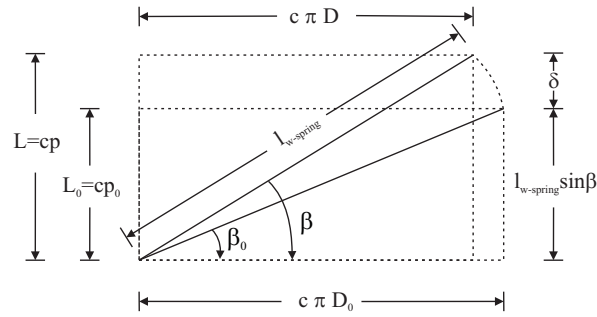
Figure A.3: Determination of the total spring deflection δ (longitudinal spring axis vertical).

The spring deflection δ, depicted in Figure A.3 is defined as

$$\delta = l_{\text{w-spring}} \cdot (\sin\beta - \sin\beta_0) \tag{A.12}$$

$$\Downarrow \qquad l_{\text{w-spring}} \cdot \cos\beta_0 = \pi\,c\,D_0$$

$$\delta = \frac{2\,\pi\,c\,R_0}{\cos\beta_0}\,(\sin\beta - \sin\beta_0) \tag{A.13}$$

As it is well known, when a tension spring is extended, the coils tend to unwind, at least at larger deflections. The amount of this unwinding, i.e. the angular rotation may be calculated as follows.

In the unloaded configuration:

$$\phi_1 = \frac{l_{\text{w-spring}}\cos\beta_0}{2\,\pi\,R_0} \qquad \text{in degrees}$$

$$\phi_1 = \frac{l_{\text{w-spring}}\cos\beta_0}{R_0} \qquad \text{in radians} \tag{A.14}$$

Analogously, in the loaded state:

$$\phi_2 = \frac{l_{\text{w-spring}} \cos \beta}{2 \pi R} \qquad \text{in degrees}$$

$$\phi_2 = \frac{l_{\text{w-spring}} \cos \beta}{R} \qquad \text{in radians} \qquad (A.15)$$

Consequently, the angular rotation of one end with respect to the other $\Delta\phi$, corresponding with a pitch angle variation from β_0 to β is:

$$\Delta\phi = l_{\text{w-spring}} \left(\frac{\cos \beta}{R} - \frac{\cos \beta_0}{R_0} \right) \qquad \text{in radians} \qquad (A.16a)$$

$$\Delta\phi = \frac{2 \pi c R_0}{\cos \beta_0} \left(\frac{\cos \beta}{R} - \frac{\cos \beta_0}{R_0} \right) \qquad (A.16b)$$

A.1.2   Springs with ends fixed against rotation

When the spring ends are fixed, i.e. prevented from rotating about the axis of the spring during deflection, a similar analysis may be made. In this case $\Delta\phi = 0$, and consequently it is necessary to take into account the moment M_0' acting at the spring ends which prevents coils from unwinding.

Combining both load cases, axial load F' (Figure A.1) and moment M_0' (Figure A.4), results in bending and twisting moments m_b and m_t acting on the wire:

$$m_b = M_0' \cos \beta - F' R \sin \beta \qquad (A.17)$$

$$m_t = M_0' \sin \beta + F' R \cos \beta \qquad (A.18)$$

Fixing the ends against rotation imposes ϕ_1 to be equal to ϕ_2, consequently the spring diameter D is directly proportional to the initial diameter D_0 as shown by combining equations (A.14), (A.15) and (A.16b):

$$R = R_0 \frac{\cos \beta}{\cos \beta_0} \qquad\qquad D = D_0 \frac{\cos \beta}{\cos \beta_0} \qquad (A.19)$$

The change in curvature of the wire $\Delta\kappa$ and the variation in angular rotation $\Delta\theta$ due to the bending and twisting moments are:

$$\Delta\kappa = \frac{m_b}{EI} = \frac{\cos^2 \beta}{R} - \frac{\cos^2 \beta_0}{R_0} \qquad (A.20)$$
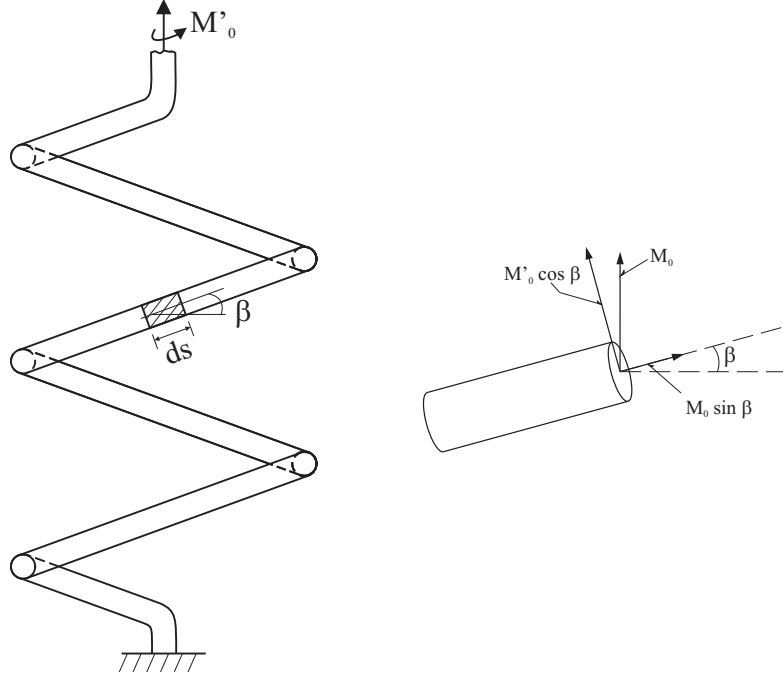
Figure A.4: Spring with ends fixed against rotation: Axial loaded open-coiled helical spring with end moments (left panel) and resulting forces and moments acting on wire part (right panel).

$$\Delta\theta = \frac{m_t}{GI_p} = \frac{\sin\beta\,\cos\beta}{R} - \frac{\sin\beta_0\,\cos\beta_0}{R_0} \tag{A.21}$$

so:

$$m_b = EI\Big(\frac{\cos^2\beta}{R} - \frac{\cos^2\beta_0}{R_0}\Big) = M_0'\cos\beta - F'\,R\,\sin\beta \tag{A.22}$$

$$m_t = GI_p\Big(\frac{\sin\beta\,\cos\beta}{R} - \frac{\sin\beta_0\,\cos\beta_0}{R_0}\Big) = M_0'\sin\beta + F'\,R\,\cos\beta \tag{A.23}$$

Reformulating (A.22) in terms of M_0' and equation (A.23) in terms of F':

$$M_0' = \Big(\frac{m_b + F'R\sin\beta}{\cos\beta}\Big) \tag{A.24}$$

$$F' = \frac{GI_p}{R\cos\beta}\left(\frac{\sin\beta\,\cos\beta}{R} - \frac{\sin\beta_0\,\cos\beta_0}{R_0}\right) - \frac{M_0'\sin\beta}{R\cos\beta} \tag{A.25}$$

Substituting equation (A.24) in (A.25):

$$F' = \frac{GI_p}{R}\left(\frac{\sin\beta}{R} - \frac{\sin\beta_0\,\cos\beta_0}{R_0\cos\beta}\right) - \left(\frac{m_b + F'R\sin\beta}{\cos\beta}\right)\cdot\frac{\sin\beta}{R\cos\beta} \tag{A.26}$$

and separating F':

$$F' + \frac{F'R\sin\beta}{\cos\beta}\cdot\frac{\sin\beta}{R\cos\beta} = \frac{GI_p}{R}\left(\frac{\sin\beta}{R} - \frac{\sin\beta_0\,\cos\beta_0}{R_0}\cdot\frac{1}{\cos\beta}\right)$$
$$-\frac{\sin\beta}{R\cos^2\beta}\cdot m_b$$

or:

$$F'\cdot\left(\frac{\cos^2\beta}{\cos^2\beta} + \frac{\sin^2\beta}{\cos^2\beta}\right) = \frac{GI_p}{R}\left(\frac{\sin\beta}{R} - \frac{\sin\beta_0\,\cos\beta_0}{R_0}\cdot\frac{1}{\cos\beta}\right)$$
$$-\frac{\sin\beta}{R\cos^2\beta}\cdot EI\left(\frac{\cos^2\beta}{R} - \frac{\cos^2\beta_0}{R_0}\right)$$

as so:

$$F' = \frac{GI_p\cos\beta}{R}\left(\frac{\sin\beta\cos\beta}{R} - \frac{\sin\beta_0\,\cos\beta_0}{R_0}\right)$$
$$-\frac{EI\sin\beta}{R}\left(\frac{\cos^2\beta}{R} - \frac{\cos^2\beta_0}{R_0}\right) \tag{A.27}$$

Knowing that $R = D/2$ en $R_0 = D_0/2$ and posing $F' = F'_{spring}$:

$$F'_{spring} = \frac{2GI_p\cos\beta}{D}\left(\frac{2\sin\beta\cos\beta}{D} - \frac{2\sin\beta_0\,\cos\beta_0}{D_0}\right)$$
$$-\frac{2EI\sin\beta}{D}\left(\frac{2\cos^2\beta}{D} - \frac{2\cos^2\beta_0}{D_0}\right) \tag{A.28}$$

Analogously, M_0' is defined as:

$$M_0' = GI_p \sin\beta \left(\frac{\sin\beta \, \cos\beta}{R} - \frac{\sin\beta_0 \, \cos\beta_0}{R_0} \right)$$
$$+ EI \cos\beta \left(\frac{\cos^2\beta}{R} - \frac{\cos^2\beta_0}{R_0} \right)$$

(A.29)

A.2 Theoretical wire stent mechanics framework

According to Jedwab [93], the equations for open-coiled helical springs, undergoing large deflections, are an appropriate base to derive the theoretical framework to study the braided wire stent mechanics under specific conditions (see section 4.1). The main parameters describing the geometrical and mechanical properties of a braided stent are the (initial) stent diameter $D_{(0)}$, the wire diameter d, the (initial) stent length $L_{(0)}$, the (initial) pitch angle $\beta_{(0)}$, the number of wires n, the modulus of Young E and the shear modulus G. Figure A.5 shows the initial cross section of crossing wires and a schematic representation of the (initial) stent pitch $p_{(0)}$. This schematic representation has to be interpreted as an unrolled stent part of one convolution of $n/2$ wires (with the same orientation). The solid line represents one full winding, the other $n/2 - 1$ wire parts are visualised as dashed lines. The index '$_e$' is used to denote external dimensions and the (logic) relation between average and external diameter is:

$$D_0 = D_{e0} - 2\,d$$

(A.30)

To derive the wire stent theoretical framework it is assumed that (i) the stent is a combination of a number of open-coiled helical springs undergoing large deflections, (ii) the extremities of the stent are not free to rotate due to the friction that the wires exert on each other at the crossing points, (iii) the springs undergo elastic deformation only and (iv) the springs possess large indices D/d.

A.2.1 Axial elongation analysis

The stent undergoes a change in pitch angle when subjected to an axial force F, so that the new pitch angle and stent average diameter are β and D, respectively. As a result, the stent has undergone an axial extension
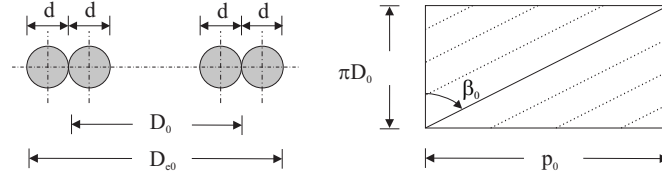
Figure A.5: Initial stent geometry of the wire stent.

δ and attains a new length L as depicted in Figure 4.2. Based on Wahl's equations for open-coiled helical springs with ends fixed against rotation, Jedwab [93] derives the following equation for the load F acting on the stent:

$$F = 2\,n \left[\frac{GI_p \cos\beta}{K_3} \left(\frac{2\,\sin\beta}{K_3} - K_1 \right) - \frac{EI \tan\beta}{K_3} \left(\frac{2\,\cos\beta}{K_3} - K_2 \right) \right] \quad \text{(A.31)}$$

with K_1, K_2, K_3, I and I_p:

$$K_1 = \frac{\sin 2\beta_0}{D_0} \qquad K_2 = \frac{2\cos^2\beta_0}{D_0} \qquad K_3 = \frac{D_0}{\cos\beta_0} \qquad \text{(A.32a)}$$

$$I = \frac{\pi\,d^4}{64} \qquad I_p = \frac{\pi\,d^4}{32} \qquad \text{(A.32b)}$$

Equation (A.31) is transformed into the notation of equation (A.28):

$$F = 2\,n \left[\frac{GI_p \cos\beta \cdot \cos\beta_0}{D_0} \left(\frac{2\,\sin\beta\,\cos\beta_0}{D_0} - \frac{2\,\sin\beta_0\,\cos\beta_0}{D_0} \right) \right.$$
$$\left. - \frac{EI \tan\beta\,\cos\beta_0}{D_0} \left(\frac{2\,\cos\beta\,\cos\beta_0}{D_0} - \frac{2\,\cos^2\beta_0}{D_0} \right) \right]$$

$$eq.(A.19) \qquad \Bigg\Downarrow \qquad \frac{D}{\cos\beta} = \frac{D_0}{\cos\beta_0}$$

$$F = 2\,n \left[\frac{GI_p \cos\beta \cdot \cos\beta}{D} \left(\frac{2\,\sin\beta\,\cos\beta}{D} - \frac{2\,\sin\beta_0\,\cos\beta_0}{D_0} \right) \right. \\ \left. - \frac{EI\,\sin\beta}{D} \left(\frac{2\,\cos^2\beta}{D} - \frac{2\,\cos^2\beta_0}{D_0} \right) \right] \tag{A.33}$$

Equation (A.33) is verified by means of the formulas derived in section A.1.2.

Equation (A.28) is valid for one spring, with ends fixed against rotation by the moment M_0. The wire stent is considered as a combination of n intertwined springs, consequently the expression for the axial load F working on the stent is:

$$F = F_{\text{stent}} = n \cdot F'_{\text{spring}}$$

$$F = 2\,n \left[\frac{GI_p \cos\beta}{D} \left(\frac{2\,\sin\beta\,\cos\beta}{D} - \frac{2\,\sin\beta_0\,\cos\beta_0}{D_0} \right) \right. \\ \left. - \frac{EI\,\sin\beta}{D} \left(\frac{2\,\cos^2\beta}{D} - \frac{2\,\cos^2\beta_0}{D_0} \right) \right] \tag{A.34}$$

Comparing equation (A.33) with (A.34) reveals the presence of an additional '$\cos\beta$' in the '$GI_p \cos\beta/K_3$' term of equation (A.31). Seen the inconsistency with the graphical representation of this formula (Figure 7 in Jedwab [93]) and the fact that this mysterious factor disappears in the other theoretical expressions derived by Jedwab to describe the stent's mechanics, an erratum seems the most probable cause for the revealed discrepancy. Subsequently, these other theoretical expressions are derived, starting from the correct expression (A.34).

As mentioned previously, equation (A.19) represents the assumption of stent ends fixed against rotation:

$$D = \frac{D_0 \, \cos \beta}{\cos \beta_0} \tag{A.35}$$

Equation (A.35) represents the actual mean stent diameter, consequently the corresponding outer stent diameter is:

$$D_e = D + 2 \, d \tag{A.36}$$

The stent is a combination of n braided helices, therefore equation (A.11) has to be adapted for a new wire length:

$$l_w = n \, c \, l_p = n \, c \, \frac{\pi \, D}{\cos \beta} \tag{A.37}$$

The axial elongation δ (equation (A.13)), due to the stent loading, is:

$$\delta = \frac{\pi c D_0}{\cos \beta_0} \left(\sin \beta - \sin \beta_0 \right) \tag{A.38}$$

As the stent ends are fixed against rotation, the elongation can also be defined as follows (see Figure 4.2):

$$\delta = L - L_0$$
$$\delta = c \, p - c \, p_0$$
$$\delta = c \, \pi (D \tan \beta - D_0 \tan \beta_0)$$
$$\delta = c \, \pi \left(\frac{D \, \sin \beta}{\cos \beta} - \frac{D_0 \, \sin \beta_0}{\cos \beta_0} \right)$$

$$eq.(A.35) \quad \Bigg\Downarrow \quad \frac{D}{\cos \beta} = \frac{D_0}{\cos \beta_0}$$

$$\delta = \frac{\pi c \, D_0}{\cos \beta_0} \left(\sin \beta - \sin \beta_0 \right) \tag{A.39}$$

With c the number of coils[2] defined by:

$$c = L_0 / p_0 \tag{A.40}$$

Reformulation of equation (A.13) leads to the following expression for the new stent length L:

$$L = L_0 + \delta$$
$$L = L_0 + \frac{\pi c D_0}{\cos \beta_0} (\sin \beta - \sin \beta_0) \tag{A.41}$$

A.2.2   Radial compression analysis

Consider a section of the stent of length L and diameter D loaded with an axial force F. Under the action of the load F, the stent extends by an incremental length dL requiring energy dW given by:

$$dW = F \cdot dL = F \cdot d(L_0 + \delta) = F \cdot d\delta \tag{A.42}$$

The same deflection δ may be produced by a radial pressure p_{outer} applied to an imaginary membrane around the stent, acting over the instantaneous surface area of the stent, $\pi D L$. This compresses the stent by a radial amount $dD/2$, thus:

$$dW = p_{outer} \, \pi \, D \, L \cdot \frac{dD}{2} \tag{A.43}$$

Combining equations (A.42) and (A.43) yields a formulation of p_{outer} in terms of F:

$$p_{outer} = \frac{2\,F}{\pi D\,L} \cdot \frac{d\delta}{dD} = \frac{2\,F}{\pi D\,L} \cdot \frac{d\delta}{d\beta} \cdot \frac{d\beta}{dD} \tag{A.44}$$

---

[2]Depending on the types of the spring ends, Wahl [136] proposes a correction factor to determine the number of active coils.

- $\frac{\mathrm{d}\delta}{\mathrm{d}\beta}$ is derived from equation (A.39):

$$\frac{\mathrm{d}\delta}{\mathrm{d}\beta} = \frac{\pi\,c\,D_0}{\cos\beta_0} \cdot \frac{\mathrm{d}}{\mathrm{d}\beta}\,(\sin\beta - \sin\beta_0) \tag{A.45}$$

$$\frac{\mathrm{d}\delta}{\mathrm{d}\beta} = \frac{\pi\,c\,D_0}{\cos\beta_0} \cdot \cos\beta \tag{A.46}$$

- $\frac{\mathrm{d}\beta}{\mathrm{d}D}$ is derived from equation (A.35):

$$\frac{\mathrm{d}D}{\mathrm{d}\beta} = \frac{D_0}{\cos\beta_0} \cdot (-\sin\beta) \tag{A.47}$$

$$\frac{\mathrm{d}\beta}{\mathrm{d}D} = -\frac{\cos\beta_0}{D_0} \cdot \frac{1}{\sin\beta} \tag{A.48}$$

Substituting the above-mentioned in equation (A.44):

$$p_{\text{outer}} = \frac{2\,F}{\pi\,D\,L} \cdot \frac{\pi\,c\,D_0}{\cos\beta_0} \cdot \cos\beta \cdot \left(-\frac{\cos\beta_0}{D_0} \cdot \frac{1}{\sin\beta}\right) \tag{A.49}$$

So:

$$p_{\text{outer}} = -\frac{2\,F\,c}{D\,L\,\tan\beta} \tag{A.50}$$

A.2.3   Stent stiffness and wire surface ratio

- The longitudinal stiffness K_L of the stent is defined by:

$$K_L = \frac{\mathrm{d}F}{\mathrm{d}L} = \frac{\mathrm{d}F}{\mathrm{d}\delta} = \frac{\mathrm{d}F}{\mathrm{d}\beta} \cdot \frac{\mathrm{d}\beta}{\mathrm{d}\delta} \tag{A.51}$$

since $\mathrm{d}L = \mathrm{d}\delta$ and both F and δ are explicit functions of β, K_L is defined as:

$$K_L = \frac{2n}{K_3\,\pi\,c\,\cos\beta}\left[\frac{GI_p}{K_3}\left(\frac{2\cos\beta}{K_3}\right) - \frac{EI}{K_3}\left(\frac{2\cos\beta}{K_3} - \frac{K_2}{\cos^2\beta}\right)\right] \tag{A.52}$$

- Analogously, the radial pressure stiffness K_p is:

$$K_p = \frac{dp_{outer}}{dD} = \frac{dp_{outer}}{d\beta} \cdot \frac{d\beta}{dD} \qquad (A.53)$$

so the radial stiffness K_p is defined by:

$$K_p = \frac{2c}{K_3 \sin\beta \, (D \, L \, \tan\beta)^2} \left[2DLn \, \tan\beta \left(\frac{GI_p}{K_3} \left(\frac{2 \, \cos\beta}{K_3} \right) - \right. \right.$$
$$\frac{EI}{K_3} \left(\frac{2 \, \cos\beta}{K_3} - K_2 \sec^2\beta \right) \Big) - F \left(\frac{DL}{\cos^2\beta} + \right.$$
$$\left. \left. K_3 \sin\beta \, (\pi c \, D - L \, \tan\beta) \right) \right] \qquad (A.54)$$

- Ratio of wire area to virtual cylindrical surface μ (see Figure A.6):
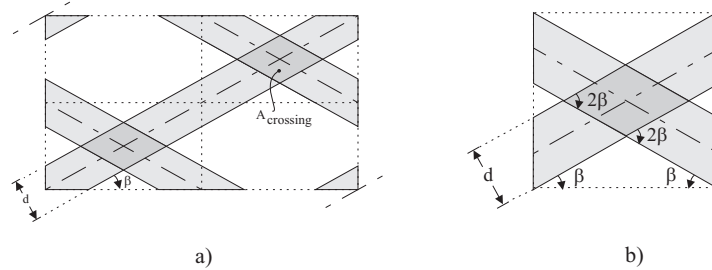
Figure A.6: Crossing stent wires and determination of cross sectional area $A_{crossing}$ (longitudinal spring axis vertical).

The ratio of wire area of the stent to the virtual cylinder surface μ is a suitable criterion to quantify the wire mesh density and is related to the area of the wire stent which is in contact with the target vessel.

μ is defined by the intersection of the mean (virtual) cylindrical area ($A_{cylinder}$) and the stent wires ($l_w d$) minus the area of intersection at each wire crossing point (this area of intersection is assumed to be the projected area $A_{crossing}$ (see Figure A.6). $A_{crossing}$ is defined as the

area of a rhombus with sides equal to $\frac{d}{\sin 2\beta}$ and height d. The number of intersections N in a given stent is found by dividing the stent into transverse slices which intersect the wire crossing points. Each slice therefore contains $n/2$ intersections, with n the number of stent wires and the axial distance between the slices is defined as d_{axial}.

$$A_{\text{cylinder}} = \pi D L \tag{A.55}$$

$$A_{\text{crossing}} = d \cdot \frac{d}{\sin 2\beta} = \frac{d^2}{\sin 2\beta} \tag{A.56}$$

$$d_{\text{axial}} = \frac{p}{n/2} = \frac{\pi D \tan \beta}{n/2} \tag{A.57}$$

Consequently, the number of intersections N is:

$$N = \frac{L}{d_{\text{axial}}} = \frac{2L}{n\pi D \tan \beta} \tag{A.58}$$

so the wire surface ratio μ is defined as:

$$\mu = \frac{L_w d - N A_{\text{crossing}}}{A_{\text{cylinder}}} \tag{A.59}$$

$$\mu = \frac{L_w d - \frac{N d^2}{\sin 2\beta}}{\pi D L} \tag{A.60}$$

Appendix B

WireStent_Demo.py script

Script B.1: WireStent_Demo.py

```
1   #!/usr/bin/env python pyformex.py
2   # $Id$
3   #
4   # This file is part of pyFormex 0.5 Release Fri Aug 10
5   # 12:04:07 2007 pyFormex is a Python implementation of
6   # Formex algebra
7   # Website: http://pyformex.berlios.de/
8   # Copyright (C) Benedict Verhegghe
9   # (benedict.verhegghe@ugent.be)
10  #
11  # This program is distributed under the GNU General Public
12  # License version 2 or later (see file COPYING for details)
13  #
14  """Wire Stent Demo"""
15  #
16  # This Demo − developed by Matthieu De Beule − is intended
17  # for educational purposes by rewriting the WireStent.py
18  # example and adding lots of drawing instructions and
19  # comments. More details regarding the used definitions
20  # can be found in the Pyformex reference manual.
21  ##
22
23  # needed if we import this from another script
24  from formex import *
25
26  class DoubleHelixStent:
27      """Constructs a double helix wire stent.
28
29      A stent is a tubular shape such as used for opening
30      obstructed (blood) vessels. This stent is made from
31      sets of wires spiraling in two directions.
32      The geometry is defined by the following parameters:
33        L  : length of the stent
34        De : external diameter of the stent
35        D  : average stent diameter
36        d  : wire diameter
37        be : pitch angle (degrees)
38        p  : pitch
39        nx : number of wires in one spiral set
40        ny : number of modules in axial direction
41        ds : extra distance between the wires (default is
```

```
42                    0.0 for touching wires)
43          dz : maximal distance of wire center to average
44                  cylinder
45          nb : number of elements in a strut (a part of a
46                  wire between two crossings), default 4
47     The stent is created around the z-axis.
48     By default, there will be connectors between the wires
49     at each crossing. They can be switched off in the
50     constructor.
51     The returned formex has one set of wires with property
52     1, the other with property 3. The connectors have
53     property 2. The wire set with property 1 is winding
54     positively around the z-axis.
55     """
56     def __init__(self, De, L, d, nx, be, ds=0.0, nb=4,
57                           connectors=True):
58         """Create the Wire Stent."""
59         D = De - 2*d - ds
60         r = 0.5*D
61         dz = 0.5*(ds+d)
62         p = math.pi*D*tand(be)
63         nx = int(nx)
64         ny = int(round(nx*L/p))  # The actual length may
65                     differ a bit from L
66         # a single bumped strut, oriented along the
67         #        x-axis
68         bump_z=lambda x: 1.-(x/nb)**2
69         A=Formex(pattern('1'),3)
70         GD.message("This Demo is intended for educational
71                     purposes by rewriting the WireStent.py
72                     example and adding lots of drawing
73                     instructions and comments. More details
74                     regarding the used definitions can be found
75                     in the Pyformex reference manual.")
76         GD.message("\nStep 1: Create a Formex: a line of
77                     length 1 (with property 3) oriented along
78                     the X-axis
79             A = Formex(pattern('1'),3)")
80         draw(A, view='bottom')
81         pause()
82         B=Formex(A.replic(nb,1.0),1)
83         GD.message("Step 2: Copy the Formex nb times in
84                     the X(0)-direction
85             B = Formex(A.replic(nb,1.0),1)")
86         draw(B, view='last')
87         pause()
88         clear()
89         base = Formex(B.bump1(2,[0.,0.,dz],bump_z,0),1)
90         GD.message("Step 3: Create a bump in the Z(2)-
91                     direction
92             base = Formex(B.bump1(2,[0.,0.,dz],bump_z,0)
93                     ,1)")
94         draw(base, view='last')
95         pause()
96         clear()
97         # scale back to size 1.
98         base = base.scale([1./nb,1./nb,1.])
99         GD.message("Step 4: Rescale the base line to
100                    size 1
101            base = base.scale([1./nb,1./nb,1.])")
102        draw(base, view='last')
103        pause()
104        clear()
105        # NE and SE directed struts
106        NE = base.shear(1,0,1.)
107        NE.setProp(1)
108        GD.message("Step 5: Skew the base line to NE-
```

```
109                    direction
110                    NE = base.shear(1,0,1.)")
111           # The nxt two lines serve to rotate the camera up
112              #      over 30°, i.e. 6 times the rotUp definition
113              #      from cameraMenu
114           GD.canvas.camera.rotate(30,1,0,0)
115           GD.canvas.update()
116           draw(NE)
117           pause()
118           clear()
119           SE = base.reflect(2).shear(1,0,-1.)
120           SE.setProp(3)
121           GD.message("Step 6: Create a mirrored base line
122                    and skew it to SE-direction
123                    SE = base.reflect(2).shear(1,0,-1.)")
124           draw(SE,view='last')
125           pause()
126           clear()
127           cell=(NE+SE)
128           GD.message("Step 7: Create the base cell by
129                    combining the NE and SE formices
130                    cell = (NE+SE)")
131           draw(cell,view='last')
132           pause()
133           clear()
134           # a unit cell of crossing struts
135           cell1 = (cell).rosette(2,180)
136           GD.message("Step 8: Create the base module
137                    (cell1) of two crossing wires by replicating
138                    the base cell by an angular rotation
139                    cell1 = (cell).rosette(2,180)")
140           draw(cell1,view='last')
141           pause()
142           clear()
143           # add a connector between first points of NE
144                    and SE
145           if connectors:
146               cell1 += Formex([[NE[0][0],SE[0][0]]],2)
147           GD.message("Step 9: Add a connector between the
148                    first points of NE and SE of the base module
149                    cell1 += Formex([[NE[0][0],SE[0][0]]],2)")
150           draw(cell1,view='last')
151           pause()
152           clear()
153           # and create its mirror
154           cell2 = cell1.reflect(2)
155           GD.message("Step 10: Create a mirror in Z(2)-
156                    direction of the base module
157                    cell2 = cell1.reflect(2)")
158           draw(cell2,view='last')
159           pause()
160           clear()
161           # and move both to appropriate place
162           self.cell1 = cell1.translate([1.,1.,0.])
163           self.cell2 = cell2.translate([-1.,-1.,0.])
164           # the base pattern cell1+cell2 now has size
165              #     [-2,-2]..[2,2]
166           # Create the full pattern by replication
167           dx = 4.
168           dy = 4.
169           module=(self.cell1+self.cell2)
170           GD.message("Step 11: Extend the base module with
171                    its mirrored and translated copy
172                    module = (self.cell1+self.cell2)")
173           draw(module,view='last')
174           pause()
175           clear()
```

```
176            F = module.replic2(nx,ny,dx,dy)
177            GD.message("Step 12: Replicate the base module in
178                  both directions of the base plane
179               F = module.replic2(nx,ny,dx,dy)")
180            draw(F,view='last')
181            pause()
182            clear()
183            # fold it into a cylinder
184            C=F.translate([0.,0.,r])
185            GD.message("Step 13: Translate the full patern
186                  over the stent radius in Z-direction
187               C=F.translate([0.,0.,r])")
188            draw(C,view='last')
189            pause()
190            clear()
191            self.F = C.cylindrical(dir=[2,0,1],
192                  scale=[1.,360./(nx*dx),p/nx/dy])
193            GD.message("Step 14: Roll the nearly planar grid
194                  into a cylinder
195               self.F = C.cylindrical(dir=[2,0,1]
196                  ,scale=[1.,360./(nx*dx),p/nx/dy])")
197            draw(self.F,view='front')
198            pause()
199            clear()
200            draw(self.F,view='left')
201            pause()
202            clear()
203            self.ny = ny
204
205      def all(self):
206            """Return the Formex with all bar elements."""
207            return self.F
208
209
210  if __name__ == "draw":
211
212      # show an example
213  #   The following default values are obtained from Jedwab
214  #        and Clerc (except for L=87.5 and b=30.85)
215      D = 16.71
216      L = 40.
217      d = 0.22
218      n = 12
219      b = 40
220      res = askItems([['Diameter',D],['Length',L],
221                  ['WireDiam',d],['NWires',n],['Pitch',b]])
222      D = float(res['Diameter'])
223      L = float(res['Length'])
224      d = float(res['WireDiam'])
225      n = int(res['NWires'])
226      b = float(res['Pitch'])
227
228      H = DoubleHelixStent(D,L,d,n,b).all()
229      draw(H,view='iso')
```

List of Figures

List of Tables

List of scripts

Bibliography

[1] F. Auricchio, M. Di Loreto, and E. Sacco. Finite element analysis of a stenotic artery revascularization through a stent insertion. *Computer Methods in Biomechanics and Biomedical Engineering*, 4: 249–263, 2001.

[2] G. A. Holzapfel, C. A. J. Schulze-Bauer, and M. Stadler. Mechanics of angioplasty: wall, balloon and stent. *Mechanics in Biology - AMD-Vol. 242 and BED-Vol. 46*, pages 141–156, 2000.

[3] F. Migliavacca, L. Petrini, M. Colombo, F. Auricchio, and R. Pietrabissa. Mechanical behavior of coronary stents investigated through the finite element method. *J Biomech*, 35(6):803–811, Jun 2002.

[4] L. H. Timmins, M. R. Moreno, C. A. Meyer, J. C. Criscione, A. Rachev, and J. E. Jr Moore. Stented artery biomechanics and device design optimization. *Med Biol Eng Comput*, 45(5):505–513, May 2007.

[5] F. Migliavacca, L. Petrini, V. Montanari, I. Quagliana, F. Auricchio, and G. Dubini. A predictive study of the mechanical behaviour of coronary stents by computer modelling. *Med Eng Phys*, 27(1):13–18, Jan 2005.

[6] Wikipedia: artery. `http://en.wikipedia.org/wiki/Artery`.

[7] R. Ross. Atherosclerosis–an inflammatory disease. *N. Engl. J. Med.*, 340:115–126, 1999.

[8] G.K. Hansson. Inflammation, atherosclerosis, and coronary artery disease. *N. Engl. J. Med.*, 352:1685–1695, 2005.

[9] R.J. Esper, R.A. Nordaby, J.O. Vilariño, A. Paragano, J.L. Cacharrón, and R.A. Machado. Endothelial dysfunction: a comprehensive appraisal. *Cardiovasc Diabetol*, 5:4, 2006.

[10] G.M. Chisolm and D. Steinberg. The oxidative modification hypothesis of atherogenesis: an overview. *Free Radic. Biol. Med.*, 28:1815–1826, Jun 2000.

[11] A. Tedgui and Z. Mallat. Cytokines in atherosclerosis: pathogenic and regulatory pathways. *Physiol. Rev.*, 86:515–581, Apr 2006.

[12] S. Glagov, E. Weisenberg, C.K. Zarins, R. Stankunavicius, and G.J. Kolettis. Compensatory enlargement of human atherosclerotic coronary arteries. *N. Engl. J. Med.*, 316:1371–1375, 1987.

[13] Atherosclerosis. `http://www.surrey.ac.uk`.

[14] J. Frohlich, M. Dobiasova, S. Lear, and K.W. Lee. The role of risk factors in the development of atherosclerosis. *Crit Rev Clin Lab Sci*, 38:401–440, Oct 2001.

[15] M. De Beule, E. Maes, O. De Winter, W. Vanlaere, and R. Van Impe. Artificial neural networks and risk stratification: A promising combination. *Mathematical and Computer Modelling*, doi:10.1016/j.mcm.2006.12.024, 2007.

[16] H.C. Stary, A.B. Chandler, R.E. Dinsmore, V. Fuster, S. Glagov, W. Insull, M.E. Rosenfeld, C.J. Schwartz, W.D. Wagner, and R.W. Wissler. A definition of advanced types of atherosclerotic lesions and a histological classification of atherosclerosis. A report from the Committee on Vascular Lesions of the Council on Arteriosclerosis, American Heart Association. *Circulation*, 92:1355–1374, Sep 1995.

[17] J.A. Schaar, F. Mastik, E. Regar, C.A. den Uil, F.J. Gijsen, J.J. Wentzel, P.W. Serruys, and A.F. van der Stehen. Current diagnostic modalities for vulnerable plaque detection. *Curr. Pharm. Des.*, 13: 995–1001, 2007.

[18] S. Waxman, F. Ishibashi, and J.E. Muller. Detection and treatment of vulnerable plaques and vulnerable patients: novel approaches to prevention of coronary events. *Circulation*, 114:2390–2411, Nov 2006.

[19] C.J. Mullany. Cardiology patient pages. Coronary artery bypass surgery. *Circulation*, 107:e21–22, 2003.

[20] MedicineNet. `http://www.medicinenet.com/coronary_artery_bypass_graft/page4.htm`.

[21] D.S. Baim and W Grossman. Complications of cardiac catherization. Cardiac catherization, Angiography and Intervention, Williams & Wilkins, Baltimore, pp. 17, 1996.

[22] B. Meier. The first patient to Undergo Coronary Angioplasty. *N. Engl. J. Med.*, 344(2):144–145, 2001.

[23] Website Taxus stent. `http://www.taxus-stent.com/usa/patient_coronary.html`.

[24] American Heart Association. Heart Disease and Stroke Statistics - 2007 Update. *Dallas, Texas: American Heart Association*, pages 1–43, 2007.

[25] D. E. Kandzari, J. E. Tcheng, and J. P. Zidar. Coronary artery stents: evaluating new designs for contemporary percutaneous intervention. *Catherization and Cardiovascular Interventions*, 56(4):562–576, Aug 2002.

[26] A. Kastrati, J. Mehilli, J. Dirschinger, J. Pache, K. Ulm, H. Schuhlen, M. Seyfarth, C. Schmitt, R. Blasini, F. J. Neumann, and A. Schomig. Restenosis after coronary placement of various stent types. *Am J Cardiol*, 87(1):34–39, Jan 2001.

[27] A. C. Morton, D. Crossman, and J. Gunn. The influence of physical stent parameters upon restenosis. *Pathol Biol (Paris)*, 52(4):196–205, 2004.

[28] C. Rogers, D. Y. Tseng, J. C. Squire, and E. R. Edelman. Balloon-artery interactions during stent placement: a finite element analysis approach to pressure, compliance, and stent design as contributors to vascular injury. *Circ Res*, 84(4):378–383, Mar 1999.

[29] A. O. Frank, P. W. Walsh, and James E. Jr Moore. Computational fluid dynamics and stent design. *Artif Organs*, 26(7):614–621, Jul 2002.

[30] M. C. Morice, P. W. Serruys, J. E. Sousa, J. Fajadet, E. Ban Hayashi, M. Perin, A. Colombo, G. Schuler, P. Barragan, G. Guagliumi, F. Molnar, and R. Falotico. A randomized comparison of a sirolimus-eluting stent with a standard stent for coronary revascularization. *N Engl J Med*, 346(23):1773–1780, Jun 2002.

[31] J. E. Sousa, M. A. Costa, A. Abizaid, F. Feres, A. C. Seixas, L. F. Tanajura, L. A. Mattos, R. Falotico, J. Jaeger, J. J. Popma, P. W. Serruys, and A. G. M. R. Sousa. Four-year angiographic and intravascular ultrasound follow-up of patients treated with sirolimus-eluting stents. *Circulation*, 111(18):2326–2329, May 2005.

[32] P. W. Serruys, M. J. B. Kutryk, and A. T. L. Ong. Coronary-artery stents. *N Engl J Med*, 354(5):483–495, Feb 2006.

[33] A. Farb, G. Sangiorgi, A. J. Carter, V. M. Walley, W. D. Edwards, R. S. Schwartz, and R. Virmani. Pathology of acute and chronic coronary stenting in humans. *Circulation*, 99(1):44–52, 1999.

[34] Y. Ikari, K. Hara, T. Tamura, F. Saeki, and T. Yamaguchi. Luminal loss and site of restenosis after palmaz-schatz coronary stent implantation. *The American journal of cardiology*, 76(3):117–120, 1995.

[35] J.C. Squire. *Dynamics of Endovascular Stent Expansion.* PhD thesis, Massachusetts Institute of Technology, US, 2000.

[36] H. Takebayashi, G. S. Mintz, S. G. Carlier, Y. Kobayashi, K. Fujii, T. Yasuda, R. A. Costa, I. Moussa, G. D. Dangas, R. Mehran, A. J. Lansky, E. Kreps, M. B. Collins, A. Colombo, G. W. Stone, M. B. Leon, and J. W. Moses. Nonuniform strut distribution correlates with more neointimal hyperplasia after sirolimus-eluting stent implantation. *Circulation*, 110(22):3430–3434, 2004.

[37] C. W. Hwang, D. Wu, and E. R. Edelman. Physiological transport forces govern drug distribution for stent-based delivery. *Circulation*, 104(5):600–605.

[38] C. Kaiser, H. P. Brunner-La Rocca, P. T. Buser, P. O. Bonetti, S. Osswald, A. Linka, A. Bernheim, A. Zutter, M. Zellweger, L. Grize, and M. E. Pfisterer. Incremental cost-effectiveness of drug-eluting stents compared with a third-generation bare-metal stent in a real-world setting: randomised Basel Stent Kosten Effektivitats Trial (BASKET). *Lancet*, 366(9489):921–929, Sep 2005.

[39] R. Virmani, G. Guagliumi, A. Farb, G. Musumeci, N. Grieco, T. Motta, L. Mihalcsik, M. Tespili, O. Valsecchi, and F. D. Kolodgie. Localized hypersensitivity and late coronary thrombosis secondary to a sirolimus-eluting stent: should we be cautious? *Circulation*, 109(6): 701–705, Feb 2004.

[40] R. Balossino. *A computational study of minimally-invasive devices for the treatment of coronary disease.* PhD thesis, Politecnico di Milano, I, 2007.

[41] H.B. Barner. Status of percutaneous coronary intervention and coronary artery bypass. *Eur J Cardiothorac Surg*, 30:419–424, 2006.

[42] F. Eefting, H. Nathoe, D. van Dijk, E. Jansen, J. Lahpor, P. Stella, W. Suyker, J. Diephuis, H. Suryapranata, S. Ernst, C. Borst, E. Buskens, D. Grobbee, and P. de Jaegere. Randomized comparison between stenting and off-pump bypass surgery in patients referred for angioplasty. *Circulation*, 108:2870–2876, Dec 2003.

[43] C. Lally, P.J. Prendergast, and D. Kelly. Stents. Wiley Encyclopaedia of Biomedical Engineering, John Wiley & Sons.

[44] F. Auricchio. *Shape-memory alloys: applications, micromechanics, macromodelling and numerical simulations.* PhD thesis, University of California at Berkeley, US, 1995.

[45] R. Wang and K. Ravi-Chandar. Mechanical response of a metallic aortic stent - Part II: A beam on elastic foundation model. *J Appl Mech*, 71:706–712, 2004.

[46] R. Morgan and A. Adam. Use of metallic stents and balloons in the esophagus and gastrointestinal tract. *J Vasc Interv Radiol*, 12(3): 283–297, 2001.

[47] E. M. Walser, B. Robinson, S. A. Raza, O. S. Ozkan, E. Ustuner, and J. Zwischenberger. Clinical outcomes with airway stents for proximal versus distal malignant tracheobronchial obstructions. *J Vasc Interv Radiol*, 15(5):471–477, May 2004.

[48] M. Hussain, T. J Greenwell, J. Shah, and A. Mundy. Long-term results of a self-expanding wallstent in the treatment of urethral stricture. *BJU International*, 94(7):1037–1039, 2004.

[49] I. Borisch, O. W Hamer, N. Zorger, S. Feuerbach, and J. Link. In vivo evaluation of the carotid wallstent on three-dimensional contrast material-enhanced MR angiography: influence of artifacts on the visibility of stent lumina. *J Vasc Interv Radiol*, 16(5):669–677, May 2005.

[50] C. P. Saad, S. Murthy, G. Krizmanich, and A. C. Mehta. Self-expandable metallic airway stents and flexible bronchoscopy: long-term outcomes analysis. *Chest*, 124(5):1993–1999, Nov 2003.

[51] A.J. Narracott. *Balloon folding pattern affects the symmetry of stent expansion: Experimental and computational evidence.* PhD thesis, University of Sheffield, UK, 2001.

[52] R. Rieu, P. Barragan, V. Garitey, P.O. Roquebert, J. Fuseri, P. Commeau, and J. Sainsous. Assessment of the trackability, flexibility, and conformability of coronary stents: a comparative analysis. *Catheter Cardiovasc Interv*, 59:496–503, Aug 2003.

[53] T.C. Poerner, B. Ludwig, S.H. Duda, P. Diesing, G. Kalmár, T. Süselbeck, J.J. Kaden, M. Borggrefe, and K.K. Haase. Determinants of stent expansion in curved stenotic lesions: an in vitro experimental study. *J Vasc Interv Radiol*, 15:727–735, Jul 2004.

[54] J.A. Ormiston, E. Currie, M.W. Webster, P. Kay, P.N. Ruygrok, J.T. Stewart, R.C. Padgett, and M.J. Panther. Drug-eluting stents for coronary bifurcations: insights into the crush technique. *Catheter Cardiovasc Interv*, 63:332–336, 2004.

[55] M. Perry, S. Oktay, and J. C. Muskivitch. Finite element analysis and fatigue of stents. *Min Invas Ther and Allied Technol*, 11(4):165–171, 2002.

[56] Website pyFormex. `http://pyFormex.berlios.de`.

[57] L. Lanoye. *Fluid-Structure Interaction of Blood Vessels*. PhD thesis, Ghent University, B, 2007.

[58] J. Mackerle. Finite element modelling and simulations in cardiovascular mechanics and cardiology: a bibliography 1993-2004. *Comput Methods Biomech Biomed Engin*, 8(2):59–81, Apr 2005.

[59] FDA Center for Devices and Radiological Health, Non Clinical Tests and Recommended Labeling for Intravascular Stents and Associated Delivery Systems - Guidance for Industry and FDA Staff. pages 1–48, Jan 2005.

[60] Website Ghent University Centre for X-ray Tomography (UGCT). `http://www.UGCT.UGent.be`.

[61] M.A. Saab. Applications of high-pressure balloons in the medical device industry. *Medical Device & Diagnostic Industry Magazine, NH, USA (1999)*, 1999.

[62] G. Mani, M. D. Feldman, D. Patel, and C M. Agrawal. Coronary stents: a materials perspective. *Biomaterials*, 28(9):1689–1710, 2007.

[63] B. P. Murphy, P. Savage, P. E. McHugh, and D. F. Quinn. The stress-strain behavior of coronary stent struts is size dependent. *Ann Biomed Eng*, 31(6):686–691, Jun 2003.

[64] C Dumoulin and B Cochelin. Mechanical behaviour modelling of balloon-expandable stents. *J Biomech*, 33(11):1461–1470, Nov 2000.

[65] F. Etave, G. Finet, M. Boivin, J. C. Boyer, G. Rioufol, and G. Thollet. Mechanical properties of coronary stents determined by using finite element analysis. *J Biomech*, 34(8):1065–1075, Aug 2001.

[66] J.P. McGarry, B.P. O'Donnell, P.E. McHugh, and McGarry J.G. Analysis of the mechanical performance of a cardiovascular stent design based on micromechanical modelling. *Computational Materials Science*, 31:421–438, 2004.

[67] L. Gu, S. Santra, R. A. Mericle, and A. V. Kumar. Finite element analysis of covered microstents. *J Biomech*, 38(6):1221–1227, Jun 2005.

[68] G. A. Holzapfel, M. Stadler, and T. C. Gasser. Changes in the mechanical environment of stenotic arteries during interaction with stents: computational assessment of parametric stent designs. *J Biomech Eng*, 127(1):166–180, Feb 2005.

[69] M. De Beule, R. Van Impe, B. Verhegghe, P. Segers, and P. Verdonck. Finite element analysis and stent design: Reduction of dogboning. *Technol Health Care*, 14(4-5):233–241, 2006.

[70] J. Bedoya, C. A. Meyer, L. H. Timmins, M. R. Moreno, and J. E. Moore. Effects of stent design parameters on normal artery wall mechanics. *J Biomech Eng*, 128(5):757–765, Oct 2006.

[71] C. Lally, F. Dolan, and P. J. Prendergast. Cardiovascular stent design and vessel stresses: a finite element analysis. *J Biomech*, 38(8):1574–1581, Aug 2005.

[72] G. A. Holzapfel, M. Stadler, and C. A. J. Schulze-Bauer. A layer-specific three-dimensional model for the simulation of balloon angioplasty using magnetic resonance imaging and mechanical testing. *Ann Biomed Eng*, 30(6):753–767, Jun 2002.

[73] D. K. Liang, D. Z. Yang, M. Qi, and W. Q. Wang. Finite element analysis of the implantation of a balloon-expandable stent in a stenosed artery. *Int J Cardiol*, 104(3):314–318, Oct 2005.

[74] P. D. Ballyk. Intramural stress increases exponentially with stent diameter: a stress threshold for neointimal hyperplasia. *J Vasc Interv Radiol*, 17(7):1139–1145, Jul 2006.

[75] R. V. Marrey, R. Burgermeister, R. B. Grishaber, and R. O. Ritchie. Fatigue and life prediction for cobalt-chromium stents: A fracture mechanics analysis. *Biomaterials*, 27(9):1988–2000, Mar 2006.

[76] G. J. Hall and E. P. Kasper. Comparison of element technologies for modeling stent expansion. *J Biomech Eng*, 128(5):751–756, Oct 2006.

[77] W. Q. Wang, D. K. Liang, D. Z. Yang, and M. Qi. Analysis of the transient expansion behavior and design optimization of coronary stents by finite element method. *J Biomech*, 39(1):21–32, 2006.

[78] K. Takashima, T. Kitou, K. Mori, and K. Ikeuchi. Simulation and experimental observation of contact conditions between stents and artery models. *Med Eng Phys*, 29(3):326–335, Apr 2007.

[79] W. Wu, W. Q. Wang, D. Z. Yang, and M. Qi. Stent expansion in curved vessel and their interactions: A finite element analysis. *J Biomech, doi:10.1016/j.jbiomech.2006.11.009 (2007)*, Jan .

[80] M. De Beule, P. Mortier, S.G. Carlier, B. Verhegghe, R. Van Impe, and P. Verdonck. Realistic finite element-based stent design: The impact of balloon folding. *J Biomech*, 41:383–389, 2008.

[81] L. B. Tan, D. C. Webb, K. Kormi, and S. T. Al-Hassani. A method for investigating the mechanical properties of intracoronary stents using finite element numerical simulation. *Int J Cardiol*, 78(1):51–67, Mar 2001.

[82] P. J. Prendergast, C. Lally, S. Daly, A. J. Reid, T. C. Lee, D. Quinn, and F. Dolan. Analysis of prolapse in cardiovascular stents: a constitutive equation for vascular tissue and finite-element modelling. *J Biomech Eng*, 125(5):692–699, Oct 2003.

[83] L. Petrini, F. Migliavacca, F. Auricchio, and G. Dubini. Numerical investigation of the intravascular coronary stent flexibility. *J Biomech*, 37(4):495–501, Apr 2004.

[84] K. Mori and T. Saito. Effects of stent structure on stent flexibility measurements. *Ann Biomed Eng*, 33(6):733–742, Jun 2005.

[85] P. Savage, B. P. O'Donnell, P. E. McHugh, B. P. Murphy, and D. F. Quinn. Coronary stent strut size dependent stress-strain response investigated using micromechanical finite element models. *Ann Biomed Eng*, 32(2):202–211, Feb 2004.

[86] F.D. Whitcher. Simulation of in vivo loading conditions of nitinol vascular stent structures. *Computers & Structures*, 64(5/6):1005–1011, 1997.

[87] F. Migliavacca, L. Petrini, P. Massarotti, S. Schievano, F. Auricchio, and G. Dubini. Stainless and shape memory alloy coronary stents: a computational study on the interaction with the vascular wall. *Biomech Model Mechanobiol*, 2(4):205–217, Jun 2004.

[88] L. Petrini, F. Migliavacca, P. Massarotti, S. Schievano, G. Dubini, and F. Auricchio. Computational studies of shape memory alloy behavior in biomedical applications. *J Biomech Eng*, 127(4):716–725, Aug 2005.

[89] P. Theriault, P. Terriault, V. Brailovski, and R. Gallo. Finite element modeling of a progressively expanding shape memory stent. *J Biomech*, 39(15):2837–2844, 2006.

[90] W. Wu, M. Qi, X. P. Liu, D. Z. Yang, and W. Q. Wang. Delivery and release of nitinol stent in carotid artery and their interactions: A finite element analysis. *J Biomech, doi:10.1016/j.jbiomech.2007.02.024 (2007)*, May .

[91] A. R. Assali, S. Sdringola, A. Moustapha, M. Rihner, A. E. Denktas, M. A. Lefkowitz, M. Campbell, and R. W. Smalling. Endovascular repair of traumatic pseudoaneurysm by uncovered self-expandable stenting with or without transstent coiling of the aneurysm cavity. *Catheter Cardiovasc Interv*, 53(2):253–258, Jun 2001.

[92] S. Resnick, V. Rome, and R. Vogelzang. Use of a partially deployed wallstent to act as an inferior vena cava filtration device during coil embolization of a high-flow arteriovenous fistula. *J Vasc Interv Radiol*, 17(2 Pt 1):369–372, Feb 2006.

[93] M. R. Jedwab and C. O. Clerc. A study of the geometrical and mechanical properties of a self-expanding metallic stent–theory and experiment. *J Appl Biomater*, 4(1):77–85, Spring 1993.

[94] R. Wang and K. Ravi-Chandar. Mechanical response of a metallic aortic stent - Part I: Pressure-diameter relationship. *J Appl Mech*, 71: 697–705, 2004.

[95] S. Canic, K. Ravi-Chandar, Z. Krajcer, D. Mirkovic, and S Lapin. Mathematical Model Analysis of Wallstent and AneuRx - Dynamic Responses of Bare-Metal Endoprosthesis Compared with Those of Stent-Graft. *Tex Heart Inst J*, 32(4):502–506, 2005.

[96] M. Brand, M. Ryvkin, S. Einav, and L. Slepyan. The Cardiocoil stent-artery interaction. *J Biomech Eng*, 127(2):337–344, Apr 2005.

[97] J. P. Nuutinen, C. Clerc, and P. Tormala. Theoretical and experimental evaluation of the radial force of self-expanding braided bioabsorbable stents. *J Biomater Sci Polym Ed*, 14(7):677–687, 2003.

[98] Y. He, N. Duraiswamy, A. O. Frank, and J. E. Jr Moore. Blood flow in stented arteries: a parametric comparison of strut design patterns in three dimensions. *J Biomech Eng*, 127(4):637–647, Aug 2005.

[99] J. F. Jr LaDisa, L. E. Olson, I. Guler, D. A. Hettrick, J. R. Kersten, D. C. Warltier, and P. S. Pagel. Circumferential vascular deformation after stent implantation alters wall shear stress evaluated with time-dependent 3D computational fluid dynamics models. *J Appl Physiol*, 98(3):947–957, Mar 2005.

[100] N. Benard, R. Perrault, and D. Coisne. Computational approach to estimating the effects of blood properties on changes in intra-stent flow. *Ann Biomed Eng*, 34(8):1259–1271, Aug 2006.

[101] B. Balakrishnan, A. R. Tzafriri, P. Seifert, A. Groothuis, C. Rogers, and E. R. Edelman. Strut position, blood flow, and drug deposition: implications for single and overlapping drug-eluting stents. *Circulation*, 111(22):2958–2965, Jun 2005.

[102] M. Gay, L. Zhang, and W. K. Liu. Stent modeling using immersed finite element method. *Comput Methods Appl Mech Engrg*, 195:4358–4370, 2006.

[103] H. Müller. Development of metallic bioabsorbable intravascular implants. ESVB 2005, New Technologies in vascular biomaterials - Fundamentals about stents; eds. Chafke, N. and Durand, B. and Kretz, J.G., 2005.

[104] Website Ghent University Stent Research Unit. `http://www.stent-IBiTech.UGent.be`.

[105] Bonsignore D. Stoeckel and Duda. A survey of stent designs. *Minimally Invasive Therapy and Allied Technologies*, 11(4):137–147, 2002.

[106] P.A. Pedro A. Lemos, F. Saia, J. M.R. Ligthart, C. A. Arampatzis, G. Sianos, K. Tanabe, A. Hoye, M. Degertekin, J. Daemen, E. McFadden, S. Hofma, P. C. Smits, P. de Feyter, W. J. van der Giessen, R. T. van Domburg, and P. W. Serruys. Coronary Restenosis After Sirolimus-Eluting Stent Implantation: Morphological Description and Mechanistic Analysis From a Consecutive Series of Cases . *Circulation*, 108:257–260, 2003.

[107] S. Timoshenko. Strength of materials (part i: Elementary theory and problems). Van Nostrand Reinhold, New York, pp. 45, Chap. 2, 1955.

[108] Website efunda. `http://www.efunda.com`.

[109] Website The BumPer Cluster. `http://bumps.ugent.be/bumper/`.

[110] Engineer's handbook. `http://engineershandbook.com/`.

[111] J. Jr de Ribamar Costa, G. S. Mintz, S. G. Carlier, R. A. Costa, K. Fujii, K. Sano, M. Kimura, J. Lui, G. Weisz, I. Moussa, G. Dangas, R. Mehran, A. J. Lansky, E. M. Kreps, M. Collins, G. W. Stone, J. W. Moses, and M. B. Leon. Intravascular ultrasonic assessment of stent diameters derived from manufacturer's compliance charts. *Am J Cardiol*, 96(1):74–78, 2005.

[112] M. De Beule, P. Mortier, R. Van Impe, B. Verhegghe, P. Segers, and P. Verdonck. Plasticity in the Mechanical Behaviour of Cardiovascular Stents during Stent Preparation (crimping) and Placement (expansion). *Key Engineering Materials*, 340-341:847–852, 2007.

[113] P. Poncin and J. Proft. Stent tubing: understanding the desired attributes. *Proceedings of the Materials and Processes for Medical Devices Conference, Anaheim, USA*, 2003.

[114] A. Colombo, G. Stankovic, and J.W. Moses. Selection of coronary stents. *J Am Coll Cardiol*, 40(6):1021–33, 2002.

[115] A.M. Wahl. *Mechanical Springs, 2nd edition*, pages 241–254. 1963.

[116] A.M. Wahl. *Mechanical Springs, 2nd edition*, pages 56–59. 1963.

[117] Website GNU. `http://www.gnu.org/licenses/gpl.html`.

[118] J. B. Zwischenberger, G. R. Wittich, E. vanSonnenberg, R. F. Johnson, S. K. Alpard, S. K. Anand, and R. J. Morrison. Airway simulation to guide stent placement for tracheobronchial obstruction in lung cancer. *Ann Thorac Surg*, 64(6):1619–1625, Dec 1997.

[119] T. A. Ischinger. Carotid stenting: which stent for which lesion? *J Interv Cardiol*, 14(6):617–623, Dec 2001.

[120] Hibbit, Karlsson, and Sorensen. Abaqus manual 6.5.

[121] S. V. Lossef, R. J. Lutz, J. Mundorf, and K. H. Barth. Comparison of mechanical deformation properties of metallic stents with use of stress-strain analysis. *J Vasc Interv Radiol*, 5(2):341–349, 1994.

[122] T. P. Murphy. Comparing the SMART stent with the Wallstent iliac endoprosthesis: reading between the lines. *J Vasc Interv Radiol*, 15 (9):907–909, 2004.

[123] A. R. Pelton, J. DiCello, and S. Miyazaki. Self-expanding nitinol stents: material and design considerations. *Min. Invas. Ther. & Allied Tech.,*, 9(1):107–118, 2000.

[124] Website Argonne Optimization Technology Center. `http://www-fp.mcs.anl.gov/otc/guide/`.

[125] J. Lagarias, J. Reeds, M. Wright, and P. Wright. Convergence properties of the Nelder-Mead Simplex Method in Low Dimensions. *SIAM Journal on Optimization*, 9(1):112–147, 1998.

[126] Website Travis E. Oliphant's Modules to enhance Numerical Python. `http://www.pylab.sourceforge.net`.

[127] Wikipedia: Monte Carlo method. `http://en.wikipedia.org/wiki/Monte_Carlo_method`.

[128] Website Cardiatis. `http://www.cardiatis.com`.

[129] G. A. Holzapfel and D.E. Kiousis. Biomechanical characterization of the stented artery. Computational solid mechanical aspects. *New technologies in vascular biomaterials - Fundamentals about stents*, pages 11–23, 2007.

[130] C. Capelli, F. Gervaso, L. Petrini, S. Lattanzio, G. Dubini, and F. Migliavacca. Effects of different boundary conditions for the simulation of balloon-expandable stent expansion in free and confined configurations. *Proceedings of the European Society of Biomechanics Workshop, Dublin, Ireland*, pages 64–65, 2007.

[131] D. Laroche, S. Delorme, T. Anderson, and R. Diraddo. In-vivo validation of a stent implantation numerical model. *Stud Health Technol Inform*, 125:265–270, 2007.

[132] P. Mortier, M. De Beule, D. Van Loo, B. Verhegghe, and P. Verdonck. Improving side branch access during bifurcation stenting - a finite element study. *Proceedings of the European Society of Biomechanics Workshop, Dublin, Ireland*, pages 66–67, 2007.

[133] T. Connolley, D. Nash, J.Y. Buffière, F. Sharif, and P.E. McHugh. X-ray micro-tomography of a coronary stent deployed in a model artery. *Med Eng Phys*, 29:1132–1141, 2007.

[134] M. Auer, P. Regitnig, R. Stollberger, F. Ebner, and G.A. Holzapfel. A methodology to study the morphologic changes in lesions during in vitro angioplasty using MRI and image processing. *Med Image Anal*, 2007.

[135] D. Van Loo, B. Masschaele, M. De Beule, P. Mortier, B. Verhegghe, L. Van Hoorebeke, and P. Verdonck. The use of micro-CT imaging for finite element stent research. *Proceedings of the European Society of Biomechanics Workshop, Dublin, Ireland*, pages 100–101, 2007.

[136] A.M. Wahl. *Mechanical Springs, 2nd edition*, pages 63–68. 1963.

Publications

Publications in international journals

- M. De Beule, R. Van Impe, B. Verhegghe, P. Segers, and P. Verdonck. Finite element analysis and stent design: Reduction of dogboning, *Technology and Health care*, 14:233-241, 2006.

- M. De Beule, E. Maes, O. De Winter, W. Vanlaere, and R. Van Impe. Artificial neural networks and risk stratification: A promising combination. *Mathematical and Computer Modelling*, 46:88-94, 2007.

- M. De Beule, P. Mortier, J. Belis, R. Van Impe, B. Verhegghe, and P. Verdonck. Plasticity as a lifesaver in the design of Cardiovascular stents. *Key Engineering Materials*, 340-341:841-846, 2007.

- M. De Beule, P. Mortier, R. Van Impe, B. Verhegghe, P. Segers, and P. Verdonck. Plasticity in the mechanical behavior of cardiovascular stents during stent preparation (crimping) and placement (expansion). *Key Engineering Materials*, 340-341:847-852, 2007.

- M. De Beule, P. Mortier, S.G. Carlier, B. Verhegghe, R. Van Impe, and P. Verdonck. Realistic finite element-based stent design: The impact of balloon folding. *Journal of Biomechanics*, 41:383-389, 2008.

- P. Mortier, M. De Beule, S. G. Carlier, R. Van Impe, B. Verhegghe, and P. Verdonck. Numerical study of the uniformity of balloon-expandable stent deployment. *Journal of Biomechanical Engineering*, accepted for publication.

- M. De Beule, S. Van Cauter, P. Mortier, D. Van Loo, R. Van Impe, P. Verdonck, and B. Verhegghe. Virtual optimization of self-expandable braided wire stents. *Medical Engineering & Physics*, submitted.

- P. Mortier, M. De Beule, D. Van Loo, P. Verdonck, and B. Verhegghe. Finite element analysis of side branch access during bifurcation stenting. *Medical Engineering & Physics*, submitted.

- M. De Beule, B. Verhegghe, M. Conti, P. Mortier, R. Van Impe, F. Auricchio, and P. Verdonck. A novel way to assess the mechanical response of self-expanding braided wire stents. In preparation.

- M. Henry, A. Polydorou, N. Frid, P. Gruffaz, A. Cavet, I. Henry, M. Hugel, D. Rufenacht, L. Augsburger, M. De Beule, P. Verdonck, H. Bonneau, C. Kang, C. Wared, and B. Chopard. Renal artery aneurysm: first human treatment with the multilayer stent. *Journal of Endovascular Therapy*. Accepted for publication.

Book chapters

- M. De Beule, Biomechanical modeling of stents: survey 1997 - 2007. *Advances in Biomedical engineering*, Elsevier, Amsterdam, The Netherlands. Accepted for publication.

- M. De Beule, Finite element wire stent design. *Angioplasty Research Progress*, Nova Science Publishers, Hauppauge (NY), United States. Accepted for publication.

Abbreviations and symbols

Abbreviations

2D	two-dimensional
3D	three-dimensional
AHA	American heart association
AS	asymmetry index
BMS	bare metal stent
C3D8R	three-dimensional 8-node brick reduced integration element
CAD	computer aided design
CAE	computer aided engineering
CFD	computational fluid dynamics
CoCr	cobalt-cromium
CT	computer tomography
DB	dogboning index
DES	drug eluting stent
DHS	double-helix stent
FDA	food and drug administration
FEA	finite element analysis
FEM	finite element method
FS	foreshortening
FSI	fluid-structure interaction
GPL	general public license
GUI	graphical user interface
IFEM	immersed finite element method
LDL	low density lipoprotein
M3D4R	4-node quadrilateral membrane element
MIS	minimally invasive surgery
MRI	magnetic resonance imaging
NE	North-East

PET	polyethylene terephthalate
R&D	research and development
R3D4	4-node bilinear rigid quadrilateral element
SMA	shape memory alloy
SE	South-East
SS316L	316-L stainless steel
WSS	wall shear stress

Symbols

c	number of coils
d	wire diameter
D	diameter
dS	length of elementary spring segment
dz	wire curvature
E	Young's modulus
F	force
G	shear modulus
I	moment of inertia
I_p	polar moment of inertia
K	stiffness
L	length
l_p	wire length of one revolution
m_b	bending moment
m_t	twisting moment
M	moment
n	total number of wires
p	pressure
q	radial line pressure
R	radius
t	thickness
T	tensile force
W	weight factor

Greek Symbols

β	pitch angle
δ	elongation
ϵ	strain
ϕ	angular rotation

κ	wire curvature
μ	micro
π	pi
σ	stress
τ	shear stress
θ	wire twist
ν	Poisson's ratio

Subscripts

0	initial
b	balloon
c	catheter
e	external
grip	intergrip
L	longitudinal
load	loaded configuration
max	maximum
mod	modified
nom	nominal
opt	optimized
ori	original
p	radial
ref	reference
start	starting
θ	circumferential
true	true
unload	unloaded configuration
w	wire
z	axial

Operators

cos	cosine
∂	partial derivative
Δ	difference
sec	secant
sin	sine
tan	tangent

Units

atm	atmosphere
GPa	gigapascal
kg	kilogram
KPa	kilopascal
μm	micrometer
m	meter
mm	millimeter
MPa	megapascal
N	Newton
Pa	Pascal